Investigation of the Genetic Etiology of Superior Coloboma and the Formation and Closure of Superior Ocular Sulcus

by

Kevin Hyunjin Yoon

A thesis submitted in partial fulfillment of the requirements for the degree of

Doctor of Philosophy

in

Molecular Biology and Genetics

Department of Biological Sciences

University of Alberta

Abstract

Congenital ocular coloboma is a rare genetic disorder that is typically observed as a cleft in the inferior aspect of the eye due to failed choroid fissure closure during embryogenesis. Together with microphthalmia (small eyes) and anophthalmia (absence of eyes), it represents 3-11% of childhood blindness worldwide. In addition to environmental factors, genetic analyses of coloboma patients have revealed many key eye development genes associated with ocular coloboma, involved in regulation of initial specification of the eye field, migration of retinal precursors, patterning of the retina, neural crest cell biology, and activity of head mesoderm.

In this thesis, we describe individuals with coloboma in the superior aspect of the iris, leading to the discovery of a novel developmental structure, referred to as the superior ocular sulcus (SOS), that is transiently present on the dorsal aspect of the optic cup during early vertebrate eye development. Through our analysis of patient exome-sequencing data and the use of zebrafish, we investigate the roles of dorsal eye patterning genes, *BMPR1A* and *TBX2*, and determine that aberrant dorsal eye patterning results in SOS closure defects, and that the SOS acts as a conduit for blood vessels.

Additionally, I investigate the role of another key dorsal-ventral (DV) eye axis patterning gene, *VAX2*, a transcription factor regulated by Shh signaling that is expressed in the ventral eye. I observe that maternal zygotic homozygous *vax2*-null embryos display SOS closure delay. In addition, overexpression of human wildtype *VAX2* mRNA in zebrafish embryos leads to SOS closure delay and perturbed expression of DV eye axis patterning genes. Analysis of the patient variant (p.Leu139Met) conclusively demonstrates decreased activity when compared to wildtype *VAX2*, indicating that the patient variant is likely to be hypomorphic. These findings suggest that

SOS closure requires a tightly-regulated expression of *vax2*, wherein both loss and increase in *vax2* expression can result in improper closure.

Subsequently, I present a brief investigation of the role of *TSC2*, a key regulator of mTOR signaling, on SOS closure. Through a morpholino-based knockdown approach, I establish that loss of *tsc2* in zebrafish results in SOS closure delay, thus identifying the mTOR signaling pathway as a possible regulator of SOS closure during eye development, independent of DV eye axis patterning.

Finally, in an effort to expand our understanding of the genetic etiology of superior coloboma and the genetic factors that regulate SOS formation and closure, I present an RNA-Seq data set generated from our models of SOS closure delay.

Overall, this thesis aims to identify genetic factors that regulate the SOS to reveal the etiology of superior coloboma, a disorder of which there is very little known. In addition, these studies of the SOS add to the current understanding of eye development as a whole, as we begin to elucidate the role of this novel developmental structure during early embryogenesis.

Preface

This thesis is an original work by Kevin H. Yoon. The studies, of which this thesis is a part, have received research ethics approval from the University of Alberta Animal Policy and Welfare Committee. The author has met the Canadian Council on Animal Care (CCAC) mandatory training requirements for animal users on the Care and Use of Animals in Research, Teaching, and Testing. All protocols were approved by the University of Alberta's Animal Care and Use Committee.

A version of Chapter 1 is published:

Yoon, K.H.*, Fox, S.C.*, Dicipulo, R., Lehmann, O.J., & Waskiewicz, A.J. (2020). Ocular coloboma: Genetic variants reveal a dynamic model of eye development. *Am J Med Genet C Semin Med Genet*, 184(3):590-610. doi: 10.1002/ajmg.c.31831. Epub 2020 Aug 27. PMID: 32852110. *joint first authors

In this review, I wrote Sections 3, 4, 5, 10; created Figures 2 and 3 (presented here as Figures 1.2 and 1.3, respectively); edited the manuscript with co-authors; and addressed all revisions related to Sections 1, 2, 3, 4, 5, and 10.

A version of Chapter 3 is published:

Hocking, J.C.*, Famulski, J.K.*, Yoon, K.H., Widen, S.A., Bernstein, C.S., Koch, S., Weiss, O., FORGE Canada Consortium, Agarwala, S., Inbal, A., Lehmann, O.J., & Waskiewicz, A.J. (2018). Morphogenetic defects underlie Superior Coloboma, a newly identified closure disorder of the dorsal eye. *PLoS Genet*, 14(3):e1007246. doi: 10.1371/journal.pgen.1007246. PMID: 29522511; PMCID: PMC5862500. *joint first authors

In this research article, I performed all of the *tbx2b* experiments, imaged and analyzed data related to *tbx2b*, created Figure 6 (presented here as Figure 3.11), and aided in the editing of the manuscript.

Subsequently, my thesis work resulted in Figure 3.12, which was not published, but is included in Chapter 3.

A version of Appendix A is published:

Yoon, K.H., Widen, S.A., Wilson, M.M., Hocking, J.C., & Waskiewicz, A.J. (2019). Visualization of the Superior Ocular Sulcus during Danio rerio Embryogenesis. *J Vis Exp*, (145). doi: 10.3791/59259. PMID: 30985739.

In this methods article, I performed all experiments, generated all figures, wrote everything except for Protocols #2 and #3, edited the manuscript, and addressed all of the revisions. In addition, I prepared the script used for preparing a video protocol presented online, for which I also demonstrated the protocols.

A version of Appendix B is published:

Kerek, E.M., Yoon, K.H., Luo, S.Y., Chen, J., Valencia, R., Julien, O., Waskiewicz, A.J., & Hubbard, B.P. (2021). A conserved acetylation switch enables pharmacological control of tubby-like protein stability. *J Biol Chem*, 296:100073. doi: 10.1074/jbc.RA120.015839. Epub 2020 Nov 23. PMID: 33187986; PMCID: PMC7948452.

In this research article, I designed and performed all experiments related to zebrafish, analyzed data, wrote portions of the original manuscript related to my work, aided in figure creation, and edited the content related to the zebrafish experiments. I directly generated the data presented in Figure 6BCEF (presented here at Figure B.6BCEF), and I prepared and provided the cell lysates required for Figure 6ADGH (presented here at Figure B.6ADGH).

Acknowledgements

First, I express my deepest gratitude to my supervisor, Dr. Andrew Waskiewicz, for his help throughout my degree. Under his guidance, I was able to grow as a critical thinker, become a better leader, and develop as an effective mentor. I would not be the scientist I am today without his tutelage.

Additionally, I would like to thank the past and present members of my supervisory committee, Drs. Ordan Lehmann, Heather McDermid, and Kirst King-Jones. I truly appreciate all of their support, patience, and encouragement throughout the many years of my degree.

Thank you to all former and present members of the Waskiewicz lab with whom I have had the great pleasure to work and get to know over the years: Dr. Jennifer Hocking, Dr. Laura Pillay, Dr. Caroline Cheng, Jennifer Weekes, Dr. Lyndsay Selland, Dr. Sonya Widen, Dr. Kacey Mackowetzky, Dr. Paul Chrystal, Melissa Wilson, Jens Herzog, Renée Dicipulo, Sabrina Fox, and Ehsan Misaghi. My thesis would not have been possible without those who came before me, and my sanity would not have been preserved without those who shared laughs with me.

In addition, I would like to thank the undergraduate students that I was able to mentor personally in the lab, as well as those I encountered throughout my teaching assistantships. Their enthusiasm for many of the things that I grew to take for granted was a wonderful reminder of why I decided to pursue a career in research. I hope I was able to spark within them what they reignited within me.

Thank you to my family and friends for supporting me throughout my degree. Especially to my Mom, Dad, and my sister, Sarah, thank you for making countless sacrifices, always supporting my decisions, understanding my choices, and helping me overcome my struggles.

Finally and most importantly, thank you to my partner, Ema Allemano. Thank you for being a patient and caring partner. Thank you for supporting me through all that life has thrown our way. Thank you for helping me become a better person. Thank you for reminding me of the big picture. Thank you for everything.

Special thanks to our ~~son~~ ~~cat~~ cat-son, Mochi, for being the cutest little big boy. His insatiable appetite for life (and food) helps me keep everything in perspective.

Table of Contents

Chapter 1

Chapter 2

Chapter 6

Chapter 7

Appendix A

List of Tables

List of Figures

List of Common Abbreviations

°C	Degrees celsius
1000G	1000 Genomes
aa	Amino acid
aldh	Aldehyde dehydrogenase
ANOVA	Analysis of variance
AP	Anterior-posterior
BCIP	5-bromo-4-chloro-3-indolyl-phosphate
BMP	Bone morphogenetic protein
bp	Base pairs
BP	Biological process
BSA	Bovine serum albumin
Carb	Carbenicillin
CC	Cellular component
cDNA	Complimentary DNA
CDS	Coding sequence
CHARGE	Coloboma, Heart defects, Atresia choanae, Growth retardation, Genital abnormalities, and Ear abnormalities
CRISPR	Clustered regularly interspaced palindromic repeats
CNV	Copy number variation
DAPI	4′,6-diamidino-2-phenylindole
DEPC	Diethylpyrocarbonate
DIC	Differential interference contrast
DIG	Digoxigenin
DMH1	Dorsomorphin homolog 1
DMSO	Dimethylsulfoxide
DNA	Deoxyribonucleic acid
DNase	Deoxyribonuclease
dNTP	Deoxyribonucleotide triphosphate
dpf	Days post-fertilization

DRV	Dorsal radial vessel
DV	Dorsal-ventral
EDTA	Ethylenediaminetetraacetic acid
EM	Embryo media
EtOH	Ethanol
ExAC	The Exome Aggregation Consortium
FGF	Fibroblast growth factor
FORGE	Finding Of Rare Disease Genes
GDF	Growth differentiation factor
GFP	Green fluorescent protein
GO	Gene ontology
gnomAD	The Genome Aggregation Database
GTP	Guanosine triphosphate
HCl	Hydrogen chloride
hpf	Hours post-fertilization
HRM	High resolution melt
HRP	Horseradish peroxidase
IPTG	Isopropyl β-D-1-thiogalactopyranoside
kb	Kilobase
KEGG	Kyoto Encyclopedia of Genes and Genomes
LB	Lysogeny broth
MAC	Microphthalmia, Anophthalmia, and Coloboma
MeOH	Methanol
MF	Molecular function
$MgCl_2$	Magnesium chloride
mL	Millilitre
mM	Millimolar
MIDAS	Microphthalmia, Dermal Aplasia, and Sclerocornea
MO	Morpholino
mRNA	Messenger RNA
µL	Microlitre

µm	Micrometre
µM	Micromolar
n.s.	Not significant
NaCl	Sodium chloride
NaOAc	Sodium oxaloacetate
NaOH	Sodium hydroxide
NBT	Nitro-blue-tetrazolium
NGS	Next-generation sequencing
nL	Nanolitre
NT	Nasal-temporal
OC	Ocular coloboma
OMIM	Online Mendelian Inheritance in Man
ORF	Open reading frame
PAM	Protospacer adjacent motif
PBS	Phosphate buffered saline
PBST	Phosphate buffered saline + 0.1% Tween-20
PCP	Planar cell polarity
PCR	Polymerase chain reaction
PFA	Paraformaldehyde
pg	Picogram
POM	Periocular mesenchyme
PTU	1-phenyl 2-thiourea
PVDF	Polyvinylidene difluoride
qPCR	Quantitative real-time polymerase chain reaction
RA	Retinoic acid
RNA	Ribonucleic acid
RNase	Ribonuclease
RNA-Seq	RNA sequencing
rpm	Revolutions per minute
RT-PCR	Reverse transcription polymerase chain reaction
SDS	Sodium dodecyl sulfate

SEM	Scanning electron microscopy
sgRNA	Single guide RNA
Shh	Sonic hedgehog
SNP	Single nucleotide polymorphism
SOS	Superior ocular sulcus
SS	Somite stage
SSC	Sodium saline citrate
T_m	Melting temperature
TBST	Tris-buffered saline + 0.1% Tween-20
Tbx	T-box transcription factor
Tg	Transgene
TSC	Tuberous sclerosis complex
UV	Ultraviolet
Vax	Ventral anterior homeobox
WES	Whole exome sequencing
Wnt	Wingless/integrated
WT	Wildtype
x g	Times gravity

Chapter 1

Introduction

A version of this chapter is published: Yoon, K.H.*, Fox, S.C.*, Dicipulo, R., Lehmann, O.J., Waskiewicz, A.J. (2020). Ocular coloboma: Genetic variants reveal a dynamic model of eye development. *Am J Med Genet C Semin Med Genet*, 184(3):590-610. doi: 10.1002/ajmg.c.31831. Epub 2020 Aug 27. PMID: 32852110. *joint first authors

1.1. Introduction

Ocular coloboma is an eye disease that occurs in 2 to 19 per 100,000 live births, and commonly manifests as a gap in the inferior region of the closed-ring structure of the iris (Fig. 1.1; Bermejo & Martínez-Frías, 1998; Lu, 1989; Morrison et al., 2002; Porges et al., 1992; Shah et al., 2011; Stoll et al., 1997). It can present anteriorly, posteriorly, or both, thereby affecting the iris, lens, retina, and optic nerve, and it is frequently blinding (Shah et al., 2012). The ocular coloboma can occur in isolated fashion or as a component of a syndrome, including CHARGE (Coloboma, Heart defects, Atresia choanae, Growth retardation, Genital abnormalities, and Ear abnormalities), Lenz, Meckel-Gruber, and MIDAS (Microphthalmia, Dermal Aplasia, and Sclerocornea). Coloboma is also part of a spectrum of ocular disorders including microphthalmia (small eye) and anophthalmia (lack of eye), with the three disorders collectively known as MAC (Microphthalmia, Anophthalmia, and Coloboma). Together with microphthalmia, coloboma has been associated with up to 10% of pediatric blindness (Chang et al., 2006; Fujiki et al., 1982; George et al., 2020).

During early eye morphogenesis, a structure called the choroid fissure forms in the inferior/ventral side of the optic cup. The resulting gap allows entry of early vasculature into the optic cup, after which the fissure fuses to enclose the vessels and complete the initial formation of the eye. The closure of the choroid fissure is a key element of optic cup formation and proper eye development, and its failure to close is known to be a cause of congenital ocular coloboma.

The vast majority of coloboma cases afflict the inferior/ventral surface of the eye. However, there are rare examples in the scientific literature of patients presenting with coloboma aligned either horizontally (toward the nasal or temporal region) or superiorly (Fig. 1.1). Studies of superior coloboma led to the identification of a second ocular groove – the superior ocular sulcus, a structure that is tightly regulated during development.

This review will discuss the discovery of loci associated with coloboma and modelling of coloboma in animal models. The original loci discovered in causing coloboma defined a series of static signaling interactions occurring within the retinal epithelium. Whilst such mechanisms remain a major cause of coloboma, recent research in mouse and zebrafish has revealed a new model for eye development that incorporates movement of neuroepithelial layers, migration of retinal precursor cells and cellular remodeling that is regulated by periocular mesenchyme (POM),

a population of cells located immediately adjacent to the closing choroid fissure. Understanding the genes, biological processes and cell populations underlying choroid fissure closure is important for identifying coloboma-associated loci and the underlying developmental etiology of this ocular disease, which in turn will aid in diagnosis and counselling of patients affected by MAC spectrum disorders.

1.2. Modeling patient variants in mouse & zebrafish

MAC spectrum disorders display recessive and dominant inheritance patterns with both unilateral and bilateral eyes affected. Coloboma patients analyzed with next generation sequencing (NGS) may display variants in the 40 known loci (a portion of which are listed in Table 1), but it is estimated that such a list explains causality of fewer than 25% of cases (Forrester & Merz, 2006; Källén et al., 1996; Schneider et al., 2009; Slavotinek, 2011; Verma & Fitzpatrick, 2007). The challenge we face is that many patients present without extensive multi-generational disease inheritance, which makes unequivocal assignment of disease causality impossible. Many computational approaches exist for identifying strong candidate novel loci, and these strategies have been discussed in great detail elsewhere (Doncheva et al., 2012; Moreau & Tranchevent, 2012; Neu et al., 2019; Piro & di Cunto, 2012; Priest, 2017; Tetreault et al., 2015; Tomar et al., 2019; Tranchevent et al., 2016; Wise et al., 2019). Once identified, novel sequence variants are classified according to their predicted pathogenicity according to standards and guidelines as recommended by the American College of Medical Genetics and Genomics. Briefly, the guidelines provide a set of criteria to categorize a variant depending on the strength of evidence of pathogenicity and benignity, which are combined to classify the variant as pathogenic, likely pathogenic, benign, or likely benign (Richards et al., 2015).

Once a candidate novel locus with strong bioinformatic scores is identified, analysis of pathogenicity will include measuring activity in cultured cells as well as studies in animal models. While simple organisms, such as yeast, worms, and flies are excellent models for high throughput screens due to their short generation times and ease of genetic manipulation, the highly evolutionarily divergent genomes and anatomical differences create difficulties in modeling human disease-associated mutations (Apfeld & Alper, 2018; Mirzoyan et al., 2019; Mohammadi,

et al., 2015). In contrast, the zebrafish genome contains 82% of the disease-associated genes found in human, and an extensive genetic toolkit available makes the zebrafish model amenable to genetic manipulation (Howe et al., 2013; Wangler et al., 2017). Furthermore, many of the phenotypes seen in humans can be observed in zebrafish, which makes it an excellent model for human diseases (Enikanolaiye & Justice, 2019; Patton & Zon, 2001; Wangler et al., 2017). Mouse shares an even greater degree of phenotypic similarity to human than zebrafish, and 97.5% of human genes have orthologs in mouse (Waterston et al., 2002). While it can be difficult to perform high throughput screens using mouse, it is an ideal model through which the genetics and the biology of human diseases can be studied (Enikanolaiye & Justice, 2019; Hmeljak & Justice, 2019).

A combination of knockdown and CRISPR-mediated knockout approaches will assess the functional relevance of gene activity in ocular development. To ascertain the effects of the patient variant, one can increase expression using mRNA injection, transgenesis, or knock-in models. Variants that display altered biological activity represent strong candidate coloboma-causing loci. Elucidating the functions of these candidate genes through studies in model organisms gives us greater insight into the genetic factors required for proper eye morphogenesis. In turn, as important signaling pathways are identified and investigated, genes crucial to proper eye morphogenesis may be identified, which allows additional disease-causing genes to be included in the analysis of patient NGS data to aid in diagnosis. The genes included in Table 1 outline both known coloboma-causing loci as well as candidate genes supported by extensive studies in model systems.

1.3. Specification of the eye field

Choroid fissure closure is a highly regulated process, and disturbances in every stage of early eye development may result in MAC. This review will discuss the biological functions of human variants and will be presented in temporal order of eye development. To understand these diseases, it is imperative to gain insight into the development of the eye itself. The presumptive site of eye formation, called the eye field, is formed from the anteriormost portion of the presumptive neural tissue, called the neural plate (Fig. 1.2). The specification of the eye field requires genetic factors that confer retinal identity to the cells, and many of these genes have been identified as disease-causing loci in human eye disorders, including MAC.

Mutations in human *SINE OCULUS HOMEOBOX 3* (*SIX3,* OMIM 603714) were initially described in patients with holoprosencephaly, a congenital forebrain malformation resulting in midline deficiencies of brain and facial structures (Wallis et al., 1999) and also with schizencephaly, a rare congenital brain malformation (Hehr et al., 2010). In addition to its effects on brain development, holoprosencephaly is characterized by a range of ocular phenotypes, such as microphthalmia, anophthalmia, and coloboma (Pineda-Alvarez et al., 2011). Following the establishment of the eye field, *Six3* represses canonical Wnt signaling to allow subsequent development of optic vesicles (Braun et al., 2003; Lagutin et al., 2003). *Six3* is a homeobox-containing transcription factor and is an ortholog of the *Drosophila* gene, *Optix* (Oliver et al., 1995; Seimiya & Gehring, 2000). Its importance is highlighted by experiments in which overexpressed *Six3* cause the formation of ectopic eye cups (Loosli et al., 1999). A zebrafish model for *six3* loss-of-function revealed that zebrafish orthologs of *six3* are important for optic nerve formation, and their absence during embryonic development results in optic disc coloboma (Samuel et al., 2016). Further studies with medaka and mice have demonstrated that *six3*/*Six3* is essential for formation of neural structures anterior to the midbrain (Lagutin et al., 2003). This suggests that *six3*/*Six3* may have a direct role in shaping the canonical Wnt-signaling gradient in the anterior neural plate. As increasing canonical Wnt-signaling levels can prevent *Six3* expression, *Six3* is expressed in areas of low Wnt expression, where it negatively modulates canonical Wnt activity in a self-reinforcing feedback loop (Braun et al., 2003; Lagutin et al., 2003).

While *Six3* is important for maintaining repression of Wnt to allow subsequent developmental stages to occur, a family of transcription factors called retinal homeobox (*Rx*) transcription factors play an integral role in optic cup morphogenesis and photoreceptor specification (Grindley et al., 1995; Mathers et al., 1997; Zhang et al., 2000). Through a screen of 75 patients with anophthalmia and/or microphthalmia, an individual with mutations in both alleles of *RETINAL ANTERIOR ANTERIOR NEURAL FOLD HOMEOBOX* (*RAX*, OMIM 601881) was identified (Voronina et al., 2004). Subsequent studies extended such phenotypes to include coloboma (Abouzeid et al., 2012; Chassaing et al., 2014; Gonzalez-Rodriguez et al., 2010; Huang et al., 2017; Lequeux et al., 2008; London et al., 2009). *Rx* genes are conserved throughout vertebrates, with one ortholog (*Rx*, also known as *Rax*) present in mice and three paralogues (*rx1, rx2,* and *rx3*) present in fish (Chuang & Raymond, 2001). *Rx* genes are responsible for regulating the initial specification of retinal cells and for controlling the rate of retinal progenitor proliferation

within the eye field (Muranishi et al., 2011; Rodgers et al., 2018). Inactivation of *Rx* genes results in complete absence of eyes, which indicates an early role of *Rx* genes in the specification of retinal progenitor cells (RPCs) (Mathers et al., 1997). Misexpression of *rx* genes in zebrafish has been shown to cause expansion of retinal tissue into the forebrain (Chuang & Raymond, 2001).

Variants in *PAIRED BOX GENE 6* (*PAX6*, OMIM 607108) have been associated a wide variety of human eye disorders, most frequently with aniridia, but also with patients with ocular coloboma, foveal hypoplasia, and keratitis (Azuma et al., 1999; Azuma et al., 2003; A. Brown et al., 1998; Hanson et al., 1993; Jordan et al., 1992; Martha et al., 1995). Pax6, a transcription factor, plays a crucial role in inducing eye formation during early stages of eye development. *Pax6* is initially expressed at the anterior neural plate, after which the expression is localized to the optic vesicles and the presumptive lens ectoderm (Del Rio-Tsonis et al., 1995; Grindley et al., 1995; Hirsch & Harris, 1997; Li et al., 1994; Puschel et al., 1992; Walther & Gruss, 1991). Misexpression of mouse, squid, or ascidian *Pax6* in *Drosophila* non-eye imaginal discs can lead to ectopic eye formation (Glardon et al., 1997; Halder et al., 1995; Tomarev et al., 1997). However, ectopic eyes will form only when misexpressed in certain competent tissues, which indicates requirement of other factors in inducing eye formation (Glardon et al., 1997; Halder et al., 1995; Tomarev et al., 1997).

Mutations in *ORTHODENTICLE HOMEOBOX 2* (*OTX2*, OMIM 600037) have been linked to ocular malformations such as anophthalmia, microphthalmia, and coloboma, thereby defining a fourth key locus for defining the initial eye field (Ashkenazi-Hoffnung et al., 2010; Dateki et al., 2008; A. Wyatt et al., 2008). *Otx2* is expressed very early throughout anterior forebrain during embryogenesis, preceding expression of any other eye field marker gene (Finkelstein & Perrimon, 1990; Simeone et al., 1993). *Otx2* forms a transcription factor network with *Six3, Rx3,* and *Pax6* to establish the eye field, and is subsequently downregulated (Chuang & Raymond, 2001; Loosli et al., 1999; Mathers et al., 1997).

1.4. Migration of retinal precursors to form optic cup

As the eye field grows, signals from the surrounding telencephalic and diencephalic cells divide the eye field into two discrete structures called optic vesicles (Fig. 1.2). The optic vesicles evaginate laterally and contact surface ectoderm, where they induce formation of the lens. Reciprocal signaling between the optic vesicle and lens result in the formation of the bilayered structure known as the optic cup (Fig. 1.3). Importantly, this process not only requires signals that confer specific cell identities, but also includes those that facilitate physical changes to cell shape as the cells migrate and fold into complex shapes.

Biallelic mutations in *VISUAL SYSTEM HOMEOBOX 2* (*VSX2*, OMIM 142993) have been identified in MAC patients, with disease-causing variants commonly associated with autosomal recessive microphthalmia and anophthalmia (Burkitt Wright et al., 2010; Ferda Percin et al., 2000; Iseri et al., 2010; Reis et al., 2011). Zebrafish and mice lacking expression of *VSX2* orthologs are microphthalmic and have reduced proliferation of retinal progenitor cells (RPCs). Alongside *Six3*, *Vsx2* enables cell proliferation by inhibiting cell cycle inhibitor, *Kip1* (Green et al., 2003; Zhu et al., 2002). Additionally, *VSX2* is widely expressed in the developing neural retina, and an investigation of *VSX2* function in human iPSC cells shows that VSX2 is a regulator of WNT signaling to maintain neural retina identity during later stages of early eye development (Capowski et al., 2016).

Cell proliferation, however, does not appear to be the principal driving force of optic vesicle evagination, as evagination still occurs in the absence of cell proliferation (Harris & Hartenstein, 1991; Kwan et al., 2012). Studies in fish indicate that optic vesicle evagination likely requires directional migratory behavior of RPCs (Rembold et al., 2006). During neurulation, cells of the neural plate converge toward the midline to close the dorsal side of a tube that will form the neural tube (Martinez-Morales & Wittbrodt, 2009; Rembold et al., 2006). RPCs also migrate towards the midline, but migrate at a much slower pace than the other cells. This differential migration pace makes the portion of the embryo that contains the eye field that wider compared to surrounding neural tissue (Fig. 1.2) (Rembold et al., 2006). During their migration towards the midline, RPCs pivot and begin migrating laterally toward the left and right sides of the embryo (Rembold et al., 2006). Cells intercalate and epithelialize, thereby enlarging the surface area of the

optic vesicles (Martinez-Morales & Wittbrodt, 2009). This process involves the activity of Rx3, as in the absence of Rx3 activity, even though RPCs are formed, all cells migrate to the midline at the same pace, and there is no outward migration of RPCs to initiate evagination of the optic vesicles (Rembold et al., 2006). It remains unclear what pathways are targeted by Rx3, although they are likely to include cell adhesion molecules (K. E. Brown et al., 2010; Cavodeassi et al., 2013).

There is strong evidence that cell polarity plays an essential role in migration of RPCs. Studies in *Xenopus* reveal that both *rx* and *pax6* are maintained by *wnt4*, a non-canonical Wnt ligand expressed around the eye field (Maurus et al., 2005). Similar effects are seen in *Xenopus* with loss of Fzd3, a key Wnt receptor in eye development and a regulator of non-canonical Wnt/PCP signaling (Rasmussen et al., 2001; Seigfried et al., 2017). This suggests that proper regulation of planar cell polarity by the non-canonical Wnt pathway is crucial during early vertebrate eye development. This is supported by studies in Fzd5, a Wnt receptor known to mediate both canonical and non-canonical signaling. Studies in zebrafish found that non-canonical Wnt/PCP signaling promote eye field development through Wnt11 and Fzd5, which antagonize canonical Wnt signaling (Cavodeassi et al., 2005). Mouse *Fzd5*$^{-/-}$ mutants failed to form eyes, with optic cup invagination defects in which the lens fails to form (Burns et al., 2008). Conditional knockout mutants for *Fzd5* exhibited both microphthalmia and coloboma, further implicating a role for Fzd5 in vertebrate eye development (C. Liu & Nathans, 2008; C. Liu et al., 2016). This was followed by analysis of a multigenerational pedigree displaying autosomal dominant ocular coloboma (C. Liu et al., 2016). Whole-exome sequencing of the affected individuals revealed a frameshift mutation in *FZD5* (C. Liu et al., 2016). Functional analysis of the frameshift mutant protein indicated that FZD5-mediated non-canonical WNT signaling was likely to be perturbed, resulting in ocular coloboma (C. Liu et al., 2016).

There is much to be investigated to elucidate the role of non-canonical Wnt/PCP signaling in eye development. Wnt8b, Fzd8, and Wnt11 all have known roles during early eye development. Wnt8b expression is sufficient to induce formation of neural retina (Takata et al., 2017). *Fzd8* is known to be expressed in the eye; the loss of a functional copy of *Fzd8* exacerbates the ocular phenotypes observed in *Fzd5*$^{-/-}$ mutant mice (C. Liu et al., 2016). Furthermore, Wnt11 promotes cohesion of eye field cells, thus facilitating the development of a discrete tissue that will become

the presumptive eye (Cavodeassi et al., 2005). Through a process modulated by FGF signaling, Xenopus Dishevelled (Xdsh) was found to interact with EphrinB1 to mediate the movement of retinal progenitor cells to the eye field, further implicating a role for non-canonical/PCP signaling in early eye morphogenesis (Lee et al., 2009; Moore et al., 2004). Although not yet identified to be disease-causing loci, these studies strongly implicate an extensive role for non-canonical Wnt/PCP signaling in ocular coloboma.

The epithelial bending observed during optic cup formation is facilitated by constriction of the cells' basal surfaces. Studies in medaka demonstrated that the transmembrane protein Ojoplano (Opo) controls basal localization of adhesion components to regulate basal constriction of RPCs (Martinez-Morales & Wittbrodt, 2009). Transcriptionally regulated by *vsx2*, Opo regulates integrin-β trafficking through antagonistic interactions with clathrin adaptors, Numb and Numbl (Bogdanovic et al., 2012; Gago-Rodrigues et al., 2015). This interaction allows *opo* to locally stabilize a focal contact point on the basal side of the RPCs by negatively regulating integrin endocytosis (Bogdanovic et al., 2012). This creates a triangular, basally-restricted cell shape to facilitate bending of the optic cup (Bogdanovic et al., 2012).

With the invagination of its distal end, the spherical optic vesicle transforms into the hemispherical optic cup with two epithelial layers: the distal epithelium closest to the lens becomes the neural retina, while the proximal epithelium closer to the optic stalk becomes the retinal pigmented epithelium. Cell tracking studies in zebrafish indicate that the optic cup grows as cells from the proximal, lens-averted epithelium flow around the distal rims of the optic cup and move into the distal, lens-facing domain (Heermann et al., 2015). This process is BMP-dependent as pan-ocular expression of BMP4 stops the flow of cells into the lens-facing layer, resulting in coloboma phenotypes (Heermann et al., 2015). Additionally, it requires actomyosin-driven constriction at the lens-facing side of the distal epithelium, which facilitates the movement of cells around the distal rim of the optic cup (Sidhaye & Norden, 2017).

Retinoic acid (RA), a derivative of vitamin A, is critically important for optic cup formation. Mutations in *RETINOL-BINDING PROTEIN* (*RBP4*, OMIM 180250), a transport protein for retinol in serum, and in *STIMULATED BY RETINOIC ACID 6* (*STRA6*, OMIM 610745), a transmembrane receptor that mediates uptake of vitamin A, have been associated anophthalmia

and microphthalmia (Casey et al., 2011; Cukras et al., 2012; White et al., 2008). Furthermore, mutations in *ALDEHYDE DEHYDROGENASE 1 FAMILY, MEMBER A3* (*ALDH1A3*, also known as *RALDH3*, OMIM 600463) are known to cause microphthalmia, anophthalmia, and coloboma (Abouzeid et al., 2014; Lin et al., 2018; Roos et al., 2014). During eye development, RA is synthesized in the optic vesicle, the surrounding mesenchyme, and the lens placode (Cvekl & Tamm, 2004; Heavner & Pevny, 2012). Vitamin A, in the form of retinol, is transported in serum by *RBP4*, and its cellular uptake is facilitated by *STRA6* (Blaner, 1989; Bouillet et al., 1997; Kawaguchi et al., 2007). Intracellularly, retinol is metabolized into RA by a group of alcohol dehydrogenases and aldehyde dehydrogenases, such as *ALDH1A3*, after which a number of transcriptional responses is mediated by RA (Nedelec et al., 2019). Investigations of *Aldh1a1* (*Raldh1*), *Aldh1a2* (*Raldh2*), and *Aldh1a3* (*Raldh3*) in mice show that disruption of RA synthesis genes result in the failure of the optic vesicle to initiate invagination (Mic et al., 2004; Molotkov et al., 2006). Thus, RA synthesis is thought to affect early optic cup development by controlling retinal morphogenetic movements rather than specifying identity or patterning (Molotkov et al., 2006). Its role in periocular mesenchyme (POM)-derived eye structures will be discussed below.

1.5. Axis formation

The epithelial bending of the optic cup occurs alongside the axial patterning that confers region-specific cell identities in the developing eye. Interactions between BMP and Shh signaling pathways across the dorsoventral (DV) axis of the developing eye patterns the early eye; BMP signaling induces dorsal fate, while Shh signaling induces ventral fate (Chang et al., 2001; Furuta et al., 1997; Murali et al., 2005). Patterning the optic cup requires a delicate interplay of multiple signaling pathways, and mutations of many of the genes involved in DV axis patterning have been linked to MAC disorders. Recent reviews have comprehensively covered this topic, so the presentation in this review is highly abbreviated (ALSomiry et al., 2019).

In both humans and model organisms, mutations in *GROWTH DIFFERENTIATION FACTOR 6* (*GDF6*, OMIM 601147) are associated with microphthalmia, Klippel-Feil syndrome, and ocular coloboma (Asai-Coakwell et al., 2007; Asai-Coakwell et al., 2009; Asai-Coakwell et al., 2013; den Hollander et al., 2010; Tassabehji et al., 2008). Additionally, mutations in other

regulators of BMP signaling, such as *GDF3* (OMIM 606522), *BMP4* (OMIM 112262), and *CHRDL1* (OMIM 300350) have all been linked to MAC disorders in humans (Bakrania et al., 2010; Webb et al., 2012; Ye et al., 2010). Previous zebrafish studies on the BMP *gdf6a*, an upstream regulator of dorsal eye patterning, found that loss of *gdf6a* led to broad decrease of BMP signaling in the dorsal eye, while ventral eye markers expanded in expression area to the dorsal eye (French et al., 2009; Gosse & Baier, 2009). Further investigations found that *gdf6a* is required to activate expression of *tbx5*, *tbx2* and *efnb2a* (Gross & Dowling, 2005; Koshiba-Takeuchi et al., 2000; Sakuta et al., 2006) as well as regulating RA signaling in the dorsal eye (French et al., 2009; Gosse & Baier, 2009; Valdivia et al., 2016).

The ventral retina is patterned by a separate signaling pathway. Shh from the ventral midline of the forebrain promotes expression of key transcription genes required for ventral retina identity, such as *vax1* and *vax2* (Ekker et al., 1995; Hallonet et al., 1999; Macdonald et al., 1995; Take-uchi et al., 2003). Mutations in *VAX1* have both been associated with coloboma in humans, while mouse model studies show that loss of *Vax2* expression leads to ocular coloboma (Barbieri et al., 2002; Barbieri et al., 1999). Current understanding of interactions between BMP signaling and Shh signaling indicates that Vax2 and Tbx5 antagonize each other. However, the exact mechanisms surrounding their interaction remains unclear, as loss of Vax2 in mice does not result in expansion of Tbx5 expression area into the ventral eye (Barbieri et al., 2002; Barbieri et al., 1999). Regardless, Vax2 acts downstream of Shh to promote differentiation of ventral structures while inhibiting that of dorsal structures.

1.6. Periocular mesenchyme (POM) – neural crest, mesoderm, and vasculature

In addition to the neurectoderm of the optic cup, there is a second population of cells surrounding the eye derived from cranial neural crest and mesoderm. These cells, known collectively as the periocular mesenchyme (POM), have many well-defined roles in ocular development; POM cells are necessary for patterning the optic cup, anterior segment genesis, and development of the extraocular muscles (Fig. 1.4; Creuzet et al., 2005; Fuhrmann et al., 2000; Gage et al., 2005). POM cells also contribute to the ocular vasculature, including the hyaloidal system that transits through the choroid fissure. POM has been implicated in choroid fissure

closure and coloboma. However, the mechanism by which these cells facilitate fissure closure is poorly understood. In this section, we outline the current understanding of neural crest cells and mesoderm in choroid fissure closure and their potential roles in coloboma.

1.7. Neural crest

Neural crest cells are a population of migratory cells that delaminate from the dorsal neural ectoderm during neural tube closure and represent a principal component of POM (Noden, 1983). Cranial neural crest cells originating from the diencephalon and anterior mesencephalon form the extraocular muscles, connective tissue of the orbit, pericytes that line the ocular blood vessels, and components of the anterior segment such as the cornea, sclera, iris stroma, and aqueous humor drainage system (Creuzet et al., 2005; Evans & Gage, 2005; Gage et al., 2005; Langenberg et al., 2008; Trost et al., 2013). Ocular defects are a prominent feature of many diseases caused by aberrancies in neural crest function, collectively termed "neurocristopathies" (Watt & Trainor, 2014).

During ocular development, periocular neural crest cells migrate anteriorly to surround the evaginating optic vesicles (Bryan et al., 2020; Langenberg et al., 2008). After optic cup invagination, cranial neural crest cells migrate around the optic cup in two streams; cells originating from the diencephalon migrate dorsally over the eye cup, whereas cells from the anterior mesencephalon migrate ventrally around the eye cup and through the choroid fissure (Bohnsack & Kahana, 2013; Chawla et al., 2016). Neural crest cells are present in the choroid fissure just after the fissure forms (Bernstein et al., 2018; Gestri et al., 2018; James et al., 2016). Although the precise signals are not yet understood, RPCs play a critical role in recruiting neural crest cells into this region (Langenberg et al., 2008). Thus, a close relationship between the developing ocular tissue and the cranial neural crest exists.

In recent years, it has become increasingly apparent that neural crest cells are necessary for choroid fissure closure. Loss of transcription factors that are expressed in periocular neural crest (*foxc1, pitx2,* and *lmxb1*, *zic2, alx1, tfap2a*) produces coloboma phenotypes in both mouse and zebrafish (Dee et al., 2013; Gage et al., 1999; Gestri et al., 2009; Lupo et al., 2011; McMahon et

al., 2009; Sedykh et al., 2017). Zebrafish eye transplants lacking neural crest contribution have properly formed choroid fissures, however the basal lamina that surround the fissure lobes are absent, suggesting that neural crest cells play a role in extracellular matrix (ECM) remodeling in the fissure (Gestri et al., 2018). Similarly, genetic ablation of all ocular neural crest results in a coloboma phenotype in zebrafish embryos (Bryan et al., 2020).

The cellular functions of ocular neural crest cells have recently been elucidated. Periocular neural crest cells produce nidogen, a molecule that crosslinks laminin and is essential for basement membrane assembly within the choroid fissure (Bryan et al., 2020; Carrara et al., 2019; Mayer et al., 1998). Reduced nidogen production is observed in *foxd3;tfap2a* mutants, resulting aberrant ocular ECM assembly. This disrupts epithelial cells movements in the optic cup during eye morphogenesis, resulting in coloboma (Bryan et al., 2020). This is consistent with other studies showing that laminin alpha-1 (another major component of the ECM) is necessary for ocular morphogenesis (Bryan et al., 2016). Loss of Laminin alpha-1 results in disrupted epithelial polarity, which causes ocular defects such as coloboma (Bryan et al., 2016). Taken together, such research supports a model wherein neural crest cells regulate the deposition and remodeling of the ECM in the vicinity of the optic fissure.

CHARGE (OMIM 214800) is one of the best characterized syndromes in which coloboma is a prominent feature (Pagon et al., 1981). More than half of CHARGE cases are caused by a heterozygous mutation in the gene *CHROMODOMAIN HELICASE DNA-BINDING PROTEIN 7* (*CHD7*, OMIM 608892) (Lalani et al., 2006; Vissers et al., 2004). *CHD7* encodes an ATP-dependent chromatin remodeler regulating apoptosis and neural crest cell survival (Schnetz et al., 2010). Notably, *Chd7*/*chd7* is expressed in neural crest cells in mouse and xenopus, and knockdown of *chd7* in Xenopus results in CHARGE syndrome phenotypes, including coloboma (Bajpai et al., 2010; Fujita et al., 2014). In Xenopus, Chd7 interacts with PBAF (polybromo- and BRG1-asscoaited factor-containing complex) and controls the regulation of genes involved in neural crest identity, including s*ox9* and *twist1* (Bajpai et al., 2010). Furthermore, induced pluripotent stem cells (iPSCS) derived from patients with CHARGE syndrome have changes in gene expression for genes associated with neural crest cell migration and adhesion (Okuno et al., 2017). Interestingly, mutations in two members of the class 3 semaphorin (SEMA3) family of guidance molecules, *SEMA3A* (OMIM 603961) and *SEMA3E* (OMIM 608166), have been found

in patients with CHARGE (Z. Z. Liu et al., 2019; Schulz et al., 2014; Ufartes et al., 2018). Overexpressing *sema3* or *sema3e* in zebrafish and Xenopus models of *chd7* deficiency rescues CHARGE phenotypes, suggesting that *CHD7* also regulates neural crest migration via control of class 3 semaphorin expression (Z. Z. Liu et al., 2019; Schulz et al., 2014; Ufartes et al., 2018). This is consistent with other experiments that demonstrate binding of Chd7 to the promoter sequences of genes encoding class 3 semaphorins (Payne et al., 2015; Ufartes et al., 2018). Taken together, this suggests that *CHD7* regulates both neural crest identity and motility, and aberrancies in neural crest function and migration in CHARGE patients contribute to the development of several phenotypes.

CHARGE is not the only neurocristopathy that has been associated with coloboma; mutations in *MICROPHTHALMIA-ASSOCIATED TRANSCRIPTION FACTOR* (*MITF,* OMIM 156845), a transcription factor typically associated with Waardenburg Syndrome Type 2A (OMIM 193510), have also been associated with coloboma (George et al., 2016). *MITF* promotes the differentiation of neural crest cells into melanocytes, and its expression is regulated by PAX3 and SOX10, transcription factors within neural crest cells (Bondurand et al., 2000; Potterf et al., 2000).

Mutations in other human genes associated with neural crest function have also been associated with coloboma. Patients with mutations in *TRANSCRIPTION FACTOR AP-2 ALPHA* (*TFAP2A,* OMIM 107580) have branchio-oculo-facial syndrome (BOFS, OMIM 113620), a condition characterized by branchial cleft sinus defects, cleft palate/lip, and occasionally hearing loss (Milunsky et al., 2008; Raveh et al., 2000; Tekin et al., 2009). Additionally, BOFS patients commonly display ocular abnormalities such as coloboma, microphthalmia and lacrimal duct obstruction (Gestri et al., 2009; Tekin et al., 2009). *TFAP2A* (OMIM 107580) encodes AP-2α, a transcription factor expressed in the periocular neural crest (Knight et al., 2003; Mitchell et al., 1991). Mouse and zebrafish models lacking *Tfap2a* display coloboma, suggesting that this locus is required for choroid fissure closure (Gestri et al., 2009). *TFAP2A* is a downstream target of the Retinoic Acid signaling pathway, which in addition to its role in early eye morphogenesis, also has roles in periocular mesenchyme-mediated eye development. Periocular neural crest cells highly regulated by RA signaling, and neural crest-specific ablation of the genes encoding retinoic acid receptors Rarβ and Rarγ results in severe ocular defects in mouse (Matt et al., 2005; Matt et al., 2008). Exogenous treatment with RA and inhibition of RA synthesis both affect the ventral

stream of periocular neural crest cells, suggesting that tight regulation of RA signaling must be maintained for proper neural crest migration toward the eye (Chawla et al., 2016). Consistent with this, neural crest-specific ablation of RA signaling results in compound eye defects, including anophthalmia, microphthalmia, and coloboma (Matt et al., 2005; Matt et al., 2008). In zebrafish, impairing RA signaling results in coloboma, further supporting a role for RA signaling in the regulation of POM (Lupo et al., 2011).

Another output of RA signaling, *PAIRED-LIKE HOMEODOMAIN TRANSCRIPTION FACTOR 2* (*PITX2,* OMIM 601542)*,* has also been implicated in coloboma. *PITX2* has previously been associated with the Axenfeld-Reiger Syndrome (ARS, OMIM 180500), characterized primarily by defects in anterior segment genesis such as iris hypoplasia, iris polycoria, iris corectopia, posterior embryotoxon, and connection of iris strands to the trabecular meshwork (Tumer & Bach-Holm, 2009). Additionally, approximately half of cases of ARS develop elevated intraocular pressure, which in turn leads to glaucoma (Tumer & Bach-Holm, 2009). Rare cases of microphthalmia and coloboma in patients with ARS have been reported, and reports of coloboma in patients with mutations in *PITX2* are also extremely rare (Hendee et al., 2018; Ozeki et al., 1999). In mice and zebrafish, *Pitx2*/*pitx2* is expressed in the periocular mesenchyme (Semina et al., 1996; Volkmann et al., 2011) and loss of *Pitx2*/*pitx2* causes coloboma (Gage et al., 1999; Hendee et al., 2018; Lupo et al., 2011).

LIM HOMEOBOX TRANSCRIPTION FACTOR 1 BETA (*LMX1B,* OMIM 602575), another POM-associated transcription factor, has been recently implicated as a causative gene for coloboma. In humans, heterozygous loss-of-function mutations in *LMX1B* cause nail patella syndrome (NPS, OMIM 161200) (Vollrath et al., 1998). NPS patients typically present with skeletal, joint, central nervous system and renal abnormalities, however elevated intraocular pressure leading to glaucoma is also observed (Vollrath et al., 1998). To date, there are no reports of human mutations in *LMX1B* that cause coloboma (Dreyer et al., 1998; Vollrath et al., 1998). However, knockdown of *lmx1b* in zebrafish causes coloboma (McMahon et al., 2009). In zebrafish, *lmx1b* is necessary for periocular mesenchyme survival and fibroblast growth factor (Fgf) signaling; knockdown of *lmx1b* results in reduced POM survival and changes in Fgf signaling in the eye, which are partially responsible for retinal patterning defects (McMahon et al., 2009). Consistent with its role in patterning, chick and mouse models with *Lmx1b* mutations have

dorsal/ventral limb patterning defects and kidney defects (H. Chen et al., 1998; Hamano et al., 2002; McMahon et al., 2009; Vogel et al., 1995). *Lmx1b* mouse mutants have much milder phenotypes compared to zebrafish, however ocular defects such as anterior segment dysgenesis have been reported (Pressman et al., 2000). *Lmx1b* mutant mice have defects in anterior segment genesis, including corneal, iris, and ciliary body defects (Pressman et al., 2000). Therefore, more research is warranted in determining whether *Lmx1b* is a locus typically associated with coloboma.

In addition to genes that are typically associated with neural crest identity and function, periocular neural crest cells mediate choroid fissure closure via patterning of the optic stalk and ensuring proper evagination from the forebrain. Failure of the optic vesicles to evaginate properly from the forebrain results in holoprosencephaly (HPE, a failure of forebrain separation) and/or coloboma. There is a significant amount of overlap in the genes and pathways that cause HPE and coloboma, and it has even been suggested that HPE and coloboma represent two different severities of the same phenotype (Gongal et al., 2011; Pineda-Alvarez et al., 2011). Mutations in the transcription factor *ZINC FINGER OF THE CEREBELLUM* 2 (*ZIC2,* OMIM 603073) are associated with holoprosencephaly (L. Y. Brown et al., 2001; S. A. Brown et al., 1998; Orioli et al., 2001; Solomon et al., 2010). *ZIC2,* the vertebrate homolog of drosophila *odd-paired,* has well-characterized roles in brain development and morphogenesis, and point mutations in the mouse homolog *Zic2* result in exencephaly and disruptions to eye spacing ranging from hypertelorism to cyclopia (Warr et al., 2008). Recently, it has been shown that *zic2*, a transcription factor expressed in the ocular mesenchyme, promotes the survival of neural crest cells, and when mutated, causes coloboma, hemorrhaging, and holoprosencephaly (Sedykh et al., 2017). *zic2* restricts hedgehog signaling in the ventral head mesenchyme, which in turn restricts *pax2* expression in the ventral eye and optic stalk, ensuring proper patterning of the optic stalk and ventral retina (Sedykh et al., 2017). *Zic2* directly regulates the expression of transcription factors important for neural crest survival, including *alx1,* suggesting that *zic2* regulates hedgehog signaling non-cell-autonomously via ensuring neural crest survival in the ventral eye (Sedykh et al., 2017). Proper *alx1* expression is also necessary for choroid fissure closure, further suggesting that the survival of neural crest cells is necessary for patterning the ventral retina (Dee et al., 2013). Given these findings, *ZIC2* and *ALX1* are potential coloboma-causing loci.

1.8. Ventral head mesenchyme and extracellular matrix remodeling

The transforming growth factor beta (Tgf-β) family of signaling ligands have also been shown to be necessary for choroid fissure closure. Mutations in Tgf-β pathway components, including *TGFBR1* (OMIM 190181)*, TGFBR2* (OMIM 190182)*, TGFB2* (OMIM 190220)and *SMAD3* (OMIM 603190)*,* have been linked to Loeys-Dietz syndrome, a disorder affecting the connective tissue and cardiovascular systems (Loeys et al., 2005; Loeys et al., 2006). Although craniofacial defects are common in this syndrome, microphthalmia, anophthalmia, and coloboma have not been reported (Busch et al., 2018). Studies utilizing transgenic zebrafish reporter lines show active Tgf-β signaling in the fissure, and many components of the Tgf-β signaling pathway are expressed in periocular tissues, including the signaling ligands Tgfb2, Tgfb3, and their receptor Tgfbr2b (Knickmeyer et al., 2018). Mutation of *Tgfb2* in mice and pharmacological inhibition of Tgf-β signaling in zebrafish both result in coloboma phenotypes, further supporting a role for this signaling pathway in choroid fissure closure. In neural crest-specific *Tgfbr2* knockout mice, mutants display microphthalmia (Ittner et al., 2005). The precise mechanism underlying Tgf-β mediated choroid fissure closure is not well understood; it has been suggested that Tgf-β signaling from the ocular mesenchyme promotes the expression of BMP antagonists in the ventral eye, thus restricting BMP signaling to the dorsal eye and allowing for the bilateral flow of epithelial cells into the fissure in the optic cup (Knickmeyer et al., 2018). Tgf-β signaling also has well defined roles in extracellular matrix remodeling, suggesting this pathway may act by breaking down the basement membrane surrounding the fissure (Knickmeyer et al., 2018; Roberts et al., 1986). Additionally, Tgf-β signaling is sufficient to transform neural crest cells into pericytes, implicating this process in promoting stability of the hyaloid vessel that transits through the choroid fissure during development (S. Chen & Lechleider, 2004).

Another member of the Tgf-β superfamily of signaling ligands, *BONE MORPHOGENETIC PROTEIN* 7 (*BMP7,* OMIM 112267)*,* is also likely a regulator of choroid fissure closure. Human patients with mutations in *BMP7* have microphthalmia and anophthalmia in addition to other systemic abnormalities (A. W. Wyatt et al., 2010). Bmp7 mutant mice have renal, skeletal and ocular abnormalities, including anophthalmia and microphthalmia (Dudley et al., 1995; Morcillo et al., 2006). In mouse, *Bmp7* is necessary for choroid fissure formation during

early ocular morphogenesis (Morcillo et al., 2006). Treatment of organotypic culture of optic vesicles with Bmp7 is sufficient to promote the expression of *Pax2* in the ventral optic cup, suggesting that Bmp7 is secreted from the surrounding ventral ocular mesenchyme and has a similar role to Shh in the early optic cup in promoting Pax2 expression in the developing optic stalk (Morcillo et al., 2006).

Degradation of the basement membrane surrounding the fissure lobes must be carried out to ensure proper fissure closure. Colobomata are a prominent feature in animal models where the basement membrane surrounding the fissure is not remodeled (Barbieri et al., 2002; Macdonald et al., 1997; Torres et al., 1996; Tsuji et al., 2012). Recent studies have shown that extracellular matrix remodeling enzymes belonging to the ADAMTS family of matrix metalloproteinases are critical regulators of fissure closure (Cao et al., 2018; Tsuji et al., 2012). Furthermore, *tln1* mutant zebrafish have a very obvious coloboma phenotype arising from an inability to degrade the basement membrane surrounding the fissure. *tln1* encodes Talin, a linker protein that connects the actin cytoskeleton to integrins on the cell surface. This suggests that actin-based protrusions facilitate fissure closure and that cell movements and dynamics must be carefully regulated for choroid fissure to occur. A recent zebrafish study has shown that F-actin deposition correlates with the entry of the hyaloid vasculature in the eye, and inhibition of VEGF signaling (and thus ocular vascularization) results in loss of ocular *tln1* expression, suggesting that these actin-based protrusions are derived from the developing ocular vasculature (Weaver et al., 2020).

1.9. Mesoderm and vasculature

In addition to neural crest, cranial mesoderm also contributes to the periocular mesenchyme, which contributes to the formation of the embryonic blood vessels (Gage et al., 2005). There are three main vascular systems that nourish the eye during development; the choroidal system, which surrounds the choroid of the developing eye cup, the hyaloidal system, which enters the eye through the choroid fissure and forms a capillary plexus posterior to the lens and nourished the developing lens and retina, and the retinal vasculature system, which serves to nourish the retina later in development (Saint-Geniez & D'Amore, 2004). In most vertebrates, the hyaloid system regresses and is replaced by the retinal vascular system, however in teleost fish (such as zebrafish)

the hyaloid system remains and ultimately becomes the mature retinal vasculature (Evans & Gage, 2005). During embryogenesis, endothelial cells derived from head mesoderm differentiate into endothelial cells that make up the hyaloidal vasculature (Gage et al., 2005). These cells enter the eye via the choroid fissure through angiogenesis, a process in which new vessels sprout and branch from pre-existing ones (Gage et al., 2005). Additionally, cranial neural crest cells differentiate into pericytes, which surround and support the ocular vasculature (Etchevers et al., 2001; Trost et al., 2013).

In humans, failure of the hyaloid system to regress causes persistent fetal vasculature, a blinding disorder characterized by remnants of the hyaloid system in the eye at birth (Promelle et al., 2019). There have been rare cases of patients presenting with both persistent fetal vasculature and coloboma, suggesting there might be a shared etiology or a cause-and-effect relationship between these two processes (Graziano et al., 2017; Ranchod et al., 2010; Rothfield et al., 2019; Takkar et al., 2016; Weiner & Nudleman, 2019). The lobes of the choroid fissure and the developing hyaloid vasculature come into contact prior to closure of the fissure, suggesting that the hyaloid vessels may act as a scaffold that is necessary for choroid fissure closure (Eckert et al., 2020). Proper maintenance and development of the hyaloid vasculature is essential for choroid fissure closure and disrupting the hyaloid vessel can lead to disrupted choroid fissure closure (James et al., 2016; Weiss et al., 2012). *lmo2* mutant zebrafish have dilated blood vessels, which prevents choroid fissure closure from occurring normally (Weiss et al., 2012). Similarly, *cloche* mutants, which lack all endothelial cells, also have delayed choroid fissure closure. It has been suggested that blood vessels themselves secrete signals that promote basement membrane breakdown and choroid fissure closure; endothelial cells have been shown to secrete ECM remodeling proteins such as matrix metalloproteinases, therefore it is plausible that blood vessels play an active role in breaking down the basement membrane surrounding the fissure prior to closure; a recent study performed in zebrafish showed that the endothelial cells of the hyaloid system produce and secrete Mmp2, a matrix metalloproteinase that has well-characterized roles in extracellular matrix breakdown and remodeling (Weaver et al., 2020). Pharmacological inhibition of *mmp2* results in choroid fissure closure defects, suggesting that *mmp2* production by the hyaloid is an essential step of choroid fissure closure (Weaver et al., 2020).

1.10. Atypical coloboma

There is a rare subset of ocular coloboma, called atypical coloboma, which is described as a coloboma that presents in the nasal, temporal, or superior aspects of the eye (Abouzeid et al., 2009; Hocking et al., 2018; Jain et al., 2018; Kumar et al., 2020; Onwochei et al., 2000). While ocular coloboma has been studied extensively and the importance of choroid fissure closure has been established, little is known regarding the atypical coloboma. Thus far, all of the identified cases appear to be sporadic, with no known family history of a similar disease. Although the etiology of atypical coloboma remains to be characterized, there is evidence to suggest a structural and genetic basis for the phenotype.

Recently, an investigation of zebrafish eye development led to the discovery of a second ocular fissure, named superior ocular sulcus or superior fissure, at the 12 o'clock position of the developing eye (Hocking et al., 2018). While the choroid fissure is observable at 20-60 hours post-fertilization (hpf) in zebrafish, the superior fissure is relatively narrow and highly transient, being visible for only 4-5 hours (Hocking et al., 2018). It is evolutionarily conserved across vertebrates, being visible during eye development of fish, chick, newt, and mouse (Hocking et al., 2018). Similar to the choroid fissure, the superior fissure appears to act as a track for vasculature guidance during eye morphogenesis, as altered superior fissure morphology results in aberrant formation of the dorsal radial vessel in the early eye (Hocking et al., 2018).

Analysis of candidate genes from exome sequencing data of five superior coloboma patients revealed rare variants in multiple genes involved in early eye DV axis patterning: *BMPR1A* (the receptor for *GDF6*) and *TBX2* (Hocking et al., 2018). Through investigation in zebrafish, both loss of *gdf6a* or *tbx2b* resulted in delay of superior fissure closure, while treatment with cyclopamine, a Shh inhibitor, was able to rescue this phenotype (Hocking et al., 2018). This demonstrates that the balance between BMP and Shh signaling pathways across the DV axis of the developing eye is important in the formation and closure of both ocular fissures.

1.11. Zebrafish as a model organism

As a model organism, zebrafish provides a number of advantages in studying eye development: it is a vertebrate model; its high fecundity (~100-200 embryos per clutch) allows experiments of large sample size; and its genome has been fully sequenced, which facilitates relative ease of genetic manipulation. In addition, its development takes place externally to the mother, and its larvae are transparent, which allows for the visualization of the developing eye with relative ease (Bilotta & Saszik, 2001). Furthermore, approximately 70% of human genes have at least one zebrafish orthologue, making it an ideal genetics-based model of human disease (Lawson & Wolfe, 2011; Howe et al., 2013).

1.12. Purpose of study and summary of research

Taken together, this thesis aims to elucidate genetic factors involved in the proper closure of the SOS. Exome sequencing data from a group of superior coloboma patients identified in Edmonton have allowed us to identify numerous genes of interest. This thesis will examine the roles of various genes involved in DV eye axis patterning, identify additional genes of interest in SOS formation and closure, and elucidate the role of an additional, separate signaling pathway, specifically mTOR signaling, on SOS closure and eye development.

In Chapter 3, I present our initial characterization of the SOS. We report the morphology of the SOS, investigate the role of dorsal eye patterning genes, *BMPR1A* and *TBX2*, identified in Patients #2 and #3, respectively, and explore the functional role of the SOS during early eye development. We test the hypothesis that loss of dorsal eye patterning leads to abnormal SOS closure. We determine that aberrant dorsal eye patterning results in SOS closure defects, and that the SOS acts as a conduit for blood vessels.

In Chapter 4, I discuss a variant of *VAX2*, a key regulator of ventral eye patterning, identified in Patient #4. I hypothesize that aberrant ventral eye patterning affects SOS closure, similar to that seen in Chapter 3. I investigate the role of *VAX2* in proper SOS closure, elucidating the effects of its loss and overexpression, to explore the functional consequences of the patient

variant. I find that either loss or overexpression of *VAX2* leads to SOS closure delay, and that the patient variant is likely to be a hypomorphic allele.

In Chapter 5, I investigate the effects of a variant of *TSC2*, a crucial regulator of mTOR signaling, identified in Patient #1. I hypothesize that increase in mTOR signaling through the loss of *tsc2* leads to SOS closure delay in zebrafish. Through a morpholino-based knockdown approach, I find that knockdown of *tsc2* results in SOS closure delay, thus identifying the mTOR signaling pathway as a possible effector of the SOS during eye development, independent of DV eye axis patterning.

In Chapter 6, I describe a preliminary study to identify changes to gene expression levels within the eye correlating with SOS closure delay through RNA-Seq.

Overall, this thesis will tease apart the genetic factors that regulate the SOS to reveal the etiology of superior coloboma, a novel disorder of which there is very little known. In addition, these studies of the SOS adds to our current understanding of eye development as a whole, as we begin to elucidate the role of this novel developmental structure during early embryogenesis.

1.13. Figures

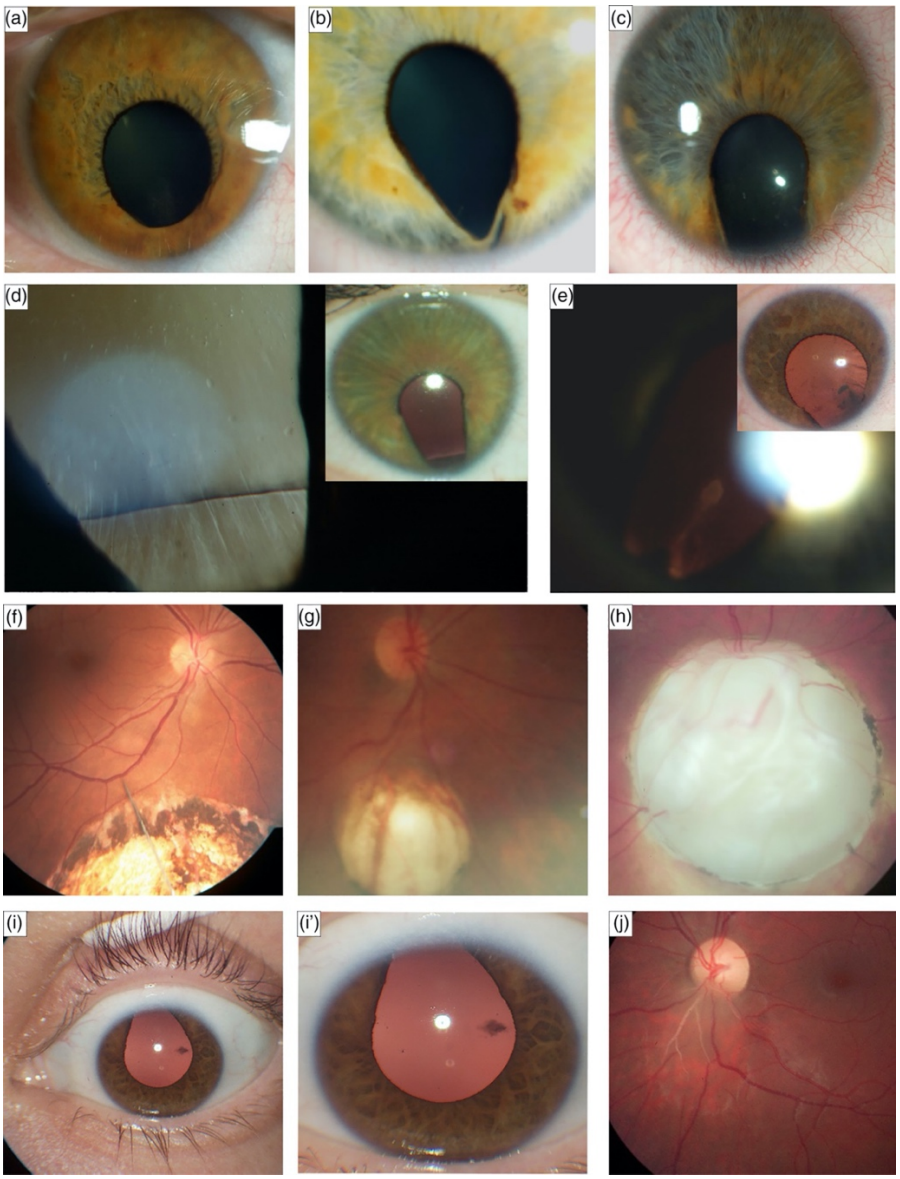

Figure 1.1: Montage illustrating ocular coloboma patient phenotypes. These vary in severity, as illustrated by subtle changes (A, B) compared to the typical appearance (C). Iris colobomas may expose the lens zonule, are associated with loss of the normal convex lens edge contour (D), with focal lens opacities frequently apparent (E). There is also frequent involvement of the posterior segment, illustrated by retino-choroidal (F, G) and optic nerve head (H) colobomata. Occasionally, atypically-positioned colobomata occur, illustrated by a superior coloboma (I) which was associated with sheathed retinal vasculature (J).

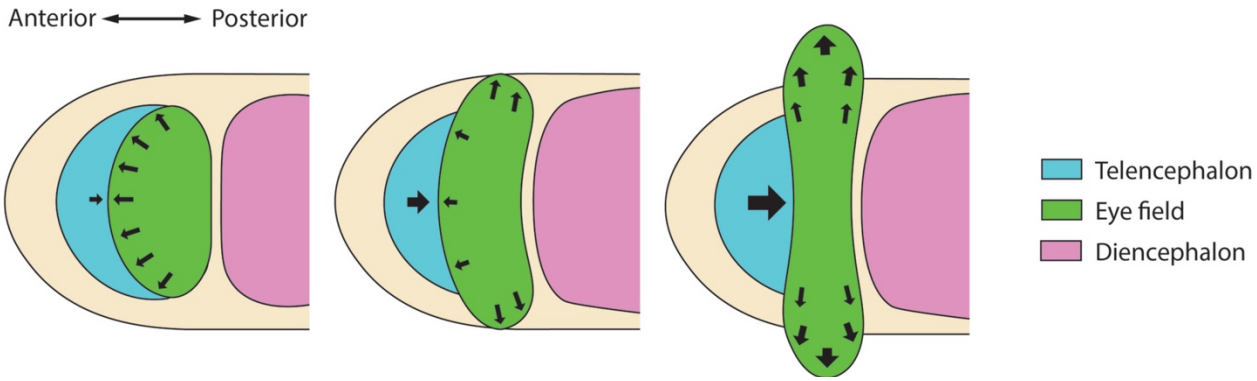

Figure 1.2: Dorsal view of the eye field during early embryogenesis. Arrows indicate movements of telencephalic cells and eye precursor cells to drive optic vesicle evagination. Following its formation, the neural plate is subdivided into anterior and posterior segments. The anterior neural plate is then subdivided rostro-caudally by a concentration gradient of canonical Wnt-signaling. Various anterior structures of the nervous system, including diencephalon, telencephalon, and eye field, are primordially defined along the canonical Wnt-signaling gradient. As the telencephalon and eye field grow, the eye field is split in two domains as Shh induces expression of *Pax2*, and the optic vesicles evaginate laterally.

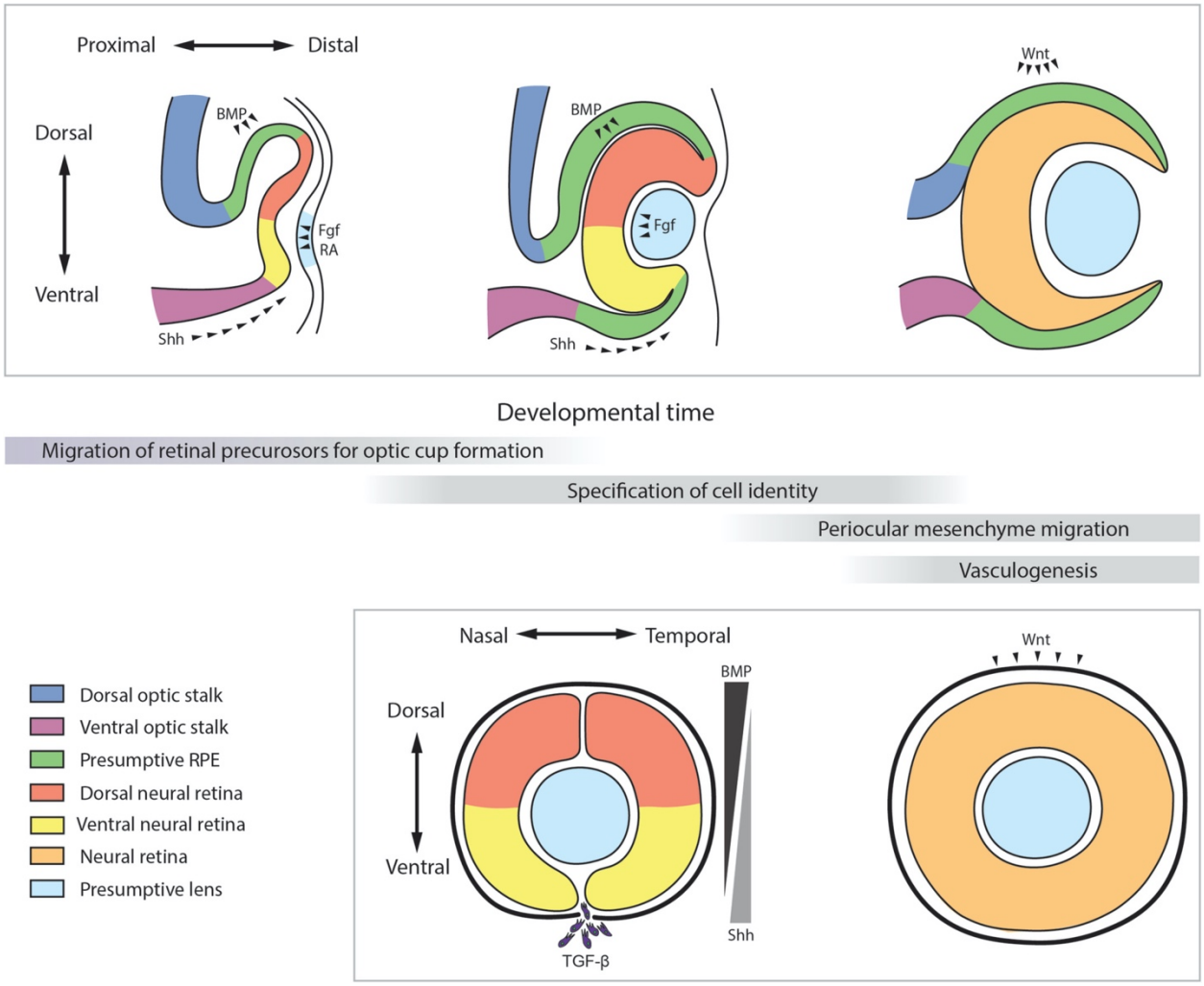

Figure 1.3: Optic cup morphogenesis. Arrows represent secretion of signaling molecules of the indicated pathways. Evagination of the optic vesicle is followed by invagination of its distal end due to the activity of the lens placode. A bi-layered optic cup is formed, and opposing gradients of BMP and Shh signaling molecules form the DV axis of the developing eye. As POM cells migrate to the ventral eye, fissures are closed, vasculogenesis begins, and cells begin to differentiate into specific retinal cells.

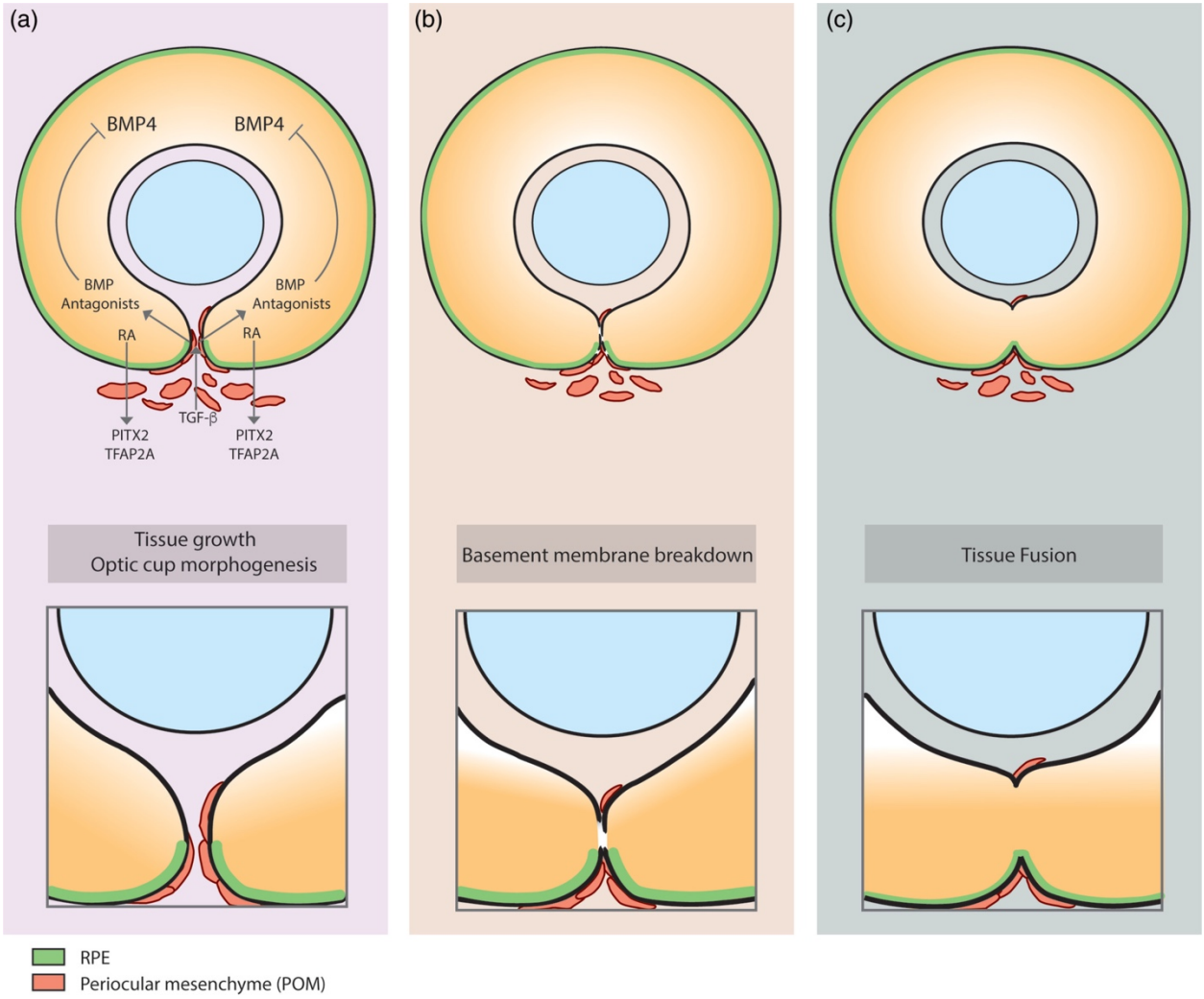

Figure 1.4: Migration of periocular mesenchyme (POM) cells during eye development. Periocular mesenchyme is a population of migratory cells combining neural crest, head mesenchyme and vasculature. During eye development, POM cells migrate into the ventral eye through the choroid fissure. As they move into the early eye, signaling interactions between POM cells (Tgf-b, RA, and BMP) and apposing retinal lobes orchestrate dissolution of extracellular matrix, thus facilitating the closure of the choroid fissure.

1.14. Tables

Table 1.1: Genes associated with microphthalmia, anophthalmia, and coloboma. Human variants are described for MAC spectrum and cranial dysmorphisms. Note that superior coloboma patients wherein no hereditability has been established are listed as yes*. a note that superior coloboma patients wherein no hereditability has been established are listed as yes.

Gene name	Human variants	Models studied	OMIM number	Cellular function
Formation of eye anlage				
SIX3	Yes	Fly, Fish, Mouse, Chick	603714	Transcription factor: regulation of Pax6, Rx, and Shh genes
SOX2	Yes	Mouse, Fish, Chick, Frog	184429	Transcription factor: regulation of Out and Rx genes
RAX/rx1/rx2/rx3	Yes	Mouse, Fish, Chick, Frog	601881	Transcription factor: regulation of Otx and Sox2 loci
PAX6	Yes	Mouse, Fish, Chick, Frog, Fly	607108	Transcription factor: regulation of Otx and Sox loci
OTX2	Yes	Mouse, Fish, Chick, Frog, Fly	600037	Transcription factor: binds Sox2, regulates Otx, Rx genes
Migration of precursors and morphogenesis				
FZD5	Yes	Mouse, Fish	601723	Growth factor receptor: binds Wnt and activates canonical and/or noncanonical signaling
FZD8	No	Mouse	606146	Growth factor receptor: binds Wnt and activates canonical and/or noncanonical signaling
WNT11	No	Mouse, Fish	603699	Growth factor: activates noncanonical Writ signaling (regulates cell polarity)
WNT5	No	Mouse, Fish	164975	Growth factor: activates noncanonical Wnt signaling (regulates cell polarity)
EPHRINB1	CFNS (304110)	Mouse, Fish, Chick, Frog	300035	Juxtacrine ligand: regulates cell adhesion, migration, polarity
ALDH1A3	Yes	Mouse, Fish, Chick, Frog	600463	Aldehyde dehydrogenase enzyme: rate-limiting enzyme in synthesis of retinoic acid
ALDH1A2	No	Mouse, Fish, Chick, Frog	603687	Aldehyde dehydrogenase enzyme: rate-limiting enzyme in synthesis of retinoic acid
RARA/B/G	No	Mouse, Fish, Chick, Frog	180240, 180220, 180190	Ligand binding receptor: binds retinoic and regulates RA-dependent transcription
RXR	No	Mouse, Fish, Chick, Frog	180246	Co-receptor for retinoic acid receptors, regulates RA-dependent transcription
CYP26A1/B1/C1	No	Mouse, Fish, Chick, Frog	602239, 605207, 608428	Retinoic acid hydroxylase: in activates RA
STRA6	Yes	Mouse, Fish, Chick, Frog	610745	Transmembrane transporter for vitamin A, precursor of RA
WNT4	No	Mouse, Fish	603490	Growth factor: activation of b-catenin
VSX2/CHX10	Yes	Mouse, Fish	142993	Transcription factor: regulates retinal gene expression
OFCC1/Ojoptano	No	Medaka	614287	Transmembrane protein that regulates cell polarity

Ocular patterning along the dorsal-ventral axis				
BMP2	No	Mouse, Fish, Chick, Frog	112261	Growth factor: activates Smad1/5/9
BMP4	Yes	Mouse, Chick, Frog	111262	Growth factor: activates Smad1/5/9
BMP7	No	Mouse, Fish, Chick, Frog	112267	Growth factor: activates Smad1/5/9
GDF6	Yes	Mouse, Fish, Frog	601147	Growth factor: activates Smad1/5/9
TBX2	Yes[a]	Mouse, Fish, Frog	600747	Transcription factor: regulates dorsal eye pattern
BMPR1A	Yes[a]	Mouse, Fish	601299	Growth factor receptor: binds Bmp/Gdf activates Smad 1/5/9
SMAD1/5/9	No	Mouse, Fish, Chick, Frog	601595, 603110, 603295	Second messenger: regulated by Bmp/Gdf
SHH	Yes	Mouse, Fish, Chick, Frog	600725	Growth factor: binds Ptc, regulates Gli
SMO	No	Mouse, Fish, Chick, Frog	601500	SHH co-receptor: inhibits Gli pathway until SHH binds
PTCH1	Yes	Mouse, Fish, Chick, Frog	601309	SHH receptor: activates Gli upon binding SHH
GLI1/2/3	No	Mouse, Fish, Chick, Frog	165220, 165230, 165240	Transcription factor: regulated by SHH
VAX1	Yes	Mouse, Fish, Chick, Frog	604294	Transcription factor: regulates ventral eye
VAX2	No	Mouse, Fish, Chick, Frog	604295	Transcription factor: regulates ventral eye
Periocular mesenchyme: neural crest, ventral head mesenchyme and vasculature				
FOXC1	Yes	Mouse, Fish, Chick, Frog	601090	Transcription factor: forkhead domain
PITX2	Yes	Mouse, Fish, Chick, Frog	601542	Transcription factor: Paired domain
LMX1B	Yes	Mouse, Fish	602575	Transcription factor: Lim domain
Z1C1	No	Mouse, Fish	600470	Transcription factor: Zinc finger
ZIC2	Yes	Mouse, Fish, Chick, Frog	603073	Transcription factor: Zinc finger
ALX1	Yes	Mouse, Fish	601527	Transcription factor: Homeodomain, Aristaless
TFAP2a	Yes	Mouse, Fish	107580	Transcription factor: AP-2 alpha
FOXD3	No	Mouse, Fish, Chick, Frog	611539	Transcription factor: forkhead domain
CHD7	Yes	Mouse, Frog	608892	Chromatin remodeling: regulates rRNA
SEMA3A	No	Mouse, Fish, Chick, Frog	603961	Semaphorin: regulates cell migration
SEMA3E	Yes	Mouse, Fish, Chick, Frog	608166	Semaphorin: regulates cell migration
BMP7	No	Mouse, Fish, Chick, Frog	112267	Growth factor: regulates Smad1/5/9
TGFBR2	No	Mouse, Fish	190182	Growth factor receptor: regulates Smad2/3
TGFB2	No	Mouse, Fish	190220	Growth factor: regulates Smad2/3
TGFB3	No	Mouse, Fish	190230	Growth factor: regulates Smad2/3
ADAMTSL1/2/3/4	No	Mouse, Fish	609198, 612277, 609199, 610113	Extracellular matrix remodeling
TLN1/2	No	Mouse, Fish, Chick, Frog	186745, 607349	Cell adhesion and migration
LMO2	No	Mouse, Fish	180835	Transcription factor: Lim domain
MMP2	No	Mouse, Fish, Chick, Frog	120360	Metalloproteinase: extracellular matrix remodeling
MMP9	No	Mouse, Fish, Chick, Frog	120361	Metalloproteinase: extracellular matrix remodeling

Chapter 2

Materials and Methods

2.1. Ethics statement

Embryonic, larval and adult zebrafish were cared for in accordance with guidelines set by the Canadian Council of Animal Care. All protocols used in this study were approved by the University of Alberta's Animal Care and Use Committee (Protocol 427).

Experiments involving chick and mouse discussed in Chapter 3 were performed at the University of Texas and approved by its institutional animal care committee (#2015–00089).

2.2. Animal care

Adult zebrafish were kept in circulating fish water at 28.5 ºC with a controlled light cycle. Embryos were grown at 25.5°C, 28.5°C, or 33°C in embryo media (EM), and developmental stages were determined according to specific morphological features outlined by Kimmel et al., 1995. When needed to be examined past 24 hours post-fertilization (hpf), the embryos were treated with 0.004% 1-phenyl 2-thiourea (PTU; Sigma-Aldrich) before 22 hpf to prevent pigmentation.

When necessary, zebrafish larvae and adults were anaesthetized using 0.168 mg/mL tricaine methanesulfonate (MS-222) or euthanized using 0.4 mg/mL. Subsequently, zebrafish were fixed at the required developmental stages in 4% paraformaldehyde (PFA) in PBS (Phosphate-buffered Saline; 137mM NaCl, 2.7mM KCl, 10mM NaH2PO4, 1.75 mM KH2PO4, pH 7.4) at room temperature for 5 hrs or overnight at 4°C on a rotating platform, unless otherwise stated. Unless otherwise noted, AB strain zebrafish were used as wildtype.

Dechorionation of embryos was performed either manually using Dumont #5 fine-pointed forceps (Fine Science Tools) or enzymatically using pronase E (Sigma-Aldrich). For enzymatic dechorionation, embryos were immersed in a solution of 2 mg/mL pronase E and swirled gently for 3-5 minutes until few chorions could be observed to lose tension and deflate. Embryos were immediately washed gently in EM multiple times, after which most embryos came out of their chorions. Any embryos remaining in their chorions were manually dechorionated using forceps.

2.3. Fin clipping

Zebrafish tail fin clips were performed for purposes of genotyping and identifying carriers for mutant alleles. Individual adult fish were anaesthetized as previously described, and a small portion of the tail fin was cut using a clean scalpel. The fish were washed with fresh water and placed in individual recovery tanks, while the amputated fin was transferred to a PCR tube on ice and used subsequently for genomic DNA extraction and PCR.

2.4. Genomic DNA extraction

For fin clips or pooled embryos, the tissue or the pooled group of embryos was immersed in 100 µL of 50 mM NaOH. For a single embryo, the embryo were immersed in 10 µL of 50 mM NaOH. Using PCR tubes, the samples were heated at 95°C for 20 minutes in a thermocycler, vortexing every 5 minutes, and then cooled on ice. The solution was neutralized using 1/10th volume of 1 M Tris-HCl, pH 8. The genomic DNA was subsequently diluted 10-fold prior to downstream applications.

2.5. Genotyping

Sequences of all genotyping primers can be found in Table 2.1.

tbx2b^{fby} mutants were genotyped by PCR followed by MseI restriction digest. Genomic DNA was extracted as above and diluted 10X for use as template. PCR was performed with Ex Taq DNA Polymerase (TaKaRa Bio Inc.). Conditions for amplification were 1 cycle at 94℃ for 2 min, 40 cycles of 94℃ for 15 seconds, 58℃ for 15 seconds, and 72℃ for 20 seconds, followed by 1 cycle at 72℃ for 3 min. The PCR products were then digested with MseI (NEB) for two hours and analyzed via gel electrophoresis using a 3% agarose gel.

vax2^{ua1031} mutants were genotyped by PCR. Genomic DNA was extracted as above and diluted 10X for use as template. PCR was performed with Taq DNA Polymerase (Thermo Fisher

Scientific). Conditions for amplification were 1 cycle at 95℃ for 2 min, 40 cycles of 95℃ for 30 seconds, 62℃ for 30 seconds, and 72℃ for 1 minute, followed by 1 cycle at 72℃ for 5 minutes. The PCR products were then analyzed via gel electrophoresis using a 2% agarose gel.

2.6. Total RNA extraction

Embryos were grown to the desired stage and dechorionated. Specific tissues were dissected manually if required. Total RNA was extracted from embryos using the RNAqueous-4PCR Total RNA Isolation kit (Invitrogen/Ambion). First, embryos were vortexed to homogenize tissue in 350 μL lysis/binding solution. 350 μL 64% EtOH was added and the solution was vortexed for 30 seconds. The solution was transferred to a filter cartridge in a collection tube and centrifuged at maximum speed for 1 minute. The flow-through was discarded, and 700 μL of wash solution #1 was added and centrifuged for 1 minute at maximum speed. The flow-through was discarded and 500 μL of wash solution #2/3 was added and centrifuged for 1 minute at maximum speed, after which this step was repeated once. The filter cartridge was transferred to a new collection tube, and 40 μL of pre-heated, 70°C elution buffer was applied to the filter cartridge and centrifuged for 30 seconds at maximum speed. Following this initial elution, an additional 30 μL of pre-heated elution buffer was applied to the same filter cartridge and centrifuged for 30 seconds at maximum speed for a total final volume of 70 μL. The extracted total RNA was stored at -80°C.

2.7. One-step reverse transcriptase PCR (RT-PCR)

One-step RT-PCR was performed using the SuperScript III One-Step RT-PCR System with Platinum Taq DNA Polymerase (Invitrogen). Each reaction was prepared with 12.5 μL 2X Reaction mix, 1 μL 5 μM forward primer, 1 μL 5 μM reverse primer, 8.5 μL DEPC-treated or nuclease-free water, 1 μL Superscript III Platinum Taq, and 1 μL RNA template. The PCR cycle conditions were as follows: 54°C for 30 minutes (cDNA synthesis); 94°C for 2 minutes (denaturation); followed by 30 cycles of 94°C for 15 seconds (denaturation), 55-65°C for 30 seconds (primer annealing), and 68 °C for 1 minute/kb (extension), followed by a final extension at 68°C for 5 minutes. Subsequently, gel electrophoresis was used to analyzed the RT-PCR products.

2.8. Gel extraction

Gel extraction was performed using the QIAquick Gel Extraction kit (Qiagen). Empty 1.7 mL microcentrifuge tubes were weighed. The desired band was cut from the gel with a clean razor blade and placed in a 1.7 mL microcentrifuge tube, after which the tubes were weighed again to determine the weight of the extracted gel slice. 3 volumes of Buffer QG to 1 volume gel was added to the tube and incubated at 50°C for 10 mins, with vortexing every 2-3 minute to dissolve the gel. 1 gel volume of 100% isopropanol was added and mixed, after which the solution was transferred to the QIAquick column in a collection tube and centrifuged for 1 minute at maximum speed. The flow-through was discarded, and 500 μL of Buffer QG was added to the column and centrifuged for 1 minute at maximum speed. The flow-through was discarded and 750 μL of Buffer PE was added to the column, and allowed to stand for 5 minutes. Subsequently, the column was centrifuged for 1 minute at maximum speed and flow-through was discarded. The column was placed back in the collection tube and centrifuged for 1 minute at maximum speed to remove residual wash buffer, after which it was transferred to a new 1.7 mL microcentrifuge tube. DNA was eluted by adding 30 μL of Elution Buffer, allowing it to stand for 1 minute, and centrifuging the column for 1 minute at maximum speed. DNA was stored at -20°C.

2.9. TOPO TA cloning

TOPO TA Cloning Kit (Thermo Fisher Scientific) was used for insertion of blunt-end PCR amplicons in a plasmid vector. To create 3' adenine overhangs following PCR reactions using Phusion DNA polymerase (Thermo Fisher Scientific), 15 µL of gel-extracted PCR product was combied with 2 µL of 10x Ex Taq Buffer, 1 µL of 10 mM dNTPs, 1 µL of TaKaRa ExTaq, and 1 µL of nuclease-free water. The reaction was then incubated for 10 minutes at 72°C. Subsequently, reactions were set up containing 2 µL gel-extracted PCR product with 3' adenine overhangs, 0.5 µL of kit-supplied salt solution (1.2 M NaCl, 0.06 M $MgCl_2$), and 0.5 µL of either pCR4-TOPO (for RNA *in situ* hybridization probe synthesis) or pCR2.1-TOPO (for other applications). The reaction was incubated at room temperature for 20 minutes to facilitate the insertion of the PCR amplicon in the plasmid vector. The plasmid vector was subsequently used for transformation reactions

2.10. Transformation

The desired plasmid was combined with 10-50 µL of One Shot TOP10 Chemically Competent *E. coli* (Thermo Fisher Scientific), incubated on ice for 20 minutes, and heat-shocked at 42°C for 45 seconds. Following an incubation on ice for 5 minutes, 100-200 µL of SOC medium was added, and the reaction was incubated at 37°C for 30-60 minutes. Transformations were spread on LB plates (1% Bacto-tryptone, 0.5% Bacto-yeast extract, 0.17 M NaCl, 1.5% Bacto-agar, pH 7) containing an antibiotic as required (carbenicillin, ampicillin, or kanamycin), and incubated at 37°C overnight.

2.11. Miniprep

A single bacterial colony was isolated and used to inoculate 2 mL of LB media (1% Bacto-tryptone, 0.5% Bacto-yeast extract, 0.17 M NaCl, pH 7) containing the antibiotic required for selection. After shaking at 37°C overnight, minipreps were performed using the QIAprep spin

Miniprep kit (Qiagen). 2 mL of the culture was transferred to a 2 mL microcentrifuge tube, and the cells were pelleted via centrifugation at maximum speed for 5 minutes, after which the supernatant was discarded. Cells were resuspended in 250 µL of cold P1 buffer. 250 µL of P2 buffer was added to the tube, and the tube was inverted 10 times to mix the reaction. 350 µL of N3 buffer was added, and tubes were inverted 10 times. The tubes were centrifugated at maximum speed for 10 minutes. The supernatant was transferred to a QIAprep spin column in a collection tube, centrifugated for 1 minute at maximum speed, and the flow-through was discarded. 750 µL of PE buffer was added and columns were centrifugated for 1 minute at maximum speed. The flow-through was discarded, and the column was centrifugated for 1 minute at maximum speed. The column was placed in a new 1.7 mL tube. 50 µL of Elution Buffer was placed on the filter of the column, and DNA was eluted via centrifugation for 1 minute at maximum speed. DNA was stored at -20°C.

2.12. Maxiprep

A single bacterial colony was isolated and used to inoculate 100 mL of LB media (1% Bacto-tryptone, 0.5% Bacto-yeast extract, 0.17 M NaCl, pH 7) containing the antibiotic required for selection. After shaking at 37°C overnight, maxipreps were performed using the QIAGEN Plasmid Maxi Kit (QIAGEN). Cells were pelleted in 50 mL conical tubes by centrifugating for 15 minute at maximum speed in 4°C, repeating as necessary to pellet the entire volume of inoculated LB media. Cells were resuspended in 10 mL of cold Buffer P1. 10 mL of Buffer P2 was added, and the solution was inverted 10 times to mix the sample. The sample was incubated for 5 minutes at room temperature, after which 10 mL of cold Buffer P3 was added. The solution was inverted 10 times, incubated on ice for 20 minutes, and centrifugated for 30 min at maximum speed in 4°C. Empty QIAGEN maxiprep columns were equilibrated by applying 10 mL of Buffer QBT. After centrifugation, the supernatant was applied to the column, taking care to avoid disturbing the pellet. The supernatant was allowed to enter the resin by gravity flow. The column was washed twice with 30 mL of Buffer QC. Using 15 mL of Buffer QF, the DNA was eluted into a new 50 mL conical tube. To precipitate the DNA, 10.5 mL of room-temperature 100% isopropanol was added to the eluted DNA, mixed, and incubated at -20°C for 15-30 minutes. DNA was pelleted by

centrifugation for 30 minutes at maximum speed in 4°C. The supernatant was carefully decanted. The DNA was washed with 1 mL of 70% EtOH and moved to a 1.7 mL tube. DNA was pelleted by centrifugation for 10 minutes at maximum speed in 4°C. The supernatant was carefully decanted, and the pellet allowed to air-dry for 5-10 minutes. The pellet was resuspended in 100-400 µL of 1xTE, pH 8.0 and stored at -20°C.

2.13. Phenol-chloroform DNA extraction

Linearized plasmid was purified through phenol-chloroform purification. 160 µL of DEPC-treated water was initially added to the linearization reaction to bring the total volume to 200 µL. 200 µL of phenol-chloroform was added, and the reaction was vortexed. Following a 5 minute centrifugation at maximum speed, the aqueous, upper layer was transferred to a new tube, taking care to avoid disturbing the lower layer. An equal volume of chloroform was added to the new tube, after which it was vortexed and centrifugated for 5 minutes at maximum speed. The aqueous, upper layer was transferred to a new tube. 1/10 volume of 3 M sodium acetate pH 5.2 was added, and the DNA was precipitated by adding 3 volumes of 100% RNase-free ethanol and leaving the tube to chill at -20°C for 15 minutes, after which it was centrifugated at maximum speed for 20 minutes at 4°C. The supernatant was decanted, and the pellet was washed with 100 µL of cold 70% ethanol/RNase-free water. After gently mixing to break the pellet loose, the tube was centrifugated at maximum speed for 15 minutes at 4°C. The supernatant was decanted, and the pellet was air-dryed for 5 minutes and resuspended in 7 µL RNase-free water.

2.14. DNA sequencing

Sequencing reactions were submitted as aliquots containing 3-6 µL of template, 0.5 µL of 5 µM sequencing primer, and water to a total volume of 10 µL to the Molecular Biology Service Unit at University of Alberta for Sanger sequencing.

Sequencing results were examined using 4Peaks (Nucleobytes). Additionally, multiple sequence alignments were performed using Clustal Omega (EMBL-EBI), and protein product sequences were analyzed using ExPASy (SIB Swiss Institute of Bioinformatics).

2.15. Antisense morpholino oligonucleotide injections

Antisense morpholino oligonucleotides (MOs) were obtained from Gene Tools LLC., and stock solutions were prepared by resuspending the lyophilized MOs to a concentration of 10 mg/mL in nuclease-free water as outlined by the manufacturer. All MOs were diluted to their respective working concentrations and stored at room temperature for short-term storage or 4°C for long-term storage. Prior to injections into 1-cell stage zebrafish embryos, the working solutions were first heated at 65°C for 10 minutes, briefly centrifuged, and allowed to cool to room temperature. Injections were performed using an ASI MPPI-2 Pressure Injector (Applied Scientific Instruments). The sequences of MOs used can be found in Table 2.2.

2.16. mRNA expression constructs and synthesis

Plasmid vector containing human *VAX2* cDNA was obtained from Dharmacon (MHS6278-202831473). A customized gBlocks® Gene Fragment (IDT) of the patient variant human *VAX2* cDNA was obtained from IDT. Primers used to amplify the human *VAX2* sequence is found in Table 2.3. Both *VAX2* sequences were verified through Sanger sequencing. Subsequently, they were ligated into their pCS2+ vectors and linearized using NotI (NEB). Following linearization, in an RNase-free manner, an *in vitro* transcription reaction was prepared with the mMessage mMachine SP6 Transcription Kit (Thermo Fisher Scientific) by combining 10 µL of 2x NTP/CAP, 2 µL of 10X Reaction Buffer, 2 µL of enzyme mix, 1 µg of purified linearized plasmid DNA, and nuclease-free water to a total reaction volume of 20 µL. The reaction was incubated for 2 hours at 37°C, after which 1 µL of DNase was added and incubated for 30 minutes at 37°C.

The reaction was purified using YM-50 Microcon columns (Amicon, EMD Millipore). 480 µL of DEPC-treated water was added to the reaction, and the entire reaction volume was placed in a column within a collection tube. The column was centrifugated for 4 minutes at 14,000 x g, and the flow-through was discarded. The column was placed inverted in a new collection tube and centrifugated for 3 minutes at 1,000 x g. 480 µL of DEPC-treated water was added to the resulting sample, and the entire reaction volume was placed in a column within a collection tube. The column was centrifugated for 4 minutes at 14,000 x g, and the flow-through was discarded. The column was placed inverted in a new collection tube and centrifugated for 3 minutes at 1,000 x g to collect the purified mRNA.

The concentration was determined through spectrophotometry using a NanoDrop ND-1000 Spectrophotometer. The mRNA was diluted to the required concentrations with DEPC-treated water and stored at -80°C.

2.17. mRNA injections

Immediately prior to injection, mRNA aliquots were retrieved from -80°C storage and thawed on ice. Dose was determined using the known concentration of the aliquot and the radius of the bolus observed when suspended in mineral oil on a micrometer slide. Subsequently, a 2 nL bolus of the mRNA aliquot was injected into the cell of 1-cell stage embryos. Injections were performed using an ASI MPPI-2 Pressure Injector (Applied Scientific Instruments).

2.18. Quantitative real-time PCR (qPCR)

Following total RNA extraction as described in 2.5, DNA was removed by incubating 70 µL of eluted RNA with 19 µL of DEPC- treated water, 10 µL of DNAseI buffer, and 1 µL of DNAseI for 30 minutes at 37°C. The total RNA was purified again using RNeasy Mini Kit (Qiagen). Total RNA was combined with 350 µL of Buffer RLT + 1% β-mercaptoethanol, vortexed, and mixed with 250 µL of 100% EtOH. The solution was placed in a column within a collection tube and centrifugated for 15 seconds at maximum speed. The flow-through was

discarded and the column was placed in a new collection tube. 500 µL of Buffer RPE was added and the column was centrifugated for 15 seconds at maximum speed. The flow-through was discarded, after which 500 µL of Buffer RPE was added to the column and centrifugated for 2 minutes at maximum speed. The column was placed in a new collection tube and centrifugated for 1 minute at maximum speed. The column was transferred to a new collection tube. The total RNA was eluted by adding 10 µL of DEPC-treated water directly on the resin and centrifugating the column for 1 minute at maximum speed. The RNA was stored at -80°C.

Using total RNA as template, cDNA was synthesized using the Affinity Script qPCR cDNA Synthesis Kit (Agilent). 9 µL of purified RNA was combined with 15 µL of 2X MM, 4.5 µL of random hexamers, and 1.5 µL of RT/RNAse block enzyme mix. The cDNA synthesis reaction was placed in a thermocycler with the following PCR cycle conditions: 25°C for 5 minutes (primer annealing); 42°C for 30 min (cDNA synthesis); and 95°C for 5 min (reaction termination). The resulting cDNA was stored at -20°C.

qPCR samples were prepared using Brilliant II SYBR Green qPCR Master Mix (Agilent). 2 µL of cDNA template was combined with 7.5 µL of 2X SYBR Master Mix, 0.45 µL of 5 µM forward primer, 0.45 µL of 5 µM reverse primer, and 4.6 µL of nuclease-free water. qPCR was performed using the Rotor Gene Q qPCR Machine (Qiagen) with the following conditions: 95°C for 10 minutes (initial denaturation), followed by 45 cycles of 95°C for 20 seconds (denaturation) and 55°C for 1 minute (annealing and extensions). Fluorescence readings were taken after each 55°C annealing and extension step. All cDNA samples were run in triplicate, and each experiment was repeated three times. The Ct value data were analyzed using the comparative Ct method ($2^{-\Delta\Delta Ct}$). All qPCR primers sequences are listed in Table 2.4. All primers were validated with a 2-fold dilution series. Only those primers producing a coefficient of determination (R^2) of 0.98 or higher were used.

2.19. CRISPR-Cas9 mutagenesis

Gene-specific oligonucleotides were designed using the CHOPCHOP (http://chopchop.cbu.uib.no/) or CrisprScan (http://www.crisprscan.org/) online tools to target 20 nucleotides at either the 5' end of the gene of interest, or at key protein domains important for function (Table 2.5). The 20-nucleotide long target site, plus a PAM sequence, was flanked by sequences containing SP6 transcription start site and a sequence that overlaps with the constant oligonucleotide, required for Cas9 recruitment, used in CRISRPR-Cas9 mutagenesis. This gene-specific oligonucleotide was annealed with the constant oligonucleotide in a reaction consisting of 7 µL of 100 µM SP6 gene-specific oligo, 7 µL of 100 µM constant oligo, 2 µL of 10X NEB Buffer 3 (NEB), and 4 µL of water. The reaction was placed in 800 mL of boiled water, which was left to cool to room temperature overnight.

The overhanging, unpaired bases of the annealed oligonucleotide product were filled in through a reaction with 2.5 µL of 10 mM dNTPs (Thermo Fisher Scientific), 4 µL of 5X T4 DNA polymerase Buffer (Thermo Fisher Scientific), 0.2 µL of 100X BSA (Thermo Fisher Scientific), 0.5 µL of T4 DNA polymerase (Thermo Fisher Scientific), 2.8 µL of water, and 10 µL of annealed oligonucleotides. The reaction was incubated at 12°C for 1 hour, after which it was purified using the GeneJet PCR Purification kit (Fermentas) to obtain the resulting single guide RNA (sgRNA) template. A 1:1 volume of binding buffer was added to the reaction and mixed. A 1:2 volume of 100% isopropanol was added and mixed. The solution was transferred to a column and centrifugated for 1 minute at maximum speed. The flow-through was discarded. 700 µL of wash buffer was added to the column, after which it was centrifugated for 1 minute at maximum speed. The flow-through was discarded. With the empty collection tube, the column was centrifugated for 1 minute at maximum speed. The column was transferred to a new collection tube. 30 µL nuclease-free water was added directly to the resin in the column, and the sgRNA template was eluted via centrifugation for 1 minute at maximum speed.

Using the SP6 MEGAScript Kit (Ambion), the sgRNA was transcribed by incubating 1 µL of sgRNA template with 0.5 µL of ATP, 0.5 µL of GTP, 0.5 µL of CTP, 0.5 µL of UTP, 0.5 µL of 10X Buffer, 0.5 µL of SP6 enzyme mix, and 1 µL of nuclease-free water for 4 hours at 37°C. To remove DNA, 14 µL of DEPC-treated water and 1 µL of DNase were added and incubated for 15

minutes. To stop the transcription and purify the reaction, 10 µL of 5 M ammonium acetate and 60 µL of 100% RNase-free EtOH were added, and the solution was incubated at -80°C until frozen, usually overnight. The solution was centrifugated for 15 minutes at maximum speed in 4°C, after which the supernatant was discarded and 1 mL of 70% RNase-free EtOH was added to wash the pellet. The solution was then centrifuged for 5 minutes at maximum speed in 4°C, after which the supernatant was discarded. The resulting pellet was dried for 5 minutes at room temperature and resuspended in 20 µL of RNase-free water.

To perform the mutagenesis, sgRNA was injected at the highest possible concentration with Cas9 protein (PNA Bio). A 6 µL mixture containing 2 µL of Cas9 protein and 4 uL of sgRNA was prepared, and zebrafish embryos were injected at the one-cell stage with a 2 nL bolus.

2.20. High resolution melt (HRM) curve analysis

To design primers for High Resolution Melt curve analysis, the following conditions were used: GC content of 50-65% (ideally 55%); melting temperature of 55-67°C (ideally 62°C); primer length of 20-27 nucleotides (ideally 22 nucleotides); and amplicon length of 70-200 base pairs (ideally 90 base pairs). Amplicons amplified the flanking sequences around the CRISPR-Cas9 target site. HRM primers were tested on genomic DNA through conventional Taq PCR (Thermo Fisher Scientific) prior to HRM analysis. The sequences of HRM primers used for *vax2* were the same primers used for genotyping as shown in Table 2.1.

HRM reactions were performed in triplicate using the Type-it HRM PCR Kit (Qiagen). Each reaction was composed of 5 µL of Master mix, 1.4 µL of 5 µM Forward Primer, 1.4 µL of 5 µM Reverse Primer, 0.2 µL of nuclease-free water, and 2 µL of genomic DNA template. HRM was performed using the Rotor Gene Q qPCR Machine (Qiagen) with the following PCR cycle conditions: 95°C for 5 minutes (initial activation), followed by 45 cycles of 95°C for 10 seconds and 55°C for 30 seconds, and finishing with a high resolution melt analysis with the temperature increasing from 65°C to 95 °C in 0.1°C increments, with a 1 second wait between each increase in temperature. HRM profiles were analyzed using the Rotor Gene Software 2.0 (Qiagen).

2.21. P0 and F1 Identification

To screen for somatic mutagenesis and assess the mutagenesis efficiency of the designed sgRNA, CRISPR-Cas9 injected embryos were raised to 24 hpf, after which 20 uninjected and 20 injected embryos were dechorionated and pooled to extraction genomic DNA as described in 2.4. The 200 to 300-base pair region surrounding the target site was PCR-amplified, gel-extracted, and TOPO cloned. Colony HRM was performed to identify potential variants. If potential variants were identified, they were miniprepped and sent for Sanger sequencing. If multiple alleles with insertions/deletions were identified, the remaining injected embryos were raised to adulthood.

To screen for germline mutations and establish the founder P0 generation, injected adults (P0) were crossed, and the embryos (F1) collected. HRM was performed in triplicate on genomic DNA from individual embryos. If potential variants were identified, the samples were PCR amplified, gel-extracted, TOPO cloned, and sent for Sanger sequenced. If desired mutations were identified, F1 generations were established by raising the embryos to adulthood, followed by fin clipping and genotyping.

2.22. Pharmacological treatments

Embryos were dechorionated via manual dechorionation or enzymatic dechorionation as previous described. At 10 hpf or 18 hpf, 15 embryos were placed in 35 mm Petri dishes with 5 mL total volume of embryo media and, depending on the experiment, 0.05–0.2 μM DMH1 (Sigma-Aldrich), 1–5 μM N,N-diethylaminobenzaldehyde (DEAB; Sigma-Aldrich), 1–10 μM cyclopamine (Sigma-Aldrich), or an equivalent volume of vehicle (DMSO or ethanol). Two dishes were used for each treatment. Embryos were grown to the desired developmental stage prior to fixing in 4% PFA or imaging in 1% low-melting temperature agarose.

For rapamycin treatment, embryos were raised to 4 hpf, dechorionated, and treated with 400 nM of rapamycin (LC Laboratories) or an equivalent volume of DMSO. The embryos were raised to 28 hpf and imaged.

2.23. Imaging

A more detailed, step-by-step protocol for live imaging techniques described here can be found in Yoon et al., 2019.

For live stereoscope analysis, the zebrafish larvae in EM were anaesthetized, examined using an Olympus SZX12 stereomicroscope, and photographed with a mounted QImaging MicroPublisher 5.0 RTV Camera.

For live imaging using a compound microscope, live embryos were anaesthetized and mounted laterally in low-melting point agarose (1.3% in EM) in a 35 mm Petri dish (Corning). Once the agarose hardened, the sample was submerged in embryo media. Using a Zeiss W Plan-Apochromat 20x/1.0 water immersion objective lens, images were captured using ZEN software (Zeiss) on a Zeiss Axio Imager Z1 compound microscope fitted with a Zeiss LSM700 laser confocal scanner.

Z-stacks were created by capturing optical slices at intervals of 2–3 μm for a total of ~60 μM, and maximum projections or surface projections were created from the resulting stacks using either ZEN (Carl Zeiss) or Imaris (Bitplane) software. All DIC images were taken on an Axiocam HR digital camera mounted on a Zeiss Axioimager Z1 compound microscope.

Photos were annotated, assembled, and processed for brightness and contrast in Adobe Photoshop software.

2.24. RNA probe synthesis and purification

Digoxigenin-labelled antisense RNA probes were transcribed either from linearized plasmid DNA containing a gene-specific insert or via PCR using gene-specific PCR primers containing an integrated T7 RNA polymerase site (Thisse and Thisse, 2008). Plasmids used for probe synthesis are listed in Table 2.6. Primers used to generate probe template PCR products are listed Table 2.7.

When using plasmids, 10 μg of plasmid DNA was linearized with the appropriate restriction enzyme according to manufacturer's instructions and purified as described in 2.12. When performing PCR-based probe synthesis, PCR amplification was done using the One-Step RT-PCR kit (Thermo Fisher Scientific), and DNA was gel extracted using QIAquick Gel Extraction Kit (Qiagen).

Taking care to prepare on ice, 2 μg of linearized, purified plasmid DNA or PCR product was incubated with 2 μL of 10X transcription buffer, 1 μl of the appropriate RNA polymerase (SP6, T7, T3; Roche), 2 μl of DIG labeling mix (Roche), 1 μl RNaseOUT (Thermo Fisher Scientific), and DEPC-treated water to 20 μL for 2 hours at 37°C. Halfway through incubation, and addition 1 μL of RNA polymerase was added to the reaction. 1 μl of TURBO DNase (Thermo Fisher Scientific) was added, and the reaction was incubated for 5 minutes at 37°C. To stop RNA transcription, 2 μl of 0.2M EDTA, pH 8.0 was added.

Probe purification was performed using SigmaSpin Post-reaction Clean-up columns (Sigma-Aldrich). The column was placed in a collection tube, and centrifugated for 2 minutes at 750 x g. The base of the column was broken off, the lid was removed, and the column was spun for another 2 minutes at 750 x g. The column was placed in a new collection tube, and the probe synthesis reaction was added directly to the column, after which it was centrifugated for 4 minutes at 750 x g to be collected. 2 uL of 0.25 M EDTA, pH 8.0 and 2 μl of RNaseOUT (Thermo Fisher Scientific) was added to the purified probe, and the probe was stored at -80°C.

2.25. Wholemount *in situ* hybridization

All steps were performed at room temperature with gentle agitation unless otherwise noted.

Fixed embryos were washed four times in PBS + 0.1% Tween-20 (PBST) for 5 minutes. For 24 hpf embryos, permeabilization was performed with proteinase K in PBST for 5 minutes. The samples were refixed in 4% PFA in PBS for 20 minutes and washed four times in PBST for 5 minutes. Embryos were incubated in hybridization solution (50% formamide, 5X sodium saline citrate (SSC), 50 µg/ml heparin, 0.1% Tween-20, 0.092 M citric acid) with 500 µg/ml tRNA for 1 hour at 65°C, after which they were incubated overnight at 65°C in hybridization solution + tRNA containing DIG-labeled RNA probe at 1/50-1/200 dilution.

The samples were washed at 65°C for 5 minutes in 66% hybridization solution/33% 2X SSC, 5 minutes in 33% hybridization solution/66% 2X SSC, 5 minutes in 2X SSC, 20 minutes in 0.2X SSC + 0.1% Tween-20, and for 5 minutes twice in 0.1X SSC + 0.1% Tween-20. Subsequently, the samples were washed at room temperature 5 minutes in 66% 0.2X SSC/33% PBST, 5 minutes in 33% 0.2X SSC/66% PBST, and 5 mins in PBST. The samples were blocked with 2% sheep serum and 2 mg/ml bovine serum albumin (BSA) in PBST for 2-4 hours at room temperature. Embryos were incubated in a 1/5,000 dilution of anti-DIG alkaline phosphatase-conjugated Fab fragments (Roche) in blocking solution for 2 hours at room temperature or overnight at 4°C. Following antibody incubation, embryos were washed five times in PBST for 15 minutes. Colouration was performed by washing embryos four times in colouration buffer (100 mM Tris-HCl, pH 9.5, 50 mM MgCl2, 100 mM NaCl, 0.1% Tween-20) for 5 minutes. Embryos were incubated in 45 µl 4-nitro blue tetrazolium chloride solution (NBT; Roche) and 35 µl 5-bromo-4-chloro-3-indolyl- phosphate, toluidine-salt solution (BCIP; Roche) diluted in 10 ml of colouration buffer at room temperature or 4°C until the desired colouration level was reached. The colouration reaction was stopped by washing embryos in 100% MeoH + 0.1% Tween-20 and stored overnight at 4°C. To prepare for storage, embryos were rehydrated through a series of MeOH-PBST washes (70% MeOH/PBST, 50% MeOH/PBST, 30% MeOH/PBST, PBST). The samples were stored in PBST at 4°C until imaging.

Wholemount embryos were imaged in 3% methylcellulose with an Olympus stereoscope with a Qimaging micropublisher camera. When required, embryos were manually deyolked in PBST, put through a series of glycerol-PBS washes (30%, 50%, and 70% glycerol) in PBS before being dissected and mounted on slides in 70% glycerol. Slide-mounted samples were imaged on a Zeiss AxioImager Z1 compound microscope with Axiocam HR digital camera (Carl Zeiss Microscopy, LLC).

2.26. Anti-Laminin immunohistochemistry

Embryos were dechorionated and fixed in freshly-made 4% PFA for 2 hours at room temperature, after which they were washed four times in 1X PBST for 5 minutes. The embryos were permeabilized in 10 μg/mL proteinase K for 5 minutes at room temperature. Alternatively, they were washed with water + 0.1% Tween-20 for 5 minutes at room temperature, permeabilized using ice-cold acetone for 8 minutes at -20°C, and washed once more with water + 0.1% Tween-20 for 5 minutes at room temperature. The embryos were washed four times in 1X PBST for 5 minutes, and blocked in a solution of 5% goat serum (Thermo Fisher Scientific) and 2 mg/mL bovine serum albumin (BSA; Sigma-Aldrich) in 1X PBST for 2 hours on a room temperature shaker. Then they were incubated overnight in anti-Laminin primary antibody produced in rabbit (L9393; Thermo Fisher Scientific) at 1/200 dilution in block on a 4°C shaker. They were washed five times in 1X PBST for 15 minutes, after which they were incubated in anti-rabbit Alexa Fluor488 secondary antibody at 1/1,000 dilution in 1X PBST for 2 hours on a room temperature shaker or overnight on a 4°C shaker. They were washed four times in 1X PBST for 15 minutes. The samples were manually deyolked, dissected, and mounted on slides. Images were captured on a Zeiss Axio Imager Z1 microscope with a Zeiss LSM700 laser confocal scanner.

2.27. Western blot

Embryos were enzymatically dechorionated as described in 2.2 and raised to 70% epiboly on agarose-coated Petri dishes. cOmplete™ Mini, EDTA-free Protease Inhibitor Cocktail tablets (Roche) were added to deyolking buffer (55 mM NaCl, 1.8 mM KCl, 1.25 mM $NaHCO_3$ in water) and wash buffer (110 mM NaCl, 3.5 mM KCl, 10 mM Tris, pH 8.5, 2.7 mM $CaCl_2$ in water), with 1 tablet being used per 7-10 mL of each buffer. Embryos were placed in 1.7 mL microcentrifuge tubes, taking care to remove as much embryo media as possible. On ice, 1 mL of deyolking buffer was added, and the embryos were pipetted with a P1000 pipette to disrupted the yolk, keeping the pipetting consistent between samples. The samples were vortexed for 30 seconds at 1100 rpm, after which they were pelleted via centrifugation at 1,000 x g for 1 minute at room temperature or 4°C. The supernatant was removed, and 1 mL of wash buffer was added to the samples. Again, the samples were vortexed for 30 seconds at 1100 rpm, after which they were pelleted via centrifugation at 1,000 x g for 1 minute at room temperature or 4°C. The supernatant was removed. 3 µL of 1X sample loading buffer (4X NuPAGE sample loading buffer (Thermo Fisher Scientific) in water) + 2.5% β-mercaptoethanol (Sigma-Aldrich) per embryo used was added to the samples, and the tubes were vortexed for 30 seconds at maximum speed to lyse the cells, after which the samples were stored at -80°C.

To run the samples on a Bis-Tris SDS-PAGE 4-12% gradient gel (Thermo Fisher Scientific), the cell lysates were boiled for 5 minutes at 98°C, placed on ice, and centrifugated for 5 minutes at maximum speed in 4°C. After placing the gel in the gel box, 200 mL of 1X MOPS-SDS Buffer was added to the centre chamber. After confirming that there were no leaks, 500 uL of Antioxidant solution (Thermo Fisher Scientific) was added to the centre chamber, and 600 mL of 1X MOPS-SDS Buffer was added to the outer chamber of the gel box. 10 µL of cell lysate supernatant was added as needed, with an equal volume of Benchmark Pre-stained Protein Ladder (Thermo Fisher Scientific) used per lane as required. All remaining wells were loaded with an equal volume of 1X sample loading buffer. The gel was run for 1 hour at 200 V.

After the protein gel electrophoresis was complete, the gel was equilibrated in 2X Transfer Buffer for 10 minutes on a room temperature shaker. For each gel, eight pieces of 3.5” x 3” Whatman paper was soaked in 2X Transfer Buffer + 10% MeOH. For each gel, one PVDF

membrane cut to the same size was soaked in 100% MeOH, rinsed twice with distilled water, and placed in 2X Transfer Buffer + 10% MeOH. To perform the semi-dry transfer, a sandwich of four Whatman papers, one PVDF membrane, one gel, and four Whatman papers was prepared, taking care to remove bubbles between the layers. The semi-dry transfer was performed for 53 minutes at 20 V.

Following the semi-dry transfer, the PVDF membrane was soaked in 100% MeOH and rinsed with distilled water. The membrane was blocked for 1 hour at room temperature or overnight on a 4°C shaker. The blocking solution used was highly dependent on the primary antibody used. Most common blocking solutions used were as follows: 5% milk in TBST; BLOTTO (Thermo Fisher Scientific); 1% ovalbumin, 1% BSA, 1% Sheep serum in TBST; and 5% BSA, 2-3% ovalbumin. Following block, the membrane was incubated in primary antibody diluted in blocking solution for 1 hour at room temperature or overnight on a 4°C shaker. Anti-α-tubulin antibody produced in mouse (Abcam) was used at 1/10,000 dilution in 5% milk in TBST, while anti-VAX2 antibody produced in rabbit (Thermo Fisher Scientific) was used at 1/1,000 dilution in 1% ovalbumin, 1% BSA, 1% Sheep serum in TBST. Following the primary antibody incubation, the membrane was washed four times in TBST for 5 minutes, after which it was incubated in a secondary antibody solution for 1 hour at room temperature. For anti-α-tubulin antibody produced in mouse (Abcam), anti-mouse HRP-conjugated secondary antibody (Sigma-Aldrich) was used at 1/10,000 dilution in TBST, while for anti-VAX2 antibody produced in rabbit (Thermo Fisher Scientific), anti-rabbit HRP-conjugated secondary antibody (Sigma-Aldrich) was used at 1/10,000 dilution in TBST. Subsequently, the membrane was washed four times in TBST for 5 minutes, and incubated in Pierce Super Signal West Pico Chemiluminescent Substrate Solutions (Thermo Fisher Scientific) for 3 minutes in the dark. The membrane was transferred to a dampened Whatman paper soaked in TBST, wrapped in plastic wrap, and imaged using ChemiDoc MP Imaging System (Bio-Rad Laboratories Inc.).

2.28. RNA-Seq

Two RNA sequencing experiments were performed. The eyes of embryos treated with DMH-1 (Sigma-Aldrich), a known pharmacological inhibitor of BMP signaling, and the heads of embryos injected with 25 pg of WT *VAX2* mRNA were dissected and stored in 10-fold (w/v) volume of DNA/RNA Shield (Zymo Research) at -20°C until ready for shipping. The samples and their respective controls were sent to CD Genomics (Shirley, NY, USA) for RNA extraction, library prep, next-generation sequencing, and bioinformatics analysis. Alignment analysis was performed using GRCz11 zebrafish reference genome build. Degree of differential gene expression level is expressed in Log(2)FoldChange as per common convention.

2.29. Statistics

Two-factor analysis was done by Students t test. Multivariable analysis was performed by two-tailed, one or two-factor ANOVA with Tukey posthoc test.

2.30. Exome sequencing

Whole exome sequencing was performed on genomic DNA from each proband (#1 - #5) as part of FORGE Canada Consortium at the McGill University and Genome Quebec Innovation Centre. Exome target enrichment was performed using the Agilent SureSelect 50Mb (V3) All Exon Kit and sequencing was performed on the Illumina HiSeq 2000, multiplexing three samples per lane. The mean coverage of coding sequence regions, after accounting for duplicate reads was greater than 70x. WES data was analyzed by performing alignment with BWA, duplicate read removal with Picard, local insertion/deletion realignment with GATK, variant calling with SAM-tools, and annotation with Annovar and custom scripts (Beaulieu et al., 2014). Subsequently, exome sequencing was repeated commercially (Beijing Genomics Institute). In parallel, array CGH was performed to identify any causative copy number variations (CNV) using an Affymetrix cytoscan HD array that comprises approximately 1,800,000 CNV and 700,000 genotyping probes.

Within patients #1–5, we identified 783, 843, 942, 708, and 721 rare (<1%) non-synonymous and stop-gain/loss variants, respectively. By filtering such variants using MutationTaster (score >0.95), patients #1–5 contain 163, 155, 139, 112, and 148 higher probability variants, respectively. Subsequent prioritization included literature searches associating genes with ocular function and zfin.org examination of in situ hybridization expression patterns within the developing eye at 18–24 hpf, yielding a restricted subset of high priority variants in each proband.

2.31. Chick and mouse embryos, immunohistochemistry, and imaging

For the chick studies, fertilized Leghorn eggs (Texas A&M, Bryan, TX) were incubated at 38°C in a humidified forced-draft incubator. Chick embryos were staged according to Hamburger and Hamilton (1951) and Swiss Webster mice were collected at E10.5. Immunohistochemistry was performed as previously described (Eom et al., 2011). Chick embryos were stained with antibodies against Laminin-1 (Developmental Hybridoma Studies Bank, 3HL1; 1:250), whereas for mouse Laminin alpha 1 stains, we utilized a different antibody (Sigma, L9393). Alexa-Fluor conjugated Goat anti-Rabbit IgG (Life Technologies, 411008; 1:250) was used for fluorescent detection (Amarnath and Agarwala, 2017). Antibodies used in the current study were validated for use in chicks in previous studies (Amarnath and Agarwala, 2017; Halfter and Von Boxberg, 1992). DAPI staining was used for detecting nuclei. Confocal images were obtained with an Olympus IX51 spinning disc microscope and data analyses carried out with Slidebook Pro (3I, CO). Images are presented as single 0.5–0.8 μm thick optical sections. The position in the dorsal- ventral plane is based on the acquisition of multiple serial sections and respective alignment to those sections (just ventral) that contain lens tissue.

2.32. Scanning electron microscopy (SEM)

Embryos at 22 hpf from AB wildtype and *gdf6a*$^{+/-}$ incrosses were fixed overnight in 2.5% Glutaraldehyde; 2% PFA. After washing in 0.1 M phosphate buffer, embryos were gradually dehydrated in ethanol, transferred to Hexamethyldisilazane (HMDS; Electron Microscopy

Sciences) and left to dry overnight. Embryos were then mounted on SEM stubs, sputter coated with Au/Pd using a Hummer 6.2 Sputter Coater (Anatech), and imaged on a XL30 scanning electron microscope (FEI) operating at 20 kV.

2.33. Members of FORGE Consortium Canada

FORGE Canada Consortium: Finding of Rare Disease Genes in Canada; Steering Committee: Kym Boycott (leader; University of Ottawa), Jan Friedman (co-lead; University of British Columbia), Jacques Michaud (co-lead; Universite de Montreal), Francois Bernier (University of Calgary), Michael Brudno (University of Toronto), Bridget Fernandez (Memorial University), Bartha Knoppers (McGill University), Mark Samuels (Universite de Montreal), Steve Scherer (University of Toronto).

2.34. Acridine orange staining

Live 27 hpf embryos were treated with 10 μg/mL of acridine orange (Thermo Fisher Scientific) in embryo media + PTU for 1 hour at 28.5°C to facilitate staining of cells undergoing apoptosis. At 28 hpf, the embryos were removed from the acridine orange solution, rinsed five times with embryo media + PTU, and placed in clean Petri dishes to be live-imaged. Embryos were anaesthetized and imaged under a fluorescence stereomicroscope. Images were captured with ZEN software (Zeiss).

2.35. Tables

Table 2.1: Genotyping primers

Gene	Primer Sequence (5'-3')
cyp1b1	F - CCATCTCAGATATTTTCGGGG
	R - GTTATTTACCTGACAAGTAGCAG
gdf6a	F - GCGTTTGATGGACAAAGGTC
	R - CCGGGTCCTTAAAATCATCC
tbx2b	F - TGTGACGAGCACTAATGTCTTCCTC
	R - GCAAAAAGCATCGCAGAACG
vax2	F - ACTATTCGGGAGATCGTGCTG
	R - CTGTGTCTCAGAGAGATTGAGCTG

Table 2.2: Morpholino Oligonucleotide Sequences

Gene	Morpholino Sequence (5'-3')	Type
p53	GCGCCATTGCTTTGCAAGAATTG	Translation blocking
tsc2	ACTCTTTACTGGGCTGTTTATTCAT	Translation blocking
tsc2	AACAGTGTTATTTACCGTCTGCGAG	Splice blocking

Table 2.3: mRNA Overexpression Construct Primers

Gene	Primer Sequence (5'-3')
VAX2	F - CACAGGATCCACCATGGGCGATGGGGGCGCCGAGCG
	R - CACATCTAGATTAAGTGTTAGCTTTCTTGCAGCTGC

Table 2.4: qPCR primers

Gene	Forward Primer (5'-3')
bmp4	F - CACAGTATCTGCTCGACCTCTA
	R - GATATGAGTTCGTCCTCTGGGATG
ef1a	F - CCTTCGTCCCAATTTCAGG
	R - CCTTGAACCAGCCCATGT
efnb2a	F - ATACTGGAACACCACGAACAC
	R - GTGGGCAAACTATGTCCATCT
tbx5a	F - GGAATTTAAGGCCTCACGGTA
	R - GTCCCTTTCCCTTTCATCTGTCTC
vax2	F - CTCTCTGAGACACAGGTGAAAG
	R - GATTCGGAGGTGGATGATGAG

Table 2.5: CRISPR Target Sequences/Oligonucleotides

Gene	Target Site (5'-3')	Oligo Sequence (5'-3')
Constant oligo	n/a	AAAAGCACCGACTCGGTGCCACTTTTTCAAGTTG ATAACGGACTAGCCTTATTTTAACTTGCTATTTCT AGCTCTAAAAC
vax2 (target site 3 – exon 2)	TGGACCGGCCGAA GCGCACG**CGG**	ATTTAGGTGACACTATATGGACCGGCCGAAGCGC ACGGTTTTAGAGCTAGAAATAGCAAG
vax2 (target site 4 – exon 2)	GTTCCAGCGTTGT CAGTATG**TGG**	ATTTAGGTGACACTATAGTTCCAGCGTTGTCAGT ATGGTTTTAGAGCTAGAAATAGCAAG

Table 2.6: Plasmid-based RNA Probes

Gene	Vector	Antibiotic	RE	RNAP
aldh1a2	pSPORT	Carbenicillin	EcoRI	SP6
aldh1a3	pCR4-TOPO	Carbenicillin	NotI	T3
bambia	pCR4-TOPO	Carbenicillin	NotI	T3
efnb2a	pCR4-TOPO	Carbenicillin	NotI	T3
ephb2	pCR4-TOPO	Carbenicillin	NotI	T3
vax2	pCR4-TOPO	Carbenicillin	NotI	T3

Table 2.7: PCR-based RNA Probes

Gene	Forward Primer (5'-3')	Length (bp)	T_m (°C)	RNAP
bmp4	F - CCATCTCAGATATTTTCGGGG	1278	52	SP6
	R - GTTATT TACCTGACAAGTAGCAG			
tbx2b	F - ATGGCTTACCACCCTTTCCACG	1144	53	T3
	R - CGTCTTTCTTCTCCGCAATAGGC			
tbx5a	F - TGTGACGAGCACTAATGTCTTCCTC	713	52	T3
	R - GCAAAAAGCATCGCAGAACG			

Chapter 3

Morphogenetic defects underlie Superior Coloboma, a newly identified closure disorder of the dorsal eye

A version of this chapter is published: Hocking, J.C.*, Famulski, J.K.*, Yoon, K.H., Widen, S.A., Bernstein, C.S., Koch, S., Weiss, O., FORGE Canada Consortium, Agarwala, S., Inbal, A., Lehmann, O.J., Waskiewicz, A.J. (2018).)Morphogenetic defects underlie Superior Coloboma, a newly identified closure disorder of the dorsal eye. *PLoS Genet*, 14(3):e1007246. doi: 10.1371/journal.pgen.1007246. PMID: 29522511; PMCID: PMC5862500. *joint first authors

In this research article, I performed all of the *tbx2b* experiments, imaged and analyzed data related to *tbx2b*, created Figure 6 (presented here as Figure 3.11), and aided in the editing of the manuscript. Subsequently, my thesis work resulted in Figure 3.12, which was not published, but is included in Chapter 3. The rest of the article has been abridged, and is only presented to provide necessary context and background that inform the rest of the thesis.

**Supplemental videos referenced in this chapter may be found in online supporting information (doi: 1007246)

3.1. Introduction

Aberrant ocular morphogenesis during embryonic development frequently results in reduced visual acuity or blindness. Morphological development of the eye begins with evagination of retinal precursors from the forebrain to produce bilateral optic vesicles and subsequent invagination of the associated ectoderm to create the lens (Bazin-Lopez et al., 2015; Fuhrmann, 2010). Each optic vesicle reorganizes into a bilayered optic cup, with the distal (lens-facing) layer forming the presumptive neural retina and the proximal layer forming the retinal pigmented epithelium (RPE). To provide an entry point for vasculature and an exit pathway for axons of the optic nerve, a transient inferior (choroid) fissure forms along the ventral/inferior side of the optic cup and stalk. In cases where the inferior fissure fails to close, gaps remain within tissues of the eye (iris, retina, choroid and/or occasionally lens) (Chang et al., 2006; Onwochei et al., 2000). This congenital anomaly, referred to as ocular coloboma, is estimated to occur in 1 out of 4-5,000 live births and cause 3-11% of pediatric blindness (Onwochei et al., 2000; Williamson and FitzPatrick, 2014). Ocular coloboma has a complex causality encompassing mutations in over 20 genes (Gregory- Evans et al., 2004; Williamson and FitzPatrick, 2014). Although both clinically and genetically heterogeneous, coloboma predominantly affects the inferior aspect of the eye.

The posterior segment of the developing eye receives two vascular supplies (Saint- Geniez and D'Amore, 2004). The transient hyaloid vasculature is a plexus between the retina and lens, and is connected to the hyaloid artery, which enters the eye via the inferior fissure. A second circulatory system, the choroidal vasculature, grows over the surface of the optic cup to nourish the RPE and the light-sensing photoreceptor cells in the outer retina. Although development of the choroidal vessels is poorly understood, zebrafish studies demonstrated that the complex choroidal vascular plexus is preceded by a simple set of pioneer vessels (Kaufman et al., 2015; Kitambi et al., 2009). To form this so-called superficial vascular system (distinct from the superficial retinal vessels and also known as the ciliary vasculature), three radial vessels grow over the optic cup and anastomose to create an annular vessel encircling the lens. The highly stereotypical formation of the superficial vessels suggests precise developmental regulation, but the mechanisms that guide their growth are currently unknown.

In the context of studying a large cohort of patients with ocular coloboma, we identified five local patients with a novel ocular anomaly characterized by gaps in tissues of the superior eye. Although it is logical that such an anomaly represents another fissure disorder, common models of vertebrate eye development do not feature a division in the embryonic dorsal/superior eye. However, a careful examination of zebrafish, chick, and mouse eye development did reveal a transient groove, or sulcus, bisecting the dorsal optic cup. Moreover, we utilized patient exome sequencing and zebrafish models to define the importance of dorsal-ventral patterning in morphogenesis of this ocular sulcus. Functionally, the superior ocular sulcus serves as a conduit for the advancing first vessel of the superficial vasculature, and we note profound errors in vascular growth and connectivity in embryos with abnormal sulci.

3.2. Results

3.2.1. Identification of patients with superior coloboma

Over a six-year period (2007-2012), we identified five local patients with superior ocular defects affecting the iris, lens, retina, optic nerve and/or sclera (Fig. 3.1 and Table 3.1); notably, these were not associated with a family history of such anomalies. On the basis of apparent similarity to coloboma (gaps in inferior/ventral ocular tissue), yet inverse orientation, we propose the term *superior coloboma* to describe this disorder. The first patient, with tuberous sclerosis attributable to a rare *TSC2* (c.C5026T; p.R1676W) mutation, exhibited a prominent unilateral iris coloboma situated at 12 o'clock. Bilateral disease was present in a single patient (#2), and involved both iris and lens (Fig. 3.1, images 2 and 3). Two of the five patients were diagnosed in infancy, and for one (#4), examination under anesthesia was required to fully characterize pathology. As is evident from Fig. 3.1, the diversity of tissue involvement in superior colobomata recapitulates that present in inferior colobomata. We subsequently received, from pediatric ophthalmologists at US and UK tertiary referral centers, clinical data on three further patients with superior colobomata. These cases extended the range of associated phenotypes to include additional structural ocular malformations (microphthalmia, or small eye; #8). All eight patients in our cohort had profoundly reduced visual acuity, precluding normal stereopsis.

3.2.2. Exome sequencing of superior coloboma patients

To identify candidate genetic variants carried by superior coloboma patients, exome sequencing was performed on the initial five probands (S2 Table). Identified variants were prioritized by comparison to SNP databases (frequency <1%), *in silico* prediction algorithms (MutationTaster >0.95) and expression within the developing eye or previously identified connections to coloboma. We focused our efforts on understanding genetic alterations in the single patient with bilateral superior coloboma (#2, Table 3.3). In particular, we noticed that patient #2 carries compound heterozygous variants in the Retinoic Acid (RA) synthesis gene *CYP1B1* (Chambers et al., 2007) (Fig. 3.2A) as well as a rare (dbSNP: 1 in 60,706; NHLBI and 1000 Genomes: 0 in 14,000) missense variant in Bone Morphogenetic Protein (BMP) Receptor 1A (*BMPR1A*, Fig. 3.2B,C). As RA and BMPs are morphogens with essential roles in eye development, including regulation of inferior fissure closure (Behesti et al., 2006; French et al., 2009; Gosse and Baier, 2009; Kruse-Bend et al., 2012; Lupo et al., 2011; Sasagawa et al., 2002; Valdivia et al., 2016), we hypothesized that the identified mutations contributed to the patient's ocular disorders. In order to examine how disruption of eye patterning genes could lead to superior coloboma, we next turned to animal models and conducted an in depth analyses of dorsal eye morphogenesis.

3.2.3. Vertebrate studies of dorsal ocular morphogenesis

Inferior coloboma arises from failed closure of the choroid fissure located in the ventral eye. Given the comparable phenotype despite opposite orientation seen in superior coloboma patients, we hypothesized a similar etiology. Although the standard model of eye development describes an uninterrupted dorsal retina, two older studies of fish eye development identified a groove present in this space (Nordquist and McLoon, 1991; Schmitt and Dowling, 1999). To determine if such a structure exists broadly across vertebrates and whether it is a Laminin-lined space, we chose to revisit the study of dorsal eye morphogenesis in fish, chick and mouse. Using multiple microscopy methods, we identified a transient groove/sulcus in the dorsal zebrafish eye (dorsal in fish and superior in human are equivalent; for consistency with superior coloboma, we

describe this structure as the *superior ocular sulcus* [SOS]) (Fig. 3.3A-D). The sulcus is visible by stereoscope but more obvious in compound or confocal observations of live embryos (Fig. 3.3A), and most easily discernible from 21-25 hpf. When imaged under an electron microscope, the SOS can be seen to transect the distal portion of the dorsal retina (Fig. 3.3B), while single confocal optical slices reveal the SOS as a distinct space (Fig. 3.3C) lined by basal lamina (Fig. 3.3D).

To ascertain whether a similar structure exists in chick, we examined tissue sections immunostained for Laminin and counterstained with DAPI. At stage HH16, we observed the presence of a Laminin-lined division in the distal portion of the chick dorsal optic cup (n=6/8 eyes; Fig. 3.3E, Fig. 3.4). For evidence of a comparable structure in mammals, we next examined mice and found a Laminin-lined separation across the inferior portion of the dorsal optic cup at embryonic day 10.5 (Fig. 3.3F). A collaborator also shared older SEM studies of newt (*Taricha tarosa*) development, which similarly demonstrate the presence of a division across the dorsal embryonic eye (Fig. 3.5, personal communication, A. Jacobson). Thus, we present clear evidence for the existence of an evolutionarily conserved, Laminin-lined sulcus in the dorsal optic cup of multiple vertebrate species.

The inferior fissure temporarily bisects the ventral retina prior to closing through progressive fusion of the nasal and temporal margins of the ventral optic cup (Chang et al., 2006). The SOS similarly extends across the dorsal zebrafish retina (Fig. 3.3A-2D) to partially separate the nasal and temporal retinal lobes, and is also present only transiently. To determine the mechanism of SOS closure, we followed ocular morphogenesis over time. The SOS arises soon after optic cup formation (19-20 hpf) as a distinct and narrow structure (S1 Video and Fig. 3.3A,B). Notably, formation of the sulcus occurs at a time when the developing retinal pigmented epithelium is spreading around the optic cup, but is not associated with significant cell movement or apoptosis in the forming dorsal retina (S2 Video). Unexpectedly, the edges of the narrow SOS do not migrate toward one another and fuse, but instead the SOS transitions at 22-24 hpf to a shallow and wide trough and gradually disappears after 26 hpf (S3-S5 Videos and Fig. 3.6). Both phases are visible in representative SEM images (Fig. 3.3B). As we observed the transition from narrow to wide, and never detected an epithelial fusion event, it is logical to propose that the sulcus closes via cell rearrangement or shape modification, mechanisms distinct from the epithelial fusion that occurs within the choroid fissure.

3.2.4. Bmp signaling regulates closure of the superior ocular sulcus

BMP ligands (Gdf6/Bmp13 and Bmp 2, 4, and 7) pattern the eye at the time of SOS closure (Behesti et al., 2006; French et al., 2009; Gosse and Baier, 2009; Heermann et al., 2015; Kruse-Bend et al., 2012; Murali et al., 2005) and the identified *BMPR1A* patient variant alters a highly conserved residue in the kinase domain (p.Arg471His, Fig. 3.2); therefore, we tested whether reduced BMP receptor activity affects closure of the SOS. The small molecule DMH1 is an inhibitor of type IA BMP receptors, with robust and specific activity in zebrafish (Hao et al., 2010; Paul et al., 2008). Embryos were treated with DMH1 either just after gastrulation or just prior to optic cup invagination (10 and 18 hpf, respectively) and evaluated for SOS presence at 28 hpf, a time point when the sulcus is no longer visible in wild type embryos. Exposure to DMH1 prevented SOS closure in a dose-dependent manner (Fig. 3.7A,B), establishing that BMP signaling regulates sulcus morphogenesis.

We next used a zebrafish overexpression assay to evaluate whether the patient variant disrupts BMPR1A function. As injection of one-cell stage embryos with wildtype human *BMPR1A* mRNA failed to elicit alterations to dorsal-ventral axis specification, we used site- directed mutagenesis to introduce a Q233D mutation previously shown to render BMPR1A constitutively active (Zou et al., 1997). Injection of mRNA encoding the constitutively active BMPR1A receptor (caBMPR1A) efficiently induced ventralization of whole zebrafish embryos, while *caBMPR1A* carrying the patient variant (*R471H-caBMPR1A*) showed mildly reduced activity (Fig 3.7C and Fig 3.8). The patient variant therefore does not completely inactivate the protein, but this assay does suggest that it could be a hypomorphic allele and may have been one of multiple factors contributing to the development of superior coloboma. Overall, our data sup- port a role for Bmp signaling in regulating SOS closure.

Within the zebrafish eye, Bmpr1a mediates signaling from the Gdf6a (Growth Differentiation Factor 6a, Bmp13) ligand (Wang et al., 2013) and absence of Gdf6a results in almost complete loss of dorsal (superior) ocular gene expression, expansion of ventral (inferior) gene expression, and a small eye phenotype (den Hollander et al., 2010; French et al., 2009; Gosse

and Baier, 2009). Knockdown of Gdf6a signaling in wild type embryos by injection of antisense morpholinos oligonucleotides caused a highly penetrant SOS closure defect, very similar to that seen with DMH1 exposure (Fig. 3.9A-C). Recapitulation of the persistent sulcus phenotype in both homozygous (French et al., 2009; Gosse and Baier, 2009) and a subset of heterozygous *gdf6a* embryos (Fig. 3.9D,E) shows that SOS closure is sensitive to the precise level of BMP signaling. A lack of Gdf6a also affected formation of the SOS, as seen by the deeper sulcus in a representative SEM image (Fig. 3.9D, bottom right panel) and in animations showing the surface morphology of the dorsal eye in 22 hpf wild type (S6 Video), *gdf6a* heterozygous (S7 Video) and *gdf6a* homozygous (S8 Video) embryos. While the sulcus eventually closes in most Gdf6a-deficient embryos, two adult *gdf6a*$^{-/-}$ fish displayed superior colobomata (Fig. 3.9F), demonstrating that an early closure defect can lead to the disease phenotype.

There are diverse outputs of Gdf6a signaling, regulating cellular functions such as apoptosis, cell proliferation, and dorsal-ventral retinal patterning (French et al., 2009; French et al., 2013; Gosse and Baier, 2009; Valdivia et al., 2016). Because proliferative defects are visible after sulcus closure and apoptotic cells are not concentrated near the SOS (French et al., 2013), we reasoned that dorsal-ventral retinal patterning is the Gdf6a function most essential for SOS closure. During development, dorsal ocular BMP signaling is balanced by midline Sonic Hedgehog (Shh) activity (Sasagawa et al., 2002; Zhang and Yang, 2001), and *gdf6a*$^{-/-}$ mutants exhibit an expansion of the Shh downstream gene *vax2* into the dorsal retina (Gosse and Baier, 2009). We therefore tested whether increased Shh signaling in BMP-deficient embryos underlies the persistent SOS phenotype. Indeed, treatment of *gdf6a*$^{-/-}$ and *gdf6a*$^{+/-}$ embryos with the Shh inhibitor cyclopamine significantly rescued the delayed closure phenotype (Fig. 3.10A,B). Cyclopamine treatment also partially rescued patterning in the dorsal retina, as it restored the *tbx5a* expression domain in *gdf6a* heterozygotes (Fig. 3.10C,D). These data support the idea that SOS closure is dependent on proper pattern formation within the developing retina and that sulcus morphogenesis is regulated by a balance of ventral Shh and dorsal BMP signaling pathways.

3.2.5. Analysis of a second superior coloboma patient

Transcriptome analyses of Gdf6a-depleted retinas have highlighted critical regulators of dorsal-ventral patterning within the zebrafish eye (French et al., 2013). Using this dataset, we interrogated the superior coloboma patient exome data, and identified a variant in *TBX2* (p.Pro329His). Zebrafish *tbx2b* is expressed in the dorsal eye in a Gdf6a- and BMP- dependent manner (Fig. 3.11A) (Gosse and Baier, 2009). To analyze the function of zebrafish *tbx2b* in regulating sulcus morphogenesis, we compared dorsal eye morphology between wild type embryos and *tbx2b*^{fby} (*from beyond*) mutants (Snelson et al., 2008). We note a statistically significant increase in the proportion of embryos displaying an open SOS in *tbx2b*^{fby} mutants compared to wild type embryos at 28 hpf (Fig. 3.11B,C). Such experimental results support a model in which dorsal-ventral patterning within the embryonic eye provides essential cues for morphogenesis of the SOS.

Studies of *TBX2* in zebrafish are slightly complicated due to the genome duplication event in teleost evolutionary history that led to the rise of paralogous genes. Zebrafish have two paralogs of *TBX2*, which are denoted as *tbx2a* and *tbx2b* (Sedlectcaia & Evans, 2011). Although there are several studies regarding *tbx2b* in zebrafish eye development, the role of *tbx2a* has yet to be studied. Both paralogs, *tbx2a* and *tbx2b*, are expressed in overlapping dorsal regions of the developing eye. Additionally, redundancies between *tbx2a* and *tbx2b* have been shown to exist in other tissues; it has been shown that *tbx2a* and *tbx2b* expression serve as redundant regulators of heart chamber size in zebrafish heart development. However, injection of *tbx2a* translation-blocking morpholino in *tbx2b*$^{-/fby}$ embryos did not conclusively result in any changes to SOS morphology (Fig. 3.12).

3.2.6. Superior ocular sulcus functions as a conduit for superficial vasculature

Imaging of *Tg(rx3*:*GFP;kdrl*:*mCherry)* embryos revealed that the deep sulcus in *gdf6a*$^{-/-}$ mutants creates a notable divot in the optic cup immediately dorsal to the lens (Fig. 3.13A). In all cases (n = 8), the forming ectopic vessels grew directly into this space between the dorsal edge of the lens and the retina. Given the defects observed for the DRV in Bmp-deficient embryos, we conclude that dorsal retinal patterning is necessary for superficial vascular pathfinding.

Patterning of the ventral retina is regulated by Shh (Sasagawa et al., 2002; Zhang and Yang, 2001), and our earlier data suggest a balance between Bmp and Shh signaling impacts SOS morphogenesis. In contrast to loss of BMP signaling, cyclopamine inhibition of Shh signaling in wild type embryos resulted in a shallow SOS that closes early (Fig. 3.13B), and an increased proportion of embryos with multiple DRVs spread across the dorsal retina (Fig. 5.13B). A similar change in growth of the DRV was noted previously in embryos where the Shh receptor Smoothened is non-functional (Weiss et al., 2017). In summary, disrupted dorsal-ventral patterning of the retina leads to profound alteration of the superficial vasculature.

3.3. Discussion

In this manuscript, we classify superior coloboma as a separate disease with a developmental origin distinct from, but comparable to, inferior coloboma. Eight patients display gaps in tissues of the superior eye, including retina, lens, and iris. We demonstrated the existence of a transient dorsal/superior groove in vertebrate eye development that is conserved among fish, chick, newt and mouse. Failure to close the superior ocular sulcus (SOS) can result in adult zebrafish displaying a phenotype that resembles superior coloboma. Furthermore, it supports the evolutionary conservation of the SOS amongst vertebrates, an evolutionary distance of some 450 million years.

There are rare reports in the scientific literature of patients with “atypical” coloboma (Abouzeid et al., 2009; Jethani et al., 2009; Mann and Ross, 1929; Ramirez- Miranda and Zenteno, 2006; Villarroel et al., 2008), ocular anomalies contrasting with the position of the known inferior embryonic fissure. The vast majority of such cases (macular coloboma, aniridia, or nasally/temporally oriented iris coloboma) are unlikely to arise from defects of sulcus closure. However, at least two of the described atypical coloboma patients display iris colobomata with a superior orientation (Abouzeid et al., 2009; Mann and Ross, 1929). Although the embryonic mechanism was originally considered anomalous, our identification of the SOS provides a likely explanation for the unusual coloboma identified in these two patients.

Exome sequencing of our superior coloboma patients identified rare variants in the genes encoding the type 1 BMP receptor and transcription factor T-box 2. In the absence of multigenerational pedigrees of affected patients, we are unable to causally link such variants to the incidence of disease. However, the connection between BMP signaling and inferior fissure morphogenesis is well established. Indeed, variants in *GDF6* (*BMP13*), *BMP4*, and *SMOC1* are linked to inferior coloboma and microphthalmia (Abouzeid et al., 2011; Asai-Coakwell et al., 2007; Bakrania et al., 2008; Gregory-Evans et al., 2004; Williamson and FitzPatrick, 2014). Furthermore, zebrafish, *Xenopus*, chick, and mouse studies have demonstrated a key role for BMP signaling in optic cup morphogenesis, apoptosis, proliferation, and dorsal-ventral eye patterning (Abouzeid et al., 2011; Adler and Belecky-Adams, 2002; Asai-Coakwell et al., 2007; Asai-Coakwell et al., 2013; Behesti et al., 2006; French et al., 2009; Gosse and Baier, 2009; Weston et al., 2003). Consistently, abrogating BMP signaling either by DMH1 treatment or loss of Gdf6a results in profound SOS closure defects. Beyond the *gdf6a* homozygous mutant phenotype, we also detected a partially penetrant sulcus closure defect in the otherwise morphologically normal *gdf6a* heterozygotes, arguing that the sulcus is particularly sensitive to the levels of BMP signaling. Further, loss of Tbx2b function in zebrafish *fby* mutants leads to comparable aberrations in SOS morphogenesis. Such data, taken together with the detrimental nature of the patient *BMPR1A* variant, support a model whereby BMP signaling modulates SOS closure via regulation of target genes such as *tbx2*.

Research on ocular BMP signaling defines roles in regulating eye precursor cell number, apoptosis, proliferation, and dorsal-ventral gene expression (Asai-Coakwell et al., 2013; Bielen and Houart, 2012; French et al., 2009; French et al., 2013; Gosse and Baier, 2009; Pant et al., 2013; Valdivia et al., 2016). However, apoptotic cell populations are not localized to the SOS, and proliferative defects are present only after SOS closure (French et al., 2013; Pant et al., 2013). Furthermore, we note that *gdf6a* heterozygotes display aberrant sulcus closure, yet lack apoptotic or proliferative defects. In contrast, *gdf6a*$^{+/-}$ embryos display detectable alterations to dorsal-ventral gene expression, providing a correlation between patterning and SOS closure defects. To further test the role of dorsal-ventral patterning in sulcus dynamics, we asked whether rescue of the patterning defects in *gdf6a*$^{-/-}$ embryos would also promote SOS closure. Given the expansion of inferior markers into the superior retina of *gdf6a* mutants (French et al., 2009; Gosse and Baier, 2009), and the rescue of SOS defects with Shh inhibition, we conclude that the aberrant closure of

the SOS in Gdf6- and Tbx2-depleted embryos is linked to dorsal-ventral patterning defects of the vertebrate eye.

Eye morphogenesis and patterning are dependent on multiple signaling pathways, in addition to Bmp and RA. For example, overexpression of the Wnt inhibitor Dkk1 results in loss of dorsal ocular gene expression (Veien et al., 2008), and mutation of the Wnt receptor FZD5 (thought to function as a receptor for both canonical and non-canonical Wnts) causes inferior coloboma (Liu et al., 2016). In examining the prioritized list of rare variants identified in superior coloboma patients, we note rare variants in *NKD1*, *CELSR2*, *FZD4*, *SCRIB*, and *WNT9B* (components of canonical or non-canonical Wnt pathways). The rare *TSC2* (Tuberous Sclerosis Complex 2/Tuberin) variant in patient #1 plausibly implicates other cellular mechanisms in the induction of superior coloboma. TSC2 complexes with TSC1 to regulate the mTOR signaling pathway (Henske et al., 2016), and loss of either gene leads to unregulated cell growth and proliferation.

The rare incidence of superior coloboma argues that the disorder is unlikely caused by simple, single-gene inheritance. Rather, a model incorporating multi-gene inheritance or incomplete penetrance is more plausible. Seven of the eight patients with superior coloboma in the current study display unilateral disease, also a common characteristic of inferior coloboma (Nakamura et al., 2011). The highly penetrant defects found in zebrafish *gdf6a* mutant larvae, which only infrequently result in an adult superior coloboma phenotype (Fig. 3.10F), are consistent with an impressive ability of the developing eye to recover from embryonic defects. However, the absence of an obvious coloboma does not preclude abnormal SOS morphogenesis generating more subtle abnormalities, such as vascular misrouting. Although defining the relative contribution of heritability and environment is challenging, other disorders offer potential insight. Characterized by appreciable globe enlargement, high myopia represents an ocular disorder with substantial genetic and environmental components, where unilateral cases account for up to one third of the total (Fitzgerald et al., 2005). Anisometropia represents a second example of an asymmetric developmental ocular phenotype (Barrett et al., 2013), and the pattern apparent in the current cases (Fig. 3.1) corresponds with such examples.

Here, we have characterized a previously unrecognized developmental structure with a significant disease connection. Further studies will be needed to discern the exact mechanisms of sulcus formation and resolution, and to more deeply analyze the causes of superior coloboma.

3.4. Figures

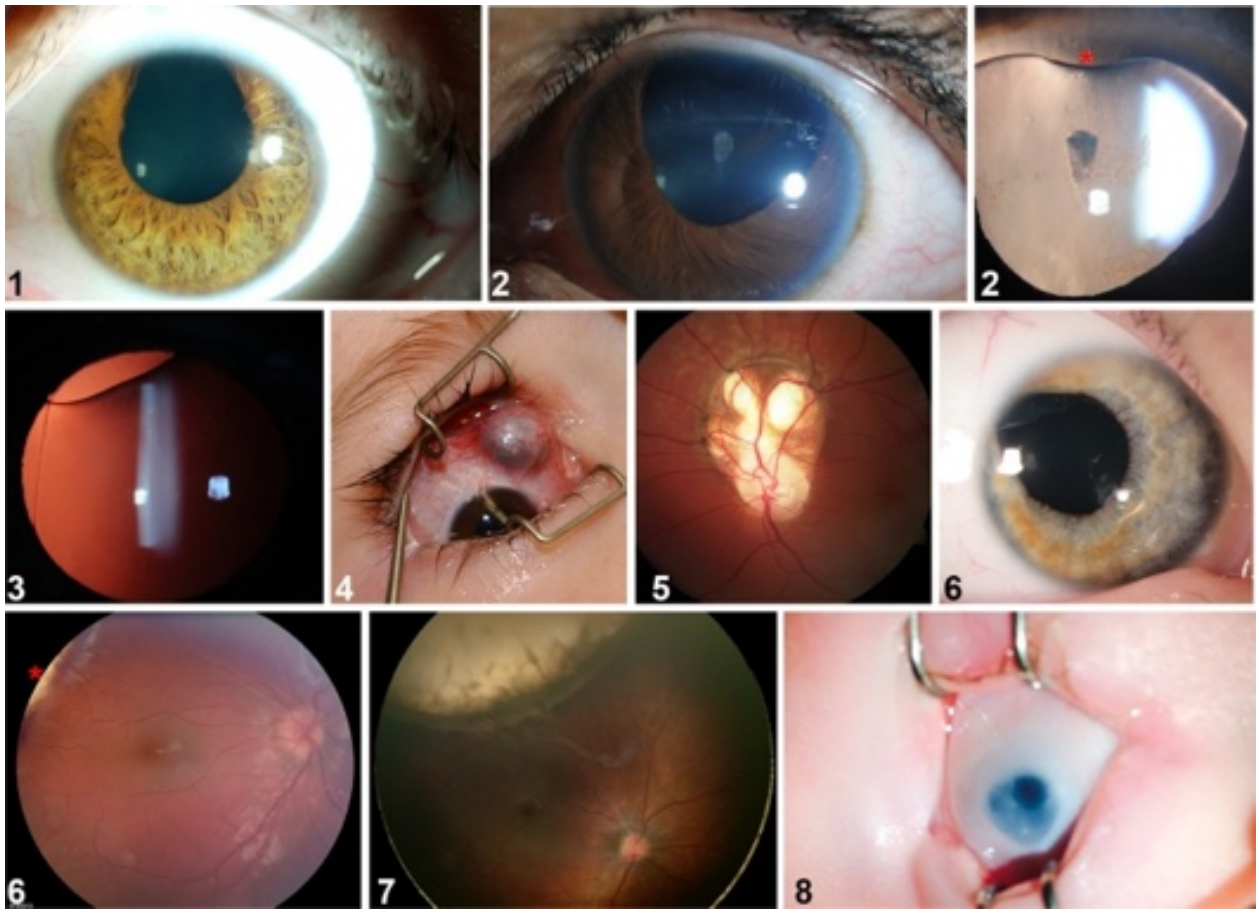

Figure 3.1: Superior coloboma. Montage from patients with superior coloboma (numbers represent patients described in S1 Table). #1: unilateral superior iris coloboma. #2: first panel, asymmetrically-sized iris defects with bilateral pupil involvement, left eye shown; second panel, superior lenticular coloboma (asterisk) associated with a lens zonule defect. #3: lenticular coloboma, lens edge visible with retro- illumination. #4: superior scleral defect with uveal (choroid) protrusion. #5: superior retino-choroidal coloboma extending from optic disc in patient with Dandy-Walker Syndrome. #6: first panel, iris coloboma; second panel, edge of retino-chorodial coloboma (asterisk). #7: extensive retino-choroidal coloboma. #8: intra-operative photograph of a superior iris coloboma in a microphthalmic eye.

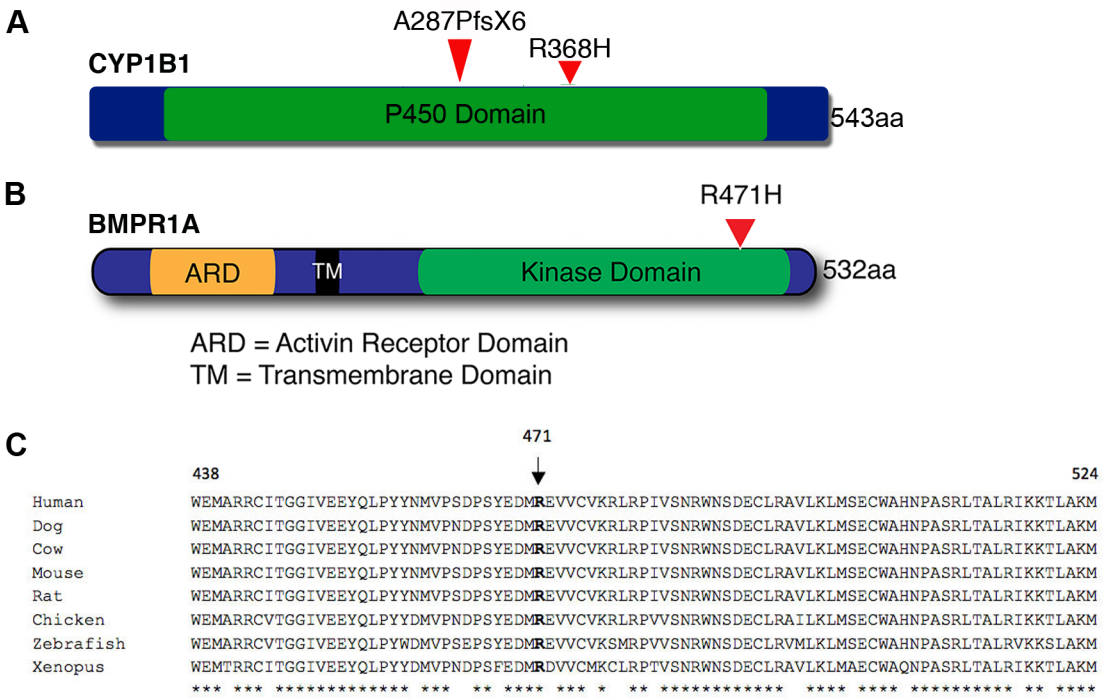

Figure 3.2: Genetic variants identified in bilateral superior coloboma patient. (A) Diagram of the human CYP1B1 protein, with the compound heterozygous mutations carried by patient#2 indicated. (B) Diagram of the human BMPR1A protein showing rare variant present in patient#2. (C) Alignment illustrating the evolutionary conservation of the BMPR1A protein kinase domain. The altered residue (p.**R**471H) is depicted in bold, with invariant residues denoted by *.

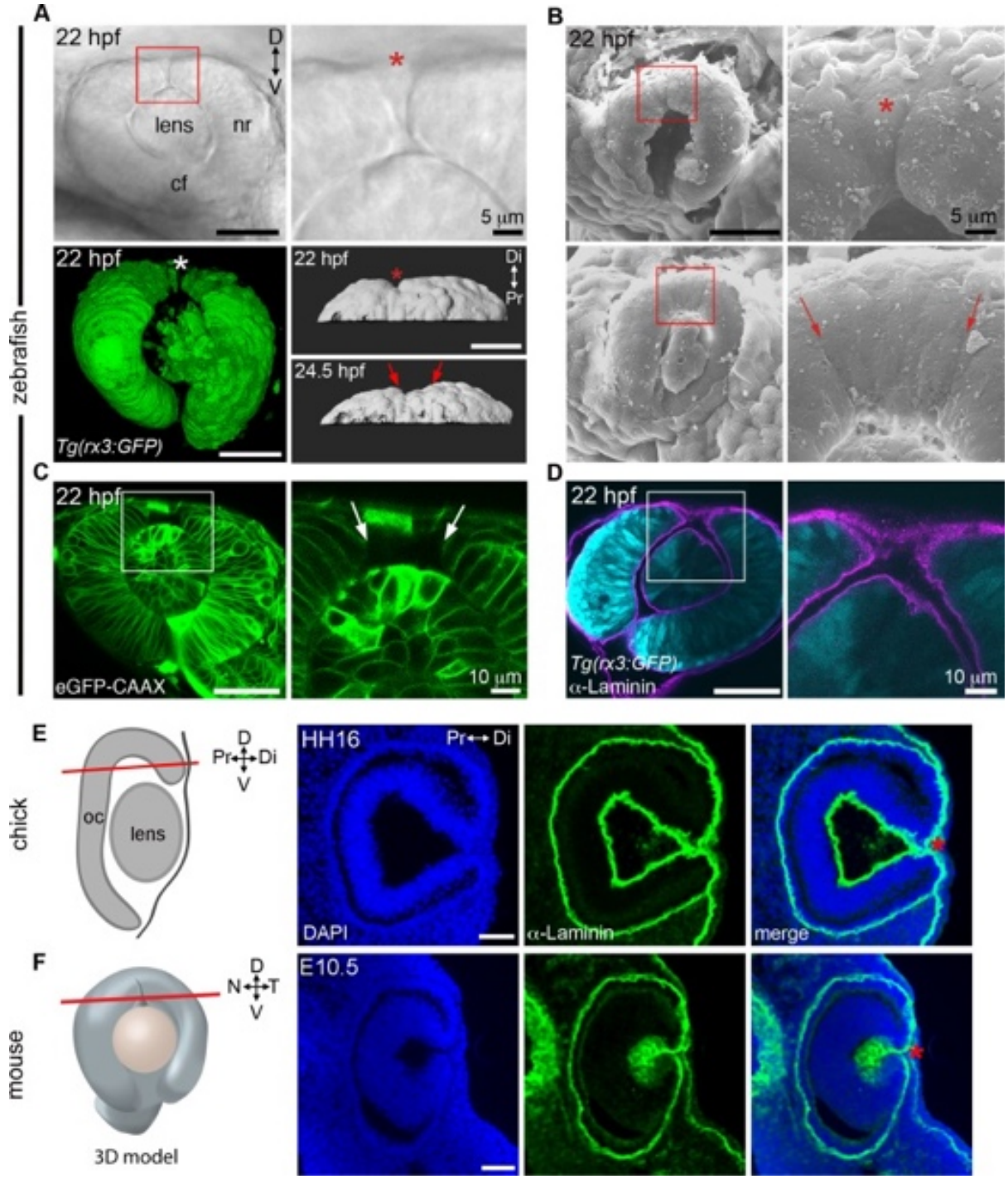

Figure 3.3: The superior ocular sulcus in zebrafish, chick and mouse. (A) Zebrafish eyes displaying superior ocular sulci (SOS) marked by an asterisk or arrows. Top row: lateral view DIC image of the eye of a live embryo, photographed on a compound microscope. Enlarged view is shown in panel on right. Bottom row: Left, lateral view surface projection of the eye of a live *Tg(rx3*:*GFP)* embryo; Right, surface projection dorsal views of eyes from a *Tg(rx3*:*GFP)* embryo.

(B) Scanning electron micrographs showing SOS at narrow (top row) and wide (bottom row) phases. Red boxes denote regions enlarged in panels on the right. (C) Single optical section, lateral view, through the eye of an embryo injected with *eGFP-CAAX* mRNA to label the cell membranes, with right panel showing enlarged view of boxed area. (D) Single optical section, lateral view, through eye of *Tg(rx3*:*GFP)* embryo (cyan) immunolabelled for Laminin to highlight the basal lamina (magenta). (E) Diagram showing chick eye with red line demonstrating the plane of section employed on the right. Representative horizontal section through the dorsal eye of a HH16 chick, stained with a Laminin antibody (green) and DAPI (blue). A dorsal, Laminin-lined space is evident in the distal portion of optic cup (asterisk). (F) Diagram showing 3D model of an embryonic eye with red line demonstrating plane of section for both mouse and chick sections. Right three panels are a representative horizontal section through the dorsal eye of an embryonic day 10.5 (E10.5) mouse, stained with a Laminin antibody (green) and DAPI (blue). A dorsal, Laminin-lined space is evident in the distal portion of optic cup (asterisk). Except where noted, scale bars are 50 μm. cf, choroid fissure; D-V, dorsal- ventral; HH, Hamburger Hamilton embryonic stage; hpf, hours post fertilization; N-T, nasal-temporal; nr, neural retina; Pr-Di, proximal-distal.

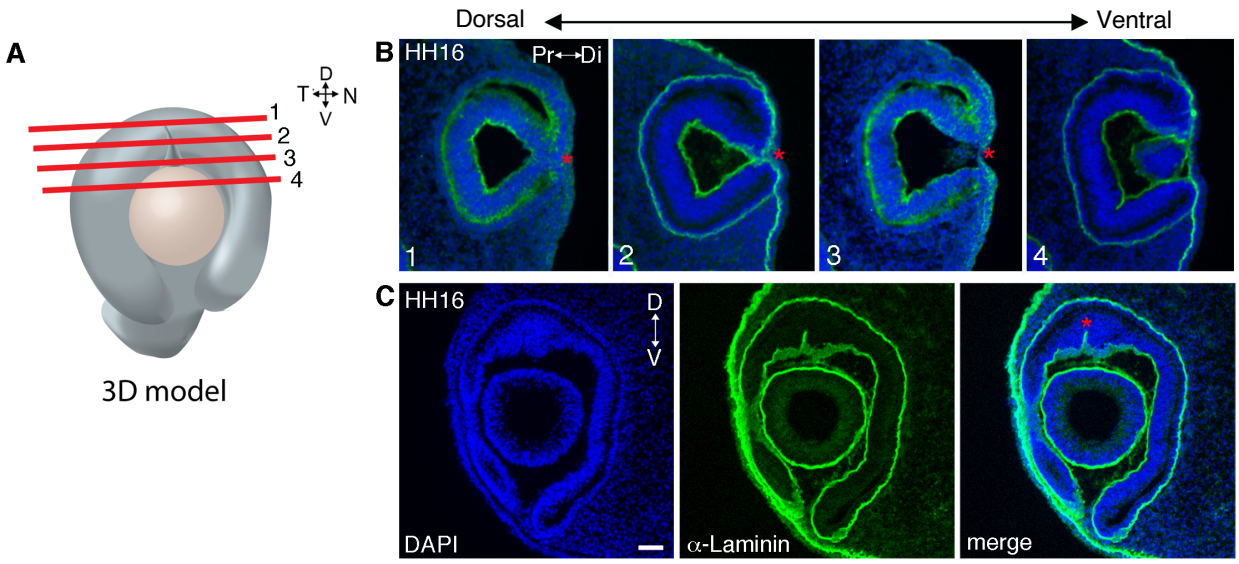

Figure 3.4: Superior ocular sulcus in chick. (A) 3D Model of the eye depicting where the eye was sectioned to create the serial horizontal sections shown in B. B) Serial cryostat sections of a chick HH16 stage eye stained with DAPI (blue) and α-Laminin antibody (green). First three sections are dorsal to the lens and third one is through the lens. (C) Tangential section of HH16 chick eye labeled with DAPI (blue) and α-Laminin antibody (green). D, dorsal; V, ventral; Di, distal; Pr, proximal; HH, Hamburger Hamilton. Red asterisks indicate superior ocular sulcus. Scale bar is 50 μm.

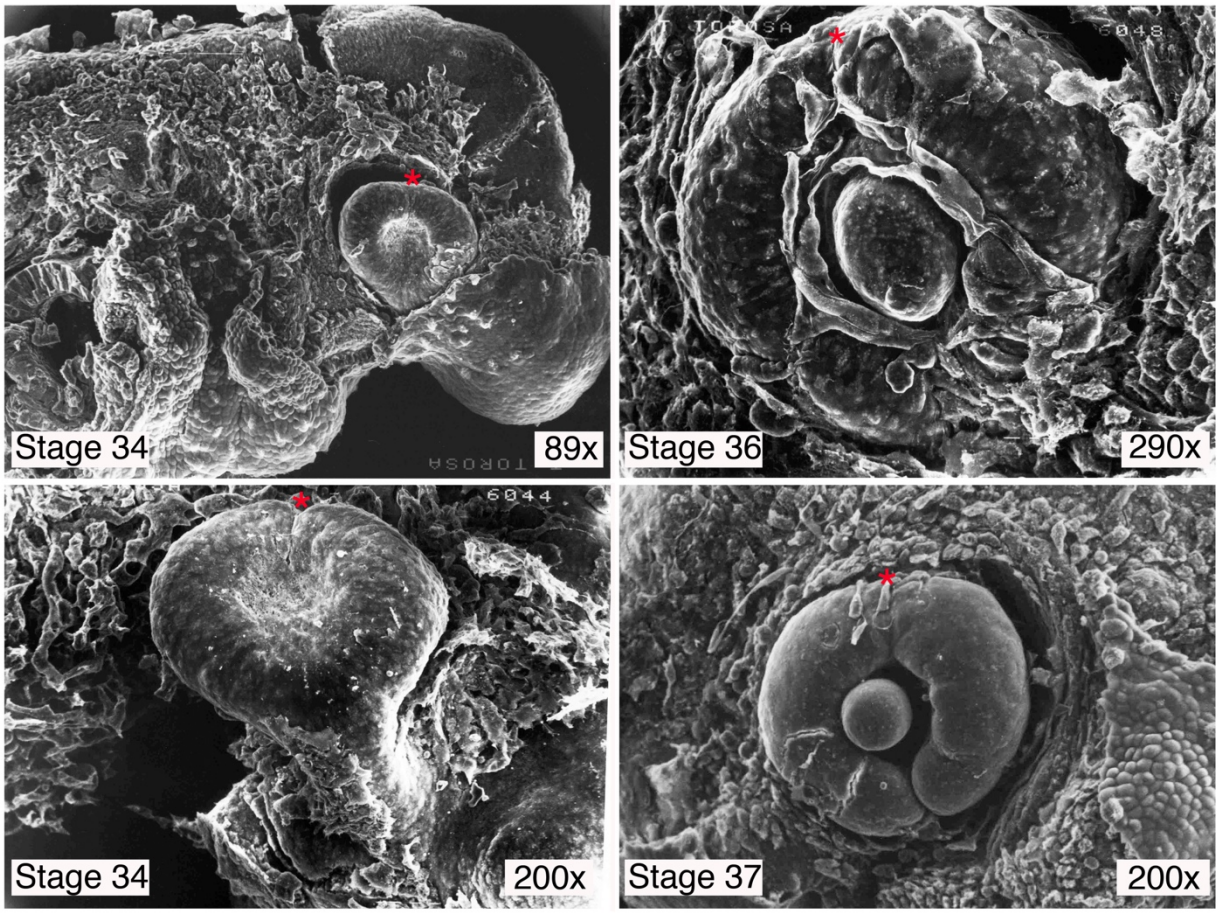

Figure 3.5: Superior ocular sulcus in newt. Scanning electron microscopy images of newt (*Taricha tarosa*) ocular development. Panels on left display SEM images of stage 34 embryos after partial dissection of surface tissues. Panels on right show slightly older embryos (stage 36–37), with vasculature intact in the stage 36 example. Red asterisks indicate superior ocular sulcus.

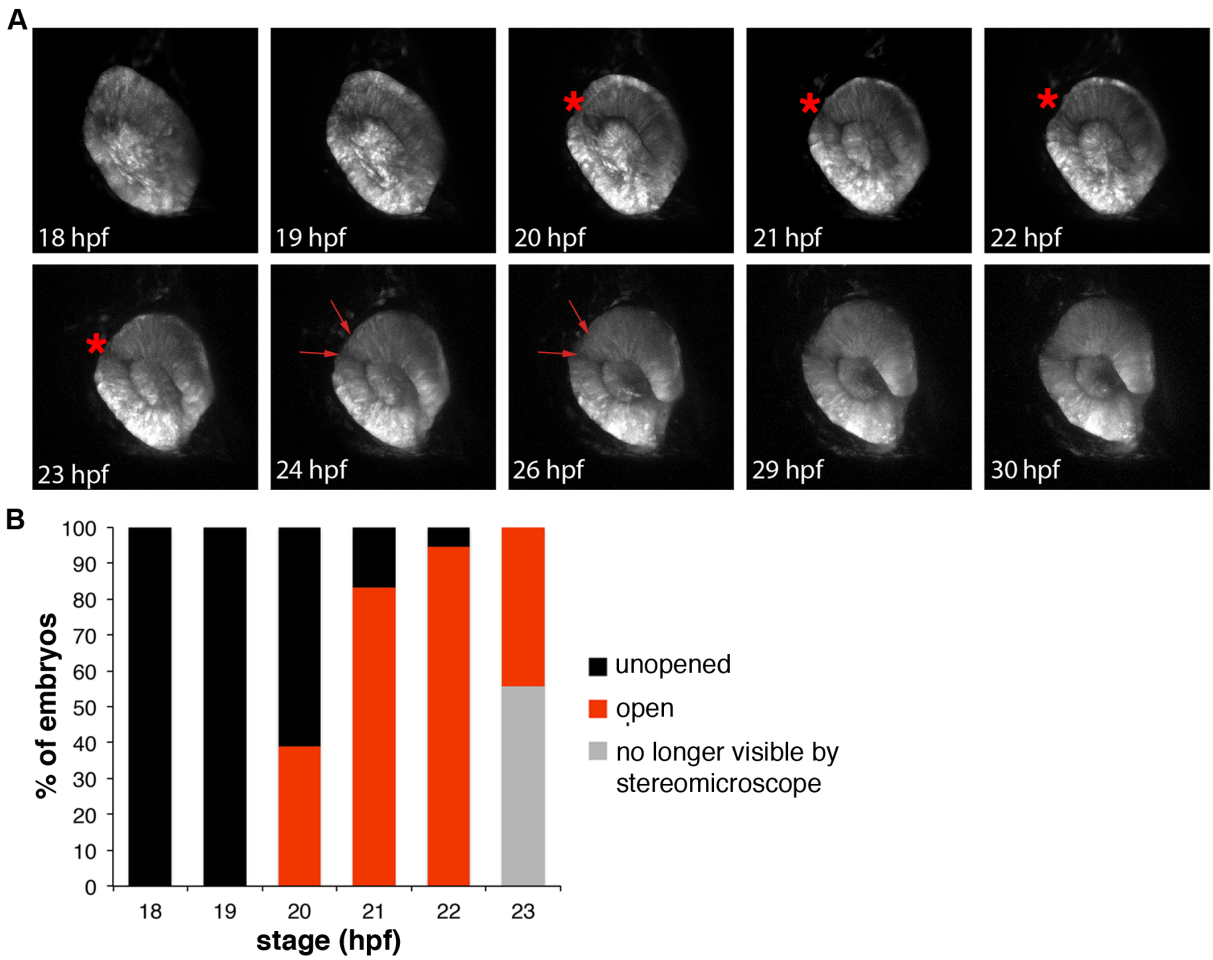

Figure 3.6: Dynamics of the zebrafish superior ocular sulcus. (A) Time-lapse images showing lateral views of the eye of a *Tg(rx3:GFP)* embryo. The superior ocular sulcus appears as a narrow groove across the dorsal retina at ~20 hpf (red asterisk), becomes wider by 24 hpf (red arrows) and disappears after 26 hpf. (B) Timing of SOS as viewed under a stereomicroscope. The wide and shallow phase is not visible by stereomicroscope, so the red bars indicate the per- centage of embryos with a narrow and distinct sulcus.

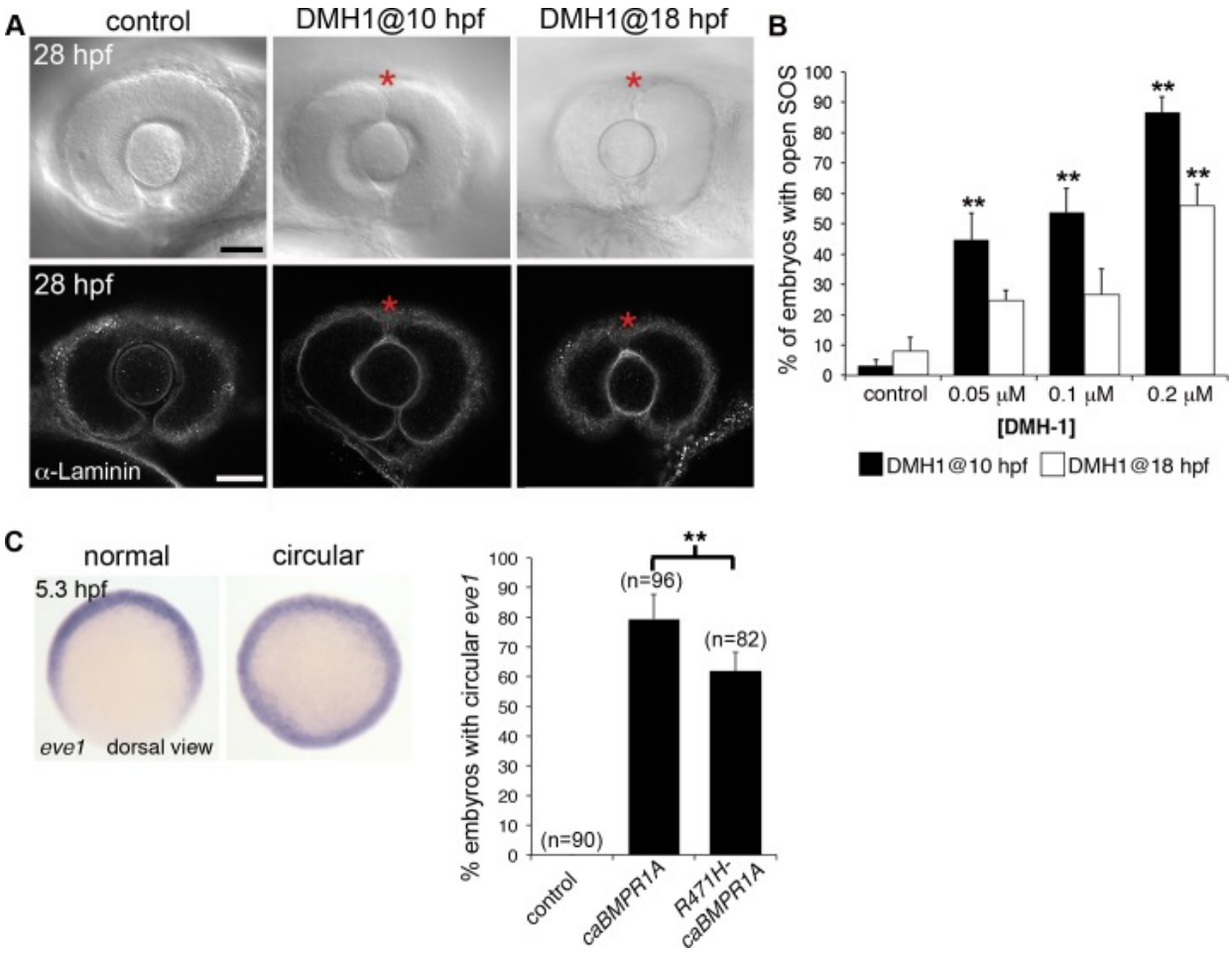

Figure 3.7: The role of BMPR1 signaling in closure of the superior ocular sulcus. (A-B) Effect of Bmpr1 antagonist DMH1 on SOS closure. Lateral view DIC images of eyes from live embryos (first row) and single optical slices of eyes processed for anti-Laminin immunofluorescence (second row) following exposure to control media or 0.02 μM DMH1, starting at either 10 or 18 hpf (A). SOS is marked by red asterisk. Quantification of delayed sulcus closure in DMH1-treated embryos (B). N = 3 experiments, n = 89 or 90 embryos for each condition. Data are means ± SEM. Statistics is a one-way ANOVA for each time series with Tukey's post-hoc test: $^{**}P<0.01$. (C) Injection of *caBMPR1A* mRNA into one-cell stage zebrafish embryos caused expansion of *eve1* gene expression into a circular ring in whole embryos at 50% epiboly (5.3 hpf). Significantly fewer embryos exhibited circular *eve1* expression when injected with *R471H-caBMPR1A*. N = 3 experiments. Data are means ± SEM. Statistics is a two-tailed *t* test: $^{*}P<0.05$. Scale bars are 50 μm.

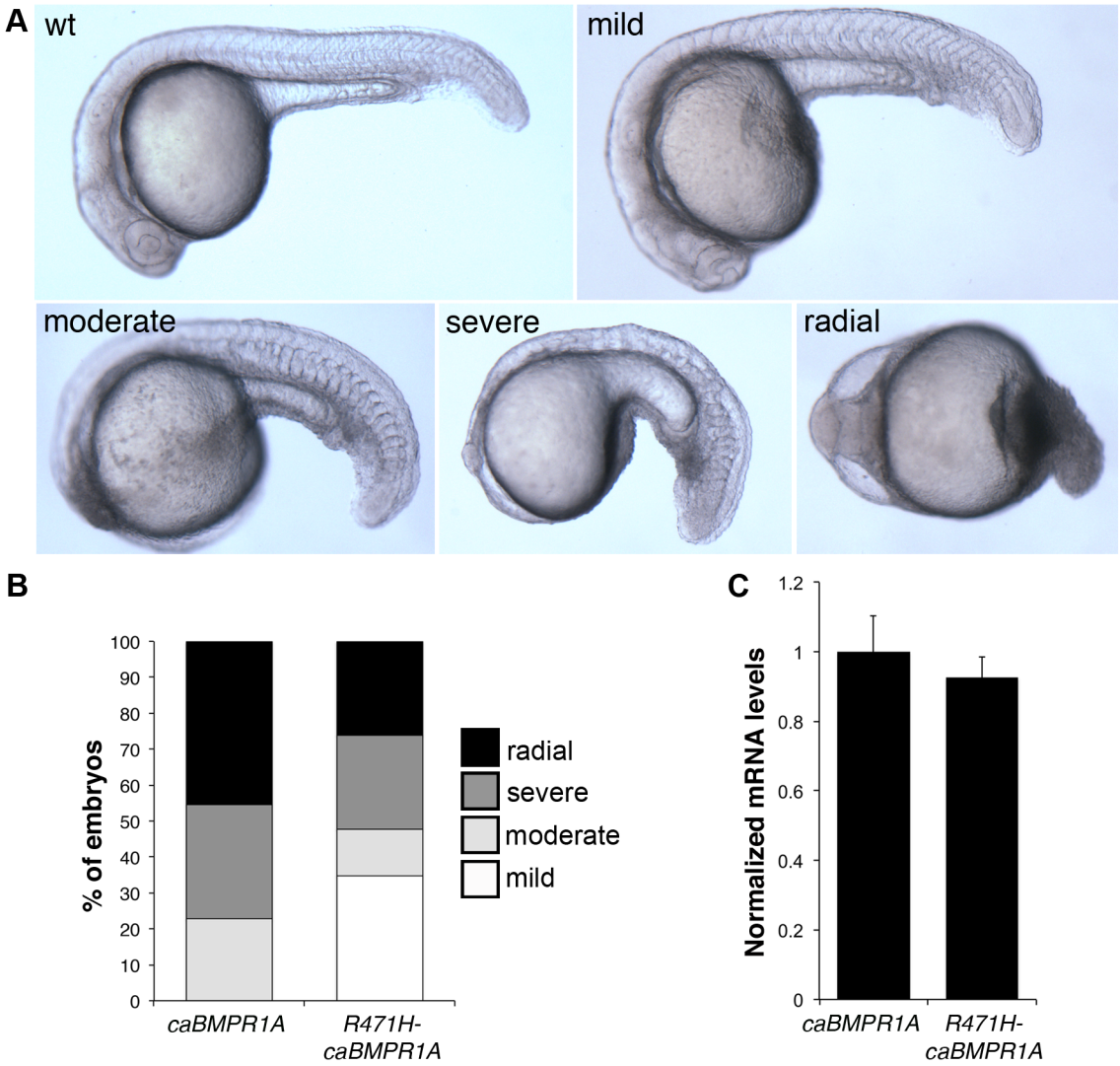

Figure 3.8: Human variant in BMPR1A reduces protein function. (A) One cell-stage zebrafish embryos were injected with *caBMPR1A* or *R471H-caBMPR1A* mRNA, and assessed at 24 hpf for morphological abnormalities by categorization according to the pictures shown. (B) Graph showing percentage of embryos injected with *caBMPR1A* (n = 22 embryos) or *R471H-caBMPR1A* (n = 23 embryos) that fit into each category of morphological abnormality. (C) qPCR showing equal amounts of injected RNA for each condition. Statistics is two-tailed *t* test.

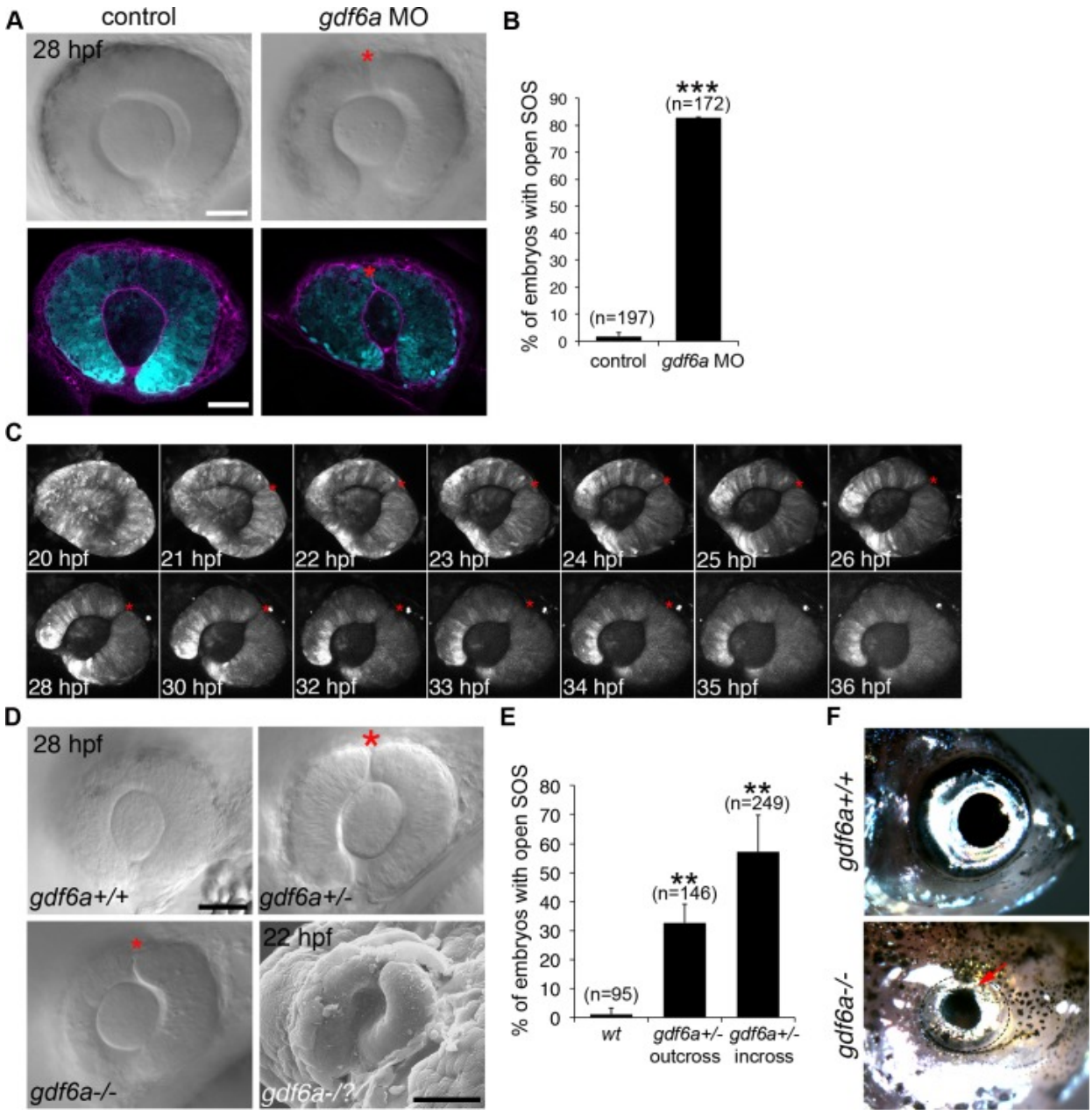

Figure 3.9: The role of Gdf6a signaling in superior ocular sulcus morphogenesis. (A) Delayed SOS closure caused by Gdf6a knockdown. *Tg(rx3*:*GFP)* zebrafish eyes (cyan) from uninjected and Gdf6a morpholino-injected embryos shown as DIC images of live embryos and single optical slices following anti-Laminin antibody staining (magenta). SOS marked by red asterisk. (B) Quantification of embryos with delayed sulcus closure, as assessed at 28 hpf. (C) Time series of maximum projection confocal images of a *Tg(rx3*:*GFP)* embryo injected with *gdf6a* morpholino. (D) DIC images of wildtype, *gdf6a*$^{+/-}$ and *gdf6a*$^{-/-}$ eyes (SOS marked by red asterisk). Bottom right panel shows SEM image of a Gdf6a-deficient eye with a pronounced sulcus. (E) Quantification of

gdf6a$^{-/-}$ mutants (or siblings) with delayed SOS closure. (F) Adult wildtype zebrafish (top panel) showing normal eye morphology and a *gdf6a*$^{-/-}$ zebrafish (bottom panel) with superior coloboma (red arrow). N = 3 experiments for graphs in B and E. n = number of embryos. Data are means ± SEM. Statistics in B is a two-tailed *t* test, and in E is one-way ANOVA with Tukey's test: ***P*<0.01, *** *P*<0.001. Scale bars are 50 μm.

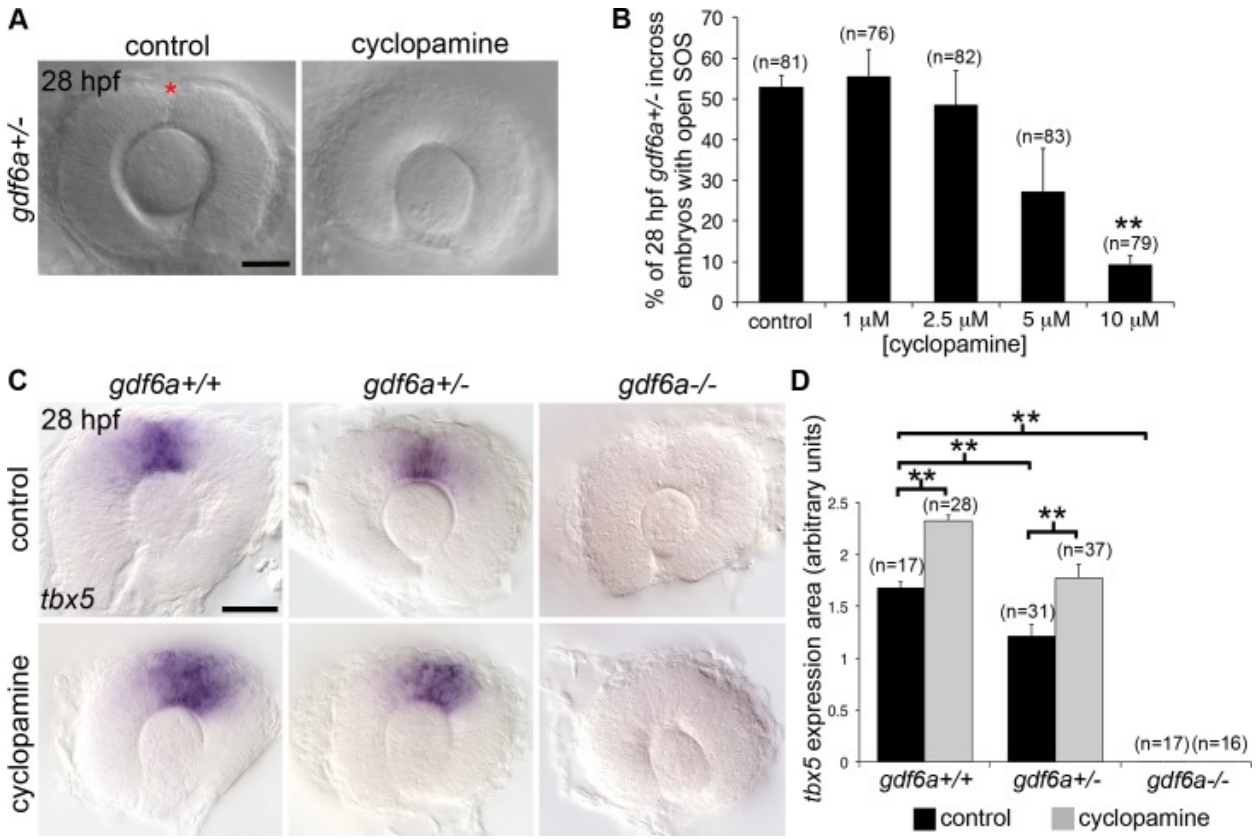

Figure 3.10: Inhibition of Hedgehog signaling rescues closure of the superior ocular sulcus in Gdf6a-deficient embryos. (A-B) Effect of Hedgehog inhibition (cyclopamine treatment) on SOS closure in Gdf6a-deficient embryos. DIC images of *gdf6a*$^{+/-}$ eyes, treated with either control solution (left) or 10 μM cyclopamine (right) (A). SOS marked by red asterisk. Quantification of effect of cyclopamine treatment on SOS closure in *gdf6a*$^{+/-}$ incross embryos (B). (C-D) Effect of cyclopamine on dorsal retinal patterning in Gdf6a-deficient embryos. *tbx5* RNA expression in eyes from 28 hpf *gdf6a*$^{+/+}$, *gdf6a*$^{+/-}$, and *gdf6a*$^{-/-}$ embryos with or without cyclopamine treatment (C). Quantification of effect of cyclopamine treatment on area of *tbx5* expression (D). n = number of embryos, N = 4 (B) or 3 (D) experiments. Data are means ± SEM. Data in B and D are means ± SEM; Statistics in B is a one-way ANOVA with Tukey's test, D is two-way ANOVA with Tukey's test: $^{**}P<0.01$. Scale bars are 50 μm.

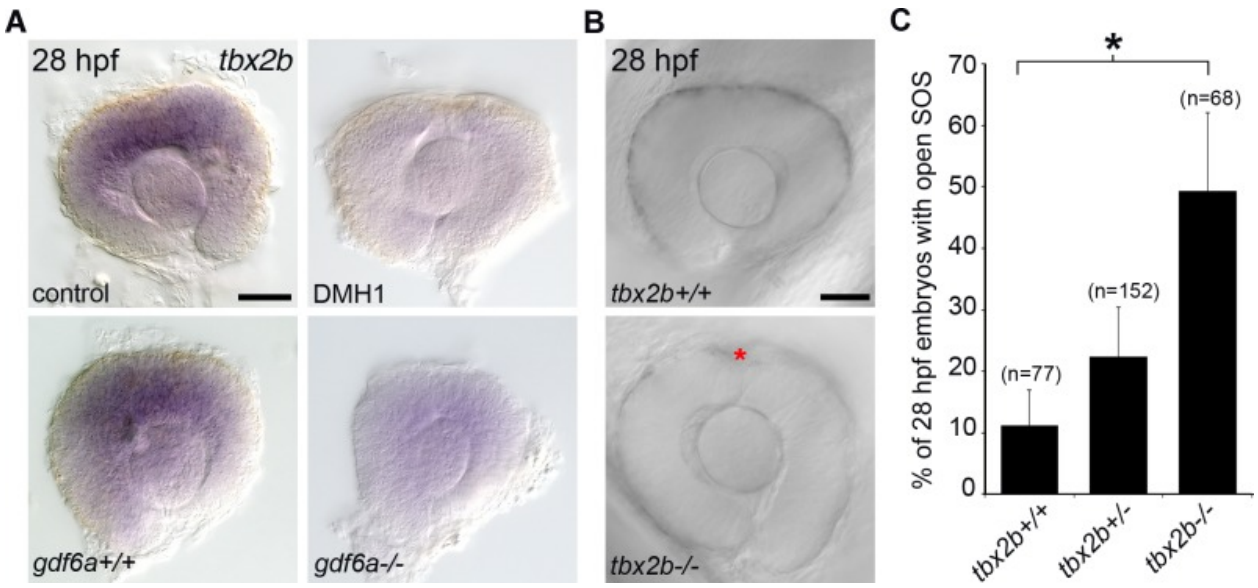

Figure 3.11: Analysis of Tbx2b and closure of the superior ocular sulcus. (A) Whole-mount in situ hybridization for zebrafish *tbx2b* in control and BMP- depleted embryos. Top panels are eyes dissected from control and DMH1-treated embryos; bottom panels are from *gdf6a*$^{+/+}$, and *gdf6a*$^{-/-}$ embryos. (B-C) Analysis of SOS closure in Tbx2b-depleted embryos. DIC images of eyes from live *tbx2b*$^{+/+}$ (top panel) and *tbx2b*^{fby} (bottom panel) embryos (B). Quantification of SOS closure in wild type and *tbx2bfby* mutant zebrafish eyes (C). Data are means ± SEM; one-way ANOVA with Tukey's test: *P<0.05. Scale bars are 50 μm.

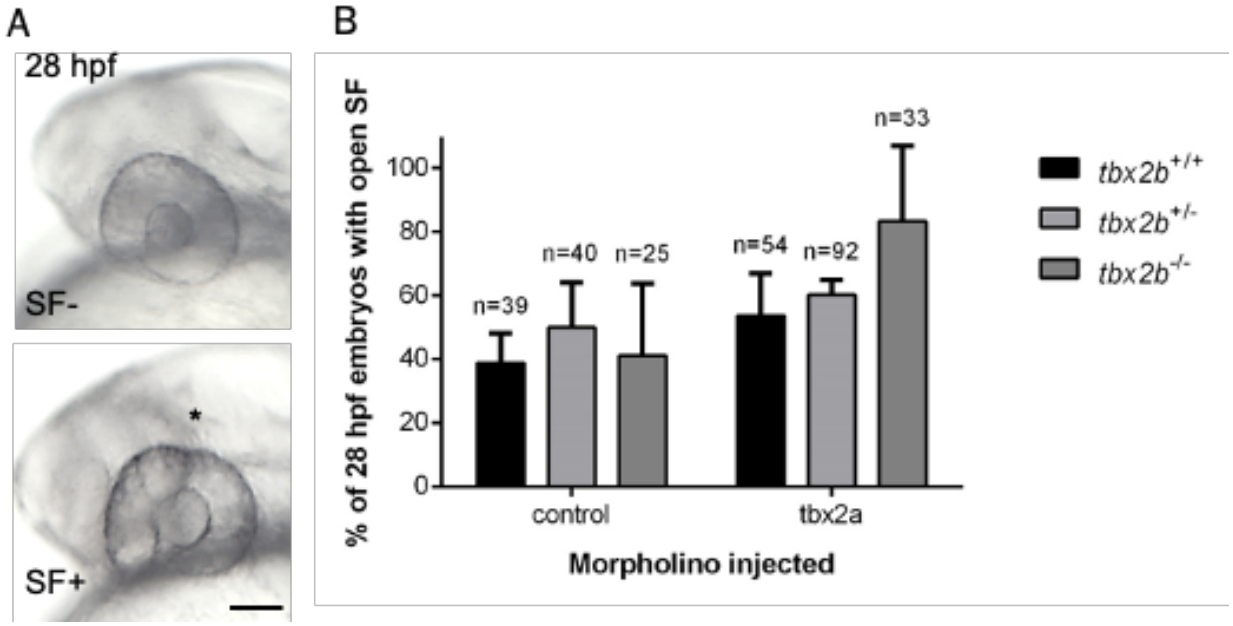

Figure 3.12: Knockdown of *tbx2a* does not exacerbate SOS closure delay in *tbx2b*$^{-/fby}$ embryos. (A) Live stereoscope imaging of 28 hpf zebrafish embryos injected with 4 ng of *tbx2a* translation-blocking morpholino and 2 ng of p53 translation-blocking morpholino oligonucleotides at the one-cell stage. (B) Analysis of SOS closure in *tbx2a* morpholino injection in Tbx2b-deficient embryos. Data are means ± SEM. Scale bar is 50 μm.

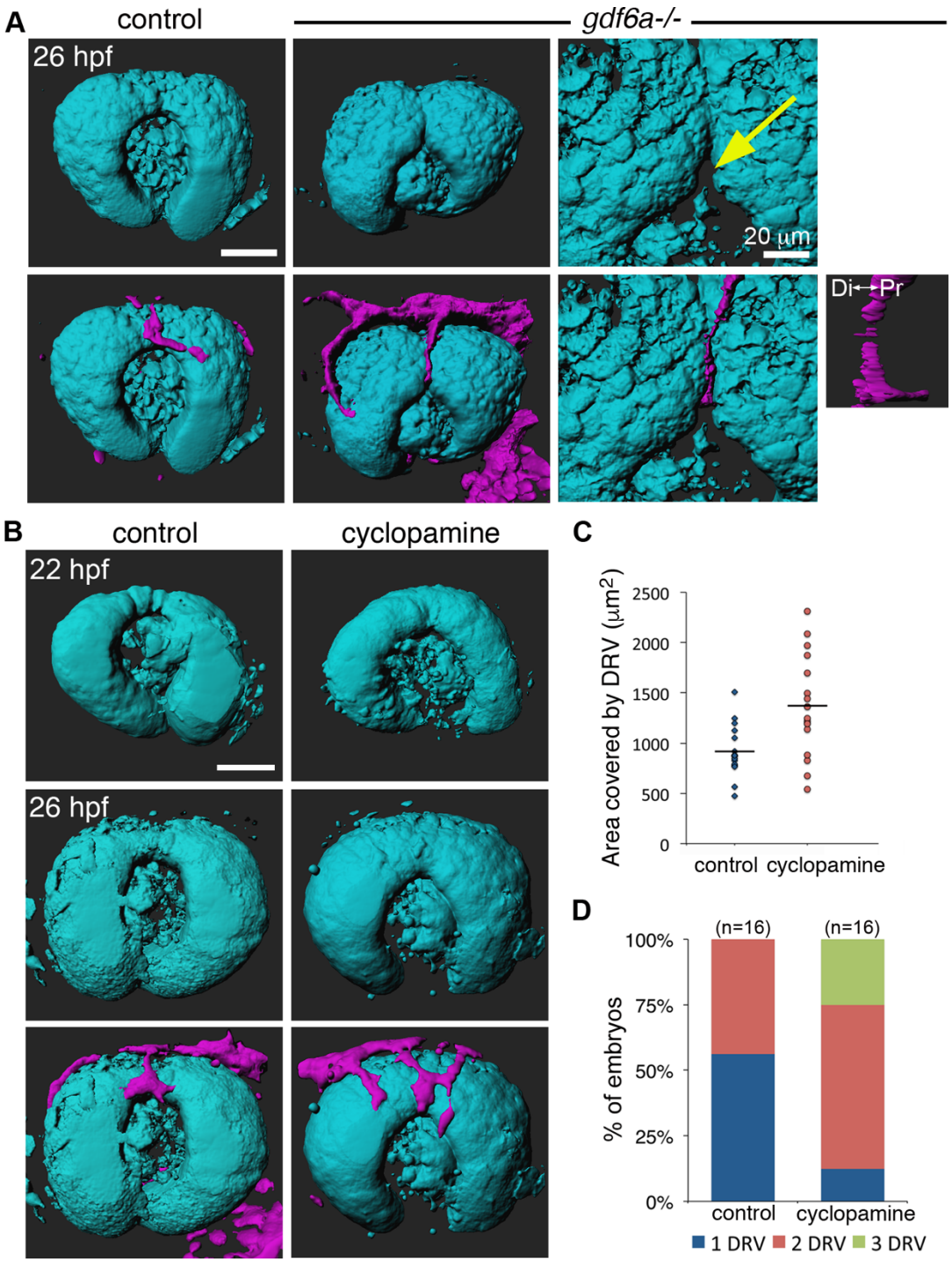

Figure 3.13: Aberrant SOS closure leads to abnormal vasculature. (A) Surface projections of 26 hpf *Tg*(*rx3*:*GFP;kdrl*:*mCherry*) wild type and *gdf6a*$^{-/-}$ embryos, shown without vessels (top row) and with vessels (bottom row). Last column shows expanded views of same *gdf6a*$^{-/-}$ eye, highlighting the divot in the dorsal retina at the inferior edge of the superior ocular sulcus (yellow arrow). Small panel is 90° lateral rotation of vessel in adjacent panel, showing the DRV turn and

extend toward the hyaloid vasculature. (B) Surface projections of *Tg*(*rx3*:*GFP;kdrl*:*mCherry*) embryos before (22 hpf) and after (26 hpf) DRV formation, with and without cyclopamine treatment. (C-D) Quantification of the area and number of DRV vessel(s) in control and cyclopamine-treated 26 hpf embryos. n=number of embryos. Scale bars are 50 μm unless otherwise noted. Di-Pr, distal-proximal.

3.5. Tables

Table 3.1: Superior coloboma patient information.

Patient #	Age at diagnosis	Laterality and eye(s) affected	Ocular Phenotype	Other findings	Clinical Center
1	23 years	Unilateral, OS	Iris coloboma, with anomalous retinal vasculature and localized sheathing of retinal arteries	Tuberous Sclerosis	Edmonton, Canada
2	21 years	Bilateral	Asymmetric phenotypic severity: OD. Two small superior iris lesions, with pupillary distortion OS. Large superior iris coloboma, small superior lenticular (lens) coloboma with a small defect in the lens zonule	Congenital glaucoma, Parental consanguinity	Edmonton, Canada
3	8 months	Unilateral, OS	Unilateral lenticular coloboma	Nil	Edmonton, Canada
4	14 months	Unilateral, OD	Superior scleral defect with superior retinal colobomatous changes, Situs inversus (displaced vessels)	Nil	Edmonton, Canada
5	23 years	Unilateral, OS	Unilateral superior retinal and optic nerve coloboma	Dandy-Walker syndrome	Edmonton, Canada
6	5 years	Unilateral, OD	Iris and retinochoroidal coloboma	Tri-atrial heart	National Eye Institute, USA
7	2 years	Unilateral, OD	Retinochoroidal coloboma and mild microphthalmia	Ovarian torsion in infancy	Cambridge, UK
8	2 months	Unilateral, OS	Iris coloboma with microphthalmia. Right eye is microphthalmic with complete corneal opacity.	Cardiac and renal anomalies. Epilepsy	University of Michigan, USA

OD=right eye, OS=left eye

Table 3.2: Genetic variants in superior coloboma patients. Exome sequencing of superior coloboma patients identified rare variants (<1% frequency in general population) that were subsequently prioritized on the basis of high Mutation Taster score (>0.95) and prior association with ocular gene expression or function.

Patient #	Gene Name	Type	Variant	Mutation Taster
1	AARS	nonsynonymous SNV	NM_001605:c.G2791A:p.G931S	0.999887
	ACACB	nonsynonymous SNV	NM_001093:c.G764T:p.G255V	0.99999
	ACOT2	nonsynonymous SNV	NM_006821:c.G688A:p.G230S	0.990961
	ADARB1	nonsynonymous SNV	NM_001112:c.A1582G:p.I528V	0.999823
	AGAP1	nonsynonymous SNV	NM_014914:c.G2343C:p.M781I	0.996577
	AGRN	nonsynonymous SNV	NM_198576:c.G1528A:p.G510S	0.998726
	AKAP11	nonsynonymous SNV	NM_016248:c.C2009T:p.T670M	0.99034
	ALG12	nonsynonymous SNV	NM_024105:c.C727T:p.L243F	0.985411
	AMBP	nonsynonymous SNV	NM_001633:c.A575G:p.E192G	0.986294
	ANUBL1	nonsynonymous SNV	NM_001128324:c.C2173T:p.P725S	0.999547
	ARHGAP6	nonsynonymous SNV	NM_013423:c.A2245G:p.R749G	0.994809
	ARNTL2	nonsynonymous SNV	NM_001248003:c.A1267G:p.K423E	0.994232
	ARPC4-TTLL3,TTLL3	nonsynonymous SNV	NM_001025930:c.C766T:p.R256W	0.999629
	ASB16,C17orf65	nonsynonymous SNV	NM_080863:c.A668G:p.E223G	0.99505
	ASPH	nonsynonymous SNV	NM_001164750:c.G968A:p.R323H	0.99961
	B3GNTL1	nonsynonymous SNV	NM_001009905:c.G103A:p.E35K	0.999444
	C18orf1	nonsynonymous SNV	NM_004338:c.G122A:p.R41H	0.999923
	C18orf8	nonsynonymous SNV	NM_013326:c.C596G:p.A199G	0.971201
	CACHD1	nonsynonymous SNV	NM_020925:c.A1168G:p.T390A	0.994878
	CAD	nonsynonymous SNV	NM_004341:c.T2297C:p.M766T	0.999554
	CALCA	nonsynonymous SNV	NM_001033952:c.T197C:p.L66P	0.971328
	CD101	nonsynonymous SNV	NM_004258:c.C605T:p.S202F	0.985083
	CEBPZ	nonsynonymous SNV	NM_005760:c.T1801A:p.F601I	0.997209
	CLRN1	nonsynonymous SNV	NM_001195794:c.A20T:p.K7I	0.990343
	COG1	nonsynonymous SNV	NM_018714:c.C1049T:p.T350M	0.9989
	CSAD	nonsynonymous SNV	NM_001244706:c.G445A:p.D149N	0.999049
	CSPG4	nonsynonymous SNV	NM_001897:c.G449A:p.G150D	0.998279
	DCLK2	nonsynonymous SNV	NM_001040260:c.A1531G:p.I511V	0.998626
	DCLK3	nonsynonymous SNV	NM_033403:c.C1801T:p.R601C	0.997839
	DEPDC5	nonsynonymous SNV	NM_001242897:c.C3875T:p.A1292V	0.996425
	DHODH	nonsynonymous SNV	NM_001361:c.G890A:p.R297H	0.999256
	DNAH2	nonsynonymous SNV	NM_020877:c.G8281A:p.V2761M	0.952925
	DSE	nonsynonymous SNV	NM_001080976:c.A844G:p.I282V	0.987638
	EIF4ENIF1	nonsynonymous SNV	NM_001164502:c.G2146A:p.G716R	0.992868

Patient #	Gene Name	Type	Variant	Mutation Taster
	ENPP7	nonsynonymous SNV	NM_178543:c.C273G:p.H91Q	0.986687
	EPG5	nonsynonymous SNV	NM_020964:c.C3248T:p.S1083L	0.987832
	EPRS	nonsynonymous SNV	NM_004446:c.A1256G:p.Y419C	0.99985
	FAT2	nonsynonymous SNV	NM_001447:c.T1331C:p.V444A	0.999986
	FBN3	nonsynonymous SNV	NM_032447:c.G3932C:p.G1311A	0.999294
	FBXO43	nonsynonymous SNV	NM_001029860:c.C1708T:p.R570W	0.987168
	FGL1	nonsynonymous SNV	NM_004467:c.A419T:p.Y140F	0.950515
	FHL1	nonsynonymous SNV	NM_001159699:c.A161G:p.N54S	0.998281
	FKTN	nonsynonymous SNV	NM_006731:c.A1336G:p.N446D	0.999963
	FRK	nonsynonymous SNV	NM_002031:c.C1358T:p.P453L	0.993664
	FZD4	nonsynonymous SNV	NM_012193:c.G477A:p.M159I	0.998516
	GALNT7	nonsynonymous SNV	NM_017423:c.T973A:p.C325S	0.999886
	GDAP2	nonsynonymous SNV	NM_001135589:c.G368A:p.R123Q	0.999557
	GDF9	nonsynonymous SNV	NM_005260:c.C307T:p.P103S	0.98725
	GNGT1	nonsynonymous SNV	NM_021955:c.G148A:p.E50K	0.961805
	GPT	nonsynonymous SNV	NM_005309:c.G320A:p.R107K	0.982595
	GRK4	nonsynonymous SNV	NM_001004056:c.T1274C:p.L425P	0.999994
	HPSE2	nonsynonymous SNV	NM_001166245:c.G1282C:p.V428L	0.993032
	HSPG2	nonsynonymous SNV	NM_005529:c.G8848A:p.G2950R	0.99999
	HSPG2	nonsynonymous SNV	NM_005529:c.G8422T:p.V2808F	0.987389
	HTRA2	nonsynonymous SNV	NM_013247:c.G1195A:p.G399S	0.999242
	IGFBP5	nonsynonymous SNV	NM_000599:c.C412T:p.R138W	0.992419
	ITGB4	nonsynonymous SNV	NM_001005619:c.G1544A:p.R515H	0.999921
	JUB	nonsynonymous SNV	NM_032876:c.C131T:p.P44L	0.999441
	KATNB1	nonsynonymous SNV	NM_005886:c.C1319G:p.P440R	0.980114
	KIAA0564	nonsynonymous SNV	NM_015058:c.A5297C:p.D1766A	0.99998
	KIAA0564	nonsynonymous SNV	NM_001009814:c.G2693A:p.R898K	0.994132
	KIAA1109	nonsynonymous SNV	NM_015312:c.C11129T:p.P3710L	0.993222
	KIAA1524	nonsynonymous SNV	NM_020890:c.C877A:p.P293T	0.997155
	LGI2	nonsynonymous SNV	NM_018176:c.A1355G:p.Q452R	0.965635
	LIG1	nonsynonymous SNV	NM_000234:c.G1226A:p.R409H	0.968591
	LRRC30	nonsynonymous SNV	NM_001105581:c.G604A:p.A202T	0.973978
	MBD5	nonsynonymous SNV	NM_018328:c.G1382A:p.R461H	0.998132
	MCL1	nonsynonymous SNV	NM_021960:c.C680T:p.A227V	0.962198
	MET	nonsynonymous SNV	NM_000245:c.A901G:p.T301A	0.992353
	MICALCL	stopgain SNV	NM_032867:c.C1717T:p.R573X	1
	MINA	nonsynonymous SNV	NM_001042533:c.C419T:p.P140L	0.999992
	MOGS	nonsynonymous SNV	NM_006302:c.G2062A:p.A688T	0.999989
	MPP5	nonsynonymous SNV	NM_022474:c.C422A:p.S141Y	0.988384
	MRPS9	nonsynonymous SNV	NM_182640:c.G790A:p.E264K	0.981068

Patient #	Gene Name	Type	Variant	Mutation Taster
	NKD1	nonsynonymous SNV	NM_033119:c.G1224C:p.E408D	0.99079
	NPC1	nonsynonymous SNV	NM_000271:c.C709T:p.P237S	0.973584
	NT5DC2	nonsynonymous SNV	NM_001134231:c.G1460A:p.R487H	0.999999
	OR4C3	stopgain SNV	NM_001004702:c.G522A:p.W174X	1
	PDZRN3	nonsynonymous SNV	NM_015009:c.C454T:p.H152Y	0.956837
	PKP1	nonsynonymous SNV	NM_001005337:c.C2050T:p.R684W	0.992554
	PLK3	nonsynonymous SNV	NM_004073:c.C1841T:p.T614I	0.999553
	POLE	nonsynonymous SNV	NM_006231:c.G6418A:p.E2140K	0.960716
	PRPF4B	nonsynonymous SNV	NM_003913:c.G857A:p.R286H	0.974959
	RAD51D	nonsynonymous SNV	NM_133629:c.A362G:p.E121G	0.996905
	RANGRF	stopgain SNV	NM_001177801:c.G181T:p.E61X	1
	RBPMS2	nonsynonymous SNV	NM_194272:c.G385A:p.A129T	0.999946
	RCL1;RCL1	nonsynonymous SNV	NM_005772:c.G385A:p.V129I	0.999999
	RFX6	nonsynonymous SNV	NM_173560:c.C718T:p.L240F	0.954539
	ROPN1L	stopgain SNV	NM_031916:c.T135A:p.Y45X	1
	RPL3L	nonsynonymous SNV	NM_005061:c.C224T:p.A75V	0.99136
	RPS6	nonsynonymous SNV	NM_001010:c.G152A:p.R51Q	0.997829
	RRP7A	nonsynonymous SNV	NM_015703:c.G704A:p.R235Q	0.982204
	SCARB1	nonsynonymous SNV	NM_001082959:c.C965T:p.P322L	0.999946
	SEC24C	nonsynonymous SNV	NM_198597:c.T1160C:p.M387T	0.997577
	SEZ6L2	nonsynonymous SNV	NM_001114100:c.G1210A:p.D404N	0.970063
	SLC10A2	nonsynonymous SNV	NM_000452:c.C868T:p.P290S	0.952685
	SLIT3	nonsynonymous SNV	NM_003062:c.G4475A:p.S1492N	0.998936
	SPATA2	nonsynonymous SNV	NM_001135773:c.G878A:p.R293H	0.996562
	SRPX	nonsynonymous SNV	NM_001170750:c.G365A:p.R122Q	0.999915
	STXBP5	nonsynonymous SNV	NM_001127715:c.C1234G:p.L412V	0.999951
	SULT1C2	nonsynonymous SNV	NM_001056:c.G583A:p.E195K	1
	SYPL2	nonsynonymous SNV	NM_001040709:c.A638G:p.N213S	0.997836
	TAF1L	nonsynonymous SNV	NM_153809:c.C1909T:p.P637S	0.999501
	TCERG1	nonsynonymous SNV	NM_001040006:c.G76A:p.A26T	0.997675
	TMED1	nonsynonymous SNV	NM_006858:c.C641T:p.T214M	0.991969
	TNFRSF10D	nonsynonymous SNV	NM_003840:c.C293G:p.P98R	0.965296
	TOE1	nonsynonymous SNV	NM_025077:c.G1022A:p.R341H	0.999761
	TPD52	nonsynonymous SNV	NM_001025252:c.G166A:p.E56K	0.989814
	TPP1	stopgain SNV	NM_000391:c.C622T:p.R208X	1
	TSC2	nonsynonymous SNV	NM_001077183:c.C5026T:p.R1676W	0.999986
	TSR1	nonsynonymous SNV	NM_018128:c.C2250A:p.H750Q	0.999775
	TUB	nonsynonymous SNV	NM_177972:c.G1126A:p.V376I	0.998975
	TULP1	nonsynonymous SNV	NM_003322:c.G797T:p.G266V	0.996546
	UGGT2	nonsynonymous SNV	NM_020121:c.A4142G:p.H1381R	0.971946

Patient #	Gene Name	Type	Variant	Mutation Taster
	VRK2	nonsynonymous SNV	NM_001130480:c.T104C:p.I35T	0.995967
	WDR78	nonsynonymous SNV	NM_024763:c.G1453A:p.G485S	0.974364
	WSCD1	nonsynonymous SNV	NM_015253:c.C902T:p.T301I	0.992983
	XAF1	stopgain SNV	NM_199139:c.G343T:p.E115X	1
	ZMIZ2	nonsynonymous SNV	NM_174929:c.G2404A:p.G802R	0.998878
	ZNF653	nonsynonymous SNV	NM_138783:c.G1054A:p.E352K	0.992989
	ZSWIM5	nonsynonymous SNV	NM_020883:c.G1222A:p.D408N	0.998206
2	ACTL6A	nonsynonymous SNV	NM_004301:c.T673A:p.S225T	0.994509
	ACTN1	nonsynonymous SNV	NM_001102:c.G532A:p.G178S	0.999938
	ACVRL1	nonsynonymous SNV	NM_001077401:c.C1445T:p.A482V	0.999706
	AGAP3	nonsynonymous SNV	NM_031946:c.C2419T:p.H807Y	0.998519
	AIM1L	nonsynonymous SNV	NM_001039775:c.G3252C:p.K1084N	0.99975
	ANKRD30A	stopgain SNV	NM_052997:c.G328T:p.E110X	1
	ARPP21	nonsynonymous SNV	NM_016300:c.A1055T:p.E352V	0.960229
	ASPM	nonsynonymous SNV	NM_018136:c.C4213T:p.R1405C	0.999919
	BICC1	nonsynonymous SNV	NM_001080512:c.C1462T:p.P488S	0.98711
	BLVRB	nonsynonymous SNV	NM_000713:c.G439A:p.V147M	0.998419
	BMPR1A	nonsynonymous SNV	NM_004329:c.G1412A:p.R471H	0.970915
	C16orf62	nonsynonymous SNV	NM_020314:c.C2980T:p.R994C	0.999285
	C1QTNF1	nonsynonymous SNV	NM_198594:c.A236T:p.Y79F	0.968666
	C6orf165	nonsynonymous SNV	NM_001031743:c.C1220A:p.A407E	0.979929
	CAV2	nonsynonymous SNV	NM_001206748:c.C161T:p.T54I	0.995632
	CBFA2T2	nonsynonymous SNV	NM_001032999:c.G564C:p.K188N	0.999108
	CCDC124	nonsynonymous SNV	NM_001136203:c.G406C:p.V136L	0.963876
	CD36	stopgain SNV	NM_001127444:c.T1079G:p.L360X	1
	CHFR	nonsynonymous SNV	NM_001161347:c.A613G:p.K205E	0.997104
	CHST13	nonsynonymous SNV	NM_152889:c.C150G:p.S50R	0.978808
	CLCNKA	nonsynonymous SNV	NM_001042704:c.C935T:p.T312I	0.951936
	CLSTN1	nonsynonymous SNV	NM_014944:c.G532A:p.V178M	0.962173
	CMTM6	nonsynonymous SNV	NM_017801:c.A271G:p.T91A	0.999853
	COL10A1	nonsynonymous SNV	NM_000493:c.T23G:p.L8W	0.998959
	COL19A1	nonsynonymous SNV	NM_001858:c.C1276T:p.P426S	0.999822
	CRHR2	nonsynonymous SNV	NM_001202482:c.C1160A:p.A387D	0.999255
	CTSC	nonsynonymous SNV	NM_001814:c.A1088C:p.E363A	0.999985
	CYP1A1	nonsynonymous SNV	NM_000499:c.C712T:p.P238S	0.999742
	CYP1A1	nonsynonymous SNV	NM_000499:c.T857C:p.I286T	0.99848
	CYP1B1	nonsynonymous SNV	NM_000104:c.G1103A:p.R368H	0.970216
	DHRS9	nonsynonymous SNV	NM_001142271:c.G856C:p.D286H	0.99818
	DHX38	nonsynonymous SNV	NM_014003:c.A2947G:p.I983V	0.999192
	DIP2B	nonsynonymous SNV	NM_173602:c.C4453T:p.R1485W	0.999991

Patient #	Gene Name	Type	Variant	Mutation Taster
	DLK1	nonsynonymous SNV	NM_003836:c.G352A:p.G118R	0.998927
	DLK1	nonsynonymous SNV	NM_003836:c.G366C:p.K122N	0.961886
	DNMT3L	nonsynonymous SNV	NM_013369:c.G209A:p.G70E	0.999785
	DOCK5	nonsynonymous SNV	NM_024940:c.G2698A:p.E900K	0.993012
	DPY19L4	nonsynonymous SNV	NM_181787:c.G578T:p.G193V	0.99991
	DPY19L4	nonsynonymous SNV	NM_181787:c.G560T:p.S187I	0.999307
	DSCAM	nonsynonymous SNV	NM_001389:c.G701A:p.R234H	0.979737
	EAF1	nonsynonymous SNV	NM_033083:c.G619A:p.D207N	0.976956
	ECE2	nonsynonymous SNV	NM_001037324:c.G1879A:p.G627S	0.999355
	EIF1AD	nonsynonymous SNV	NM_001242481:c.G173T:p.R58L	0.999981
	EPB41	nonsynonymous SNV	NM_001166005:c.G640A:p.V214I	0.999983
	ETV4	nonsynonymous SNV	NM_001079675:c.C1309T:p.R437C	0.999087
	EXOC3L1	nonsynonymous SNV	NM_178516:c.C724G:p.R242G	0.996994
	FIBIN	nonsynonymous SNV	NM_203371:c.G287A:p.R96H	0.999931
	FMN2	nonsynonymous SNV	NM_020066:c.C4123A:p.L1375I	0.998708
	FMNL1	nonsynonymous SNV	NM_005892:c.C655T:p.R219C	0.998201
	FURIN	nonsynonymous SNV	NM_002569:c.G1343A:p.R448Q	0.997805
	GPAA1	nonsynonymous SNV	NM_003801:c.A863G:p.Q288R	0.992603
	GRHPR	nonsynonymous SNV	NM_012203:c.G488A:p.R163H	1
	GRIA1	nonsynonymous SNV	NM_000827:c.T707C:p.M236T	0.989621
	HHIP;HHIP	nonsynonymous SNV	NM_022475:c.C1762T:p.P588S	0.999972
	IFT57	nonsynonymous SNV	NM_018010:c.A1232G:p.N411S	0.991636
	IGHMBP2	nonsynonymous SNV	NM_002180:c.C46G:p.L16V	0.984176
	INCA1	stopgain SNV	NM_001167985:c.C64T:p.R22X	1
	ISOC2	nonsynonymous SNV	NM_001136202:c.G193A:p.A65T	0.95843
	ITGB6	nonsynonymous SNV	NM_000888:c.G871A:p.G291R	0.998767
	JAGN1	nonsynonymous SNV	NM_032492:c.A244G:p.I82V	0.971736
	KCND1	nonsynonymous SNV	NM_004979:c.C1447T:p.H483Y	0.997645
	KDM4B	nonsynonymous SNV	NM_015015:c.G2968A:p.G990S	0.987827
	KIAA0196	nonsynonymous SNV	NM_014846:c.G50A:p.R17K	0.999465
	KIAA1199	nonsynonymous SNV	NM_018689:c.C3625T:p.H1209Y	0.96181
	KIAA1524	nonsynonymous SNV	NM_020890:c.G823C:p.E275Q	0.95502
	KIAA1609	nonsynonymous SNV	NM_020947:c.C1061T:p.T354M	0.999949
	KIF18A	nonsynonymous SNV	NM_031217:c.C725T:p.T242I	0.987023
	KRR1	nonsynonymous SNV	NM_007043:c.A184G:p.T62A	0.99983
	LAMA4	nonsynonymous SNV	NM_001105206:c.G3239A:p.R1080Q	0.997947
	LAMA5	nonsynonymous SNV	NM_005560:c.G10411A:p.G3471S	0.999959
	LAMB4	nonsynonymous SNV	NM_007356:c.C575G:p.P192R	0.999177
	LAMC2	nonsynonymous SNV	NM_005562:c.C2080T:p.R694C	0.994374
	LAS1L	nonsynonymous SNV	NM_031206:c.C1082G:p.P361R	0.988139

Patient #	Gene Name	Type	Variant	Mutation Taster
	LRP2	nonsynonymous SNV	NM_004525:c.G13803A:p.M4601I	0.999811
	LTV1	nonsynonymous SNV	NM_032860:c.A1121C:p.K374T	0.999935
	MAT1A	nonsynonymous SNV	NM_000429:c.C505T:p.R169C	0.999528
	MCM5	nonsynonymous SNV	NM_006739:c.G375C:p.Q125H	0.999992
	MIOS	nonsynonymous SNV	NM_019005:c.C1928A:p.A643D	0.999022
	MKS1	stopgain SNV	NM_001165927:c.C478T:p.R160X	1
	MMP2	nonsynonymous SNV	NM_001127891:c.C1481T:p.S494L	0.994768
	MMP9	nonsynonymous SNV	NM_004994:c.A344G:p.K115R	0.985048
	N4BP3	nonsynonymous SNV	NM_015111:c.C994T:p.R332C	0.998841
	NCOR1	nonsynonymous SNV	NM_001190440:c.G6956A:p.R2319Q	0.966004
	NEUROD1	nonsynonymous SNV	NM_002500:c.C590A:p.P197H	0.999982
	NFS1	nonsynonymous SNV	NM_021100:c.A437G:p.K146R	0.999916
	NMBR	nonsynonymous SNV	NM_002511:c.C443A:p.P148H	0.999971
	NUPL1	nonsynonymous SNV	NM_001008564:c.T460C:p.S154P	0.994282
	OR4C3	stopgain SNV	NM_001004702:c.G522A:p.W174X	1
	OR51I2	nonsynonymous SNV	NM_001004754:c.G3C:p.M1I	1
	OXA1L	nonsynonymous SNV	NM_005015:c.C1246G:p.P416A	0.999007
	PCDH15	stopgain SNV	NM_001142767:c.T1283G:p.L428X	1
	PCDH18	nonsynonymous SNV	NM_019035:c.G2790C:p.Q930H	0.999055
	PCK1	nonsynonymous SNV	NM_002591:c.G512A:p.R171Q	0.999995
	PDCD2	nonsynonymous SNV	NM_002598:c.A677G:p.E226G	0.998262
	PDE1C	nonsynonymous SNV	NM_001191056:c.G1166A:p.R389H	0.998114
	PIGU	nonsynonymous SNV	NM_080476:c.G998A:p.G333E	0.999993
	PIK3R5	nonsynonymous SNV	NM_001142633:c.G511A:p.V171M	0.991058
	PITHD1	nonsynonymous SNV	NM_020362:c.C181T:p.R61W	0.999998
	PLCG2	nonsynonymous SNV	NM_002661:c.C413T:p.T138M	0.993735
	PLCH1	nonsynonymous SNV	NM_014996:c.T3485C:p.I1162T	0.998529
	PLXNA3;PLXNA3	nonsynonymous SNV	NM_017514:c.A3440G:p.K1147R	0.996782
	POLH	nonsynonymous SNV	NM_006502:c.G626T:p.G209V	0.999889
	PPYR1	nonsynonymous SNV	NM_005972:c.G767A:p.R256Q	0.99992
	PTPN14	nonsynonymous SNV	NM_005401:c.C2225T:p.A742V	0.998494
	RAB25	nonsynonymous SNV	NM_020387:c.A59G:p.E20G	0.99999
	RANBP10	nonsynonymous SNV	NM_020850:c.G925A:p.E309K	0.998698
	RNF31	nonsynonymous SNV	NM_017999:c.A2846C:p.N949T	0.985124
	RPL8	nonsynonymous SNV	NM_000973:c.A292G:p.I98V	0.999923
	RPS6KB2;RPS6KB2	nonsynonymous SNV	NM_003952:c.C800T:p.P267L	0.997891
	SCTR	stopgain SNV	NM_002980:c.C181T:p.Q61X	1
	SCUBE2	nonsynonymous SNV	NM_001170690:c.G2095A:p.A699T	0.991195
	SGK2	nonsynonymous SNV	NM_016276:c.G800A:p.R267Q	0.999114
	SH3RF1	nonsynonymous SNV	NM_020870:c.G2311A:p.G771S	0.984581

Patient #	Gene Name	Type	Variant	Mutation Taster
	SIPA1L1	nonsynonymous SNV	NM_015556:c.C3056T:p.T1019M	0.99995
	SLC26A1	nonsynonymous SNV	NM_022042:c.G1511A:p.R504H	0.997285
	SLIT2	nonsynonymous SNV	NM_004787:c.G4333C:p.D1445H	0.993067
	SMYD2	nonsynonymous SNV	NM_020197:c.A1150G:p.M384V	0.963403
	SOD2	nonsynonymous SNV	NM_000636:c.G198C:p.E66D	0.999998
	SS18	nonsynonymous SNV	NM_001007559:c.G698C:p.G233A	0.958465
	SSH2	nonsynonymous SNV	NM_033389:c.G4192A:p.G1398S	0.998872
	STK16	nonsynonymous SNV	NM_001008910:c.C262T:p.R88W	0.998665
	SYNE1	nonsynonymous SNV	NM_033071:c.G12229C:p.D4077H	0.990532
	TLR10	nonsynonymous SNV	NM_001017388:c.T1255C:p.W419R	0.989287
	TMEM106C	nonsynonymous SNV	NM_001143841:c.T319C:p.F107L	0.999314
	TMEM181	nonsynonymous SNV	NM_020823:c.C1006T:p.R336W	0.999997
	TRH	nonsynonymous SNV	NM_007117:c.G248A:p.R83H	0.999936
	TRIM45	nonsynonymous SNV	NM_001145635:c.G1495A:p.G499R	0.999972
	TRPM5	nonsynonymous SNV	NM_014555:c.G2755A:p.G919S	0.992174
	TSPAN31	nonsynonymous SNV	NM_005981:c.C276G:p.I92M	0.955662
	TWF1	nonsynonymous SNV	NM_002822:c.C1028T:p.A343V	0.998383
	UBE2D4	nonsynonymous SNV	NM_015983:c.G79A:p.G27S	0.99998
	ULK2	nonsynonymous SNV	NM_001142610:c.C724T:p.P242S	0.995306
	USP25	nonsynonymous SNV	NM_013396:c.C1622G:p.T541R	0.999824
	VASH2	nonsynonymous SNV	NM_024749:c.G851A:p.R284Q	0.960635
	WDR16	nonsynonymous SNV	NM_001080556:c.C254T:p.A85V	0.999446
	XDH	stopgain SNV	NM_000379:c.A2164T:p.K722X	1
	ZNF560	stopgain SNV	NM_152476:c.C2080T:p.R694X	1
	ZSWIM5	nonsynonymous SNV	NM_020883:c.G2326A:p.D776N	0.999161
3	ABCB6	nonsynonymous SNV	NM_005689:c.G2168A:p.R723Q	0.999992
	ABCC10	nonsynonymous SNV	NM_033450:c.G1567A:p.V523M	0.999489
	ADAMTS10	nonsynonymous SNV	NM_030957:c.G217A:p.E73K	0.996312
	AFAP1	nonsynonymous SNV	NM_198595:c.C1991T:p.S664L	0.999862
	AK2	nonsynonymous SNV	NM_001199199:c.G436A:p.E146K	0.999998
	ANP32E	nonsynonymous SNV	NM_001136478:c.A564T:p.E188D	0.98776
	ATG2A	nonsynonymous SNV	NM_015104:c.G3635A:p.R1212H	0.998787
	BBS5;BBS5	nonsynonymous SNV	NM_152384:c.G620A:p.R207H	0.998605
	BCLAF1	stopgain SNV	NM_001077440:c.C886T:p.R296X	1
	BLOC1S3	nonsynonymous SNV	NM_212550:c.C322G:p.L108V	0.985367
	BRAT1	nonsynonymous SNV	NM_152743:c.C1828T:p.R610W	0.999889
	C19orf28	nonsynonymous SNV	NM_001042680:c.G1415A:p.R472Q	0.987627
	C6orf226	nonsynonymous SNV	NM_001008739:c.G3A:p.M1I	1
	CDK7	nonsynonymous SNV	NM_001799:c.C854T:p.T285M	0.998645
	CDNF	nonsynonymous SNV	NM_001029954:c.G461C:p.W154S	0.999964

Patient #	Gene Name	Type	Variant	Mutation Taster
	CFHR2	nonsynonymous SNV	NM_005666:c.G215A:p.C72Y	0.970249
	CIT	nonsynonymous SNV	NM_001206999:c.C923G:p.S308C	0.986636
	CLDND1	nonsynonymous SNV	NM_001040181:c.A215G:p.N72S	0.999725
	CLSTN3	nonsynonymous SNV	NM_014718:c.G502T:p.A168S	0.999992
	COL8A2	nonsynonymous SNV	NM_005202:c.G911A:p.R304Q	0.999031
	CPEB1	nonsynonymous SNV	NM_001079535:c.G475A:p.D159N	0.999896
	CSMD2	nonsynonymous SNV	NM_052896:c.G6355A:p.E2119K	0.993159
	CTSH	nonsynonymous SNV	NM_004390:c.A479G:p.K160R	0.987819
	DNAH2	nonsynonymous SNV	NM_020877:c.C12974G:p.P4325R	0.954532
	EDEM2	nonsynonymous SNV	NM_001145025:c.T584C:p.I195T	0.999998
	ELMO1	nonsynonymous SNV	NM_001206480:c.C1042T:p.R348C	0.999927
	EPG5	nonsynonymous SNV	NM_020964:c.A3303C:p.Q1101H	0.967409
	EPHX1	nonsynonymous SNV	NM_000120:c.C387A:p.H129Q	0.999997
	EXOC3L1	nonsynonymous SNV	NM_178516:c.T223A:p.Y75N	0.999236
	FGA	stopgain SNV	NM_000508:c.C502T:p.R168X	1
	FKTN	nonsynonymous SNV	NM_006731:c.A1336G:p.N446D	0.999963
	FNDC3A	nonsynonymous SNV	NM_014923:c.A1697G:p.E566G	0.999846
	FPGS	nonsynonymous SNV	NM_001018078:c.C1246T:p.R416C	0.999863
	GAMT	nonsynonymous SNV	NM_000156:c.T79C:p.Y27H	0.999933
	GFM2	nonsynonymous SNV	NM_032380:c.C446T:p.T149I	0.999956
	GIPC3	nonsynonymous SNV	NM_133261:c.G389C:p.G130A	0.99996
	GOT1	nonsynonymous SNV	NM_002079:c.G257A:p.R86H	0.996362
	GPX4	nonsynonymous SNV	NM_001039847:c.G358A:p.A120T	0.994371
	GRHL3	nonsynonymous SNV	NM_001195010:c.C1223T:p.T408M	0.99959
	HCN3	nonsynonymous SNV	NM_020897:c.C1441T:p.R481W	0.978825
	HIVEP2	nonsynonymous SNV	NM_006734:c.A3725G:p.Y1242C	0.988015
	HYI	nonsynonymous SNV	NM_001190880:c.A287G:p.Y96C	0.997171
	IFT80;IFT80	nonsynonymous SNV	NM_001190242:c.C665T:p.S222F	0.999776
	IGFBP7	nonsynonymous SNV	NM_001553:c.G403A:p.A135T	0.989269
	IL31RA	stopgain SNV	NM_001242636:c.G466T:p.E156X	1
	ILK	nonsynonymous SNV	NM_001014795:c.G165A:p.M55I	0.999949
	ITGAV	nonsynonymous SNV	NM_001145000:c.A2735G:p.Y912C	0.999913
	ITSN2	nonsynonymous SNV	NM_019595:c.C3928T:p.R1310W	0.999215
	KIAA0907	nonsynonymous SNV	NM_014949:c.A1784G:p.Y595C	0.996422
	KLHDC4	nonsynonymous SNV	NM_001184854:c.G1345C:p.G449R	0.951719
	KRT8	nonsynonymous SNV	NM_002273:c.G1022A:p.R341H	0.999793
	KRT8	nonsynonymous SNV	NM_002273:c.G1319C:p.G440A	0.950244
	LAMB2	nonsynonymous SNV	NM_002292:c.G4307A:p.R1436H	0.979082
	LYST	nonsynonymous SNV	NM_000081:c.A10630G:p.N3544D	0.967171
	MAN1B1	nonsynonymous SNV	NM_016219:c.A1286G:p.H429R	0.998394

Patient #	Gene Name	Type	Variant	Mutation Taster
	MBOAT1	nonsynonymous SNV	NM_001080480:c.T1234C:p.F412L	0.999171
	MTHFD1	nonsynonymous SNV	NM_005956:c.G878A:p.R293H	0.99966
	MXRA8	nonsynonymous SNV	NM_032348:c.G1186A:p.D396N	0.989249
	MYH11	nonsynonymous SNV	NM_002474:c.C739T:p.R247C	0.999983
	NID2	nonsynonymous SNV	NM_007361:c.C2249T:p.P750L	0.961615
	NQO2;NQO2	nonsynonymous SNV	NM_000904:c.G173A:p.G58D	0.99356
	NRG2	nonsynonymous SNV	NM_001184935:c.G1508A:p.R503H	0.985524
	NUDC	nonsynonymous SNV	NM_006600:c.G661A:p.E221K	0.999543
	NUPL1	nonsynonymous SNV	NM_001008564:c.T460C:p.S154P	0.994282
	NXF1;NXF1	nonsynonymous SNV	NM_001081491:c.C640G:p.L214V	0.996002
	P2RY4	stopgain SNV	NM_002565:c.G1043A:p.W348X	0.999358
	PAM	nonsynonymous SNV	NM_138821:c.G1861C:p.G621R	0.999999
	PLEKHG2	nonsynonymous SNV	NM_022835:c.C1358G:p.P453R	1
	POLE	nonsynonymous SNV	NM_006231:c.G6418A:p.E2140K	0.960716
	POLG	nonsynonymous SNV	NM_001126131:c.G803C:p.G268A	0.999747
	POLR3E	nonsynonymous SNV	NM_018119:c.C824T:p.T275M	0.999927
	POU4F2	nonsynonymous SNV	NM_004575:c.C417A:p.D139E	0.962715
	PRPF19	nonsynonymous SNV	NM_014502:c.A478G:p.M160V	0.996125
	RC3H1	nonsynonymous SNV	NM_172071:c.G1154A:p.R385H	0.992264
	RPS3	nonsynonymous SNV	NM_001005:c.C716A:p.P239Q	0.999438
	RTTN	nonsynonymous SNV	NM_173630:c.C5060G:p.S1687C	0.986797
	SAFB2	nonsynonymous SNV	NM_014649:c.A1369G:p.T457A	0.999961
	SHROOM3	nonsynonymous SNV	NM_020859:c.A2834T:p.D945V	0.976907
	SLC16A3	nonsynonymous SNV	NM_001042422:c.C390A:p.F130L	0.99718
	SMARCA1	nonsynonymous SNV	NM_139035:c.G2222C:p.R741P	0.999736
	SMG6	nonsynonymous SNV	NM_001170957:c.T3075G:p.D1025E	0.97331
	SMYD2	nonsynonymous SNV	NM_020197:c.A1150G:p.M384V	0.963403
	SNX30	nonsynonymous SNV	NM_001012994:c.A425C:p.K142T	0.999952
	SOX8	nonsynonymous SNV	NM_014587:c.C585A:p.H195Q	0.993473
	STEAP4	nonsynonymous SNV	NM_024636:c.G953T:p.R318L	0.995803
	STRN	nonsynonymous SNV	NM_003162:c.C1138T:p.P380S	0.999004
	SV2B	nonsynonymous SNV	NM_014848:c.T421G:p.C141G	0.999895
	TAAR1	nonsynonymous SNV	NM_138327:c.G773A:p.G258E	0.994191
	TAF1L	nonsynonymous SNV	NM_153809:c.C3046T:p.R1016C	0.999975
	TBX2	nonsynonymous SNV	NM_005994:c.C986A:p.P329H	0.973971
	THUMPD1	nonsynonymous SNV	NM_017736:c.C79A:p.R27S	0.997938
	TMEM85	nonsynonymous SNV	NM_016454:c.T413C:p.I138T	0.999363
	TRMT11	nonsynonymous SNV	NM_001031712:c.A916G:p.I306V	0.99581
	TSHZ3	nonsynonymous SNV	NM_020856:c.C1054T:p.L352F	0.99999
	TST	nonsynonymous SNV	NM_003312:c.C853G:p.P285A	0.999865

Patient #	Gene Name	Type	Variant	Mutation Taster
	TTC14	nonsynonymous SNV	NM_001042601:c.C515T:p.S172F	0.997118
	TTC30B	nonsynonymous SNV	NM_152517:c.G856A:p.D286N	0.999989
	UGGT2	nonsynonymous SNV	NM_020121:c.A3802T:p.N1268Y	0.999321
	ULK2	nonsynonymous SNV	NM_001142610:c.C724T:p.P242S	0.995306
	UNC79	nonsynonymous SNV	NM_020818:c.C298G:p.L100V	0.97198
	USP48;USP48	nonsynonymous SNV	NM_032236:c.A2386G:p.I796V	0.98697
	USP8	nonsynonymous SNV	NM_001128610:c.T802A:p.L268I	0.997561
	VPS13D	nonsynonymous SNV	NM_015378:c.G4831A:p.E1611K	1
	WDR35	nonsynonymous SNV	NM_020779:c.C3019T:p.R1007C	0.999912
	WSCD1	nonsynonymous SNV	NM_015253:c.C902T:p.T301I	0.992983
	ZCCHC4	nonsynonymous SNV	NM_024936:c.G214C:p.D72H	0.997358
4	AADAC	nonsynonymous SNV	NM_001086:c.G1070A:p.R357H	0.968956
	ABCA4	nonsynonymous SNV	NM_000350:c.C6721G:p.L2241V	0.990942
	ACACB	nonsynonymous SNV	NM_001093:c.A4442T:p.D1481V	0.999998
	ADAMTS15	nonsynonymous SNV	NM_139055:c.T1324C:p.Y442H	0.999918
	ADAT1	nonsynonymous SNV	NM_012091:c.C1129T:p.R377C	0.997996
	ADCY6	nonsynonymous SNV	NM_015270:c.G413A:p.R138H	0.996328
	ADRA1A	nonsynonymous SNV	NM_000680:c.T599G:p.I200S	0.957852
	AGL	nonsynonymous SNV	NM_000645:c.G1430A:p.R477H	0.99234
	ALG6	nonsynonymous SNV	NM_013339:c.T391C:p.Y131H	0.999939
	ARHGAP21	nonsynonymous SNV	NM_020824:c.C2908G:p.L970V	0.999912
	ARPP21	nonsynonymous SNV	NM_016300:c.G2220C:p.Q740H	0.956551
	ATF5	nonsynonymous SNV	NM_001193646:c.C421T:p.L141F	0.964918
	CC2D1B	nonsynonymous SNV	NM_032449:c.C2038T:p.H680Y	0.967756
	CDH3	nonsynonymous SNV	NM_001793:c.G1285A:p.V429I	0.997145
	CDH4	nonsynonymous SNV	NM_001794:c.G1607A:p.R536Q	0.998951
	CDKN1B	nonsynonymous SNV	NM_004064:c.G187T:p.D63Y	0.996651
	CHRNA10	nonsynonymous SNV	NM_020402:c.G598A:p.V200M	0.990703
	CLCNKB	nonsynonymous SNV	NM_001165945:c.G1370A:p.C457Y	0.996654
	CLN5	stopgain SNV	NM_006493:c.C694T:p.Q232X	1
	COL9A3;COL9A3	nonsynonymous SNV	NM_001853:c.C1547T:p.P516L	0.999969
	CPS1	nonsynonymous SNV	NM_001122634:c.G2773A:p.G925S	0.995938
	CPVL	nonsynonymous SNV	NM_019029:c.C1043G:p.T348S	0.981603
	CSMD2	nonsynonymous SNV	NM_052896:c.A7997G:p.N2666S	0.999988
	DDR2	nonsynonymous SNV	NM_006182:c.C1474T:p.P492S	0.96065
	DIP2B	nonsynonymous SNV	NM_173602:c.C1450T:p.R484W	0.99997
	DNAH9	nonsynonymous SNV	NM_001372:c.T3926G:p.I1309S	0.980987
	EFCAB4A	nonsynonymous SNV	NM_173584:c.A200T:p.Q67L	0.999781
	EME1	nonsynonymous SNV	NM_001166131:c.G1640A:p.R547H	0.998638
	EPX	nonsynonymous SNV	NM_000502:c.G437A:p.R146H	0.997289

Patient #	Gene Name	Type	Variant	Mutation Taster
	FERMT1	nonsynonymous SNV	NM_017671:c.T722C:p.V241A	0.97774
	FMN2	nonsynonymous SNV	NM_020066:c.G3542A:p.G1181E	0.999142
	GCAT	nonsynonymous SNV	NM_001171690:c.C1237T:p.R413W	1
	GFM2	nonsynonymous SNV	NM_170691:c.C2089G:p.R697G	0.999995
	GPI	stopgain SNV	NM_000175:c.G937T:p.E313X	1
	GPR17	nonsynonymous SNV	NM_001161417:c.G223A:p.V75M	0.988762
	GRIK4	nonsynonymous SNV	NM_014619:c.C500G:p.A167G	0.999321
	HEATR5B	nonsynonymous SNV	NM_019024:c.T245C:p.I82T	0.962443
	HOXC11	nonsynonymous SNV	NM_014212:c.C726G:p.F242L	0.972933
	HPS1	nonsynonymous SNV	NM_000195:c.C1718G:p.P573R	0.998361
	IGFBP5	nonsynonymous SNV	NM_000599:c.C412T:p.R138W	0.992419
	INPP4B	nonsynonymous SNV	NM_001101669:c.T1781C:p.V594A	0.999598
	IQGAP2	nonsynonymous SNV	NM_006633:c.G2905A:p.V969I	0.975348
	IQGAP2;IQGAP2	nonsynonymous SNV	NM_006633:c.C2681T:p.T894I	0.999897
	KAZALD1	nonsynonymous SNV	NM_030929:c.G707A:p.G236D	0.997013
	LMCD1	nonsynonymous SNV	NM_014583:c.C913T:p.R305W	0.965828
	LRBA	nonsynonymous SNV	NM_001199282:c.A4261G:p.S1421G	0.992564
	LRRK1	nonsynonymous SNV	NM_024652:c.C1246A:p.L416M	0.962459
	LUC7L2	nonsynonymous SNV	NM_016019:c.A861C:p.E287D	0.990717
	MANBA	nonsynonymous SNV	NM_005908:c.G2482A:p.V828I	0.977631
	MAPRE1	nonsynonymous SNV	NM_012325:c.G389C:p.R130T	0.999991
	MICAL1	nonsynonymous SNV	NM_001159291:c.G293A:p.R98Q	0.994186
	MINA	nonsynonymous SNV	NM_001042533:c.C419T:p.P140L	0.999992
	MON2	nonsynonymous SNV	NM_015026:c.A2518G:p.T840A	0.999978
	MPP3	nonsynonymous SNV	NM_001932:c.C617A:p.S206Y	0.999494
	MYH1	nonsynonymous SNV	NM_005963:c.T1303C:p.Y435H	0.995119
	MYH10	nonsynonymous SNV	NM_005964:c.C2894T:p.A965V	0.992154
	NALCN	nonsynonymous SNV	NM_052867:c.C2305T:p.H769Y	0.996386
	NARS2	nonsynonymous SNV	NM_001243251:c.A218G:p.K73R	0.97168
	NEDD9	nonsynonymous SNV	NM_006403:c.G784A:p.D262N	0.999807
	NUDT16	nonsynonymous SNV	NM_001171905:c.C67G:p.L23V	0.998334
	PARK2	nonsynonymous SNV	NM_013988:c.G733A:p.D245N	0.998566
	PMPCA	nonsynonymous SNV	NM_015160:c.T1307C:p.M436T	0.999929
	PRKCE	nonsynonymous SNV	NM_005400:c.T896C:p.I299T	0.999162
	PSMD1	nonsynonymous SNV	NM_001191037:c.A1051G:p.M351V	0.998558
	PTPN21	nonsynonymous SNV	NM_007039:c.A2983G:p.M995V	0.991544
	PTPN22	nonsynonymous SNV	NM_012411:c.A2077G:p.R693G	0.972937
	PTPRH	nonsynonymous SNV	NM_001161440:c.G1958A:p.G653D	0.999508
	PUS7	nonsynonymous SNV	NM_019042:c.C367T:p.H123Y	0.999092
	RAB40B	nonsynonymous SNV	NM_006822:c.C788G:p.P263R	0.998892

Patient #	Gene Name	Type	Variant	Mutation Taster
	RFWD3	nonsynonymous SNV	NM_018124:c.C1082T:p.S361F	0.984736
	RICTOR	nonsynonymous SNV	NM_152756:c.T1989G:p.I663M	0.963034
	RPS6KB2;RPS6KB2	nonsynonymous SNV	NM_003952:c.C800T:p.P267L	0.997891
	SBF1	nonsynonymous SNV	NM_002972:c.G1918C:p.E640Q	0.998315
	SCRIB	nonsynonymous SNV	NM_015356:c.G571A:p.D191N	0.956013
	SDK1	nonsynonymous SNV	NM_152744:c.C6590G:p.P2197R	0.99838
	SERPIND1	nonsynonymous SNV	NM_000185:c.G623A:p.R208H	0.999998
	SFXN4	nonsynonymous SNV	NM_213649:c.A795T:p.E265D	1
	SLC35E3	nonsynonymous SNV	NM_018656:c.G182C:p.C61S	0.9996
	SPAG5	nonsynonymous SNV	NM_006461:c.A1G:p.M1V	0.994842
	TAGLN	nonsynonymous SNV	NM_001001522:c.G437A:p.R146H	0.957856
	TBC1D5	nonsynonymous SNV	NM_001134380:c.A1124G:p.Y375C	0.999883
	TBX21	nonsynonymous SNV	NM_013351:c.C1421G:p.P474R	0.99529
	THAP6	nonsynonymous SNV	NM_144721:c.A419C:p.H140P	0.959775
	TRIM36	nonsynonymous SNV	NM_018700:c.A1283G:p.K428R	0.958679
	TRIM45	nonsynonymous SNV	NM_001145635:c.G1253A:p.G418E	0.999999
	TRIM69	stopgain SNV	NM_182985:c.C145T:p.R49X	1
	UTP20;UTP20	nonsynonymous SNV	NM_014503:c.G325A:p.D109N	0.991391
	VAX2	nonsynonymous SNV	NM_012476:c.C415A:p.L139M	0.999972
	ZC3H10	nonsynonymous SNV	NM_032786:c.C380T:p.P127L	0.99827
	ZSWIM1	stopgain SNV	NM_080603:c.G26A:p.W9X	0.999992
	ZSWIM5	nonsynonymous SNV	NM_020883:c.C793T:p.R265C	0.999991
5	ABCB4	nonsynonymous SNV	NM_000443:c.G1769A:p.R590Q	0.999999
	ABCC12	stopgain SNV	NM_033226:c.C2491T:p.Q831X	1
	ACTN1	nonsynonymous SNV	NM_001102:c.C2597T:p.P866L	0.999999
	ACTRT1	nonsynonymous SNV	NM_138289:c.G529A:p.A177T	0.986573
	ADCY3	nonsynonymous SNV	NM_004036:c.C1673A:p.P558H	0.996295
	ADCY5	nonsynonymous SNV	NM_001199642:c.G2203A:p.V735I	0.989953
	AGFG1	nonsynonymous SNV	NM_001135187:c.T416C:p.V139A	0.969113
	AIFM3	nonsynonymous SNV	NM_001018060:c.C1370G:p.T457S	0.998899
	ALDH5A1	nonsynonymous SNV	NM_001080:c.G886A:p.A296T	0.999898
	AMACR	nonsynonymous SNV	NM_001167595:c.G367A:p.D123N	0.99999
	ANO3	nonsynonymous SNV	NM_031418:c.C164T:p.S55F	0.983811
	ATP7B	nonsynonymous SNV	NM_001005918:c.C3413G:p.P1138R	0.999924
	BCL9	nonsynonymous SNV	NM_004326:c.G3633A:p.M1211I	0.969422
	BMP5	nonsynonymous SNV	NM_021073:c.G542A:p.R181Q	0.999127
	C6orf170	nonsynonymous SNV	NM_152730:c.A3695C:p.E1232A	0.961507
	C7orf62	stopgain SNV	NM_152706:c.C115T:p.R39X	1
	CASP8	nonsynonymous SNV	NM_001080125:c.T2C:p.M1T	1
	CAT	nonsynonymous SNV	NM_001752:c.G1169A:p.G390D	0.999953

Patient #	Gene Name	Type	Variant	Mutation Taster
	CELSR2	nonsynonymous SNV	NM_001408:c.A3800G:p.H1267R	0.997746
	CHAT	nonsynonymous SNV	NM_001142929:c.G844A:p.D282N	0.999735
	CHRND	nonsynonymous SNV	NM_000751:c.C1066T:p.P356S	0.999036
	CLIC5	nonsynonymous SNV	NM_001114086:c.C770A:p.P257H	0.999876
	CNIH3	nonsynonymous SNV	NM_152495:c.G172C:p.E58Q	0.989502
	COL11A1	nonsynonymous SNV	NM_080630:c.C2573A:p.P858Q	0.99532
	COL27A1;COL27A1	nonsynonymous SNV	NM_032888:c.C4754T:p.P1585L	0.999194
	COMMD1	nonsynonymous SNV	NM_152516:c.C358T:p.R120W	0.999021
	CPA5	nonsynonymous SNV	NM_001127442:c.C235T:p.P79S	0.999222
	CRELD2	nonsynonymous SNV	NM_001135101:c.C565G:p.R189G	0.999934
	CRIM1	nonsynonymous SNV	NM_016441:c.A1235C:p.H412P	0.99938
	CROT	nonsynonymous SNV	NM_021151:c.G1733A:p.C578Y	0.979371
	CRYGD	nonsynonymous SNV	NM_006891:c.A130G:p.M44V	0.996676
	CTSH	nonsynonymous SNV	NM_004390:c.A479G:p.K160R	0.987819
	CUL7	stopgain SNV	NM_001168370:c.C2170T:p.Q724X	1
	DBH	nonsynonymous SNV	NM_000787:c.A602G:p.N201S	0.999861
	DISP1	nonsynonymous SNV	NM_032890:c.T3287C:p.M1096T	0.993265
	EDEM1	nonsynonymous SNV	NM_014674:c.G1892A:p.R631H	0.993018
	EEPD1	nonsynonymous SNV	NM_030636:c.G1264A:p.D422N	0.998316
	ENPP1	nonsynonymous SNV	NM_006208:c.C1094T:p.P365L	0.999971
	EPX	nonsynonymous SNV	NM_000502:c.T1635G:p.F545L	0.983494
	FAT4	nonsynonymous SNV	NM_024582:c.C12064T:p.R4022W	0.977535
	FBN1	nonsynonymous SNV	NM_000138:c.G3748T:p.D1250Y	0.99991
	FDXR	nonsynonymous SNV	NM_004110:c.G416A:p.R139Q	0.999236
	FGL1	nonsynonymous SNV	NM_004467:c.A419T:p.Y140F	0.950515
	FRK	stopgain SNV	NM_002031:c.G562T:p.E188X	1
	FRS3	nonsynonymous SNV	NM_006653:c.A446G:p.N149S	0.998663
	GATA2	nonsynonymous SNV	NM_001145662:c.C481G:p.P161A	0.974929
	GGA3	nonsynonymous SNV	NM_001172704:c.G95T:p.R32M	0.99693
	GJB2	nonsynonymous SNV	NM_004004:c.T101C:p.M34T	0.997115
	GPAA1	nonsynonymous SNV	NM_003801:c.G1540A:p.A514T	0.975232
	GPN2	nonsynonymous SNV	NM_018066:c.G82C:p.G28R	0.994224
	HAO1	nonsynonymous SNV	NM_017545:c.C773T:p.S258L	0.999979
	HCRTR1	nonsynonymous SNV	NM_001525:c.G499A:p.G167S	0.952048
	HSP90B1	nonsynonymous SNV	NM_003299:c.C962T:p.P321L	0.999972
	IGFBP5	nonsynonymous SNV	NM_000599:c.C412T:p.R138W	0.992419
	IRF3	nonsynonymous SNV	NM_001197122:c.G175A:p.E59K	0.987756
	IRX4	nonsynonymous SNV	NM_016358:c.G1318A:p.D440N	0.992029
	KAZALD1	nonsynonymous SNV	NM_030929:c.G707A:p.G236D	0.997013
	KCND3	nonsynonymous SNV	NM_004980:c.A1456G:p.T486A	0.999976

Patient #	Gene Name	Type	Variant	Mutation Taster
	KIAA0020	nonsynonymous SNV	NM_014878:c.C1241G:p.T414S	0.999706
	KIAA0317	nonsynonymous SNV	NM_001039479:c.G148A:p.V50M	0.999039
	KIAA0528	nonsynonymous SNV	NM_014802:c.A2669C:p.K890T	0.999047
	KIAA1033	nonsynonymous SNV	NM_015275:c.G967T:p.V323L	0.999055
	LAMA5	nonsynonymous SNV	NM_005560:c.G10034T:p.G3345V	0.999638
	LAMB1	nonsynonymous SNV	NM_002291:c.T4640C:p.I1547T	0.999513
	LGALS4	nonsynonymous SNV	NM_006149:c.G719A:p.R240H	0.952837
	LRRC47	nonsynonymous SNV	NM_020710:c.G1741A:p.V581I	0.976696
	LRRCC1	stopgain SNV	NM_033402:c.C916T:p.Q306X	1
	MOB3C	nonsynonymous SNV	NM_145279:c.A388G:p.M130V	0.997595
	MPP5	nonsynonymous SNV	NM_022474:c.C422A:p.S141Y	0.988384
	MYOT	nonsynonymous SNV	NM_006790:c.A546T:p.E182D	0.960053
	NARFL	nonsynonymous SNV	NM_022493:c.G277A:p.E93K	0.999978
	NCOR1	nonsynonymous SNV	NM_001190440:c.A4266C:p.L1422F	0.998894
	NDUFA2	nonsynonymous SNV	NM_001185012:c.C40G:p.L14V	0.998986
	NDUFS1	nonsynonymous SNV	NM_001199982:c.A747C:p.R249S	0.999163
	NOX5	nonsynonymous SNV	NM_001184779:c.C343G:p.P115A	0.970301
	NPR1	nonsynonymous SNV	NM_000906:c.G1621A:p.G541S	0.999889
	NUDT16	nonsynonymous SNV	NM_001171905:c.C67G:p.L23V	0.998334
	NVL	nonsynonymous SNV	NM_001243146:c.A994G:p.T332A	0.968042
	NXNL1	nonsynonymous SNV	NM_138454:c.G190A:p.E64K	0.999693
	OCA2	nonsynonymous SNV	NM_000275:c.G1327A:p.V443I	0.967111
	OR4C3	stopgain SNV	NM_001004702:c.G522A:p.W174X	1
	OTOF	nonsynonymous SNV	NM_194322:c.C2993T:p.T998M	0.999687
	P2RY4	stopgain SNV	NM_002565:c.G1043A:p.W348X	0.999358
	PBRM1	nonsynonymous SNV	NM_018165:c.G2183A:p.R728H	0.999687
	PDCD11	nonsynonymous SNV	NM_014976:c.A5570G:p.K1857R	0.999015
	PEX11G	nonsynonymous SNV	NM_080662:c.C646T:p.L216F	0.99922
	PLB1	nonsynonymous SNV	NM_001170585:c.C3934A:p.P1312T	1
	PLD2	nonsynonymous SNV	NM_001243108:c.G2057C:p.G686A	0.999969
	PLEC	nonsynonymous SNV	NM_201378:c.G10016C:p.G3339A	0.997421
	PLSCR2	nonsynonymous SNV	NM_001199979:c.A756T:p.R252S	0.994462
	RAB13	nonsynonymous SNV	NM_002870:c.C142T:p.R48C	0.999634
	RAF1	nonsynonymous SNV	NM_002880:c.A1721G:p.Y574C	0.999819
	RASGRP2	nonsynonymous SNV	NM_001098670:c.C1466G:p.S489C	0.97466
	RBBP8	nonsynonymous SNV	NM_002894:c.A467G:p.E156G	0.998483
	RBM24	nonsynonymous SNV	NM_153020:c.G274A:p.V92I	0.991025
	RNF133	nonsynonymous SNV	NM_139175:c.G3A:p.M1I	0.996355
	ROBO2	nonsynonymous SNV	NM_001128929:c.C2372T:p.P791L	0.994361
	RRAS	nonsynonymous SNV	NM_006270:c.G397A:p.D133N	0.989016

Patient #	Gene Name	Type	Variant	Mutation Taster
	RRP7A	nonsynonymous SNV	NM_015703:c.G704A:p.R235Q	0.982204
	SDHD	nonsynonymous SNV	NM_003002:c.C299G:p.T100S	0.999697
	SH3D21	nonsynonymous SNV	NM_024676:c.T1799C:p.L600P	0.975425
	SHPRH	nonsynonymous SNV	NM_001042683:c.A4960T:p.T1654S	0.998802
	SIGIRR	nonsynonymous SNV	NM_001135053:c.C239A:p.S80Y	0.995001
	SLC12A9	nonsynonymous SNV	NM_020246:c.C571T:p.R191W	0.970996
	SLC25A40	nonsynonymous SNV	NM_018843:c.C368T:p.T123I	0.997629
	SLFNL1	stopgain SNV	NM_144990:c.G250T:p.E84X	1
	SNW1	nonsynonymous SNV	NM_012245:c.G55A:p.E19K	0.999514
	SORBS1	nonsynonymous SNV	NM_001034957:c.G956A:p.R319H	0.994991
	STARD5	nonsynonymous SNV	NM_181900:c.C583T:p.R195C	0.953848
	SUMF2	nonsynonymous SNV	NM_001042470:c.G427A:p.D143N	0.97932
	TIMM17B	nonsynonymous SNV	NM_005834:c.C139T:p.R47W	0.980665
	TIMM44	nonsynonymous SNV	NM_006351:c.C753G:p.N251K	0.999996
	TMEFF2	nonsynonymous SNV	NM_016192:c.A317G:p.N106S	0.994678
	TMEM186	nonsynonymous SNV	NM_015421:c.T194A:p.I65N	0.997795
	TMEM214	nonsynonymous SNV	NM_001083590:c.G1370A:p.R457Q	0.999271
	TRAK1	nonsynonymous SNV	NM_001042646:c.C2354T:p.S785L	0.981485
	TUBB3	nonsynonymous SNV	NM_001197181:c.G170A:p.C57Y	0.999955
	UBE2CBP	nonsynonymous SNV	NM_198920:c.C1142A:p.S381Y	0.998664
	UBQLN4	nonsynonymous SNV	NM_020131:c.G893A:p.R298Q	0.999289
	UNC79	nonsynonymous SNV	NM_020818:c.C298G:p.L100V	0.97198
	VIT	nonsynonymous SNV	NM_001177969:c.A183T:p.K61N	0.996027
	WNT9B	nonsynonymous SNV	NM_003396:c.C555A:p.D185E	0.994449
	WWP1	nonsynonymous SNV	NM_007013:c.G2220C:p.K740N	0.999957
	XPO4	nonsynonymous SNV	NM_022459:c.A446G:p.N149S	0.99668
	XPO6	nonsynonymous SNV	NM_015171:c.G3056A:p.R1019Q	0.998833
	ZBTB11	nonsynonymous SNV	NM_014415:c.T3071C:p.L1024S	0.998507
	ZC3H13	nonsynonymous SNV	NM_015070:c.G2144A:p.R715Q	0.997613
	ZNF543	stopgain SNV	NM_213598:c.G203A:p.W68X	1

Chapter 4

A key eye patterning gene, *VAX2*, affects the closure of superior ocular sulcus, a novel feature of eye development

4.1. Introduction

Ocular coloboma is an eye disorder characterized by gaps in tissues of the iris, optic nerve, retina, and lens, and is frequently blinding, being associated with up to 10% of pediatric blindness worldwide (Chang et al., 2006; Fujiki et al., 1982; George et al., 2020). Ocular coloboma occurs in 2-19 per 100,000 live births, and together with microphthalmia and anophthalmia, comprises a spectrum of ocular disorders called MAC (Bermejo & Martínez-Frías, 1998; Lu, 1989; Morrison et al., 2002; Porges et al., 1992; Shah et al., 2011; Stoll et al., 1997; Shah et al., 2012). Coloboma typically affects the ventral/inferior eye, but in rare cases occurs in the superior/dorsal eye, a condition called either atypical or superior coloboma. Both types of coloboma are associated with aberrant early eye development, wherein an ocular fissure fails to close.

During early eye development, the eye forms two transient fissures, the choroid fissure in the ventral eye and the superior sulcus in the dorsal eye. Both fissures are aligned with early vasculature and facilitate the passage of blood vessels that nourish the developing lens (Saint-Geniez & D'Amore, 2004; Kaufman et al., 2015; Kitambi et al., 2009; Hocking et al., 2018). Over 40 genes have been associated with the causality of ocular coloboma, yet the majority of patients possess mutations in novel, undiscovered loci (Yoon et al., 2020). Although the mechanisms controlling choroid fissure closure have been extensively characterized, the superior ocular sulcus (SOS) has only recently been identified, and the mechanisms that regulate its closure remain mostly unstudied. Therefore, the focus of our study is to uncover novel regulators of SOS closure. Previous studies have demonstrated that the SOS is narrow and highly transient, being visible in zebrafish only between 20-23 hpf (Hocking et al., 2018). The sulcus is evolutionarily conserved across vertebrates, including fish, chick, newt, and mouse eye development (Hocking et al., 2018).

Genetic causes of ocular coloboma are often linked to genes involved in early eye developmental processes, such as the formation of eye anlage, eye axis patterning, early cellular morphogenesis, and neural crest cell migration (Yoon et al., 2020). Consistent with this, the initial investigation of superior coloboma revealed detrimental patient variants in *BMP receptor 1a* and *T-box transcription factor 2* (Hocking et al., 2018). Studies in zebrafish, chick and mouse have demonstrated that Bmp signaling initiates regional gene expression in the dorsal eye. (French et al., 2009; Gosse & Baier, 2009) Loss of Bmp signaling in zebrafish blocks closure of the SOS

(Hocking et al., 2018). Studies of zebrafish *tbx2b* demonstrated that its expression is regulated by Bmp signaling and that loss of *tbx2b* blocks SOS closure (Gosse & Baier, 2009; Hocking et al., 2018). Taken together, such studies demonstrated that Bmp and Tbx2 function to establish dorsal eye identity and are required for SOS closure.

Although the importance of dorsal eye-specific programs is clear, there is also evidence that cells within the ventral retina play a role in regulating SOS closure. Patterning of the ventral eye is principally controlled by the secreted morphogen, Shh (Ekker et al., 1995; Hallonet, et al., 1999; Macdonald et al., 1995; Take-uchi et al., 2003). Manipulation of Shh signaling resulted in aberrant SOS formation and loss of Shh was able to rescue partial depletion of Bmp. This implies a model whereby morphogenesis of early ocular fissures is dependent on a balance between dorsal and ventral gene expression programs. Consistent with this model, other studies have demonstrated that loss of dorsal eye signaling results in ventral coloboma (Asai-Coakwell et al., 2009).

Here, I describe a superior coloboma patient with a *Ventral anterior homeobox 2* (*VAX2*) variant, altering a conserved residue within the homeodomain. Zebrafish *vax2* is expressed within the ventral retina during the developmental time period in which the superior sulcus is closing. To investigate loss of *vax2*, I generated a CRISPR-Cas9 mutant and studied its phenotype in early eye development. I observe a significant, albeit partial block in superior sulcus closure. In addition, analysis of the human variant demonstrates a reduction in biological activity, implying that it is detrimental to protein structure and function. Vax2 functions as a regulator of ventral eye gene expression, which further supports a model whereby closure of the vertebrate superior sulcus is dependent on the proper establishment of ocular dorsal-ventral axis patterning.

4.2. Results

4.2.1. Description of the patient variant allele

Through our previous study presented in Chapter 3, we identified a 14-month old patient exhibiting unilateral superior coloboma in the right eye (Fig. 4.1A). Whole exome sequencing revealed 19,191 variants present in the patient. *In silico* algorithms predicted 92 variants as detrimental, and analysis of the published expression domains of these loci revealed 19 with ocular expression (Hocking et al., 2018). Given that previous studies have demonstrated that superior coloboma is caused by aberrant ocular development, in this study we prioritized genes with known or suspected roles in ocular development. As such, we focused our efforts on studying the rare variant of *VAX2* (Gene ID: 25806; NM_012476), a homeodomain transcription factor expressed in the ventral portion of the eye. The nonsynonymous single-nucleotide variant (c.C415A) results in an amino acid substitution in the homeodomain of the protein (p.Leu139Met) (Fig. 4.1B). This residue is highly conserved throughout evolution from fish to human (Fig. 4.1C). In addition, this residue is conserved in 90 out of 101 human ANTP class homeodomain proteins (Fig. 4.1D). Analysis through *in silico* modeling of the variant revealed that this amino acid substitution is highly likely to create a significant change to the structure and function of VAX2 (MutationTaster - 0.999972; Polyphen2 – 0.984; SIFT - 0). Although this variant is predicted to be detrimental by all algorithms, it is present in an appreciable portion of the human population (gnomAD allele frequency – 0.003838). This represents a paradox, and requires us to investigate the nature of this allele using animal model studies.

4.2.2. Generation of vax2-null allele

Loss of *vax2* has already been implicated in formation of ocular coloboma in animal models (Barbieri et al., 2002; Take-uchi et al., 2003). While definitive ocular coloboma phenotypes are observed in *Vax2*-null mutant mice, such analyses did not characterize defects in superior sulcus closure (Barbieri et al., 2002). Studies in zebrafish have been restricted to antisense morpholino-mediated knockdown experiments and similarly did not analyze dorsal eye development (Take-uchi et al., 2003). Therefore, to assess the function of Vax2 in dorsal eye

development, I created a zebrafish *vax2* mutant through CRISPR-Cas9 mutagenesis. I generated an 83-basepair deletion in exon 2, resulting in the loss of +311 to +393 (Fig. 4.2). The *vax2*^{ua1031} allele results in p.Lys104ArgfsX11 protein sequence change, in which a frameshift mutation at residue 104 results in a short 11 residue polypeptide, followed by a terminator, thus truncating the protein to 115 amino acids from the wildtype length of 307 amino acids (Fig. 4.3). The premature STOP codon severely disrupts the translation of the homeodomain region (SMART 103-165 aa; SM00389). The lack of in-frame initiator MET residues within the predicted transcript predicts a loss of the DNA binding region of CRISPR-Cas9 generated allele of Vax2 (Fig. 4.3).

4.2.3. Characterization of vax2-null zebrafish

Initial stereomicroscope observations of homozygous *vax2*$^{ua1031/ua1031}$ embryos failed to reveal any defects on SOS closure, presenting no other observable phenotypes, and the fish were viable and fertile. However, other zebrafish CRISPR-Cas9 mutant studies have only been able to observe phenotypes when removing the maternally-derived mRNA/protein (Gritsman et al., 1999; Mintzer et al., 2001). Since homozygous zebrafish *vax2* mutants are viable and fertile, I crossed *vax2*$^{ua1031/ua1031}$ with *vax2*$^{ua1031/ua1031}$ to generate MZ*vax2*$^{ua1031/ua1031}$. I observed SOS closure by stereomicroscope analysis at 28 hpf and saw a significant difference in SOS closure, with closure being delayed in MZ*vax2*$^{ua1031/ua1031}$ (Fig. 4.4A-D). This is a partially penetrant phenotype; 98% of wildtype embryos display a closed SOS at 28 hpf (3/136 open SOS), 18% of heterozygous MZ*vax2* individuals (26/145; P = 0.00173202, ANOVA) and 27% of homozygous *MZvax2* $^{ua1031/ua1031}$ mutants (44/161; P = 0.00037043, ANOVA) show SOS closure delay (Fig. 4.4E). Interestingly, this implies a maternal effect of *vax2* mRNA deposited in the egg prior to fertilization; *MZvax2*$^{ua1031/ua1031}$ mutants display an SOS phenotype, while zygotic *vax2*$^{ua1031/ua1031}$ do not. A degree of haploinsufficiency could be observed, as the difference in prevalence of SOS closure delay between heterozygotes and *MZvax2* $^{ua1031/ua1031}$ mutants was found to be statistically significant (P = 0.02990897; ANOVA) (Fig. 4.4E). Ocular coloboma, microphthalmia, and anophthalmia were not present in any embryos observed up to 72 hpf.

4.2.4. Creation of an assay for overexpressed VAX2

To create an assay to assess the activity of the detected human variant, I chose to investigate the effects of increased *vax2* activity on zebrafish eye development. I generated capped mRNA for human (hs) *VAX2* from a xxx plasmid. I microinjected hs wildtype *VAX2* mRNA into zebrafish at the one-cell stage. Initial stereomicroscope observations of the eye at 28 hpf revealed a delayed SOS closure phenotype in hs *VAX2* mRNA-injected embryos (Fig. 4.5A). Laminin stain of the injected embryos at 28 hpf showed an increased prevalence of SOS closure delay in a dosage-dependent manner in embryos injected with hs *VAX2* mRNA, confirmed by the delayed dissolution of basement membrane in the dorsal aspect of the developing eye (Fig. 4.5B). In a triplicate experiment, compared to 2.5% open fissures found in the control group (5/213), 14.3% of embryos injected with 12.5 pg hs *VAX2* mRNA (22/156; P = 0.00011, *t* test) and 50.6% of embryos injected with 25 pg hs *VAX2* mRNA (109/217; P = 0.0018, *t* test) exhibited SOS closure delay (Fig. 4.5C). In addition, 49.1% of embryos injected with 50 pg of hs *VAX2* mRNA showed SOS closure delay (109/217; P = 0.0103; *t* test), while an additional 14.5% presented with microphthalmia (33/205), a phenotype not observed at lower doses or in the control group (Fig. 4.5C). Furthermore, hs wildtype *VAX2* mRNA-injected embryos exhibited SOS closure delay up to 50 hpf, but this phenotype was not visible by 72 hpf (Fig. 4.6). Translation of injected hs *VAX2* mRNA was verified through Western blot analysis (Fig. 4.7).

4.2.5. Analysis of activity of patient variant VAX2

I obtained a custom-made gBlocks gene fragment from IDT containing the cDNA sequence for hs *VAX2* containing the patient-specific c.C415A substitution (p.Leu139Met), with sequence confirmed by Sanger sequencing, after which the gene fragment was subcloned into pCS2+ and transcribed to obtain patient-variant mRNA, To compare the biological activity of wildtype and variant Vax2, I microinjected one-cell zebrafish embryos with an equal 25 pg dose of mRNA and evaluated for SOS closure delay phenotypes at 28 hpf. Injection of the patient variant mRNA revealed a significant decrease in activity compared to that of wildtype mRNA. Whereas I observed SOS closure delay in 48.9% of embryos upon injection of 25 pg wildtype *VAX2* (n =

86/175), only 35.4% of embryos exhibited SOS closure delay when injected with patient variant *VAX2* mRNA (n = 53/151; P = 0.02, *t* test) (Fig. 4.8). As the wildtype protein is translated in similar levels compared to the p.Leu139Met variant, it is likely that the difference in protein activity is due to the amino acid substitution and not an artifact of uneven dosage delivery (Fig. 4.7). This provides evidence that the alteration of Leu 139 to Met results in a modest reduction in biological activity, and suggests that ocular disease present in this patient may result, at least in part, from this allele.

4.2.6. Elucidating the molecular mechanisms of SOS closure delay

I attempted to understand the molecular mechanisms through which *VAX2* overexpression led to SOS closure delay. Previous studies have shown that increased apoptosis in the eye during early development is correlated with ocular coloboma (Asai-Coakwell et al., 2013; Pant et al., 2013). To determine if *VAX2* overexpression-induced SOS closure delay is associated with increased apoptosis in the early eye, embryos identified to show SOS closure delay were placed in embryo media containing acridine orange (AO) to stain cells undergoing apoptosis, and the number of apoptotic cells were counted. In a triplicate experiment, compared to the control group, I saw a significant increase in the number of apoptotic cells in embryos exhibiting SOS closure delay at 28 hpf (9.74 vs 16.44; P = 0.027, *t* test) (Fig. 4.9). Interestingly, I noted clustering of apoptotic cells in the ventral-nasal quadrant of the eye (Fig. 4.9A).

4.2.7. Consequences of VAX2 overexpression on superficial ocular vasculature

In our previous study of the SOS, I observed that embryos with SOS closure delay exhibit abnormal superficial ocular vasculature and that the SOS may act as a conduit for blood vessels during early ocular vasculogenesis (Hocking et al., 2018). Briefly, in the developing zebrafish eye, the dorsal radial vessel (DRV) grows superficially over the dorsal eye and the SOS, extending towards the lens, eventually connecting with the hyaloid vasculature, which extends through the choroid fissure. With SOS closure delay from *gdf6a* loss, we noted subsequent aberrant formation

of the DRV (Hocking et al., 2018). I observed a similar phenotype in *VAX2* overexpression, with hs *VAX2* overexpression leading to multiple DRVs that form ectopically, as well as the complete lack of DRV formation and extension towards the lens (Fig. 4.10).

4.2.7. Gene expression changes

Ocular DV axis patterning during early development is mediated via the activities of Bmp and Wnt signalling in the dorsal eye opposing Shh in the ventral eye. Such morphogens specify the precise expression domains of transcription factors and axon guidance cues in dorsal and ventral regions and notably such transcription factors demonstrate strong repressive interactions between dorsal and ventral regions. For example, prior studies have demonstrated that loss of the Bmp gene *gdf6a* results in a significant decrease in expression levels of downstream dorsal eye genes, such as *tbx5a*, *tbx2b*, and *efnb2a*, while the expression domains of ventral eye genes, such as *vax2*, *aldh1a3*, *ephb2*, and *ephb3*, are greatly expanded (French et al., 2009; Gosse & Baier, 2009). In addition, our previous study of the SOS established that proper expression of *gdf6a* and the subsequent maintenance of dorsal eye fate via Bmp signaling is crucial for proper SOS formation and closure (Hocking et al., 2018). Therefore, I sought to investigate the downstream consequences of manipulating the expression of a key ventral eye fate gene, *vax2*, to gain better understanding of how any changes to other eye DV axis patterning genes may be related to the SOS closure delay phenotypes seen in MZ*vax2* mutants and hs*VAX2* mRNA overexpression. I hypothesized that loss of *vax2* will result in the expansion of dorsal markers. I employed whole mount *in situ* hybridization for an array of dorsal eye marker genes and compared expression at 28 hpf in wildtype to that in MZ*vax2*$^{ua1031/ua1031}$ embryos. Indeed, the expression domain of *tbx5a*, a transcription factor required for dorsal eye identity, is expanded (Fig. 4.11A,D). However, the gene expression domains of other downstream dorsal markers, *tbx2b* and *efnb2a*, were unaffected (Fig. 4.11B,C,E,F). Conversely, overexpression of *VAX2* leads to downregulation of multiple key dorsal markers (Fig. 4.12). I noted a significant reduction in the expression domains of *tbx5a, tbx2b,* and *efnb2a,* with the expression domains of *tbx5a* and *efnb2a* becoming more spatially restricted to the area surrounding the SOS. Quantitative analysis of gene expression changes via qPCR revealed that expression levels of both *tbx5a* and *efnb2a* are reduced two-fold with overexpression of hs

VAX2 (Fig. 4.12G). This indicates ventralization of the retina, similar to that observed with loss of *gdf6a* (French et al., 2009).

4.3. Discussion

As the superior ocular sulcus is a recently-identified feature of eye development, little is known regarding the factors that regulate its formation and closure, the role it plays during eye development, and the consequences of its malformation. Our present study provides support for including *vax2* in the list of factors known to regulate dorsal eye morphogenesis and closure of the SOS. In addition, I present a novel zebrafish mutant model for a *vax2* loss-of-function allele, which is the first *vax2*-null mutant in zebrafish presented in the literature. Furthermore, as *vax2* is an important marker of early ventral retinal development and a key regulator of DV axis patterning, this study builds upon our previous investigation of the SOS, demonstrating that the proper maintenance of eye DV axis patterning is crucial for proper SOS formation and closure.

Past studies have shown that early DV eye axis patterning is mediated via interactions between Tbx5 and Vax2, although the exact nature of this process still remains unknown (French et al., 2009; Gosse & Baier, 2009; Barbieri et al., 2006). Our findings demonstrate that loss of *vax2* leads to an increase in the expression domain of *tbx5a*, while upregulation of *vax2* leads to downregulation of several early eye patterning genes in the dorsal eye, especially *efnb2a*. This suggests that these gene interactions are more complicated than simply maintaining a balance between *tbx5a* and *vax2*.

Interestingly, our finding that *vax2* loss results in *tbx5a* expansion in a zebrafish *vax2*-null model contradicts the previous findings in which *Vax2* loss does not result in *Tbx5* expansion in a mouse *Vax2*-null model (Barbieri et al., 2002). This may be due to a difference in the activity of its ortholog, Vax1, in the respective model organisms. Similar to *Vax2*, *Vax1* is an important regulator of eye morphogenesis, but unlike *Vax2*, it is also strongly associated with forebrain development (Hallonet et al., 1999). *Vax1* shares overlapping expression domains with *Vax2* in the ventral retina and the optic stalk, but its expression area extends further towards the midline (Take-uchi et al., 2003). Past studies show that loss of both *Vax* genes result in strong phenotypes that are not observable in *Vax* single mutants, suggesting a strong cooperative relationship between

the two *Vax* genes (Take-uchi et al., 2003; Kim & Lemke, 2006). Curiously, while *Vax2* loss is associated with ocular coloboma in animal models, loss of *VAX1* function is more strongly associated with ocular coloboma in human patient data, suggesting a difference in the amount of functional overlap or cooperative relationship between *VAX1* and *VAX2* across different species (Slavotinek et al., 2011). It is possible that these differences complicate the direct comparison of Vax2 mutant models of various species.

Previous studies of the SOS established the importance of maintaining a proper balance between Bmp signaling and Shh signaling in the early eye for proper SOS formation and closure (Hocking et al., 2018). In the ventral eye, Shh induces *vax2* expression to maintain this balance (Barbieri et al., 1999; Kim & Lemke, 2006). Our phenotypic analyses reveal that both increase and decrease in *vax2* leads to SOS closure delay, suggesting the importance of Shh signaling in modulating a proper *vax2* expression level during early eye development. Additionally, our gene expression studies reveal subtle differences in how the expression of dorsal eye genes are affected; multiple components of the dorsal eye are downregulated with *vax2* overexpression, while the same components are not changed, or subtly changed, following *vax2* loss. This discrepancy suggests that the two conditions may be working through different mechanisms that result in the same phenotype. The overexpression of *vax2* is likely affecting how the transcription factor interacts with Bmp-induced dorsal eye determinants, as supported by the changes to Bmp signaling outputs, thus further validating the importance of DV eye axis patterning in SOS formation and closure. By contrast, the SOS closure delay phenotype observed with *vax2* loss may be occurring through a divergent mechanism that is yet to be identified. Although I cannot eliminate the possibility that *vax2* loss primarily affects eye DV axis patterning due to the subtle change to *tbx5a* expression, there are many other mechanisms involved in eye development that can affect SOS formation and closure, such as morphogenesis, cell proliferation, or apoptosis. While I did not directly investigate the possibility of different mechanisms of SOS formation and closure in this study, it is feasible that, as an example, an aberrant epithelial flow of cells during early eye morphogenesis can affect the SOS, and that the loss of a key eye development gene, such as *vax2*, can disrupt this process. Further analysis of the patient exome sequencing data will aid in the identification of causal mechanisms that are independent of eye DV axis patterning.

In addition, the role of *vax2*, a transcription factor expressed specifically in the ventral eye, in the closure of the SOS, a structure in the dorsal eye, raises interesting questions regarding the role of genes beyond that of their area of expression. While this may appear counterintuitive, examples of these types of relationships exist. In fact, this is parallel to the role of another gene involved in early eye DV axis patterning. Previous studies have shown that loss of *gdf6a*, expressed specifically in the dorsal eye, leads to improper closure of the choroid fissure, a structure in the ventral eye, and its loss has been linked to ocular coloboma phenotypes in human patients and animal models (Yoon et al., 2020). Similarly, other dorsally-expressed genes such as *BMP2*, *BMP4*, and *BMP7* have been associated with ocular coloboma (Yoon et al., 2020). This may further suggest a role of vax2 in divergent processes, such as early morphogenesis and cell migration, that is yet to be elucidated.

The specific p.Leu139Met variant identified from a human patient likely results in a hypomorphic allele as demonstrated by the reduction in SOS closure delay upon mRNA overexpression. While the p.Leu139Met substitution may not appear to be a drastic change with regards to hydrophobicity, *in silico* projections still predict it to result in a detrimental effect on protein structure and function, perhaps due to increased steric hindrance from the change in amino acid side chain. The conservation of the leucine residue throughout evolution argues in favour of its importance, and it is further supported by the conservation of the leucine residue in the DNA binding regions of many (90/101) ANTP-class homeodomain transcription factors (Fig. 4.1D). However, it is worth noting that while 10 of the remaining 11 ANTP-class members replace the leucine with valine (2), isoleucine (4), or threonine (4), one member, VENTX, contains a methionine instead of a leucine (Fig. 4.1D). This implies that the replacement of the leucine with a methionine observed in the VAX2 sequence of the patient may not result in a complete loss-of-function, and this substitution can be tolerated to allow some function. While our findings suggest that this allele is not hypermorphic, and that it is likely to be hypomorphic, the possibility remains that it is neomorphic in its activity.

While the loss of Vax2 activity alone may not be sufficient to cause a superior coloboma phenotype that persists after the early stages of embryonic development, there may be a combinatorial effect that stems from mutations in genes involved in other signaling pathways, independent of those involved in DV eye axis patterning. As other variants identified in the exome

sequencing data are investigated, we should be able to gain a better understanding of the exact signaling pathways that are involved in SOS formation and closure. Through previous analysis of the superior coloboma patient exome sequencing, we identified rare variants in components of the non-canonical Wnt/PCP signaling pathway, such as *SCRIB*, *FZD4*, *CELSR2*, and *WNT9B*, which affect tissue polarity and cell movement. Furthermore, we have previously noted a rare variant of *TSC2*, a key regulator of mTOR signaling pathway, which controls cell proliferation, growth, and death (Betz & Hall, 2013). Altogether, this suggests the importance of pathways that are independent of eye DV axis patterning in SOS formation and closure, and future investigations of these variants will add complexity to our current understanding of superior coloboma.

In our previous investigation of the SOS, we determined that the loss of dorsal factors in eye axis patterning (*GDF6*, *TBX2*) results in SOS closure delay (Hocking et al., 2018). Here, I found that the manipulation of a ventral factor results in a similar phenotype. Overexpression of *vax2* during early zebrafish development leads to the perturbation of dorsal eye markers, resulting in an imbalance across the early DV axis of the eye and leading to a delay in SOS closure, similar in manner to our previous observations when dorsally-induced Bmp signaling was disrupted. By contrast, I propose that loss of *vax2* may work through a divergent mechanism to result in the same aberrant SOS closure phenotype as I do not observe similar changes to the downstream factors of eye DV axis patterning.

Taken together, this study demonstrates the importance of proper *vax2* expression, and I provide further support for a model in which maintenance of proper eye DV axis patterning is a key component of proper SOS formation and closure. Future studies will be required to explore the roles of other mechanisms in SOS formation and closure, and to broaden our current understanding of superior coloboma.

4.4. Figures

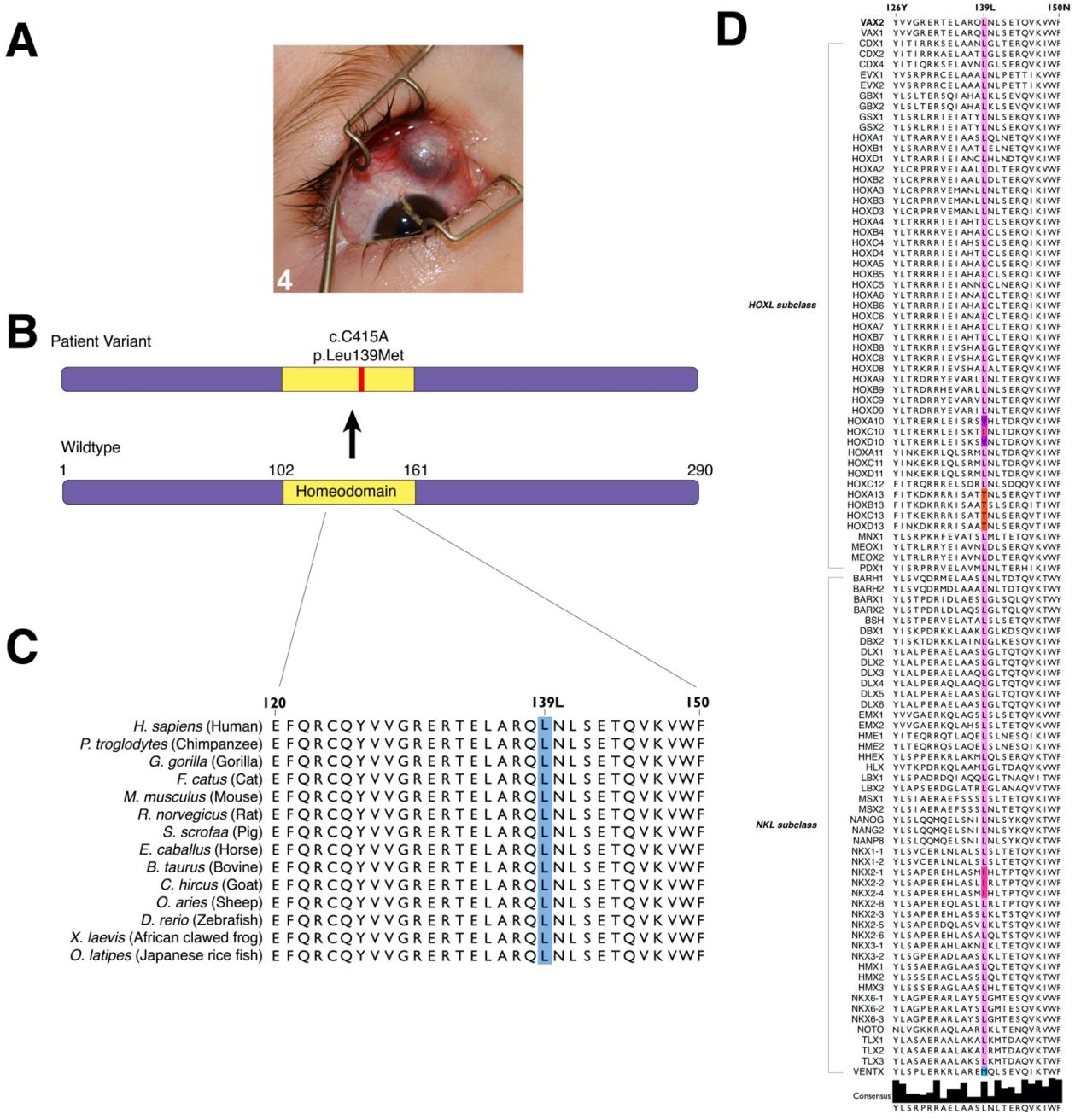

Figure 4.1: Identification of superior coloboma patient variant *VAX2* allele. (A) Unilateral superior coloboma with uveal protrusion in Patient #4. (B) Diagram of the human VAX2 protein with the homeodomain and the patient variant indicated. (C) Alignment illustrating the high degree of evolutionary conservation of the VAX2 homeodomain, with the altered residue highlighted in blue. (D) Alignment illustrating the conservation of the leucine residue in the DNA binding domain

of ANTP class homeodomain proteins. Proteins that contain a leucine residue at the equivalent position is marked with pink, valine with purple, isoleucine with magenta, threonine with red, and methionine with blue. The consensus sequence is depicted below the alignment.

```
Wildtype      ATGTTTGATCAAGCCACGAGTATGGGCGATGGAATCGCCGAGGACCGAAACCACTGTGGA      60
ua1031        ATGTTTGATCAAGCCACGAGTATGGGCGATGGAATCGCCGAGGACCGAAACCACTGTGGA      60
              ************************************************************

Wildtype      TCCAATTCGTTGTGCCGTGACCGCGGCAGAGAGTCGAAAAGCCGGACGGAAGTGGGGAAC      120
ua1031        TCCAATTCGTTGTGCCGTGACCGCGGCAGAGAGTCGAAAAGCCGGACGGAAGTGGGGAAC      120
              ************************************************************

Wildtype      CGGTCACCTGTGCAGAGCTCTACCGACACACCGGGGACTTCGGCATCCACACCGACCTCA      180
ua1031        CGGTCACCTGTGCAGAGCTCTACCGACACACCGGGGACTTCGGCATCCACACCGACCTCA      180
              ************************************************************

Wildtype      TCCAGCGAGGATGGACACGATAAACTTTTAGGAGTCGATCCCGACTACTGTCGGAGGATT      240
ua1031        TCCAGCGAGGATGGACACGATAAACTTTTAGGAGTCGATCCCGACTACTGTCGGAGGATT      240
              ************************************************************

Wildtype      CTGGTCAGAGACGCCAAGGGCACTATTCGGGAGATCGTGCTGCCCAAAGGGCTGGATCTG      300
ua1031        CTGGTCAGAGACGCCAAGGGCACTATTCGGGAGATCGTGCTGCCCAAAGGGCTGGATCTG      300
              ************************************************************

Wildtype      GACCGGCCGAAGCGCACGCGGACCTCGTTCACGGCGGAGCAGCTGTACCGGCTGGAGCTC      360
ua1031        GACCGGC-------------------------------------------------------      307
              *******

Wildtype      GAGTTCCAGCGTTGTCAGTATGTGGTCGGCCGAGAGCGCACGGAGCTCGCCAGACAGCTC      420
ua1031        -------------------------------CGAGAGCGCACGGAGCTCGCCAGACAGCTC      337
                                             ****************************

Wildtype      AATCTCTCTGAGACACAGGTGAAAGTGTGGTTTCAAAACCGCCGCACCAAACAGAAGAAG      480
ua1031        AATCTCTCTGAGACACAGGTGAAAGTGTGGTTTCAAAACCGCCGCACCAAACAGAAGAAG      397
              ************************************************************

Wildtype      GACCAGACCAAGGACACAGACAAGCGCTCATCATCCACCTCCGAATCCCTCGCCACATGC      540
ua1031        GACCAGACCAAGGACACAGACAAGCGCTCATCATCCACCTCCGAATCCCTCGCCACATGC      457
              ************************************************************

Wildtype      AACATCCTGCGTCTCCTGGAGCAGGGGCGTCTCCTGTCGGTACCCGCGCCTCCTCCAAAC      600
ua1031        AACATCCTGCGTCTCCTGGAGCAGGGGCGTCTCCTGTCGGTACCCGCGCCTCCTCCAAAC      517
              ************************************************************

Wildtype      CCACTGCTGGCGCACCCACATCCAGGCAACGGCTCTCTGCTGGGCAGCCCGTCTGTGTCC      660
ua1031        CCACTGCTGGCGCACCCACATCCAGGCAACGGCTCTCTGCTGGGCAGCCCGTCTGTGTCC      577
              ************************************************************

Wildtype      ACCTCCTCTGGGGTGAGTAGCTCCACCACACCTCCCGGAGCTGGCAGCGGGACGTTCGGA      720
ua1031        ACCTCCTCTGGGGTGAGTAGCTCCACCACACCTCCCGGAGCTGGCAGCGGGACGTTCGGA      637
              ************************************************************

Wildtype      CTGTCGCTGTCTTCTTTAAGTGGCACTCCACCTTCACCGCGGCTGGGCGTCCCGCCGCCG      780
ua1031        CTGTCGCTGTCTTCTTTAAGTGGCACTCCACCTTCACCGCGGCTGGGCGTCCCGCCGCCG      697
              ************************************************************

Wildtype      TCCCTTTGCTTTACCATGCCTCTCCTGAGCGGCGCACATCACGAACTGCCATCGGGATAC      840
ua1031        TCCCTTTGCTTTACCATGCCTCTCCTGAGCGGCGCACATCACGAACTGCCATCGGGATAC      757
              ************************************************************

Wildtype      GGCTGCGGGACGTCAGCGTTCGAGCCCTACATGAGGATAGAGCGCAAGGATGGAGAGTTA      900
ua1031        GGCTGCGGGACGTCAGCGTTCGAGCCCTACATGAGGATAGAGCGCAAGGATGGAGAGTTA      817
              ************************************************************

Wildtype      GGAGGGAAGAAGACGGTGTCCTAA  924
ua1031        GGAGGGAAGAAGACGGTGTCCTAA  841
              ************************
```

Figure 4.2: Alignment of zebrafish *vax2*^{1031} coding sequence with wildtype *vax2*. The *vax2*^{1031} allele containing an 83-basepair deletion in exon 2 was generated via CRISPR-Cas9 mutagenesis, resulting in the loss of +311 to +393. Alignments were generated using ClustaslOmega pair-wise alignment tool. Black asterisk indicates nucleotide sequences that do not differ between the two sequences.

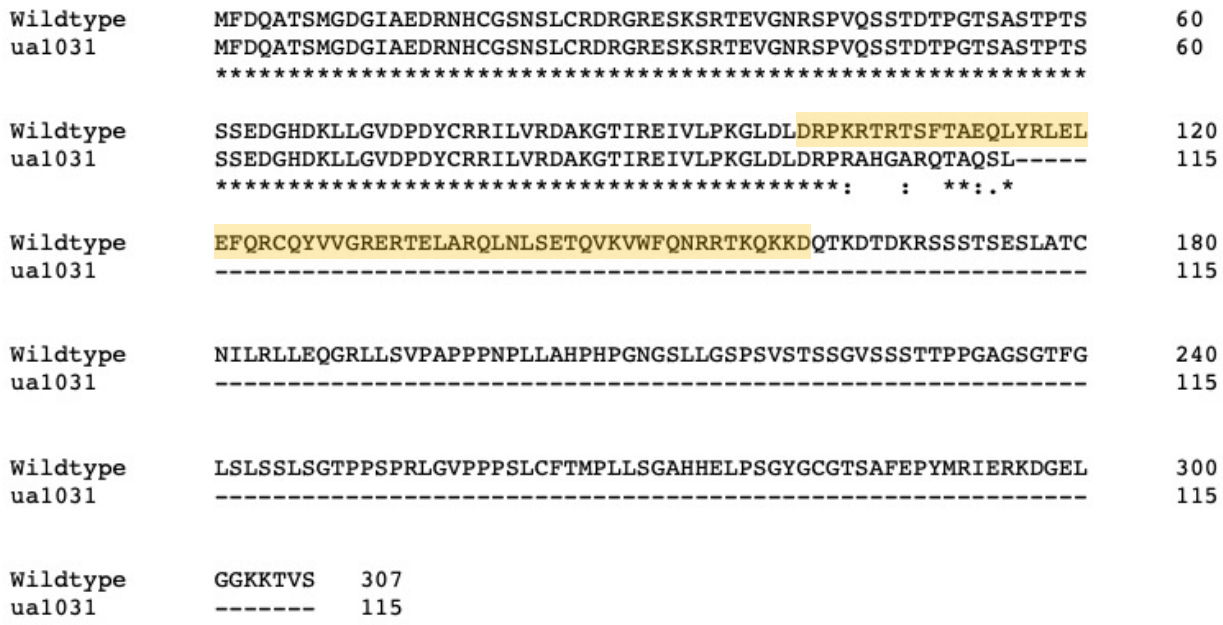

Figure 4.3: Alignment of wildtype zebrafish Vax2 mutant protein sequence with the truncated Vax2 encoded by *vax2*^{1031}. The mutation generated and shown in Fig. 4.2 results in p.Lys104ArgfsX11 protein sequence change, in which a frameshift mutation at residue 104 results in a short 11 residue polypeptide and a premature STOP codon, thus truncating the protein to 115 amino acids and disrupting the translation of the homeobox region. The homeodomain region present in the wildtype protein sequence is highlighted in yellow. Alignments were generated using ClustalOmega pair-wise alignment tool. Black asterisk indicates amino acid residues that do not differ between the two sequences.

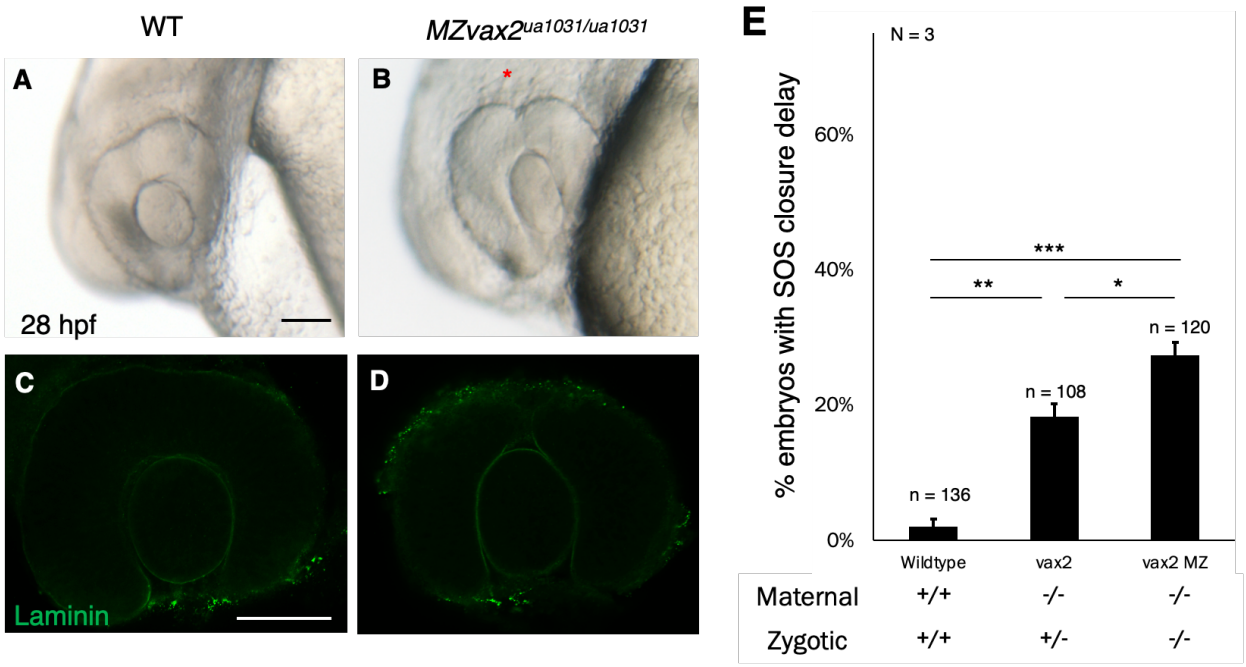

Figure 4.4: Maternal zygotic *vax2*$^{1031/1031}$ mutants display SOS closure delay. (A-B) Stereomicroscope images of wildtype and MZ*vax2*$^{1031/1031}$ mutants at 28 hpf. Embryos were anaesthetized and live-imaged on agarose-coated plates. Red asterisk indicates SOS closure delay phenotype. (C-D) Immunostaining of alpha-Laminin, a basement membrane protein, in wildtype and MZ*vax2*$^{1031/1031}$ mutants at 28 hpf. Embryos were deyolked, and the eyes were dissected and mounted laterally prior to imaging via confocal microscopy. Embryos were used for genomic DNA extraction and genotyped. (E) Quantification of the proportion of embryos showing SOS closure delay according to genotype as indicated. N = 3 experiments. Data are means ± SEM. Statistics is a two-tailed t test: * P<0.05, ** P<0.01, *** P<0.001. Scale bars are 50 μm.

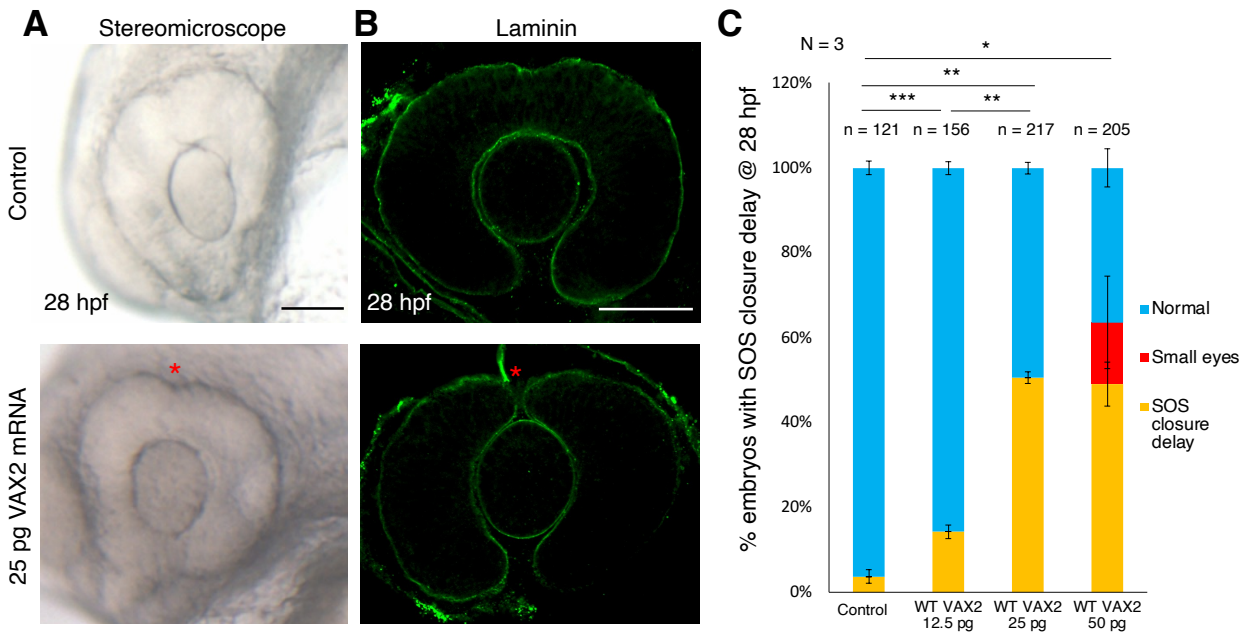

Figure 4.5: Overexpression of human wildtype *VAX2* leads to SOS closure delay in zebrafish embryos. (A) Stereomicroscope images of 28 hpf zebrafish embryos injected at the one-cell stage with 25 pg of *gfp* (control) and hs wildtype *VAX2* mRNA, respectively. Embryos were anaesthetized and live-imaged on agarose-coated plates. Red asterisk indicates SOS closure delay phenotype. (B) Immunostaining of alpha-Laminin in control group and hs wildtype *VAX2* overexpression group, respectively. Embryos were fixed at 28 hpf, immunostained, and deyolked. The eyes were dissected and mounted laterally prior to imaging via confocal microscopy. Red asterisk indicates SOS closure delay phenotype. (C) Quantification of the proportion of embryos showing SOS closure delay and microphthalmia according to dosage injected as indicated. N = 3 experiments. Data are means ± SEM. Statistics is a one-way ANOVA with Tukey's test: * $P<0.05$, ** $P<0.01$, *** $P<0.001$. Scale bars are 50 µm.

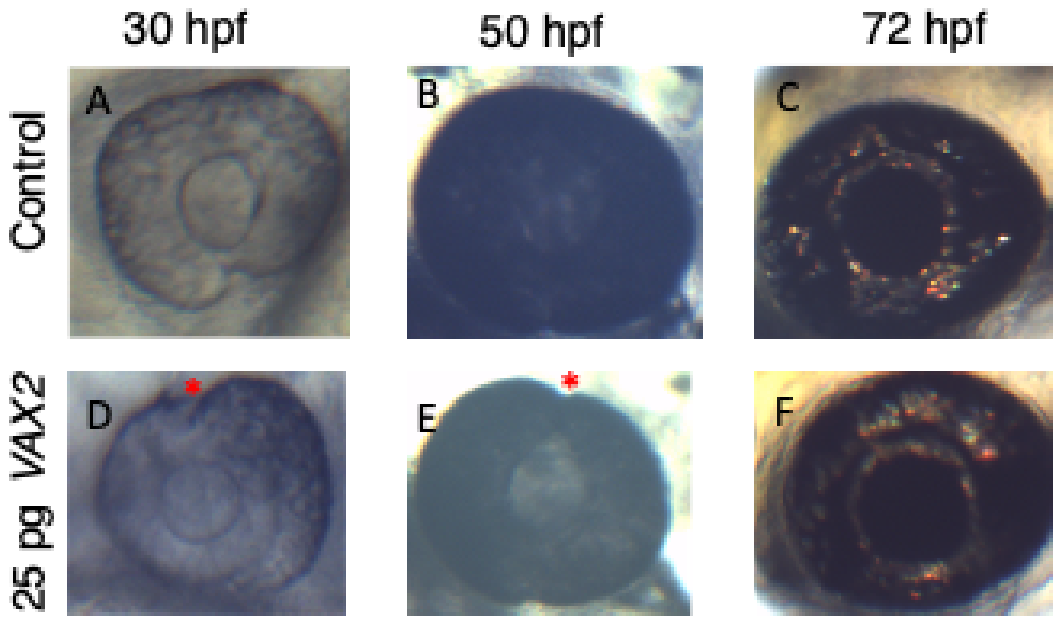

Figure 4.6: *VAX2* overexpression-induced SOS closure delay persists until 50 hpf. (A-F) Embryos were injected with 25 pg *gfp* (control) mRNA (A-C) or 25 pg hs wildtype *VAX2* mRNA mRNA (D-F) and imaged at 30 hpf, 50 hpf, and 72 hpf to observe changes to the SOS closure delay phenotype. Embryos were live-imaged on agarose-coated Petri dishes. Representative images are shown. Red asterisk indicates SOS closure delay phenotype.

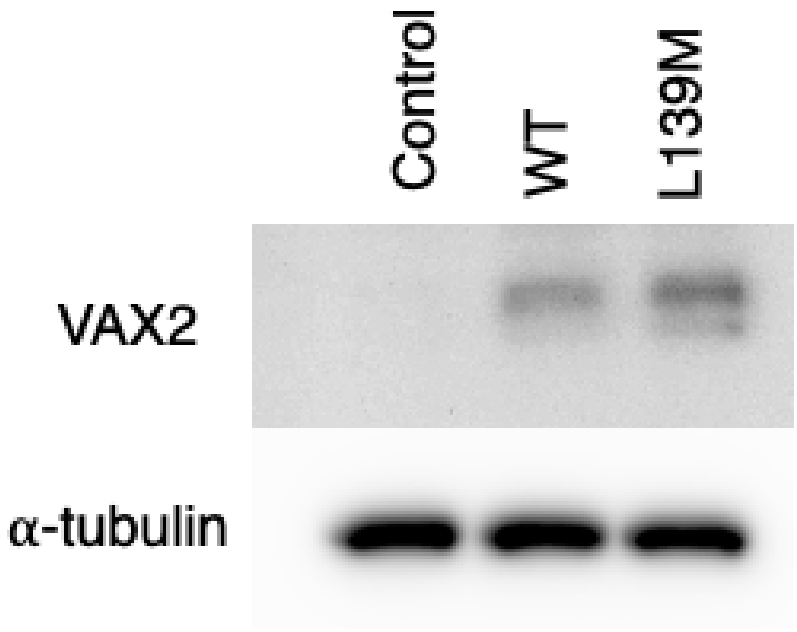

Figure 4.7: Injected human *VAX2* mRNA is translated to protein in zebrafish embryos. Western blot analysis was performed using anti-VAX2 antibody to detect the presence of translated VAX2 in zebrafish embryos following injection of 200 pg *VAX2* mRNA at the one-cell stage. 50 embryos were collected at 70% epiboly for preparation of cell lysates. Anti-alpha-tubulin antibody was used as a loading control.

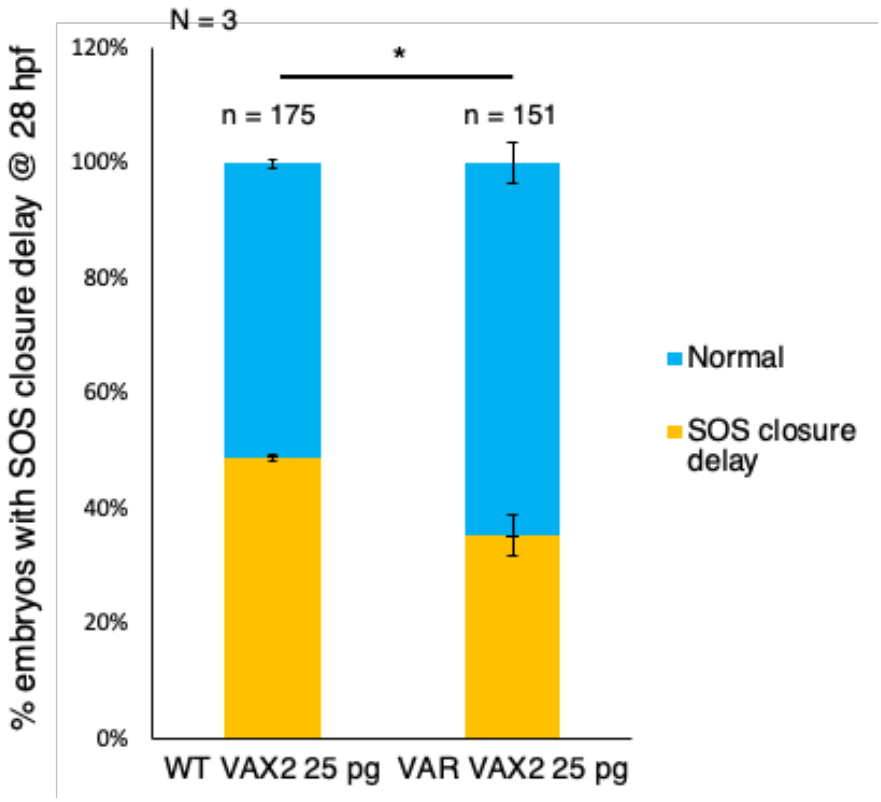

Figure 4.8: Patient variant, p.Leu139Met, leads to reduction in SOS closure delay compared to wildtype *VAX2* injection. Embryos were injected with 25 pg hs wildtype and patient variant *VAX2* mRNA, respectively, at the one-cell stage, raised to 28 hpf, and observed for SOS closure delay phenotypes under the stereomicroscope. Variant *VAX2*-injected embryos exhibited lower prevalence of SOS closure delay (wildtype, 48.9%; variant 35.4%). N = 3 experiments. Data are means ± SEM. Statistics is a two-tailed t test: * $P<0.05$.

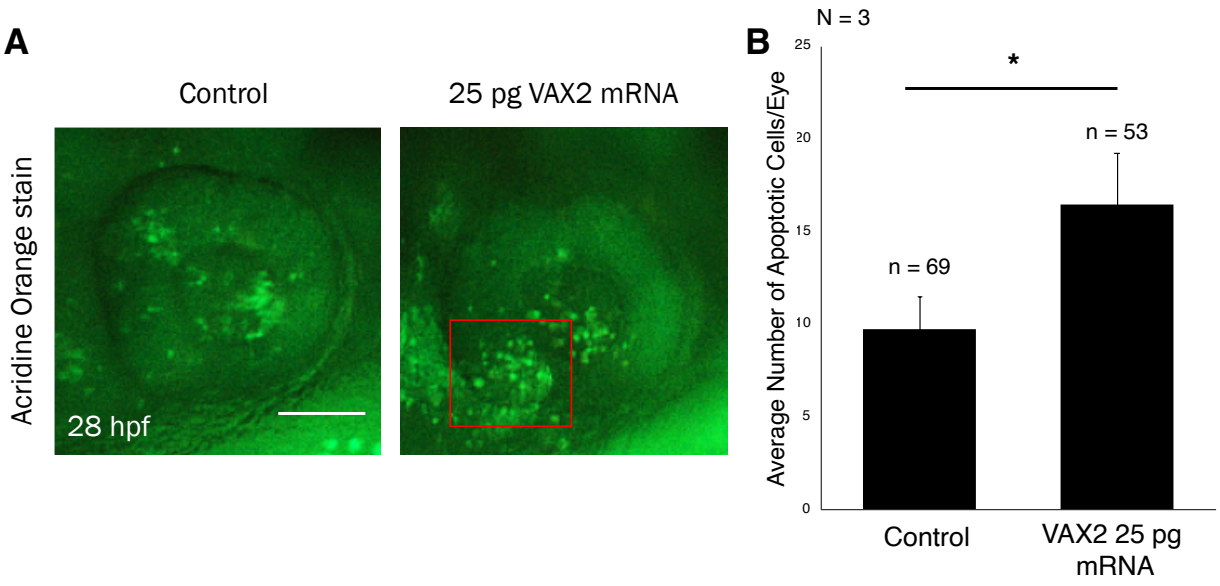

Figure 4.9: *VAX2* overexpression leads to increased apoptosis. (A) Live, 27 hpf embryos were treated with 10 µg/mL of acridine orange for 1 hour at 28.5°C and examined at 28 hpf under a fluorescence stereomicroscope. Green puncta represent apoptotic cells as stained by acridine orange (AO). Red square show clustering of apoptotic cells in the ventral-nasal quadrant of the eye. (B) Quantification of apoptotic cells observed after AO staining. N = 3 experiments. Data are means ± SEM. Statistics is a two-tailed t test: * $P<0.05$.

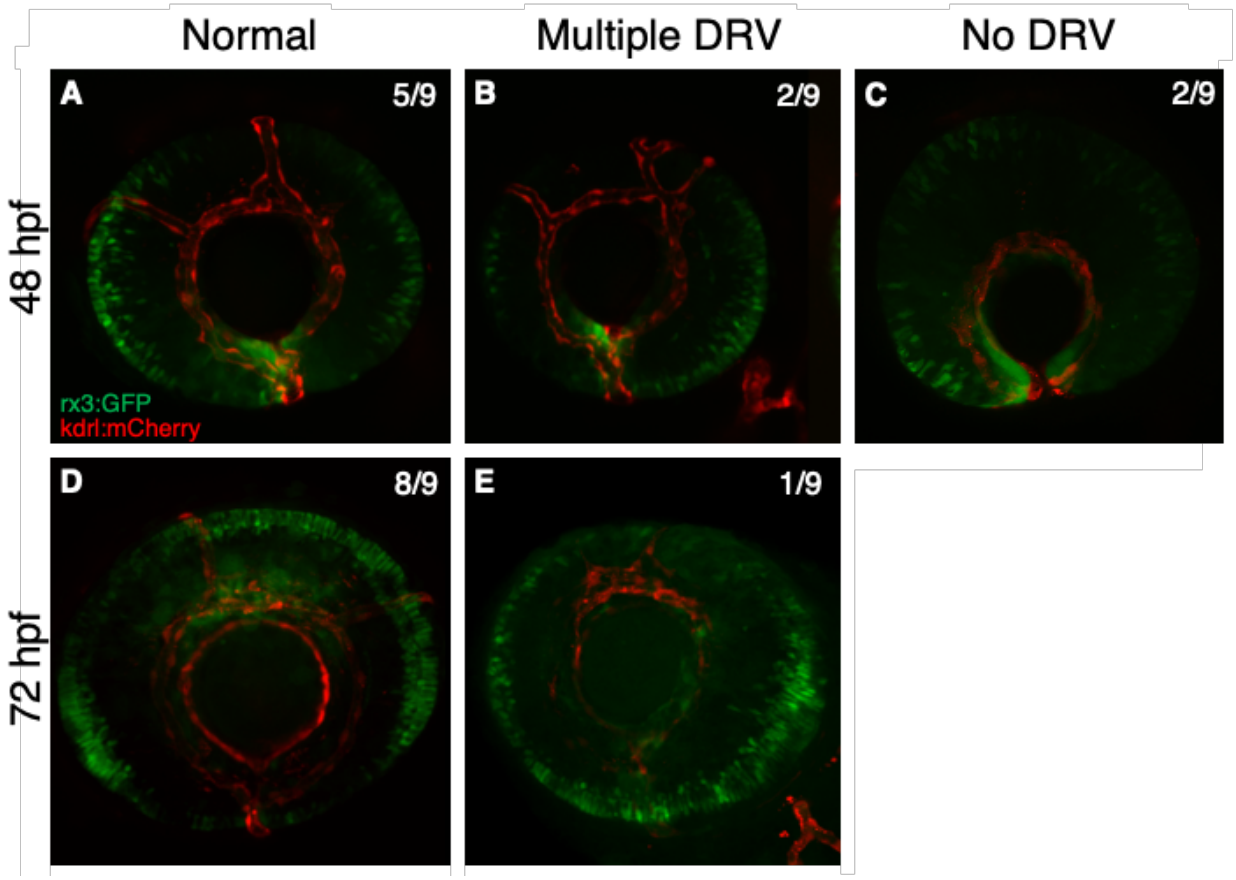

Figure 4.10: Vasculature phenotypes observed in human wildtype *VAX2* mRNA-injected embryos. (A-E) *rx3:gfp;kdrl:mCherry* embryos were injected at the one-cell stage with 25 pg of hs wildtype *VAX2* mRNA, raised in E3 media, and imaged at 48 hpf (A-C) and 72 hpf (D-E) using confocal microscopy. Phenotypes were categorized as Normal (1 DRV; A,D), Multiple DRV (B,E), or No DRV (C). Prevalence of each phenotype is indicated above.

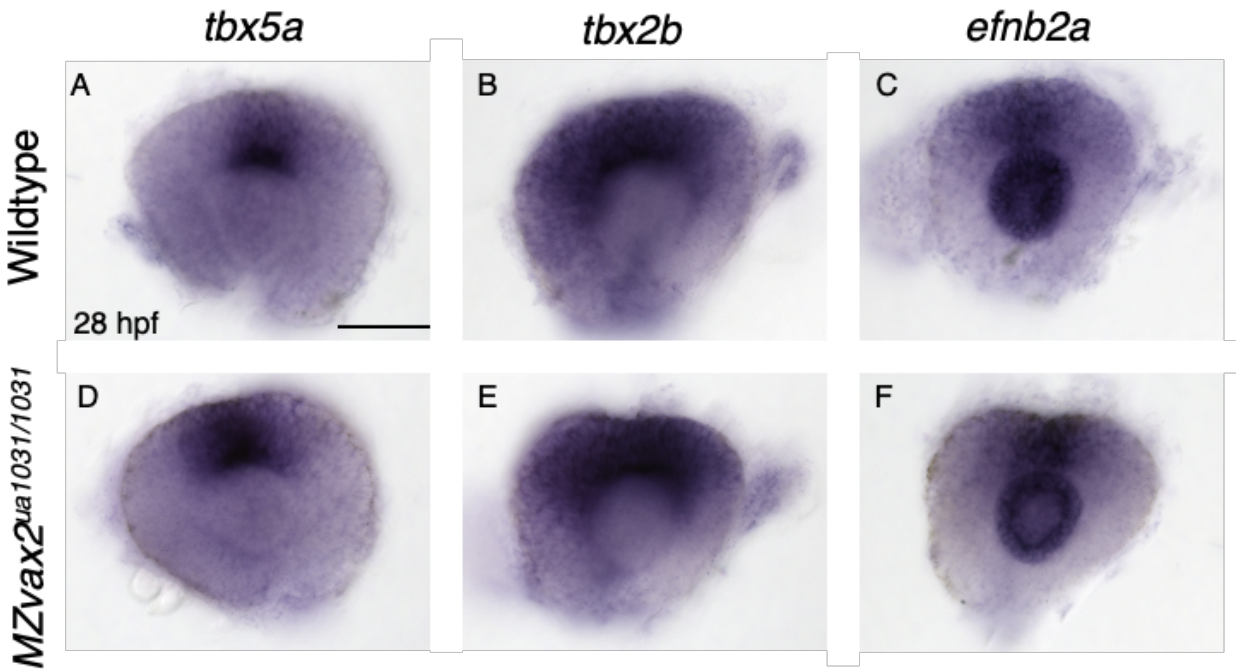

Figure 4.11: Maternal zygotic *vax2*$^{1031/1031}$ mutants display altered expression domain of *tbx5a*, a dorsal marker gene. (A-F) DIC images of dissected and laterally mounted eyes, showing gene expression pattern of dorsal eye markers, *tbx5a*, *tbx2b*, and *efnb2a*. Wholemount *in situ* hybridization was performed for dorsal eye markers in wildtype (A-C) and *MZvax2*$^{1031/1031}$ mutant embryos (D-F) at 28 hpf. Embryos were deyolked and dissected, and the eyes were mounted laterally to be imaged. Embryos were used for genomic DNA extraction and genotyped. Representative images are shown (n = 30 for each probe).

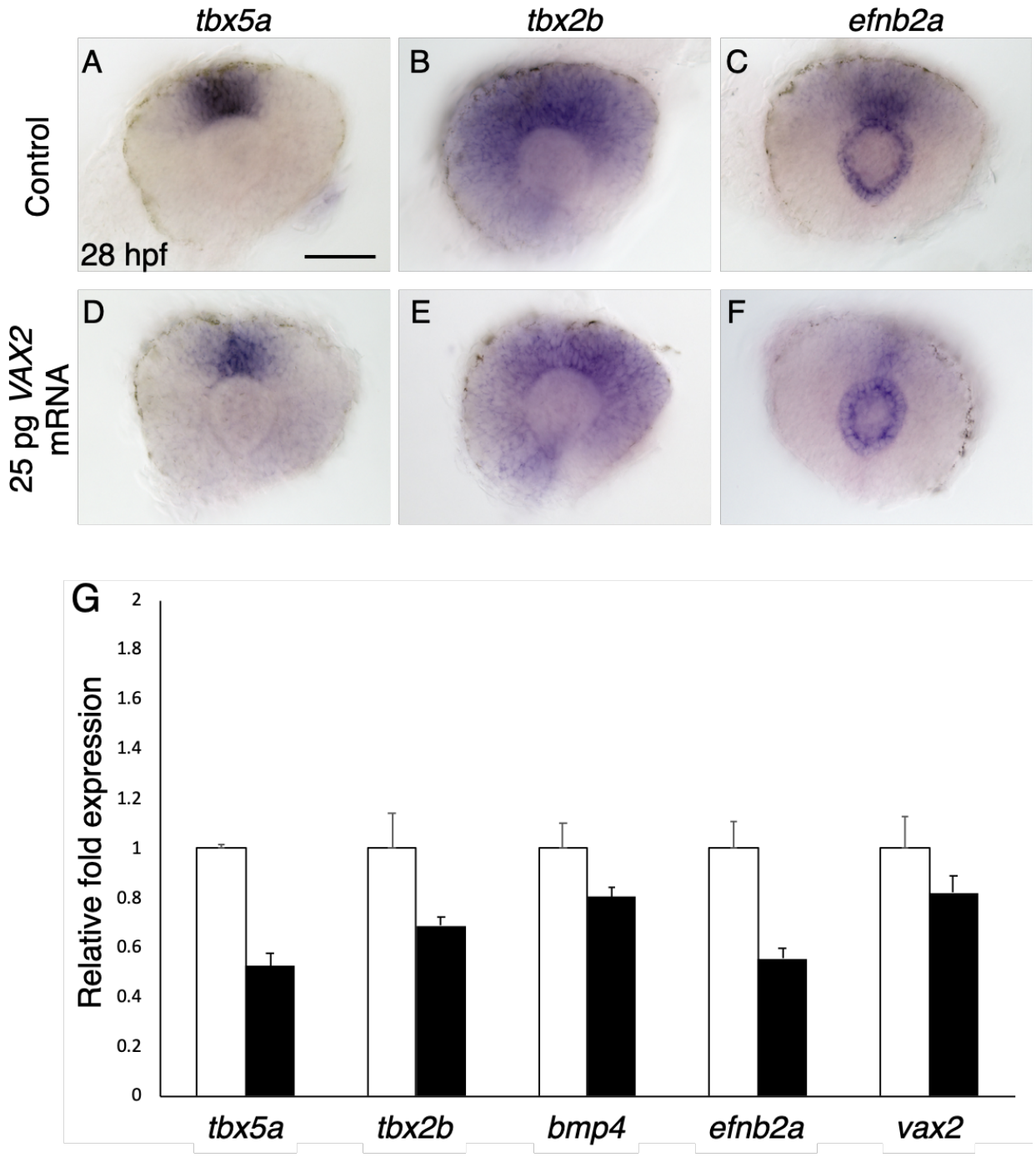

Figure 4.12: Overexpression of *VAX2* leads to reduced expression of dorsal eye markers. (A-F) DIC images of dissected and laterally mounted eyes, showing gene expression pattern of dorsal eye markers, *tbx5a*, *tbx2b*, and *efnb2a*, at 28 hpf. Wholemount *in situ* hybridization was performed for dorsal eye markers in control (A-C) and hs wildtype *VAX2* mRNA-injected embryos (D-F). Embryos were deyolked and dissected, and the eyes were mounted laterally to be imaged.

Representative images are shown (n = 30 for each probe). (G) Quantitative real-time PCR (qPCR) analysis of gene expression changes in hs wildtype *VAX2* mRNA-injected embryos (black bars) compared to wildtype (white bars). 60 embryos were pooled into each group for total RNA extraction, cDNA synthesis, and qPCR analysis. All cDNA samples were run in triplicate, and each experiment was repeated three times (N = 3). The Ct value data were analyzed using the comparative Ct method ($2^{-\Delta\Delta Ct}$). Primers were validated with a 2-fold dilution series. Data are means ± SEM.

Chapter 5

Investigation of *TSC2*, an inhibitor of mTOR signaling, in SOS closure

5.1. Introduction

Mammalian/mechanistic target of rapamycin (mTOR) is a protein serine/threonine kinase that is conserved throughout evolution and plays a crucial role in the regulation of cell growth, proliferation, and survival (Wang & Proud, 2011; Khor et al., 2016; Betz & Hall, 2013). The mTOR protein functions via two discrete multi-protein complexes called mTORC1 and mTORC2. mTORC1 is composed of mTOR, Raptor, and mLST8, and regulates cell growth via control of protein anabolism, nucleotide biosynthesis, lipogenesis, glycolysis, and autophagy (Betz & Hall, 2013; Averous & Proud, 2006; Ma & Blenis, 2009; Ben-Sahra et al., 2013; Robitaille et al., 2013; Laplante & Sabatini, 2009; Hosokawa et al., 2009). Conversely, mTORC2 is composed of mTOR, Rictor, SIN1, and mLST8, and regulates cell growth via regulation of lipogenesis, glucose metabolism, actin cytoskeleton, and apoptosis (Betz & Hall, 2013; Garcia-Martinez & Alessi, 2008; Hagiwara et al., 2012; Cybulski & Hall, 2009; Datta et al., 1997).

The mTOR signaling pathway is negatively regulated by *TSC complex subunit 1* (*TSC1)* and *TSC2*. TSC1 and TSC2 form a complex that dephosphorylate RHEB-GTP, a key upstream activator of mTORC1, and they control unchecked cell growth and proliferation (Dibble et al., 2012). However, TSC1 and TSC2 cannot function alone, and thus, a mutation in either *TSC1* or *TSC2* results in constitutive activation of mTORC1, leading to tuberous sclerosis complex (TSC), a rare genetic disease that results in benign tumour growth (Laplante & Sabatini, 2009). While TSC often presents as hamartomatous lesions in multiple organs, interestingly, it has been noted in previous case studies that some patients presenting with TSC also have an "atypical" coloboma of the iris, which is described as a coloboma that deviates from its inferior, 6 o'clock position in the eye (Huang and Manning, 2008; De Waele et al., 2015; Curatolo, 2015; Rowley et al. 2001; Williams & Taylor, 1985; Eagle et al., 2000).

Investigation of the genetic variations present in a superior coloboma patient from Edmonton, Alberta, revealed a variant allele of *TSC2*, an important regulator of cell proliferation and apoptosis. To study its possible role in superior ocular sulcus (SOS) formation and closure, a translation-blocking morpholino oligonucleotide was used to knockdown *tsc2* in early zebrafish development. Knockdown of *tsc2* was shown to result in SOS closure delay, revealing a possible role for *tsc2* in regulation of SOS closure. In addition, I attempted to rescue the phenotypes caused

by *tsc2* loss through the use of rapamycin, a pharmacological inhibitor of mTOR signaling. This study reveals a possible role for mTOR signaling in the regulation of SOS closure, thus suggesting a mechanism of SOS regulation that is independent of DV eye axis patterning that had been previously investigated (Chapters 3 and 4).

5.2. Results

5.2.1. Identification of a TSC2 variant in a superior coloboma patient

We identified a 23-year-old patient exhibiting unilateral superior coloboma in the left eye, as well as TSC (Fig. 5.1). Whole exome sequencing revealed 18,989 variants present in the patient. Within this data set, we discovered a rare variant of *TSC2* (Gene ID: 7249; OMIM: 191092; NM_001077183), a key negative regulator of mTOR signaling. Specifically, the patient was heterozygous for a nonsynonymous single-nucleotide variant (c.C5026T), resulting in the substitution of a highly conserved amino acid residue (p.Arg1676Trp) within the Rap GTPase activating protein domain (Fig. 5.1). *In silico* modeling of the variant showed that this amino acid substitution is likely to create a significant change to the structure and function of TSC2 (Polyphen2 – 1; SIFT - 0). Indeed, as the patient had been diagnosed with TSC, it was highly likely that TSC2 function was severely disrupted.

5.2.2. Morpholino knockdown of tsc2 during early zebrafish development

To assess the effects of *tsc2* loss on zebrafish eye development and SOS morphology, I injected *tsc2* translation-blocking morpholino at the one-cell stage. When *tsc2* translation-blocking morpholino was injected, I observed SOS closure delay phenotypes similar to those previously observed in our studies of DV eye axis patterning genes and their effects on SOS closure (Fig. 5.2A). Injection of 4 ng *tsc2* translation-blocking morpholino resulted in a significant increase in embryos exhibiting SOS closure delay at 28 hpf (57%; n = 150/261; $P<0.00001$) compared to those injected with control morpholino (2%; n = 5/233) (Fig. 5.2B).

5.2.3. Rapamycin treatment of tsc2 morpholino-injected embryos

Next, I attempted to rescue the SOS closure delay phenotype by treating the embryos with rapamycin, an inhibitor of mTOR signaling (Ballou & Lin, 2008). I posited that the effect of *tsc2* knockdown, which results in constitutive activation of mTOR signaling, could be rescued through rapamycin exposure, which would inhibit mTOR signaling. However, when *tsc2* morpholino-injected embryos were exposed to rapamycin, I did not observe any rescue of the SOS closure delay phenotype (Fig. 5.2B).

5.3. Discussion

In this study, I conducted a phenotypic analysis of *tsc2* loss through morpholino-mediated knockdown, specifically examining its effects on SOS closure. Our investigation shows that loss of *tsc2* results in SOS closure delay, revealing a possible role for *tsc2* in eye development. While our previous studies have focused on examining the effects of DV eye axis patterning genes on SOS closure, this investigation provides evidence to suggest that mTOR signaling may play a role in the proper closure of the SOS during early eye development and that aberrant upregulation of mTOR signaling may contribute to the superior coloboma observed in TSC patients.

In addition, I performed a pharmacological analysis to rescue morpholino-induced phenotype by treating *tsc2*-morpholino-injected embryos with rapamycin. As rapamycin serves a similar role as TSC2 in inhibiting mTORC1, previous studies of *tsc2* in zebrafish have shown that rapamycin treatment is able to reverse the effects of *tsc2* loss (Khor et al., 2016; Kim et al., 2011). Therefore, I hypothesized that rapamycin treatment should allow normal SOS closure even in *tsc2* knockdown conditions. However, I did not observe any rescue with rapamycin exposure.

Previous animal model studies have focused primarily on hamartomas and tumorigenesis, and a similar focus is reflected in many clinical studies of TSC. However, there are very rare clinical descriptions of TSC patients that present with atypical coloboma. A recently-published

report describes two cases studies of TSC patients that presented with unilateral atypical iris coloboma (Bacci et al., 2021). Sanger sequencing of these patients revealed known, heterozygous, pathogenic variants of *TSC2*: c.3131+1G>A and c.3099C>G:p.Tyr1033Ter, respectively (Bacci et al., 2021). These variants are predicted introduce premature stop codons and result in the loss of various functional domains, including the GTPase activating protein domain, the location of the variant identified in our study (Bacci et al., 2021). Taken together with our findings that *tsc2* loss leads to SOS closure delay, this may suggest a possible causal role of *TSC2* variants and a particular importance of the GTPase activating protein domain in relation to superior coloboma.

While the result of our study suggests that *tsc2* loss results in SOS closure delay, it remains to be seen whether this phenotype is solely due to changes in the mTOR signaling pathway or is acting through a BMP-dependent pathway. While mTOR signaling is typically associated with cell proliferation and growth, a study by Sun et al. in 2010 found that TSC1 and TSC2 regulate *Drosophila* germline stem cell differentiation via BMP-dependent and BMP-independent pathways. However, another report by Thien et al. in 2015 investigating the role of mTOR signaling during epithelial-to-mesenchymal transition reports a lack of association between mTOR signaling and BMP signaling. While further studies are required, these findings pose an interesting question that asks whether a loss in *tsc2* leads to SOS closure delays through a mechanism that is truly independent of BMP signaling and DV eye axis patterning.

Overall, our study provides evidence that *tsc2* loss can lead to aberrant SOS closure, suggesting that mTOR signaling may be an important regulator of proper SOS closure during early eye development. While further studies are required to examine that exact mechanisms through which mTOR signaling affects SOS closure, these findings add yet another possible avenue of investigation to our current understanding of SOS formation and closure.

5.4. Figures

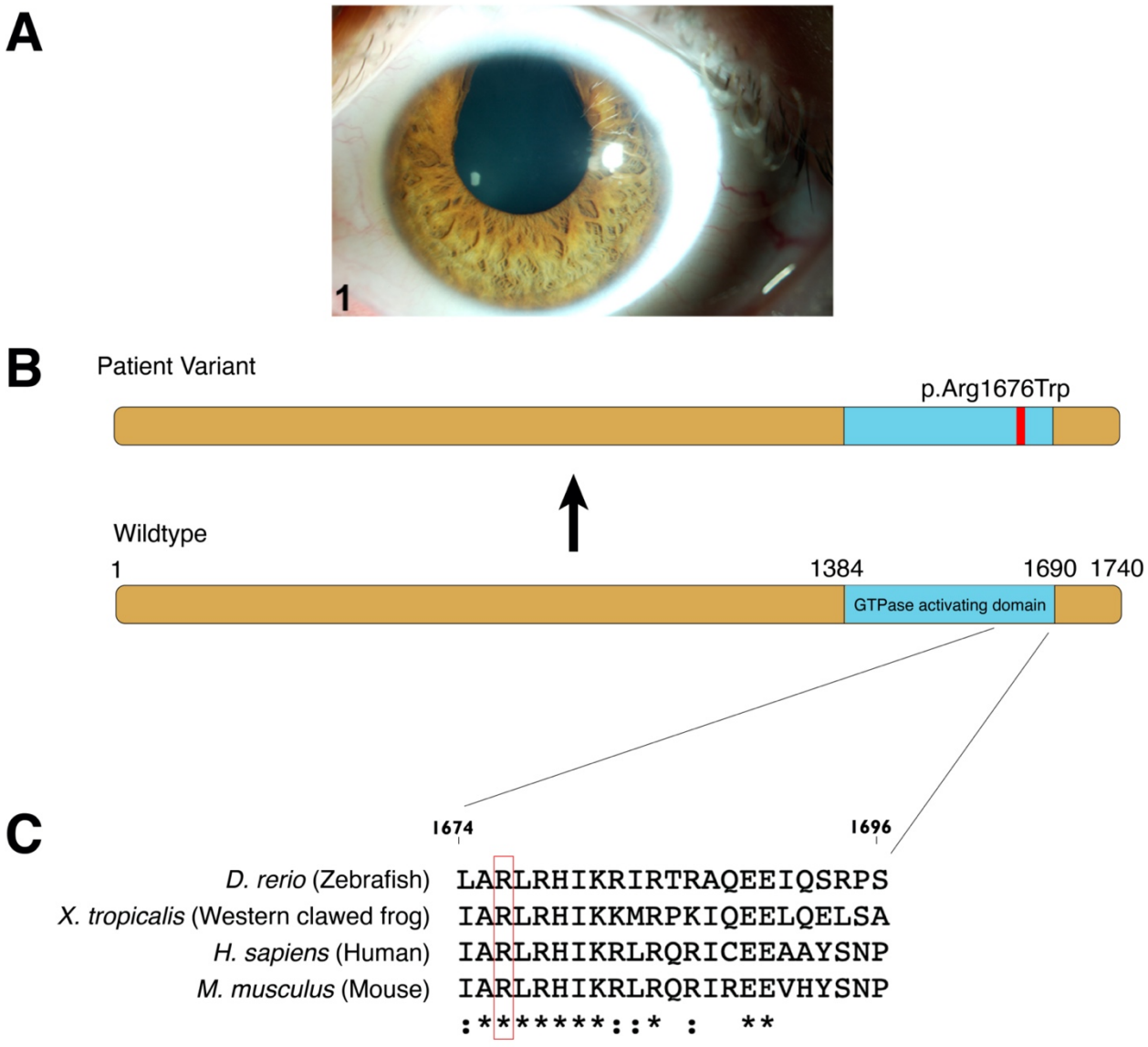

Figure 5.1: Variant of *TSC2* identified in a superior coloboma patient. (A) Unilateral superior iris coloboma presenting in Patient #1. (B) Diagram of the human TSC2 protein exhibiting the p.Arg1676Trp variant present in Patient #1. (C) Alignment illustrating the evolutionary conservation of TSC2 amino acid sequence in the GTPase activating domain surrounding the location of the altered residue. The altered residue is noted by a red box.

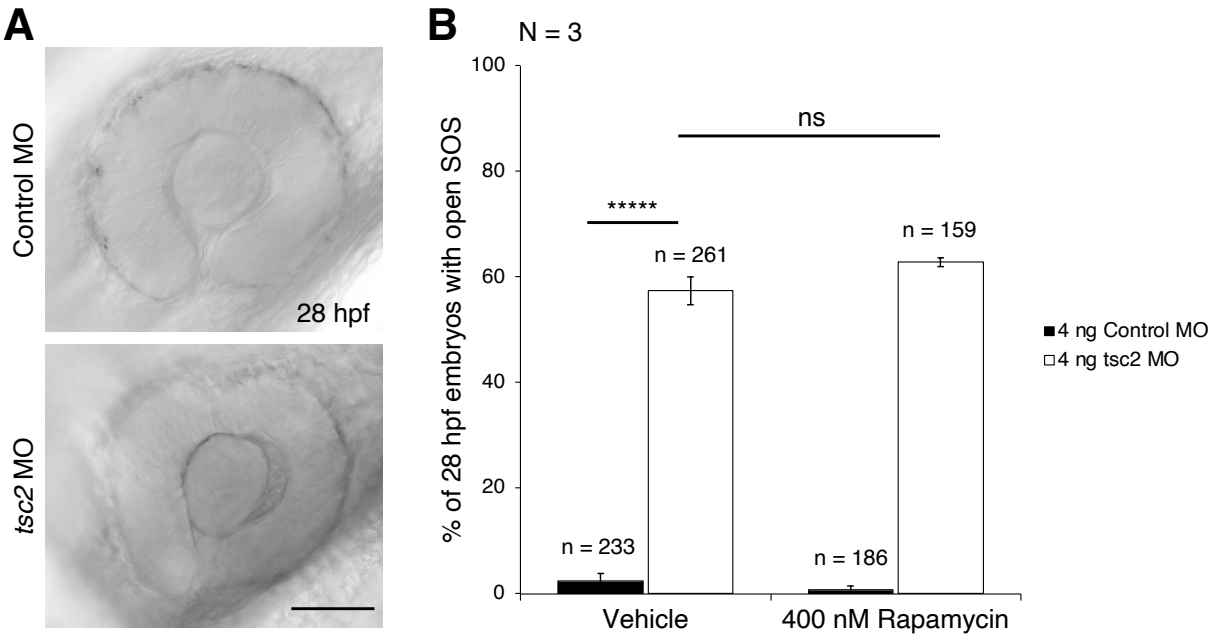

Figure 5.2: Morpholino-mediated knockdown of *tsc2* and rapamycin treatment. (A) DIC images of 28 hpf zebrafish embryos exhibiting SOS closure delay following injection of 4 ng translation-blocking *tsc2* morpholino. (B) Quantification of embryos with delayed sulcus closure and their respective experimental conditions. N = 3 expriments. n = number of embryos. Two-tailed *t* test. Data are means ± SEM. *****P<0.00001. Scale bar is 50 μm.

Chapter 6

RNA-Seq analysis of SOS closure delay models

6.1. Introduction

As discussed in previous chapters, we identified a rare, atypical coloboma phenotype affecting the superior eye, which hinted at the presence of a previously unidentified, presumptive fissure-like structure in the superior aspect of the eye during development. Subsequently, we discovered a transient structure, which we named superior ocular sulcus (SOS) in the dorsal aspect of the zebrafish eye during early eye development, specifically at the 12 o'clock position, where it is present for around three hours from 20 hours post fertilization (hpf) to 23 hpf in wildtype zebrafish larvae (Hocking et al., 2018). Similar to the choroid fissure, the SOS appears to play a role in vasculature formation during eye morphogenesis, as aberrant SOS closure results in malformations of the dorsal radial vessel in the embryonic eye (Hocking et al., 2018). While the presence of this structure, termed superior ocular sulcus (SOS), has not been confirmed in human eye development, it is highly probable that the SOS is present during human eye development as eye development in zebrafish is a highly similar process to that in humans. The established understanding of eye development does not account for this sulcus, and the factors that affect its formation and closure is not yet fully understood.

Eye morphogenesis is a complex process that requires many developmental processes, such as the formation of eye anlage, eye axis patterning, early cellular morphogenesis, and neural crest cell migration, and many of the genes involved in these processes are associated with many eye disorders (Yoon et al., 2020). Congruously, through our analysis of patient-derived exome sequencing data and the subsequent studies in zebrafish, we determined that manipulation of dorsal-ventral (DV) eye axis patterning affects SOS closure. In our initial investigation of the SOS, we discovered that loss of Bmp signaling-mediated dorsal eye identity results in the failure of the SOS to close normally (Chapter 3; Hocking et al., 2018). Additionally, we found that aberrant expression of a ventral eye marker, *vax2*, also results in blockage of proper SOS closure (Chapter 4). In addition to DV eye axis patterning, we have begun to identify additional signaling pathways that affect SOS closure – loss of Wnt/planar cell polarity (PCP) signaling or mTOR signaling also lead to abnormal SOS closure (Wilson, 2020; Chapter 5).

While the identification of these putative genetic factors involved in the etiology of superior coloboma has been promising, our reliance on patient-derived exome sequencing data has

been challenging. The exome sequencing data lack any information regarding inheritance; as each patient data set does not include any pedigree information, the variants identified may be *de novo*, singleton SNPs, making identification of candidate genes very difficult. This is further complicated by the fact that the five patients for whom we have obtained exome sequencing data do not share any variants that we have identified to affect SOS closure. While information regarding gene expression area, known gene function, and *in silico* projections of protein structure and function are used to make the best possible decision in identifying candidate genes, without any other data set with which to cross-reference, these complications place a great burden-of-proof on pilot animal model studies of candidate genes, which can be both financially costly and labour-intensive.

In this study, our main purpose is to identify additional genes and pathways of interest involved in SOS closure through transcriptomic analysis of known models of SOS closure delay. I performed RNA-Seq to identify differences in gene transcripts between the eyes of wildtype zebrafish embryos at 28 hpf and those that show SOS closure delay through DMH-1 treatment or human *VAX2* mRNA overexpression. Through this analysis, I discovered changes to genes known to be involved in eye development, and gene ontology (GO) analysis revealed that the greatest number of genes found to have differential gene expression were involved in protein synthesis, cell differentiation, and genetic information processing. The data presented in this chapter is a representation of the genetic changes that occur in correlation with SOS closure delay, and it will be a useful dataset through which our previous datasets can be cross-referenced to identify more candidate genes involved in SOS formation and closure.

6.2. Results

6.2.1. RNA-Seq analysis of 28 hpf embryos with improper SOS closure

I conducted RNA-Seq of established SOS closure delay models discussed previously throughout this thesis: DMH-1-treated embryos (eyes only) and human wildtype VAX2 mRNA-injected embryos (whole head anterior to the eye) at 28 hpf.

Compared to wildtype embryos, embryos treated with DMH-1 showed 60 genes that were upregulated by at least 2-fold, whereas 75 genes were downregulated by 2-fold (Table 6.1). I identified genes previously identified to be involved in eye development and studied in zebrafish, such as *sec13* (Schmidt et al., 2013), *scinla* (Jia et al., 2007), *stra6* (Casey et al., 2014), and *ruvbl2* (Zhao et al., 2013). In addition, I identified orthologs of genes that have been associated with eye disease, but not yet investigated in zebrafish, such as *nkap* (Fiordaliso et al., 2019), *prpf4* (Chen et al., 2014), *ift88* (Chekuri et al., 2018), and *ncapg2* (Kahn et al., 2019).

Comparatively, *VAX2* overexpression led to upregulation of 80 genes by at least 2-fold, while 94 genes were downregulated by 2-fold (Table 6.2). In addition to those genes previously identified to be involved in eye development and studied in zebrafish, such as *tbx5a*, *aldh1a2*, *sec13* (Schmidt et al., 2013), *fbxw11b* (Holt et al., 2019), *smad9* (Wei et al., 2014) and *scinla* (Jia et al., 2007), I identified orthologs of genes that have been associated with eye diseases, but not yet investigated in zebrafish, such as *epha2a* (Harding et al., 2021), *epha4l* (Rothe et al., 2017), *ephb3b* (Fu & Sretavan, 2012), *ift88* (Chekuri et al., 2018), *aifm1* (Bogdanova-Mihaylova et al., 2019), and *pmp22a* (Brandt et al., 2016).

6.2.2. GO analysis of genes with differential expression following DMH-1 treatment

Gene ontology (GO) analysis can be further categorized into three root categories: biological process (BP), cellular component (CC), and molecular function (MF). Through GO analysis of embryos following DMH-1 treatment, I found that the greatest number of differentially-expressed genes in terms of BP involved were translation (10/98), peptide biosynthesis (10/98),

and DNA repair (7/98) (Table 6.3). Accordingly, examination of the GO analysis through CC terms revealed that many of the genes with differential expression were compartmentalized in various parts of the nucleus (nucleolus (8/91), nuclear chromosome (6/91), nucleoplasm (5/91)), and the ribosome (6/91) (Table 6.4). Appropriately, in terms of MF, the greatest number of genes were categorized as being involved in acting as structural constituents of ribosomes (5/93), guanyl-nucleotide exchange factor activity (5/93), and performing catalytic activity related to DNA (4/93) (Table 6.5). Furthermore, annotation of the RNA-Seq data according KEGG (Kyoto Encyclopedia of Genes and Genomes) BRITE terms demonstrates that 138 genes identified through RNA-Seq are involved in genetic information processing, and 53 genes are involved in signaling and cellular processes (Fig. 6.1).

6.2.3. GO analysis of genes with differential expression following VAX2 overexpression

GO analysis using BP classification terms revealed that, following *VAX2* overexpression, the greatest number of differentially-expressed genes were involved in cell cycle regulation (9/131), cell differentiation regulation (8/131), enzyme-linked receptor protein signaling pathways (8/131), and regionalization (7/131) (Table 6.6). Similarly to DMH-1 treatment, *VAX2* overexpression led to the greatest number of genes categorized in CC terms of nucleus (nucleolus (7/128) nucleoplasm (6/128), nuclear chromosome (5/128)), as well as mitochondria (7/128) and synapse (5/128) (Table 6.7). Perhaps due to VAX2 being a transcription factor, in terms of MF, greatest number of genes were categorized as being involved in RNA polymerase II regulatory region sequence-specific DNA binding (9/127), protein dimerization activity (7/127), and cofactor binding (6/127) (Table 6.8). Classification of the RNA-Seq data according to KEGG BRITE annotations reveals that 188 genes identified through RNA-Seq following *VAX2* overexpression are involved in genetic information processing, while 48 genes are involved in signaling and cellular processes, and 41 genes are involved in metabolism. In addition, categorization of the data using KEGG pathway annotations according to environmental information processing show that 85 genes identified through RNA-Seq are involved in signal transduction (Fig. 6.2).

6.3. Discussion

Through our RNA-Seq analysis of our established SOS closure delay models, I aimed to examine the differential gene expression that correlate with SOS closure delay and expand our understanding of the genetic factors involved in SOS closure. Our analysis revealed expected changes to gene expression of genes known to be involved in DV eye axis patterning (i.e. *tbx5a* – downregulated via *VAX2* overexpression) and eye regionalization (i.e. *aldh1a2* – upregulated via both), as well as many genes previously associated with eye diseases, such as *stra6* (downregulated via DMH-1 treatment), which has been previously associated with MAC disorders (Casey et al., 2014).

Our previous studies indicate that proper SOS closure is required for development of superficial ocular vasculature. In accordance with this, I found that *VAX2* overexpression led to downregulation of *foxf1*, whose orthologs have been associated with angiogenesis in various developing organs, including the eye (Ren et al., 2014). In addition, I found DMH-1 treatment led to downregulation of *ptgs2b*, which is a component of the VEGF signaling pathway (Schultz et al., 2017). This provides further evidence to suggest that dysregulation of SOS closure leads to changes that affect vasculogenesis during eye development.

Interestingly, I discovered that the expression of an ortholog of *OTUD5*, *otud5b*, was upregulated by over 4-fold with overexpression of *VAX2*. *OTUD5* is a positive regulator of mTORC1 and mTORC2 (Cho et al., 2021). In addition, I found that the expression of *tsc1b*, a co-regulator of mTORC1 alongside *tsc2*, was decreased more than 2-fold. As discussed in Chapter 5, I have previously observed that aberrant upregulation of mTORC1 via *tsc2* knockdown leads to SOS closure delay. While there have been no direct associations previously established between *VAX2* and mTOR signaling, these findings suggest that there may be an overlap in mechanism through which *VAX2* overexpression and *tsc2* knockdown each leads to SOS closure delay. Even if *VAX2* does not directly regulate mTOR signaling, it is possible that aberrant *VAX2* expression leads to cellular changes that, in turn, lead to upregulation of mTOR signaling.

I noted 25 genes that were differentially expressed in both DMH-1 treatment and *VAX2* overexpression conditions (Chi-square test, $P<0.00001$; Table 6.9, Fig. 6.3). Of particular note

was the identification of *sec13* in our dataset, being differentially expressed more than 4-fold in both DMH-1-treated embryos and *VAX2* mRNA-injected embryos. SEC13 has been previously identified to be a subunit of GATOR2, a subcomplex of GATOR, which is a critical regulator of the pathway that signals amino acid sufficiency to mTORC1 (Bar-Peled et al., 2013). GATOR inhibits mTORC1, and downregulation of GATOR should lead to upregulation of mTORC1 (Hesketh et al., 2020). Alongside the identification of *otud5b* and *tsc1b* downregulation discussed in the previous paragraph, this finding adds further evidence to suggest that there may be a prominent role for mTOR signaling in SOS formation and closure that must be investigated further.

Taken together, this RNA-Seq analysis provides us with a look at the gene expression changes that correlate with SOS closure delay. I identified that expression of genes involved in protein synthesis, cell differentiation, and genetic information processing were the most affected. Of note, I identified multiple factors of mTOR signaling that were differentially expressed, which followed similar patterns of change under both DMH-1 treatment and *VAX2* overexpression, as well as supporting the findings of Chapter 5. Furthermore, this dataset adds to our growing understanding of SOS biology, and it provides us with another criterion through which our previous datasets can be cross-referenced to identify more candidate genes involved in SOS formation and closure.

6.4. Figures

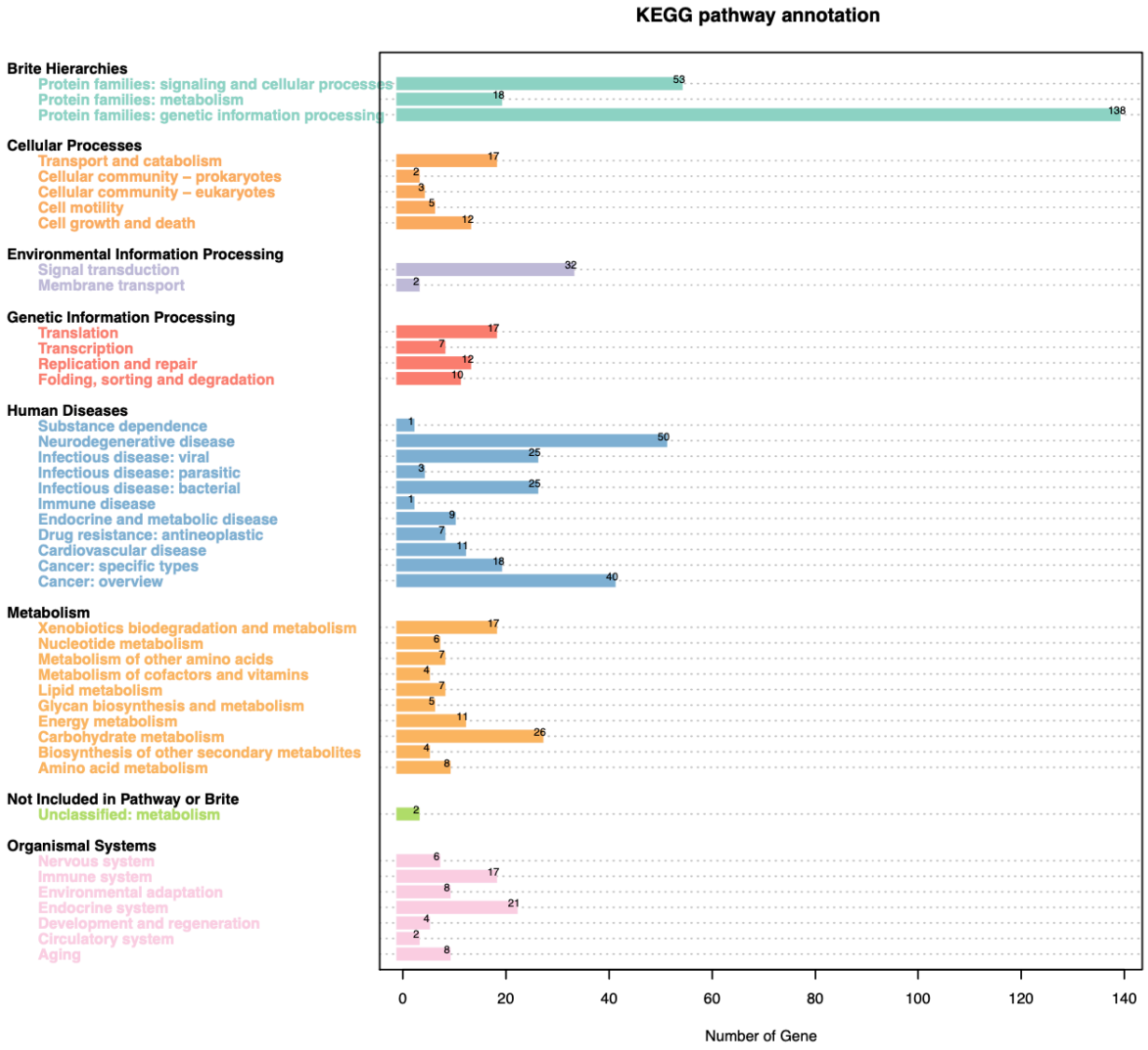

Figure 6.1: KEGG Classification of differentially-expressed genes following DMH-1 treatment. Embryos were treated with DMH-1 and eye tissue was collected at 28 hpf. RNA-Seq was performed, and the genes identified to be differentially expressed compared to that of wildtype were categorized according to KEGG pathways.

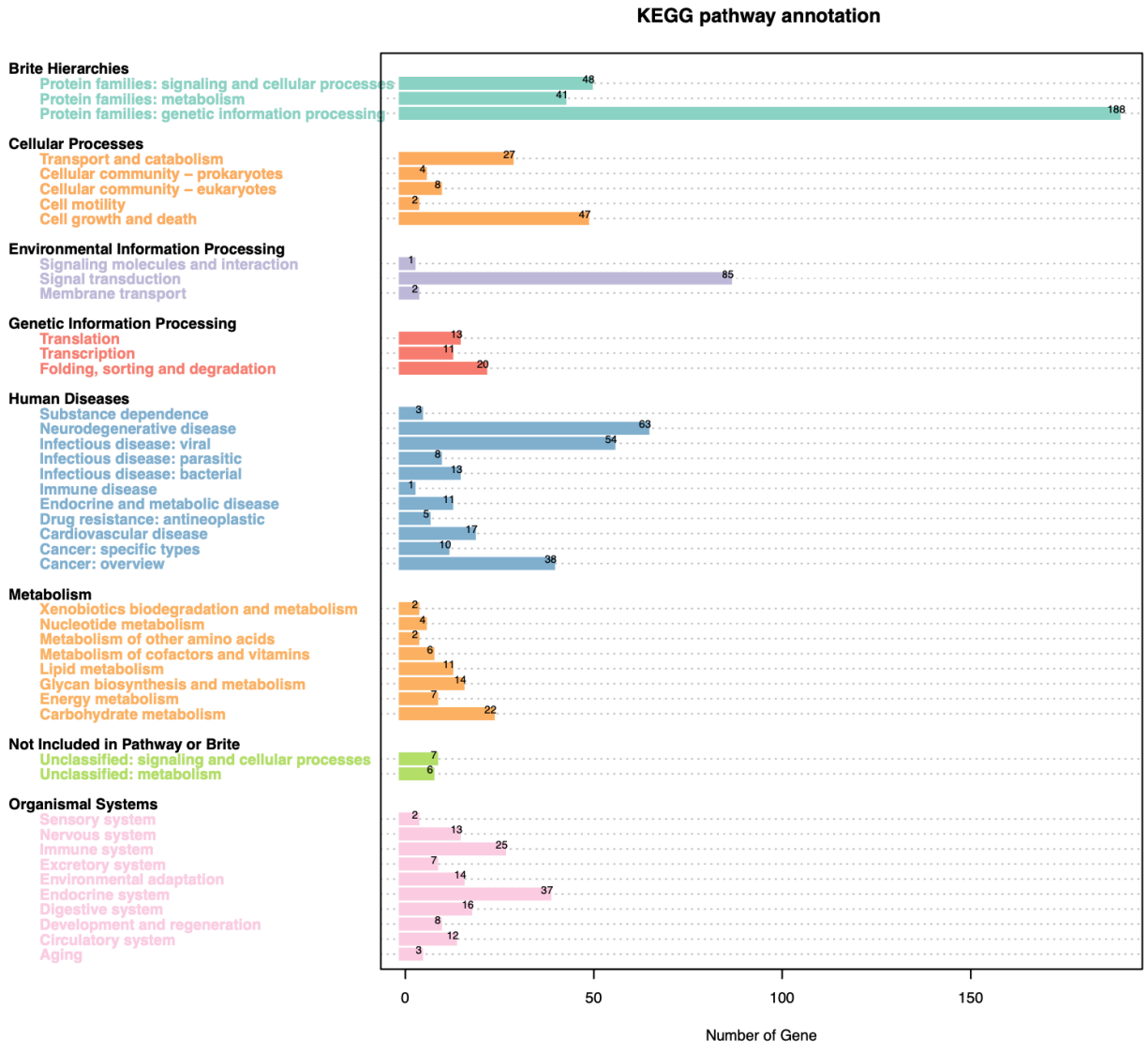

Figure 6.2: KEGG Classification of differentially-expressed genes following *VAX2* overexpression. Embryos were injected with 25 pg of human VAX2 mRNA at the one-cell stage and head tissue was collected at 28 hpf. RNA-Seq was performed, and the genes identified to be differentially expressed compared to that of wildtype were categorized according to KEGG pathways.

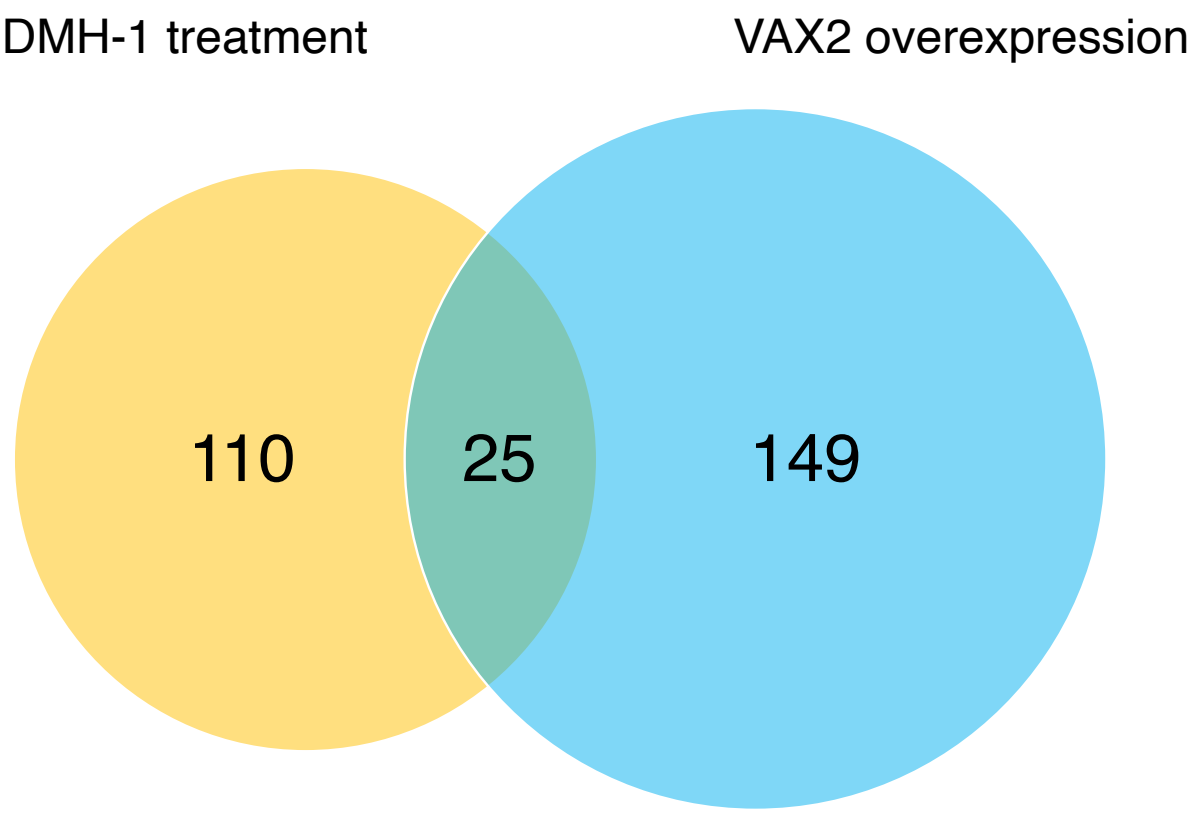

Figure 6.3: Venn diagram of RNA-seq results. Genes with at least 2-fold difference (increase or decrease) in expression from the two experimental conditions were compared, and genes present in both experimental conditions were noted. Of 135 genes with 2-fold differential expression following DMH-1 treatment and 174 genes with 2-fold differential expression following *VAX2* overexpression, 25 genes were shared. Chi-square test ($P<0.00001$) was performed to validate that observed number of shared genes were significantly different from that expected through false discovery. Table 6.9 lists the 25 genes identified in both groups.

6.5. Tables

Table 6.1: List of genes differentially-expressed by at least 2-fold in the eye at 28 hpf following DMH-1 treatment.

Genes	logFoldChange	Q-Value	Regulated	COG Annotation	eggNOG Annotation
gar1	2.43942246874098	8.56417632717653e-23	up	Translation, ribosomal structure and biogenesis	Required for ribosome biogenesis. Part of a complex which catalyzes pseudouridylation of rRNA. This involves the isomerization of uridine such that the ribose is subsequently attached to C5, instead of the normal N1
sec13	2.34187184225564	1.54496549032262e-17	up	Function unknown	DDE superfamily endonuclease
etf1b	2.29997957963006	1.62877663103278e-21	up	Translation, ribosomal structure and biogenesis	translation release factor activity
plk1	2.24980922279183	1.95964085671218e-20	up	Cell cycle control, cell division, chromosome partitioning	polar body extrusion after meiotic divisions
ndufa12	2.14211983246417	6.04768313470854e-15	up	Energy production and conversion	Accessory subunit of the mitochondrial membrane respiratory chain NADH dehydrogenase (Complex I), that is believed not to be involved in catalysis. Complex I functions in the transfer of electrons from NADH to the respiratory chain. The immediate electron acceptor for the enzyme is believed to be ubiquinone
mrpl18	2.10101650001506	2.4182635854967e-16	up	Translation, ribosomal structure and biogenesis	ribosomal protein L18
kat8	2.00533534201048	5.87254167569792e-13	up	Chromatin structure and dynamics	histone acetyltransferase activity (H4-K5 specific)
nap1l4a	1.98166097399321	3.45760063205986e-13	up	-	nucleosome assembly
rps13	1.98009685353261	1.85699812520845e-17	up	Translation, ribosomal structure and biogenesis	small ribosomal subunit rRNA binding
fuca2	1.864490871387	9.34331767639508e-12	up	Carbohydrate transport and metabolism	fucosidase, alpha-L- 2, plasma
noc2l	1.7561839385199	2.25483029076984e-11	up	Translation, ribosomal structure and biogenesis	negative regulation of B cell apoptotic process
pdha1a	1.75327957957082	2.53128666789951e-12	up	Energy production and conversion	pyruvate dehydrogenase (acetyl-transferring) activity
zgc:110712	1.74310161079243	5.83799822428339e-09	up	Function unknown	Keratin, type I cytoskeletal 19
nae1	1.71757903439461	7.88783962174526e-09	up	-	-

fam98b	1.69767867460892	3.7696576215296e-10	up	Function unknown	Transposase
rpe	1.56930578960917	1.40669441214873e-08	up	Carbohydrate transport and metabolism	Belongs to the ribulose-phosphate 3-epimerase family
pbdc1	1.52994498709485	2.17873359438008e-07	up	-	-
rpl39	1.50467825434155	3.89623944035604e-10	up	Translation, ribosomal structure and biogenesis	ribosomal protein L39
scinla	1.4063721649951	2.38063285700244e-07	up	Cytoskeleton	cytoplasmic actin-based contraction involved in cell motility
ugdh	1.385058882305	8.20815396580761e-07	up	-	hyaluronan, chondroitin sulfate, and heparan sulfate
apitd1	1.38151945912464	1.87348057477174e-07	up	Function unknown	Apoptosis-inducing, TAF9-like domain 1
eif4a1b	1.37398219633015	8.64019444761263e-08	up	RNA processing and modification	Eukaryotic translation initiation factor 4A, isoform 1B
upf3b	1.35747016428942	8.57325655186519e-07	up	RNA processing and modification	Smg-4/UPF3 family
ccdc90b	1.28064137789322	0.000240371506783214	up	Function unknown	RNA-directed DNA polymerase from mobile element jockey-like
draxin	1.25536198778778	0.000520943225499422	up	Chromatin structure and dynamics	Reverse transcriptase (RNA-dependent DNA polymerase)
stra6	1.24819614242452	1.92916747335504e-05	up	Function unknown	Stimulated by retinoic acid
ruvbl2	1.21568515315787	2.99046798808976e-06	up	Replication, recombination and repair	Proposed core component of the chromatin remodeling Ino80 complex which is involved in transcriptional regulation, DNA replication and probably DNA repair
krt94	1.20528609695512	0.00184586132434504	up	Function unknown	Belongs to the intermediate filament family
egln3	1.20515919335867	0.000108424981013706	up	Signal transduction mechanisms	Egl nine homolog 3 isoform X1
ewsr1a	1.17523307397795	5.259370818635e-06	up	-	-
sdhc	1.17136954983114	0.000104010047400564	up	-	-
stim2a	1.15954900253667	0.00352994868649978	up	Function unknown	Podospora anserina S mat genomic DNA chromosome
gsta.1	1.15646374345509	0.000789690209061561	up	Posttranslational modification, protein turnover, chaperones	Glutathione S-transferase
polr1e	1.14284085942194	8.36587027975407e-05	up	Transcription	RNA polymerase I transcription factor binding
mgst1.2	1.13959018965472	0.000226750828826007	up	-	-
LOC100331968	1.13389795514581	0.00475592649788566	up	-	-
mrpl54	1.13013554404061	6.48506904280388e-05	up	Translation, ribosomal structure and biogenesis	ribosomal protein L54
si:ch211-160d14.9	1.1261971825612	0.00136517030177461	up	-	-

zgc:92630	1.12267449454156	0.0060753792831297	up	Secondary metabolites biosynthesis, transport and catabolism	Belongs to the short-chain dehydrogenases reductases (SDR) family
rabif	1.10512420363662	0.00136517030177461	up	-	RAB interacting factor
LOC797571	1.1018446725176	0.0010882571249976	up	Extracellular structures	Olfactomedin-4-like
mtdha	1.10081551052488	0.000150536760800221	up	Function unknown	Protein LYRIC-like isoform X1
ap1s2	1.09023591658282	0.000403214294080928	up	Intracellular trafficking, secretion, and vesicular transport	Belongs to the adaptor complexes small subunit family
pole	1.0886329353979	6.07110661101319e-05	up	Function unknown	Reverse transcriptase (RNA-dependent DNA polymerase)
helq	1.08074710570971	0.00132416334126068	up	RNA processing and modification	helicase superfamily c-terminal domain
smc2	1.07716706654452	6.98019964429848e-05	up	-	Structural maintenance of chromosomes
purab	1.0548430689989	0.0106342986847315	up	-	-
ehd1b	1.05313504573557	0.003978205003601	up	-	Belongs to the TRAFAC class dynamin-like GTPase superfamily. Dynamin Fzo YdjA family
slc43a1a	1.05253065821048	0.0067588444335147	up	Function unknown	Solute carrier family 43 (amino acid system L transporter), member 1
huwe1	1.04418216145369	0.000242879348451983	up	Posttranslational modification, protein turnover, chaperones	HECT, UBA and WWE domain containing 1, E3 ubiquitin protein ligase
nxt2	1.04352971120668	0.000823867920686046	up	-	-
si:dkey-25o16.2	1.0381513473975	0.0137393812073352	up	-	-
tmtc2a	1.02772820454622	0.00363264037817935	up	Function unknown	Transmembrane and tetratricopeptide repeat containing 2
trioa	1.01980484830926	0.00352994868649978	up	Function unknown	Transposase
s100t	1.01411089366216	0.025199012571736	up	Function unknown	S100 calcium binding protein T
aoc2	1.00821925936936	0.00503516701389048	up	Secondary metabolites biosynthesis, transport and catabolism	amine oxidase
nol6	1.00411372596199	0.000520943225499422	up	Translation, ribosomal structure and biogenesis	Nucleolar protein 6
kdelc2	1.00310755532157	0.00295320380700458	up	Function unknown	KDEL motif-containing protein 2
ctdspl3	1.0022931176237	0.00329270827861232	up	Transcription	CTD small phosphatase-like protein
rnft1	1.00107659314491	0.00295320380700458	up	Posttranslational modification, protein turnover, chaperones	RING finger and transmembrane domain-containing protein
eno1a	-1.00211546270314	0.00186486419370462	down	Carbohydrate transport and metabolism	Alpha-enolase-like

prmt5	-1.00866620956772	0.000357654252728626	down	Function unknown	Reverse transcriptase (RNA-dependent DNA polymerase)
cenpj	-1.01420157816984	0.0220720267138972	down	Function unknown	Centromere protein J
mrpl47	-1.0190613584866	0.000309973574044529	down	-	-
psme3	-1.0239847854457	0.000507734843644887	down	-	-
uchl3	-1.02556465966485	0.00037022700152482	down	Posttranslational modification, protein turnover, chaperones	Ubiquitin carboxyl-terminal esterase L3 (ubiquitin thiolesterase)
sik1	-1.03016699207507	0.000309973574044529	down	Signal transduction mechanisms	peptidyl-serine autophosphorylation
LOC565422	-1.03328361073726	0.0106490837467377	down	Carbohydrate transport and metabolism	Beta-1,3-galactosyltransferase
si:ch73-335l21.4	-1.03944740904926	0.0191139132472574	down	Posttranslational modification, protein turnover, chaperones	zinc ion binding
LOC101887113	-1.04757331396947	0.00413836080640892	down	-	-
ankrd39	-1.04769106881594	0.0026709909029318	down	Function unknown	ankyrin repeat
mgea5l	-1.049365901601	0.0141386944783305	down	Posttranslational modification, protein turnover, chaperones	Meningioma expressed antigen 5 (hyaluronidase)
mrrf	-1.0559178498648	0.00409514556401985	down	Translation, ribosomal structure and biogenesis	Mitochondrial ribosome recycling factor
selt2	-1.06254900958135	0.000153770991182826	down	Function unknown	Belongs to the SelWTH family. Selenoprotein T subfamily
LOC101883087	-1.0640208824677	0.00701301234210897	down	-	-
zgc:162193	-1.06477010656713	0.00521990724651629	down	Function unknown	FAM115-like
elf3	-1.06831204091634	0.00323521247245101	down	Transcription	E74-like factor 3 (ets domain transcription factor, epithelial-specific)
ttc14	-1.06931486062148	0.000171683300317059	down	Function unknown	tetratricopeptide repeat
si:dkey-83k24.5	-1.07438753333147	0.00549052598795994	down	-	-
krt1-c5	-1.0796809005432	0.000736789811796132	down	Function unknown	Keratin, type 1, gene c5
LOC100331480	-1.08369348236736	0.00926119129299611	down	Function unknown	Patched domain containing 3
armc9	-1.08395587166216	0.00113943596083197	down	Function unknown	Transposase
stx11b.1	-1.08523463621314	0.000948078199008667	down	Intracellular trafficking, secretion, and vesicular transport	Syntaxin 11b, tandem duplicate
LOC110440067	-1.09649866411341	0.00470422428923507	down	Signal transduction mechanisms	Pim proto-oncogene, serine threonine kinase,-related
LOC562053	-1.12498539377118	0.000435257239977574	down	-	-
exoc6b	-1.13686164578371	0.000403509926820305	down	Function unknown	Podospora anserina S mat genomic DNA chromosome
coro1cb	-1.14211971157082	0.000235438655086376	down	Cytoskeleton	Belongs to the WD repeat coronin family

irg1l	-1.14844560140115	0.000153770991182826	down	Function unknown	Immunoresponsive gene 1, like
ncapg2	-1.15308516926752	5.01884239077995e-05	down	Function unknown	inner cell mass cell proliferation
adh8b	-1.16029869392496	0.000258527118341087	down	Secondary metabolites biosynthesis, transport and catabolism	alcohol dehydrogenase
prpf4	-1.1663108104029	0.000299116105614047	down	RNA processing and modification	PRP4 pre-mRNA processing factor 4 homolog (yeast)
ttc5	-1.18247524192577	0.000403509926820305	down	Transcription	tetratricopeptide repeat
LOC555499	-1.18939054764346	0.00136517030177461	down	Function unknown	PHR domain
mrgbp	-1.19568655794748	0.000226750828826007	down	Function unknown	MRG MORF4L binding protein
cald1a	-1.19857633968503	0.000408163071394325	down	Function unknown	Caldesmon 1 like
stard14	-1.20551489316481	3.1959808609184e-05	down	Lipid transport and metabolism	(START) domain containing 10
rabl2	-1.21096481198173	0.000996808750253172	down	Intracellular trafficking, secretion, and vesicular transport	RAB, member of RAS oncogene family-like 2
mus81	-1.21918508015001	5.1765273429927e-06	down	-	-
LOC110439627	-1.2205275369055	5.45499325570382e-05	down	Function unknown	PRY
aldh1a2	-1.23565256428171	1.86616789598742e-05	down	Energy production and conversion	Aldehyde dehydrogenase 1 family member A2
clec19a	-1.23587776532225	0.000937251812775728	down	-	C-type lectin domain family 19 member A
zgc:100920	-1.23763618466437	9.95893755912523e-05	down	Function unknown	Sodium potassium-transporting ATPase subunit beta-1-interacting protein
oxa1l	-1.24042688122005	1.44859264628097e-05	down	Function unknown	Transposase
ilf3a	-1.25135482210885	1.78636652457636e-06	down	RNA processing and modification	Interleukin enhancer-binding factor
arhgef39	-1.25717801670377	0.000420211983507097	down	Signal transduction mechanisms	Rho guanine nucleotide exchange factor
eif2b2	-1.27936842248493	4.55985343993974e-06	down	Function unknown	Reverse transcriptase (RNA-dependent DNA polymerase)
elovl7b	-1.28486334746396	3.48309677200482e-06	down	Lipid transport and metabolism	fatty acid elongation, polyunsaturated fatty acid
LOC110439372	-1.31559942846656	5.36833492625962e-07	down	-	-
atrx	-1.32320428136591	1.40047624629988e-07	down	Transcription	Transcriptional regulator
nom1	-1.37106782080043	6.24463281417284e-05	down	Signal transduction mechanisms	Nucleolar protein with MIF4G domain 1
si:dkey-286j15.3	-1.39080851433694	3.54667443605934e-05	down	Function unknown	interleukin-8 biosynthetic process
pim2	-1.42335583524535	8.96718838536296e-08	down	Signal transduction mechanisms	Pim-2 proto-oncogene, serine threonine kinase
ndst3	-1.42668919553339	8.10498148470578e-07	down	Function unknown	Reverse transcriptase (RNA-dependent DNA polymerase)
mospd1	-1.43174718410478	1.54487694441135e-07	down	Intracellular trafficking, secretion, and vesicular transport	Motile sperm

tm9sf3	-1.44389952746801	1.35696030084103e-05	down	Intracellular trafficking, secretion, and vesicular transport	Endomembrane protein 70
zgc:110340	-1.4521866601742	1.87667344653146e-06	down	-	-
arpc4l	-1.47741534011283	1.08273511417411e-06	down	Cytoskeleton	Arp2/3 complex-mediated actin nucleation
LOC100330864	-1.50855837662119	3.88849192480196e-10	down	-	-
swi5	-1.51985703999473	1.91517864548894e-07	down	-	-
si:dkey-1f12.3	-1.5319228893637	2.01700009918829e-06	down	Chromatin structure and dynamics	Reverse transcriptase (RNA-dependent DNA polymerase)
junba	-1.55553359835329	6.77218848417632e-09	down	Transcription	Jun B proto-oncogene
si:dkey-17e16.17	-1.56738382860492	1.87348057477174e-07	down	Function unknown	Bicaudal D-related protein
fam96b	-1.61299807714486	8.96718838536296e-08	down	-	-
rrm2b	-1.61927447749796	1.45325921982569e-07	down	Nucleotide transport and metabolism	Ribonucleoside-diphosphate reductase subunit
rps6kb1b	-1.64401737571526	3.86068787080405e-09	down	Signal transduction mechanisms	protein serine threonine kinase activity. It is involved in the biological process described with protein phosphorylation
rasgef1ba	-1.692476206355	9.17009932541873e-08	down	Signal transduction mechanisms	family member
nkap	-1.69352642353153	7.29486643397961e-12	down	Function unknown	NFKB activating protein
fosab	-1.72346952080195	4.55596659873955e-11	down	-	-
ift88	-1.73086290760156	1.22520119399072e-08	down	Function unknown	Intraflagellar transport protein 88 homolog
psma5	-1.82103264689297	1.54337968986006e-14	down	Posttranslational modification, protein turnover, chaperones	threonine-type endopeptidase activity
mta3	-1.89362053057425	5.18043574969238e-13	down	Chromatin structure and dynamics	MTA R1 domain
ptgs2b	-2.57266903709887	1.92952459908265e-22	down	Function unknown	prostaglandin-endoperoxide synthase activity
cd63	-3.34722141483402	6.8241508193501e-39	down	Function unknown	CD63 antigen
copb1	-3.60429419305329	1.84969809669891e-47	down	Intracellular trafficking, secretion, and vesicular transport	The coatomer is a cytosolic protein complex that binds to dilysine motifs and reversibly associates with Golgi non-clathrin-coated vesicles, which further mediate biosynthetic protein transport from the ER, via the Golgi up to the trans Golgi network. Coatomer complex is required for budding from Golgi membranes, and is essential for the retrograde Golgi-to-ER transport of dilysine-tagged proteins
polr2i	-4.11671050396059	2.31846088449042e-52	down	-	-

Table 6.2: List of genes differentially-expressed by at least 2-fold in the head at 28 hpf following *VAX2* overexpression.

Gene	logFoldChange	Q-Value	Regulated	COG Annotation	eggNOG Annotation
pdha1a	3.60212374789267	9.29120348072268e-48	up	Energy production and conversion	pyruvate dehydrogenase (acetyl-transferring) activity
pbdc1	3.32952772223078	1.4310654674294e-31	up	-	-
rpl13a	3.07973929268971	4.53341386231029e-40	up	Translation, ribosomal structure and biogenesis	Ribosomal protein L13a
ciapin1	3.03601510588247	8.00623766928325e-32	up	Function unknown	Component of the cytosolic iron-sulfur (Fe-S) protein assembly (CIA) machinery. Required for the maturation of extramitochondrial Fe-S proteins. Part of an electron transfer chain functioning in an early step of cytosolic Fe-S biogenesis. Electrons are transferred to the Fe-S cluster from NADPH via the FAD- and FMN-containing protein NDOR1. Has anti-apoptotic effects in the cell. Involved in negative control of cell death upon cytokine withdrawal. Promotes development of hematopoietic cells
sdhc	3.01901841005159	6.24053053448613e-33	up	-	-
scinla	2.94559380285823	5.25721267469707e-30	up	Cytoskeleton	cytoplasmic actin-based contraction involved in cell motility
aifm1	2.65447685404802	1.18616760472094e-24	up	Signal transduction mechanisms	apoptosis-inducing factor
si:ch211-191a24.3	2.61517198186475	4.55718905184452e-20	up	Function unknown	Transposase
pmp22a	2.58413462862062	1.76007303960732e-22	up	Function unknown	Peripheral myelin protein
ccnl1a	2.52535342652718	3.69046019120087e-22	up	Cell cycle control, cell division, chromosome partitioning	Belongs to the cyclin family
nkap	2.50113842748796	3.61878196638476e-25	up	Function unknown	NFKB activating protein
aldh1a2	2.4935906715258	5.50663990894922e-19	up	Energy production and conversion	Aldehyde dehydrogenase 1 family member A2
tma16	2.44567051564055	1.6647544793631e-22	up	-	-
mrps36	2.38942276226088	5.38926910389663e-21	up	Function unknown	ribosomal protein S36
churc1	2.33330491498022	5.49925221422608e-16	up	-	-
eif1axa	2.3088290605082	5.38926910389663e-21	up	Translation, ribosomal structure and biogenesis	Translation initiation factor 1A / IF-1
nap1l4a	2.30648799091439	6.10423839975627e-20	up	-	Nucleosome assembly protein 1-like 4

ube2g1a	2.15853613578178	1.2621048489839e-14	up	Posttranslational modification, protein turnover, chaperones	ubiquitin-conjugating enzyme
zgc:162193	2.15327399615164	4.56921386247802e-15	up	Function unknown	FAM115-like
zgc:77739	2.12156354693157	1.31321422288658e-12	up	Function unknown	Chromosome 4 open reading frame 33
oxa1l	2.12045543825539	3.19983775617965e-16	up	Intracellular trafficking, secretion, and vesicular transport	60Kd inner membrane protein
otud5b	2.11471640183874	4.60540837464451e-12	up	-	protein K48-linked deubiquitination
fosab	2.10154508711769	4.68902361435937e-14	up	-	-
lias	2.09221377411727	1.06249471780031e-12	up	Coenzyme transport and metabolism	Lipoyl synthase
naa50	1.94412586847156	5.52320541359478e-13	up	Function unknown	Acetyltransferase (GNAT) domain
endouc	1.923115818913	8.70093183512539e-11	up	Function unknown	Transposase
ift88	1.91881663199302	4.71674343477616e-12	up	Function unknown	Intraflagellar transport protein 88 homolog
atp1a1b	1.85887556171772	8.25553482212557e-12	up	Inorganic ion transport and metabolism	sodium:potassium-exchanging ATPase activity
sp2	1.81708976879457	9.83477486452356e-09	up	Transcription	multicellular organism growth
swi5	1.79039183310803	1.23840906603084e-11	up	-	-
creld2	1.72759279717247	5.01194641887832e-10	up	Function unknown	Reverse transcriptase (RNA-dependent DNA polymerase)
cyr61	1.71626870233899	5.28049698593414e-11	up	Extracellular structures	Cysteine-rich, angiogenic inducer 61
tmem100b	1.7118587323554	8.90026194247547e-09	up	Function unknown	Transmembrane protein 100
arl5a	1.63987633684993	2.87360200696439e-09	up	-	-
jak1	1.63743842793459	6.93298564542871e-08	up	Signal transduction mechanisms	Janus kinase 1
junba	1.62873811225336	1.6461102937772e-09	up	Transcription	Jun B proto-oncogene
adck2	1.58226298985061	4.29591785397478e-07	up	Function unknown	aarF domain containing kinase 2
slc29a2	1.53867202397432	2.11318272454567e-09	up	Nucleotide transport and metabolism	Solute carrier family 29 (equilibrative nucleoside transporter), member 2
ctbp1	1.50732500090037	1.58444968923256e-08	up	Transcription	D-isomer specific 2-hydroxyacid dehydrogenase, NAD binding domain
myzap	1.49597310390948	2.56246549148676e-06	up	Function unknown	DDE superfamily endonuclease
fpgs	1.47222169034798	3.60785027928005e-07	up	Coenzyme transport and metabolism	Folylpolyglutamate synthase
spty2d1	1.45504746915482	5.52037577555354e-05	up	Transcription	SPT2, Suppressor of Ty, domain containing 1 (S. cerevisiae)
rabif	1.43255180599876	4.04582464868942e-07	up	-	RAB interacting factor
he2	1.40930561442848	7.90763347427201e-07	up	Posttranslational modification,	High choriolytic enzyme 1-like

				protein turnover, chaperones	
tceb1a	1.38931224681584	1.68891435384898e-05	up	Transcription	Transcription elongation factor B
fuca2	1.38509153612313	1.3127810952609e-05	up	Carbohydrate transport and metabolism	alpha-L-fucosidase activity
si:ch73-213k20.5	1.37145223611541	5.2879481320134e-05	up	-	-
rpl36a	1.36405474723907	1.57855831877824e-08	up	-	-
cxcl18b	1.36081322422642	0.000214969009171821	up	-	-
wdr32	1.3536000128469	4.36871983931728e-05	up	Transcription	DDB1- and CUL4-associated factor 10
LOC110438439	1.32685544742824	4.7964913780876e-07	up	Function unknown	Reverse transcriptase (RNA-dependent DNA polymerase)
rrp36	1.32417983369521	7.26621742194063e-07	up	Translation, ribosomal structure and biogenesis	Ribosomal RNA processing 36 homolog (S. cerevisiae)
fam91a1	1.32307052407889	2.27473163514127e-05	up	Function unknown	Transposase
rps6ka3a	1.32067208643228	4.37180551751957e-05	up	Signal transduction mechanisms	Ribosomal protein S6 kinase
cdc6	1.31296510387885	2.69158793781567e-06	up	-	Involved in the initiation of DNA replication. Also participates in checkpoint controls that ensure DNA replication is completed before mitosis is initiated
ssr3	1.29349146252015	1.87613847761341e-05	up	Intracellular trafficking, secretion, and vesicular transport	SRP-dependent cotranslational protein targeting to membrane
tpm4a	1.2874751384314	1.3869436308368e-07	up	Cytoskeleton	structural constituent of muscle
psma5	1.27949439447822	2.59073712930085e-07	up	Posttranslational modification, protein turnover, chaperones	threonine-type endopeptidase activity
med16	1.27715365691061	7.71566204290917e-05	up	Function unknown	Mediator complex subunit 16
cebpd	1.25658022798287	5.61143737746554e-07	up	Transcription	CCAAT enhancer binding protein (C EBP), delta
shcbp1	1.2360785605829	0.000260394901215512	up	Function unknown	SHC SH2-domain binding protein 1
epha2a	1.18958770956894	2.92000318523944e-05	up	Signal transduction mechanisms	Ephrin type-A receptor 2
ten1	1.17210172027667	0.000352115810787226	up	Function unknown	CST complex subunit
ephb3b	1.16795670384924	0.00292380260207231	up	Signal transduction mechanisms	Receptor
zgc:162939	1.14139330756317	0.00560113565747266	up	Function unknown	Transposase
galm	1.13984716032839	0.00730279261648454	up	RNA processing and modification	ATP-dependent RNA helicase
sdhaf2	1.12082047351161	0.000302493603801332	up	Function unknown	Podospora anserina S mat genomic DNA chromosome
socs3b	1.10285067308415	0.00011845067093122	up	Signal transduction mechanisms	suppressor of cytokine signaling
gla	1.09839331121381	0.0035401450470195	up	Carbohydrate transport and metabolism	N-acetylgalactosaminidase, alpha

cldn11a	1.09379129476702	2.31163112395044e-05	up	Function unknown	Plays a major role in tight junction-specific obliteration of the intercellular space, through calcium- independent cell-adhesion activity
slc38a8a	1.09361066840929	0.0129989633636204	up	Amino acid transport and metabolism	Solute carrier family 38 member 8
zmp:0000000660	1.06574599894068	0.00667177915336371	up	Function unknown	Transposase
micall1a	1.06221115539039	0.0157631496035908	up	Cytoskeleton	slow endocytic recycling
LOC110439587	1.05208226621164	0.0147032652563726	up	-	-
polr2i	1.03890589942005	0.000194536434210841	up	-	-
ccz1	1.03399509576265	0.000712852135463495	up	Defense mechanisms	vesicle-mediated transport
myt1a	1.00770020361575	0.00783192596931125	up	Transcription	Suppression of tumorigenicity 18
fus	1.00735534152288	0.000210959699675977	up	-	-
krt5	1.00640515529228	0.000135023689890373	up	Function unknown	Belongs to the intermediate filament family
dcaf17	1.00572137401098	0.0274686046417915	up	Function unknown	Ddb1 and cul4 associated factor 17
tbx5a	-1.00107399490373	0.00836676463282698	down	Transcription	positive regulation of cardioblast differentiation
exorh	-1.01131502477902	0.0123487916401112	down	Signal transduction mechanisms	Amino terminal of the G-protein receptor rhodopsin
pitx1	-1.01327582269492	0.0255630407146596	down	Transcription	Paired-like homeodomain transcription factor 1
lhx8a	-1.01644682882681	0.0108475483918629	down	Transcription	LIM homeobox
epha4l	-1.01702853401432	0.00304225307761465	down	Signal transduction mechanisms	EPH receptor A3
plch2a	-1.01850526612354	0.00683350299511831	down	Function unknown	Podospora anserina S mat genomic DNA chromosome
lhx6	-1.02311436589476	0.0018618943478	down	Transcription	LIM homeobox
osr2	-1.02405314187504	0.015483594167203	down	-	-
tmem130	-1.02910285773578	0.00889559582350428	down	Function unknown	Transmembrane protein 130
olfml2a	-1.03892044650005	0.0130717899171288	down	Extracellular structures	Olfactomedin-like
hexa	-1.0393737313312	0.00592971420009653	down	Carbohydrate transport and metabolism	N-acetyl-beta-D-galactosaminidase activity
metap1d	-1.04018849574465	0.0120995107849657	down	Function unknown	Transposase
ftr83	-1.04771717855342	0.0110542209527853	down	Posttranslational modification, protein turnover, chaperones	finTRIM family, member 83
si:dkey-191g9.7	-1.0504029743949	0.0119160059808155	down	Function unknown	inducer of neurite outgrowth 2
tsc1b	-1.0504029743949	0.0119160059808155	down	Function unknown	immunological memory process
fhl3a	-1.05185137905963	0.00509038117339057	down	Function unknown	Ribonuclease H protein
nkx3.2	-1.06390341042712	0.0035401450470195	down	Transcription	NK3 homeobox 2
LOC100535716	-1.06684717037958	0.012421817749978	down	Extracellular structures	peptidase inhibitor activity

ache	-1.0725551839002	0.00131462881444161	down	Signal transduction mechanisms	Belongs to the type-B carboxylesterase lipase family
heatr5a	-1.07266891243443	0.0016941197833595	down	Function unknown	HEAT repeat-containing protein
phlda2	-1.0758638356647	0.00306662831376738	down	Signal transduction mechanisms	Pleckstrin homology-like domain family A member 2
mmp11b	-1.07889620964518	0.000638611223136963	down	Function unknown	Ribonuclease H protein
p3h2	-1.08030629922316	0.0035401450470195	down	Function unknown	procollagen-proline 3-dioxygenase activity
kcnma1a	-1.08142777870692	0.00528677863983808	down	Inorganic ion transport and metabolism	large conductance calcium-activated potassium channel activity
mrps16	-1.0846157726351	0.000214969009171821	down	Translation, ribosomal structure and biogenesis	Mitochondrial ribosomal protein S16
foxf2a	-1.08488115334846	0.00014499640577857	down	Transcription	Forkhead box
hnrnpl2	-1.08508385301439	2.59440597679908e-05	down	RNA processing and modification	Heterogeneous nuclear ribonucleoprotein
ulk1a	-1.0868717053502	0.00480548038146052	down	Signal transduction mechanisms	Unc-51-like kinase 2 (C. elegans)
atoh8	-1.08735338932623	0.0018618943478	down	Function unknown	Jumping translocation breakpoint
dcaf8	-1.09335383717374	0.000925623900308005	down	Function unknown	DDB1 and CUL4 associated factor 8
n4bp2	-1.10499908546133	0.00500211283144266	down	Function unknown	Transposase
prmt5	-1.12083368893331	3.27882444914213e-05	down	Function unknown	Reverse transcriptase (RNA-dependent DNA polymerase)
chchd2	-1.13067911925617	5.10965612694344e-05	down	Function unknown	Coiled-coil-helix-coiled-coil-helix domain containing 2
picalma	-1.13075227380736	0.000475229289243264	down	-	ENTH domain
mfsd2ab	-1.1371419170278	0.00019098587340837	down	Carbohydrate transport and metabolism	major facilitator superfamily
si:ch211-212o1.2	-1.14336464388013	0.00459864963622161	down	Posttranslational modification, protein turnover, chaperones	Transmembrane protein 189-like
nbr1a	-1.15816979943619	0.00156142055174799	down	-	-
ankra2	-1.16549024817122	0.000383775239641478	down	Function unknown	Ankyrin repeat
stx5a	-1.18086974028259	4.92778709197609e-05	down	Intracellular trafficking, secretion, and vesicular transport	SNARE domain
rrm2b	-1.18795149823709	0.000560878115663899	down	Nucleotide transport and metabolism	Ribonucleoside-diphosphate reductase subunit
taf12	-1.18916999404749	2.74708066896935e-05	down	Transcription	RNA polymerase II transcriptional preinitiation complex assembly
cpne3	-1.20991844653389	2.92000318523944e-05	down	Signal transduction mechanisms	ERBB2 signaling pathway
mon1bb	-1.21731172309553	0.0016941197833595	down	Function unknown	MON1 secretory trafficking family member B
nog1	-1.21882222327305	0.000283718371719374	down	Signal transduction mechanisms	Belongs to the noggin family

mbtps1	-1.23051431869576	3.13170404352105e-06	down	Posttranslational modification, protein turnover, chaperones	Membrane-bound transcription factor
LOC100538121	-1.24991297995391	0.000573049674248983	down	Function unknown	Ribonuclease H protein
si:ch211-161m3.4	-1.25257548009275	0.00103752815261348	down	Function unknown	Zinc finger protein
en2b	-1.26889151151069	2.31163112395044e-05	down	Transcription	homeobox protein
alms1	-1.2709864734502	5.49208967036469e-06	down	Function unknown	alpha-actinin binding
rab22a	-1.27245113530219	0.000604315131282306	down	Function unknown	Transposase
sepw2b	-1.29421998298394	1.21099127017111e-05	down	Function unknown	Migration and invasion enhancer 1
slc25a26	-1.31143506942105	8.56782187572479e-06	down	Energy production and conversion	Solute carrier family 25, member 26
crygm2d19	-1.31390379707553	6.11623180913631e-06	down	Function unknown	Belongs to the beta gamma-crystallin family
foxf1	-1.32113574006502	4.53937158195372e-07	down	Transcription	FORKHEAD
mef2ca	-1.32834499788139	0.000252486893078319	down	-	-
acsl1a	-1.35600551048313	1.16218561719e-05	down	Lipid transport and metabolism	decanoate-CoA ligase activity
cdc42ep5	-1.37267429999939	1.04638803368074e-05	down	Function unknown	CDC42 effector protein (Rho GTPase binding) 1b
nxt2	-1.40231321679007	2.72566833375935e-06	down	RNA processing and modification	Nuclear transport factor 2-like export factor 2
gtf2ird1	-1.43073531472981	9.49321730684472e-06	down	-	-
atg12	-1.47062605192418	2.44431567141701e-05	down	Posttranslational modification, protein turnover, chaperones	ATG12 autophagy related 12 homolog (S. cerevisiae)
lmf2b	-1.50504788550775	8.62760785428066e-10	down	-	-
sh3glb2b	-1.50810557876398	1.3304576636969e-08	down	Chromatin structure and dynamics	Reverse transcriptase (RNA-dependent DNA polymerase)
mrrf	-1.51558909950499	4.53937158195372e-07	down	Translation, ribosomal structure and biogenesis	Mitochondrial ribosome recycling factor
yars	-1.55999210636567	1.97956876966023e-07	down	Translation, ribosomal structure and biogenesis	Tyrosyl-tRNA synthetase
eif2b2	-1.57064997542013	1.98801360446626e-09	down	Translation, ribosomal structure and biogenesis	Belongs to the eIF-2B alpha beta delta subunits family
tfg	-1.62751896711116	1.03069376080836e-10	down	Function unknown	TRK-fused gene
rabl2	-1.62777397480185	2.00837109262506e-08	down	Function unknown	Podospora anserina S mat genomic DNA chromosome
si:dkey-56m19.5	-1.64714931260644	3.91274595759128e-11	down	-	-
polr2l	-1.65126683115916	5.59578674459053e-09	down	Transcription	DNA-directed RNA polymerases I, II, and III subunit
slc8a1a	-1.72515680359329	7.44729264180353e-08	down	Function unknown	RNA-directed DNA polymerase from mobile element jockey-like
lysmd2	-1.76913768302532	4.36203825085257e-11	down	Function unknown	peptidoglycan-binding, domain containing 2

phf6	-1.77567016521142	4.84993143535415e-13	down	Transcription	PHD finger protein
cinp	-1.80324475282349	1.93324830038908e-10	down	Function unknown	Cyclin-dependent kinase 2 interacting protein
ppp2cb	-1.80726529147274	1.72626348233004e-14	down	Signal transduction mechanisms	positive regulation of microtubule binding
sdccag3	-1.90733363120822	1.19137419363771e-09	down	Function unknown	Podospora anserina S mat genomic DNA chromosome
copb1	-1.93814404069418	2.05452635325189e-12	down	Intracellular trafficking, secretion, and vesicular transport	The coatomer is a cytosolic protein complex that binds to dilysine motifs and reversibly associates with Golgi non- clathrin-coated vesicles, which further mediate biosynthetic protein transport from the ER, via the Golgi up to the trans Golgi network. Coatomer complex is required for budding from Golgi membranes, and is essential for the retrograde Golgi-to-ER transport of dilysine-tagged proteins
smad9	-1.97800297896865	1.04293504562911e-10	down	-	Mothers against decapentaplegic homolog
metap1	-1.98166155991621	2.00074817113776e-16	down	Posttranslational modification, protein turnover, chaperones	Methionine aminopeptidase
uchl3	-2.01819250580399	1.73960373918285e-15	down	Posttranslational modification, protein turnover, chaperones	Ubiquitin carboxyl-terminal esterase L3 (ubiquitin thiolesterase)
plk2b	-2.03297458713559	4.60540837464451e-12	down	Signal transduction mechanisms	Serine threonine-protein kinase
ndufa1	-2.05481198709623	4.52379551841506e-16	down	-	-
zc4h2	-2.08902312989743	3.45065193190186e-13	down	Function unknown	spinal cord motor neuron differentiation
fbxw11b	-2.18929427398103	4.74170226672901e-15	down	Function unknown	F-box and WD repeat domain containing 11
hand2	-2.24167845404083	1.1014488894779e-13	down	Transcription	Heart- and neural crest
ptx3a	-2.32017072720478	7.03625694369268e-15	down	Function unknown	general transcription factor II-I repeat domain-containing protein
tspan14	-2.38447887708184	4.38028098105661e-16	down	Function unknown	Tetraspanin 14
plk1	-2.39423494372718	2.79657341458148e-22	down	Signal transduction mechanisms	Serine threonine-protein kinase
pnisr	-2.39548845809112	6.99172274171865e-20	down	Function unknown	Arginine/serine-rich protein PNISR
sec13	-2.66644461265323	6.64825461292163e-25	down	Function unknown	Podospora anserina S mat genomic DNA chromosome
cdk1	-2.69117952614692	2.45028581798932e-29	down	Signal transduction mechanisms	Cyclin-dependent kinase
rpe	-2.8699871528484	1.06707243820085e-25	down	Carbohydrate transport and metabolism	Ribulose-phosphate 3-epimerase
si:dkey-23i12.5	-2.90903717233499	7.4581967153861e-31	down	-	-
ptbp1b	-3.09405139500648	4.28643489836922e-35	down	RNA processing and modification	erythrocyte maturation

fam32a	-3.56199395033028	3.24773322273923e-41	down	Function unknown	Family with sequence similarity 32, member A, like

Table 6.3: GO analysis of DMH-1 treated embryos by biological process. Only those GO IDs with 4 or more genes are shown.

GO ID	Description	Gene Ratio	Q-Value	Genes
GO:0006412	translation	10/98	0.0301538033590752	eif2b2/eif4a1b/etf1b/mrpl18/mrpl47/mrrf/rpl39/rps13/rps6kb1b/upf3b
GO:0043043	peptide biosynthetic process	10/98	0.0301538033590752	eif2b2/eif4a1b/etf1b/mrpl18/mrpl47/mrrf/rpl39/rps13/rps6kb1b/upf3b
GO:0006974	cellular response to DNA damage stimulus	8/98	0.139523241254068	helq/huwe1/mus81/pole/polr2i/rrm2b/ruvbl2/swi5
GO:0006259	DNA metabolic process	8/98	0.196871062114248	gar1/helq/huwe1/mus81/pole/polr2i/ruvbl2/swi5
GO:0006281	DNA repair	7/98	0.116473438896911	helq/huwe1/mus81/pole/polr2i/ruvbl2/swi5
GO:0006325	chromatin organization	7/98	0.196871062114248	kat8/mrgbp/mta3/nap1l4a/noc2l/prmt5/ruvbl2
GO:0045892	negative regulation of transcription, DNA-templated	7/98	0.196871062114248	junba/kat8/mta3/nkap/noc2l/purab/ruvbl2
GO:1902679	negative regulation of RNA biosynthetic process	7/98	0.196871062114248	junba/kat8/mta3/nkap/noc2l/purab/ruvbl2
GO:1903507	negative regulation of nucleic acid-templated transcription	7/98	0.196871062114248	junba/kat8/mta3/nkap/noc2l/purab/ruvbl2
GO:0051253	negative regulation of RNA metabolic process	7/98	0.232014014029223	junba/kat8/mta3/nkap/noc2l/purab/ruvbl2
GO:0000278	mitotic cell cycle	7/98	0.244638201926697	ewsr1a/ift88/mus81/pim2/plk1/pole/psme3
GO:0045934	negative regulation of nucleobase-containing compound metabolic process	7/98	0.25111235544303	junba/kat8/mta3/nkap/noc2l/purab/ruvbl2
GO:0022402	cell cycle process	7/98	0.254034031923182	cenpj/ewsr1a/helq/ift88/mus81/plk1/psme3
GO:0016570	histone modification	6/98	0.055344952144798	kat8/mrgbp/mta3/noc2l/prmt5/ruvbl2
GO:0016569	covalent chromatin modification	6/98	0.056959290467753	kat8/mrgbp/mta3/noc2l/prmt5/ruvbl2
GO:0032787	monocarboxylic acid metabolic process	6/98	0.135705279445508	aldh1a2/elovl7b/eno1a/irg1l/pdha1a/ptgs2b
GO:0051186	cofactor metabolic process	6/98	0.196871062114248	elovl7b/eno1a/gsta.1/mgst1.2/pdha1a/rpe
GO:0009117	nucleotide metabolic process	6/98	0.239892684446554	elovl7b/eno1a/pdha1a/rpe/rrm2b/sdhc
GO:0006753	nucleoside phosphate metabolic process	6/98	0.239892684446554	elovl7b/eno1a/pdha1a/rpe/rrm2b/sdhc
GO:0055086	nucleobase-containing small molecule metabolic process	6/98	0.303207185176369	elovl7b/eno1a/pdha1a/rpe/rrm2b/sdhc
GO:0051726	regulation of cell cycle	6/98	0.303207185176369	ewsr1a/junba/mus81/pim2/plk1/psme3
GO:0030097	hemopoiesis	6/98	0.303207185176369	fosab/gar1/kat8/mta3/nap1l4a/pim2
GO:0048534	hematopoietic or lymphoid organ development	6/98	0.303207185176369	fosab/gar1/kat8/mta3/nap1l4a/pim2
GO:0002520	immune system development	6/98	0.303207185176369	fosab/gar1/kat8/mta3/nap1l4a/pim2
GO:1901137	carbohydrate derivative biosynthetic process	6/98	0.303207185176369	elovl7b/eno1a/ndst3/pdha1a/rrm2b/ugdh
GO:0060271	cilium assembly	5/98	0.239892684446554	cenpj/ehd1b/ift88/rpe/ruvbl2

GO:0044782	cilium organization	5/98	0.25111235544303	cenpj/ehd1b/ift88/rpe/ruvbl2
GO:0019693	ribose phosphate metabolic process	5/98	0.275025011969241	elovl7b/eno1a/pdha1a/rpe/sdhc
GO:0120031	plasma membrane bounded cell projection assembly	5/98	0.303207185176369	cenpj/ehd1b/ift88/rpe/ruvbl2
GO:0022613	ribonucleoprotein complex biogenesis	5/98	0.303207185176369	gar1/noc2l/nol6/nom1/ruvbl2
GO:0030031	cell projection assembly	5/98	0.303207185176369	cenpj/ehd1b/ift88/rpe/ruvbl2
GO:0007264	small GTPase mediated signal transduction	5/98	0.322125599558874	arhgef39/rabif/rabl2/rasgef1ba/trioa
GO:0001654	eye development	5/98	0.324283951197515	aldh1a2/ift88/prpf4/scinla/sec13
GO:0150063	visual system development	5/98	0.324283951197515	aldh1a2/ift88/prpf4/scinla/sec13
GO:0018193	peptidyl-amino acid modification	5/98	0.332187566071057	kat8/mrgbp/noc2l/prmt5/ruvbl2
GO:0016573	histone acetylation	4/98	0.0301538033590752	kat8/mrgbp/noc2l/ruvbl2
GO:0006475	internal protein amino acid acetylation	4/98	0.0301538033590752	kat8/mrgbp/noc2l/ruvbl2
GO:0018393	internal peptidyl-lysine acetylation	4/98	0.0301538033590752	kat8/mrgbp/noc2l/ruvbl2
GO:0018394	peptidyl-lysine acetylation	4/98	0.0301538033590752	kat8/mrgbp/noc2l/ruvbl2
GO:0006473	protein acetylation	4/98	0.055344952144798	kat8/mrgbp/noc2l/ruvbl2
GO:0043543	protein acylation	4/98	0.152103112306906	kat8/mrgbp/noc2l/ruvbl2
GO:0018205	peptidyl-lysine modification	4/98	0.196871062114248	kat8/mrgbp/noc2l/ruvbl2
GO:0006310	DNA recombination	4/98	0.197303599015158	helq/mus81/ruvbl2/swi5
GO:0006790	sulfur compound metabolic process	4/98	0.239892684446554	elovl7b/gsta.1/mgst1.2/pdha1a
GO:0048193	Golgi vesicle transport	4/98	0.239892684446554	copb1/exoc6b/rabif/sec13
GO:0006732	coenzyme metabolic process	4/98	0.302461415045853	elovl7b/eno1a/pdha1a/rpe
GO:0042254	ribosome biogenesis	4/98	0.303207185176369	gar1/noc2l/nol6/nom1
GO:0009165	nucleotide biosynthetic process	4/98	0.303207185176369	elovl7b/eno1a/pdha1a/rrm2b
GO:1901293	nucleoside phosphate biosynthetic process	4/98	0.303207185176369	elovl7b/eno1a/pdha1a/rrm2b
GO:0007346	regulation of mitotic cell cycle	4/98	0.303207185176369	ewsr1a/mus81/pim2/psme3
GO:0009150	purine ribonucleotide metabolic process	4/98	0.303207185176369	elovl7b/eno1a/pdha1a/sdhc
GO:0006163	purine nucleotide metabolic process	4/98	0.308115502643947	elovl7b/eno1a/pdha1a/sdhc
GO:0009259	ribonucleotide metabolic process	4/98	0.312585377754574	elovl7b/eno1a/pdha1a/sdhc
GO:1903047	mitotic cell cycle process	4/98	0.312585377754574	ewsr1a/ift88/mus81/psme3
GO:0072521	purine-containing compound metabolic process	4/98	0.324283951197515	elovl7b/eno1a/pdha1a/sdhc
GO:0000226	microtubule cytoskeleton organization	4/98	0.324283951197515	cenpj/ewsr1a/ift88/ruvbl2
GO:0005975	carbohydrate metabolic process	4/98	0.324283951197515	eno1a/fuca2/ndst3/rpe
GO:0090407	organophosphate biosynthetic process	4/98	0.347209300543446	elovl7b/eno1a/pdha1a/rrm2b
GO:0048589	developmental growth	4/98	0.356413013567298	aldh1a2/ewsr1a/fosab/ruvbl2
GO:0017144	drug metabolic process	4/98	0.376630660584499	adh8b/eno1a/irg1l/sdhc

GO:0040007	growth	4/98	0.382079155045093	aldh1a2/ewsr1a/fosab/ruvbl2
GO:0009967	positive regulation of signal transduction	4/98	0.407117210952202	ift88/mtdha/sec13/ugdh
GO:0051603	proteolysis involved in cellular protein catabolic process	4/98	0.421365500230725	huwe1/psma5/psme3/uchl3
GO:0044257	cellular protein catabolic process	4/98	0.423450627819511	huwe1/psma5/psme3/uchl3
GO:0010647	positive regulation of cell communication	4/98	0.424711965800166	ift88/mtdha/sec13/ugdh
GO:0023056	positive regulation of signaling	4/98	0.424711965800166	ift88/mtdha/sec13/ugdh
GO:0007420	brain development	4/98	0.424748230146868	aldh1a2/draxin/etf1b/scinla
GO:0007017	microtubule-based process	4/98	0.431712294851786	cenpj/ewsr1a/ift88/ruvbl2
GO:0030163	protein catabolic process	4/98	0.431712294851786	huwe1/psma5/psme3/uchl3
GO:0070647	protein modification by small protein conjugation or removal	4/98	0.433680637404502	huwe1/nae1/rnft1/uchl3
GO:0060322	head development	4/98	0.444045764421144	aldh1a2/draxin/etf1b/scinla

Table 6.4: GO analysis of DMH-1 treated embryos by cellular component. Only those GO IDs with 3 or more genes are shown.

GO ID	Description	Gene Ratio	Q-Value	Genes
GO:0005730	nucleolus	8/91	0.0030470763397677	gar1/noc2l/nol6/nom1/polr1e/polr2i/rps13/upf3b
GO:0005840	ribosome	6/91	0.0281701464622933	mrpl18/mrpl47/mrpl54/rpl39/rps13/rps6kb1b
GO:0044454	nuclear chromosome part	6/91	0.0528079608232587	junba/kat8/mta3/pole/ruvbl2/swi5
GO:0000228	nuclear chromosome	6/91	0.0528079608232587	junba/kat8/mta3/pole/ruvbl2/swi5
GO:0044427	chromosomal part	6/91	0.156685400310493	junba/kat8/mta3/pole/ruvbl2/swi5
GO:0000790	nuclear chromatin	5/91	0.0528079608232587	junba/kat8/mta3/ruvbl2/swi5
GO:0000785	chromatin	5/91	0.114244331246675	junba/kat8/mta3/ruvbl2/swi5
GO:0044451	nucleoplasm part	5/91	0.158926726853991	kat8/mrgbp/mta3/polr2i/ruvbl2
GO:0044429	mitochondrial part	5/91	0.205623180941858	mrpl47/mrpl54/ndufa12/oxa1l/sdhc
GO:0044391	ribosomal subunit	4/91	0.066009018832582	mrpl47/mrpl54/rpl39/rps13
GO:0061695	transferase complex, transferring phosphorus-containing groups	4/91	0.131149126187233	pole/polr1e/polr2i/sik1
GO:0098798	mitochondrial protein complex	4/91	0.131149126187233	mrpl47/mrpl54/ndufa12/sdhc
GO:1902562	H4 histone acetyltransferase complex	3/91	0.0306722985224406	kat8/mrgbp/ruvbl2
GO:0044452	nucleolar part	3/91	0.0528079608232587	gar1/nol6/polr1e
GO:0000123	histone acetyltransferase complex	3/91	0.0597901506161241	kat8/mrgbp/ruvbl2
GO:0030117	membrane coat	3/91	0.0620027813434622	ap1s2/copb1/sec13
GO:0031248	protein acetyltransferase complex	3/91	0.0620027813434622	kat8/mrgbp/ruvbl2
GO:0048475	coated membrane	3/91	0.0620027813434622	ap1s2/copb1/sec13
GO:1902493	acetyltransferase complex	3/91	0.0620027813434622	kat8/mrgbp/ruvbl2
GO:0015934	large ribosomal subunit	3/91	0.0779825310703118	mrpl47/mrpl54/rpl39
GO:0044445	cytosolic part	3/91	0.156685400310493	eno1a/rpl39/rps13
GO:0044455	mitochondrial membrane part	3/91	0.156685400310493	ndufa12/oxa1l/sdhc
GO:0005743	mitochondrial inner membrane	3/91	0.216819748812589	ndufa12/oxa1l/sdhc
GO:0005815	microtubule organizing center	3/91	0.244578889947265	cenpj/ift88/plk1
GO:0019866	organelle inner membrane	3/91	0.252299569942971	ndufa12/oxa1l/sdhc
GO:0031966	mitochondrial membrane	3/91	0.318277502610652	ndufa12/oxa1l/sdhc
GO:0005740	mitochondrial envelope	3/91	0.349196347586807	ndufa12/oxa1l/sdhc
GO:0044432	endoplasmic reticulum part	3/91	0.453655979751808	elovl7b/rnft1/sec13

Table 6.5: GO analysis of DMH-1 treated embryos by molecular function. Only those GO IDs with 3 or more genes are shown.

GO ID	Description	Gene Ratio	Q-Value	Genes
GO:0048037	cofactor binding	6/93	0.288258612580738	aoc2/egln3/pole/ptgs2b/sdhc/ugdh
GO:0003735	structural constituent of ribosome	5/93	0.0945646346924154	mrpl18/mrpl47/mrpl54/rpl39/rps13
GO:0005085	guanyl-nucleotide exchange factor activity	5/93	0.169739325582307	arhgef39/eif2b2/rabif/rasgef1ba/trioa
GO:0051020	GTPase binding	5/93	0.288258612580738	arhgef39/eif2b2/rabif/rasgef1ba/trioa
GO:0140097	catalytic activity, acting on DNA	4/93	0.266497599045994	helq/mus81/pole/ruvbl2
GO:0016903	oxidoreductase activity, acting on the aldehyde or oxo group of donors	3/93	0.0945646346924154	adh8b/aldh1a2/pdha1a
GO:0008135	translation factor activity, RNA binding	3/93	0.266497599045994	eif2b2/eif4a1b/etf1b
GO:0004386	helicase activity	3/93	0.288258612580738	eif4a1b/helq/ruvbl2
GO:0005088	Ras guanyl-nucleotide exchange factor activity	3/93	0.288258612580738	arhgef39/rasgef1ba/trioa
GO:0016779	nucleotidyltransferase activity	3/93	0.288258612580738	pole/polr1e/polr2i
GO:0003682	chromatin binding	3/93	0.295419050255376	ewsr1a/mta3/nkap
GO:0003712	transcription coregulator activity	3/93	0.299357714770736	junba/mta3/noc2l
GO:0008134	transcription factor binding	3/93	0.313558775190939	junba/mta3/noc2l
GO:0017016	Ras GTPase binding	3/93	0.370277702319177	arhgef39/rasgef1ba/trioa
GO:0031267	small GTPase binding	3/93	0.370277702319177	arhgef39/rasgef1ba/trioa
GO:0140098	catalytic activity, acting on RNA	3/93	0.370277702319177	eif4a1b/polr1e/polr2i
GO:0003779	actin binding	3/93	0.442086295385402	cald1a/coro1cb/scinla
GO:0000977	RNA polymerase II regulatory region sequence-specific DNA binding	3/93	0.48652261428042	fosab/junba/purab
GO:0001012	RNA polymerase II regulatory region DNA binding	3/93	0.488811850784033	fosab/junba/purab
GO:0044877	protein-containing complex binding	3/93	0.507860989148506	coro1cb/mrrf/scinla
GO:0000981	DNA-binding transcription factor activity, RNA polymerase II-specific	3/93	0.507860989148506	elf3/junba/purab
GO:0000976	transcription regulatory region sequence-specific DNA binding	3/93	0.552878488685487	fosab/junba/purab

Table 6.6: GO analysis of *VAX2* overexpression embryos by biological function. Only those GO IDs with 4 or more genes are shown.

GO ID	Description	Gene Ratio	Q-Value	Genes
GO:0051726	regulation of cell cycle	9/131	0.397138538510116	alms1/ccnl1a/cdc6/cdk1/junba/plk1/plk2b/rpl36a/tsc1b
GO:0061061	muscle structure development	8/131	0.397138538510116	ache/atoh8/hand2/mef2ca/prmt5/slc8a1a/tbx5a/tpm4a
GO:0045595	regulation of cell differentiation	8/131	0.464502183852044	atoh8/churc1/epha4l/junba/mef2ca/nog1/prmt5/zc4h2
GO:0007167	enzyme linked receptor protein signaling pathway	8/131	0.464502183852044	churc1/cpne3/epha2a/epha4l/nog1/shcbp1/smad9/tsc1b
GO:0051146	striated muscle cell differentiation	7/131	0.397138538510116	ache/hand2/mef2ca/prmt5/slc8a1a/tbx5a/tpm4a
GO:0042692	muscle cell differentiation	7/131	0.397138538510116	ache/hand2/mef2ca/prmt5/slc8a1a/tbx5a/tpm4a
GO:0003002	regionalization	7/131	0.464502183852044	aldh1a2/churc1/en2b/naa50/nog1/scinla/smad9
GO:0022402	cell cycle process	7/131	0.464502183852044	alms1/cdc6/cdk1/ift88/naa50/plk1/plk2b
GO:0014706	striated muscle tissue development	6/131	0.397138538510116	atoh8/hand2/mef2ca/prmt5/tbx5a/tpm4a
GO:0060537	muscle tissue development	6/131	0.399593604146941	atoh8/hand2/mef2ca/prmt5/tbx5a/tpm4a
GO:0007169	transmembrane receptor protein tyrosine kinase signaling pathway	6/131	0.460025872884107	churc1/cpne3/epha2a/epha4l/shcbp1/tsc1b
GO:0051186	cofactor metabolic process	6/131	0.464502183852044	ciapin1/fpgs/lias/mrps36/pdha1a/rpe
GO:0048589	developmental growth	6/131	0.464502183852044	aldh1a2/epha4l/fosab/fus/krt5/sp2
GO:0001501	skeletal system development	6/131	0.464502183852044	aldh1a2/hand2/mbtps1/mef2ca/nog1/sec13
GO:0040007	growth	6/131	0.464502183852044	aldh1a2/epha4l/fosab/fus/krt5/sp2
GO:0071495	cellular response to endogenous stimulus	6/131	0.464502183852044	churc1/junba/nog1/shcbp1/smad9/tsc1b
GO:0006412	translation	6/131	0.464502183852044	eif1axa/eif2b2/mrps16/mrrf/rpl13a/rpl36a
GO:0043043	peptide biosynthetic process	6/131	0.464502183852044	eif1axa/eif2b2/mrps16/mrrf/rpl13a/rpl36a
GO:0045944	positive regulation of transcription by RNA polymerase II	6/131	0.464502183852044	junba/lhx6/lhx8a/mef2ca/osr2/tbx5a
GO:0001654	eye development	6/131	0.464502183852044	aldh1a2/atoh8/ift88/scinla/sec13/tbx5a
GO:0150063	visual system development	6/131	0.464502183852044	aldh1a2/atoh8/ift88/scinla/sec13/tbx5a
GO:0000278	mitotic cell cycle	6/131	0.465193374566939	cdc6/cdk1/ift88/naa50/plk1/plk2b
GO:0045934	negative regulation of nucleobase-containing compound metabolic process	6/131	0.469079623895896	junba/nkap/osr2/smad9/tbx5a/ten1
GO:0070647	protein modification by small protein conjugation or removal	6/131	0.469079623895896	dcaf17/otud5b/socs3b/ube2g1a/uchl3/wdr32
GO:0009719	response to endogenous stimulus	6/131	0.475283538166677	churc1/junba/nog1/shcbp1/smad9/tsc1b
GO:0001708	cell fate specification	5/131	0.397138538510116	churc1/en2b/nog1/tbx5a/zc4h2
GO:0060047	heart contraction	5/131	0.397138538510116	hand2/junba/myzap/slc8a1a/tpm4a

GO:0003015	heart process	5/131	0.397138538510116	hand2/junba/myzap/slc8a1a/tpm4a
GO:0045165	cell fate commitment	5/131	0.406554457575965	churc1/en2b/nog1/tbx5a/zc4h2
GO:0048193	Golgi vesicle transport	5/131	0.406554457575965	copb1/rabif/sec13/stx5a/tfg
GO:0072657	protein localization to membrane	5/131	0.408165979589204	arl5a/oxa1l/ssr3/tspan14/zgc:162193
GO:0055002	striated muscle cell development	5/131	0.430365312325036	ache/mef2ca/prmt5/slc8a1a/tpm4a
GO:0055001	muscle cell development	5/131	0.430365312325036	ache/mef2ca/prmt5/slc8a1a/tpm4a
GO:0008015	blood circulation	5/131	0.464502183852044	hand2/junba/myzap/slc8a1a/tpm4a
GO:0003013	circulatory system process	5/131	0.464502183852044	hand2/junba/myzap/slc8a1a/tpm4a
GO:0007368	determination of left/right symmetry	5/131	0.464502183852044	aldh1a2/atoh8/hand2/ift88/tbx5a
GO:0009799	specification of symmetry	5/131	0.464502183852044	aldh1a2/atoh8/hand2/ift88/tbx5a
GO:0009855	determination of bilateral symmetry	5/131	0.464502183852044	aldh1a2/atoh8/hand2/ift88/tbx5a
GO:0005975	carbohydrate metabolic process	5/131	0.464502183852044	fuca2/galm/gla/hexa/rpe
GO:0061024	membrane organization	5/131	0.464502183852044	oxa1l/picalma/sec13/stx5a/tfg
GO:0009117	nucleotide metabolic process	5/131	0.464502183852044	pdha1a/rpe/rrm2b/sdhaf2/sdhc
GO:0006753	nucleoside phosphate metabolic process	5/131	0.464502183852044	pdha1a/rpe/rrm2b/sdhaf2/sdhc
GO:0009628	response to abiotic stimulus	5/131	0.464502183852044	exorh/ift88/junba/kcnma1a/swi5
GO:0006325	chromatin organization	5/131	0.465193374566939	naa50/nap1l4a/prmt5/spty2d1/taf12
GO:0055086	nucleobase-containing small molecule metabolic process	5/131	0.506645356748795	pdha1a/rpe/rrm2b/sdhaf2/sdhc
GO:0045892	negative regulation of transcription, DNA-templated	5/131	0.506645356748795	junba/nkap/osr2/smad9/tbx5a
GO:1902679	negative regulation of RNA biosynthetic process	5/131	0.506645356748795	junba/nkap/osr2/smad9/tbx5a
GO:1903507	negative regulation of nucleic acid-templated transcription	5/131	0.506645356748795	junba/nkap/osr2/smad9/tbx5a
GO:0097435	supramolecular fiber organization	5/131	0.512266286192752	ache/cdc42ep5/mef2ca/slc8a1a/tpm4a
GO:0051253	negative regulation of RNA metabolic process	5/131	0.526961603776542	junba/nkap/osr2/smad9/tbx5a
GO:0030097	hemopoiesis	5/131	0.538723073934483	ciapin1/fosab/jak1/nap1l4a/smad9
GO:0007420	brain development	5/131	0.538723073934483	aldh1a2/en2b/lhx6/lhx8a/scinla
GO:0048534	hematopoietic or lymphoid organ development	5/131	0.538723073934483	ciapin1/fosab/jak1/nap1l4a/smad9
GO:0002520	immune system development	5/131	0.538723073934483	ciapin1/fosab/jak1/nap1l4a/smad9
GO:0030036	actin cytoskeleton organization	5/131	0.538723073934483	ache/cdc42ep5/mef2ca/slc8a1a/tpm4a
GO:0060322	head development	5/131	0.542955710699592	aldh1a2/en2b/lhx6/lhx8a/scinla
GO:0030029	actin filament-based process	5/131	0.548446415212225	ache/cdc42ep5/mef2ca/slc8a1a/tpm4a
GO:0033339	pectoral fin development	4/131	0.397138538510116	aldh1a2/hand2/osr2/tbx5a
GO:0055007	cardiac muscle cell differentiation	4/131	0.397138538510116	hand2/mef2ca/tbx5a/tpm4a

GO:0035051	cardiocyte differentiation	4/131	0.397138538510116	hand2/mef2ca/tbx5a/tpm4a
GO:0006888	ER to Golgi vesicle-mediated transport	4/131	0.397138538510116	copb1/sec13/stx5a/tfg
GO:0033333	fin development	4/131	0.397138538510116	aldh1a2/hand2/osr2/tbx5a
GO:0048736	appendage development	4/131	0.397138538510116	aldh1a2/hand2/osr2/tbx5a
GO:0030239	myofibril assembly	4/131	0.406554457575965	ache/mef2ca/slc8a1a/tpm4a
GO:0065004	protein-DNA complex assembly	4/131	0.406554457575965	nap1l4a/spty2d1/swi5/taf12
GO:0010927	cellular component assembly involved in morphogenesis	4/131	0.406554457575965	ache/mef2ca/slc8a1a/tpm4a
GO:0048738	cardiac muscle tissue development	4/131	0.406554457575965	hand2/mef2ca/tbx5a/tpm4a
GO:0016050	vesicle organization	4/131	0.406554457575965	picalma/sec13/stx5a/tfg
GO:0055123	digestive system development	4/131	0.430365312325036	aldh1a2/hand2/rps6ka3a/sec13
GO:0071824	protein-DNA complex subunit organization	4/131	0.430365312325036	nap1l4a/spty2d1/swi5/taf12
GO:0031032	actomyosin structure organization	4/131	0.464502183852044	ache/mef2ca/slc8a1a/tpm4a
GO:0061053	somite development	4/131	0.464502183852044	aldh1a2/churc1/copb1/naa50
GO:0051216	cartilage development	4/131	0.464502183852044	mbtps1/mef2ca/nog1/sec13
GO:0010564	regulation of cell cycle process	4/131	0.464502183852044	alms1/cdc6/plk1/plk2b
GO:0061448	connective tissue development	4/131	0.464502183852044	mbtps1/mef2ca/nog1/sec13
GO:0009314	response to radiation	4/131	0.464502183852044	exorh/ift88/junba/swi5
GO:0031099	regeneration	4/131	0.464502183852044	aldh1a2/alms1/fosab/krt5
GO:0048592	eye morphogenesis	4/131	0.464502183852044	aldh1a2/ift88/sec13/tbx5a
GO:0006732	coenzyme metabolic process	4/131	0.464502183852044	fpgs/lias/pdha1a/rpe
GO:0007005	mitochondrion organization	4/131	0.464502183852044	atg12/chchd2/oxa1l/sdhaf2
GO:1904888	cranial skeletal system development	4/131	0.464502183852044	aldh1a2/hand2/myt1a/uchl3
GO:0051301	cell division	4/131	0.464502183852044	cdc6/cdk1/plk1/plk2b
GO:0009952	anterior/posterior pattern specification	4/131	0.464502183852044	aldh1a2/churc1/en2b/naa50
GO:0060562	epithelial tube morphogenesis	4/131	0.464502183852044	aldh1a2/atoh8/hand2/tbx5a
GO:0003007	heart morphogenesis	4/131	0.464502183852044	atoh8/hand2/mef2ca/tbx5a
GO:0048732	gland development	4/131	0.464502183852044	aldh1a2/hand2/mbtps1/sec13
GO:0033365	protein localization to organelle	4/131	0.464502183852044	arl5a/nxt2/oxa1l/ssr3
GO:0071363	cellular response to growth factor stimulus	4/131	0.464502183852044	churc1/nog1/shcbp1/smad9
GO:0070848	response to growth factor	4/131	0.464502183852044	churc1/nog1/shcbp1/smad9
GO:0090596	sensory organ morphogenesis	4/131	0.465193374566939	aldh1a2/ift88/sec13/tbx5a
GO:1903047	mitotic cell cycle process	4/131	0.46594616874188	cdc6/cdk1/ift88/naa50
GO:0051640	organelle localization	4/131	0.469079623895896	ift88/picalma/stx5a/tfg
GO:0019693	ribose phosphate metabolic process	4/131	0.47700241152387	pdha1a/rpe/sdhaf2/sdhc
GO:1901700	response to oxygen-containing compound	4/131	0.501094569377881	ache/cxcl18b/junba/tsc1b
GO:0016567	protein ubiquitination	4/131	0.53542102345104	dcaf17/socs3b/ube2g1a/wdr32

GO:0043010	camera-type eye development	4/131	0.538723073934483	aldh1a2/atoh8/sec13/tbx5a
GO:0022603	regulation of anatomical structure morphogenesis	4/131	0.548446415212225	cdc42ep5/churc1/epha4l/nog1
GO:0032446	protein modification by small protein conjugation	4/131	0.55045087049606	dcaf17/socs3b/ube2g1a/wdr32
GO:0007264	small GTPase mediated signal transduction	4/131	0.571001961345614	cdc42ep5/rab22a/rabif/rabl2
GO:0048562	embryonic organ morphogenesis	4/131	0.57232511091715	aldh1a2/atoh8/hand2/tbx5a
GO:0033043	regulation of organelle organization	4/131	0.593083796762339	alms1/cdc42ep5/spty2d1/ten1
GO:0030001	metal ion transport	4/131	0.598976774726152	atp1a1b/kcnma1a/plch2a/slc8a1a
GO:0002009	morphogenesis of an epithelium	4/131	0.600942691578146	aldh1a2/atoh8/hand2/tbx5a
GO:0006259	DNA metabolic process	4/131	0.614245042682158	cdc6/polr2i/swi5/ten1

Table 6.7: GO analysis of *VAX2* overexpression embryos by cellular component. Only those GO IDs with 3 or more genes are shown.

GO ID	Description	Gene Ratio	Q-Value	Genes
GO:0005730	nucleolus	7/128	0.237745405898944	dcaf17/fam32a/fbxw11b/polr2i/polr2l/rrp36/spty2d1
GO:0044429	mitochondrial part	7/128	0.405683289368607	ciapin1/mrps16/mrps36/oxa1l/sdhaf2/sdhc/slc25a26
GO:0044451	nucleoplasm part	6/128	0.405683289368607	atoh8/med16/pnisr/polr2i/polr2l/taf12
GO:0044454	nuclear chromosome part	5/128	0.405683289368607	en2b/junba/mef2ca/swi5/ten1
GO:0000228	nuclear chromosome	5/128	0.405683289368607	en2b/junba/mef2ca/swi5/ten1
GO:0045202	synapse	5/128	0.448204355816395	ache/nog1/picalma/pnisr/zc4h2
GO:0044427	chromosomal part	5/128	0.506922368499021	en2b/junba/mef2ca/swi5/ten1
GO:0000790	nuclear chromatin	4/128	0.405683289368607	en2b/junba/mef2ca/swi5
GO:0005667	transcription factor complex	4/128	0.407816607865944	fosab/junba/smad9/taf12
GO:0005815	microtubule organizing center	4/128	0.412351308989711	alms1/ift88/plk1/plk2b
GO:0000785	chromatin	4/128	0.448204355816395	en2b/junba/mef2ca/swi5
GO:0098791	Golgi subcompartment	4/128	0.49249087410563	arl5a/copb1/fam91a1/stx5a
GO:0005740	mitochondrial envelope	4/128	0.506922368499021	ciapin1/oxa1l/sdhc/slc25a26
GO:0044431	Golgi apparatus part	4/128	0.506922368499021	arl5a/copb1/fam91a1/stx5a
GO:0098805	whole membrane	4/128	0.560400358118898	atg12/ccz1/copb1/sec13
GO:0016591	RNA polymerase II, holoenzyme	3/128	0.333431484353188	polr2i/polr2l/taf12
GO:0055029	nuclear DNA-directed RNA polymerase complex	3/128	0.405683289368607	polr2i/polr2l/taf12
GO:0000428	DNA-directed RNA polymerase complex	3/128	0.405683289368607	polr2i/polr2l/taf12
GO:0030880	RNA polymerase complex	3/128	0.405683289368607	polr2i/polr2l/taf12
GO:0030135	coated vesicle	3/128	0.405683289368607	copb1/picalma/sec13
GO:0005819	spindle	3/128	0.405683289368607	cdk1/plk1/plk2b
GO:0005759	mitochondrial matrix	3/128	0.405683289368607	mrps16/mrps36/sdhaf2
GO:0044391	ribosomal subunit	3/128	0.405683289368607	mrps16/rpl13a/rpl36a
GO:0044445	cytosolic part	3/128	0.407816607865944	rpl13a/rpl36a/tsc1b
GO:0005813	centrosome	3/128	0.407816607865944	alms1/plk1/plk2b
GO:0005840	ribosome	3/128	0.448073673936832	mrps16/rpl13a/rpl36a
GO:0061695	transferase complex, transferring phosphorus-containing groups	3/128	0.465102292816483	polr2i/polr2l/taf12
GO:0098798	mitochondrial protein complex	3/128	0.465772163611184	mrps16/mrps36/sdhc
GO:0005773	vacuole	3/128	0.485612959553385	ccz1/fuca2/nbr1a
GO:0005743	mitochondrial inner membrane	3/128	0.4983784877586	oxa1l/sdhc/slc25a26
GO:0044433	cytoplasmic vesicle part	3/128	0.506922368499021	ccz1/copb1/sec13
GO:0019866	organelle inner membrane	3/128	0.522422761524791	oxa1l/sdhc/slc25a26

GO:0044456	synapse part	3/128	0.540165545563242	picalma/pnisr/zc4h2
GO:0098590	plasma membrane region	3/128	0.563010274196065	picalma/slc29a2/zc4h2
GO:0031966	mitochondrial membrane	3/128	0.581646386339559	oxa1l/sdhc/slc25a26
GO:0030054	cell junction	3/128	0.650814617631552	ache/cldn11a/zc4h2
GO:0099512	supramolecular fiber	3/128	0.67895086935437	fhl3a/krt5/tpm4a
GO:0099080	supramolecular complex	3/128	0.67895086935437	fhl3a/krt5/tpm4a
GO:0099081	supramolecular polymer	3/128	0.67895086935437	fhl3a/krt5/tpm4a
GO:0044432	endoplasmic reticulum part	3/128	0.709400132744054	lmf2b/mfsd2ab/sec13

Table 6.8: GO analysis of *VAX2* overexpression embryos by molecular function. Only those GO IDs with 3 or more genes are shown.

GO ID	Description	Gene Ratio	Q-Value	Genes
GO:0000977	RNA polymerase II regulatory region sequence-specific DNA binding	9/127	0.221573738711303	fosab/junba/lhx6/lhx8a/mef2ca/myt1a/osr2/pitx1/tbx5a
GO:0001012	RNA polymerase II regulatory region DNA binding	9/127	0.221573738711303	fosab/junba/lhx6/lhx8a/mef2ca/myt1a/osr2/pitx1/tbx5a
GO:0000976	transcription regulatory region sequence-specific DNA binding	9/127	0.285643612040205	fosab/junba/lhx6/lhx8a/mef2ca/myt1a/osr2/pitx1/tbx5a
GO:0046983	protein dimerization activity	7/127	0.407240486158337	aifm1/atoh8/fbxw11b/hand2/mef2ca/smad9/taf12
GO:0000981	DNA-binding transcription factor activity, RNA polymerase II-specific	6/127	0.407240486158337	junba/lhx6/lhx8a/myt1a/sp2/tbx5a
GO:0048037	cofactor binding	6/127	0.407240486158337	aifm1/ciapin1/ctbp1/lias/p3h2/sdhc
GO:0000978	RNA polymerase II proximal promoter sequence-specific DNA binding	5/127	0.385614740305175	fosab/junba/mef2ca/pitx1/tbx5a
GO:0000987	proximal promoter sequence-specific DNA binding	5/127	0.385614740305175	fosab/junba/mef2ca/pitx1/tbx5a
GO:0008134	transcription factor binding	4/127	0.407240486158337	junba/pitx1/taf12/tbx5a
GO:0051020	GTPase binding	4/127	0.533253705411162	cdc42ep5/eif2b2/micall1a/rabif
GO:0016903	oxidoreductase activity, acting on the aldehyde or oxo group of donors	3/127	0.221573738711303	aldh1a2/mrps36/pdha1a
GO:0004553	hydrolase activity, hydrolyzing O-glycosyl compounds	3/127	0.407240486158337	fuca2/gla/hexa
GO:0016798	hydrolase activity, acting on glycosyl bonds	3/127	0.407240486158337	fuca2/gla/hexa
GO:0004713	protein tyrosine kinase activity	3/127	0.407240486158337	epha2a/epha4l/jak1
GO:0003735	structural constituent of ribosome	3/127	0.407240486158337	mrps16/rpl13a/rpl36a
GO:0008237	metallopeptidase activity	3/127	0.407240486158337	metap1/metap1d/mmp11b
GO:0050662	coenzyme binding	3/127	0.512351523133015	aifm1/ctbp1/p3h2
GO:0140098	catalytic activity, acting on RNA	3/127	0.613777345869569	endouc/polr2i/polr2l
GO:0022804	active transmembrane transporter activity	3/127	0.686494170454177	atp1a1b/mfsd2ab/slc8a1a
GO:0015077	monovalent inorganic cation transmembrane transporter activity	3/127	0.721837559589168	atp1a1b/kcnma1a/slc8a1a
GO:0008289	lipid binding	3/127	0.73824634683886	cpne3/exorh/picalma
GO:0046873	metal ion transmembrane transporter activity	3/127	0.741667678287759	atp1a1b/kcnma1a/slc8a1a
GO:0004175	endopeptidase activity	3/127	0.741667678287759	mbtps1/mmp11b/psma5
GO:0044877	protein-containing complex binding	3/127	0.757431942395649	mrrf/scinla/tpm4a
GO:0001883	purine nucleoside binding	3/127	0.780521710733831	arl5a/rab22a/rabl2
GO:0005525	GTP binding	3/127	0.780521710733831	arl5a/rab22a/rabl2
GO:0032550	purine ribonucleoside binding	3/127	0.780521710733831	arl5a/rab22a/rabl2

Table 6.9: List of genes found to be differentially expressed in both experimental conditions.

Gene	logFoldChange upon DMH-1 treatment		logFoldChange upon *VAX2* Overexpression		COG Annotation	eggNOG Annotation
aldh1a2	-1.23565256428171	down	2.4935906715258	up	Energy production and conversion	Aldehyde dehydrogenase 1 family member A2
eif2b2	-1.27936842248493	down	-1.57064997542013	down	Function unknown	Reverse transcriptase (RNA-dependent DNA polymerase)
fosab	-1.72346952080195	down	2.10154508711769	up	-	-
fuca2	1.864490871387	up	1.38509153612313	up	Carbohydrate transport and metabolism	fucosidase, alpha-L-2, plasma
ift88	-1.73086290760156	down	1.91881663199302	up	Function unknown	Intraflagellar transport protein 88 homolog
junba	-1.55553359835329	down	1.62873811225336	up	Transcription	Jun B proto-oncogene
mrrf	-1.0559178498648	down	-1.51558909950499	down	Translation, ribosomal structure and biogenesis	Mitochondrial ribosome recycling factor
nap1l4a	1.98166097399321	up	2.30648799091439	up	-	nucleosome assembly
nkap	-1.69352642353153	down	2.50113842748796	up	Function unknown	NFKB activating protein
nxt2	1.04352971120668	up	-1.40231321679007	down	-	-
oxa1l	-1.24042688122005	down	2.12045543825539	up	Function unknown	Transposase
pbdc1	1.52994498709485	up	3.32952772223078	up	-	-
plk1	2.24980922279183	up	-2.39423494372718	down	Cell cycle control, cell division, chromosome partitioning	polar body extrusion after meiotic divisions
polr2i	-4.11671050396059	down	1.03890589942005	up	-	-
prmt5	-1.00866620956772	down	-1.12083368893331	down	Function unknown	Reverse transcriptase (RNA-dependent DNA polymerase)
psma5	-1.82103264689297	down	1.27949439447822	up	Posttranslational modification, protein turnover, chaperones	threonine-type endopeptidase activity
rabif	1.10512420363662	up	1.43255180599876	up	-	RAB interacting factor
rabl2	-1.21096481198173	down	-1.62777397480185	down	Intracellular trafficking, secretion, and vesicular transport	RAB, member of RAS oncogene family-like 2
rpe	1.56930578960917	up	-2.8699871528484	down	Carbohydrate transport and metabolism	Belongs to the ribulose-phosphate 3-epimerase family
rrm2b	-1.61927447749796	down	-1.18795149823709	down	Nucleotide transport and metabolism	Ribonucleoside-diphosphate reductase subunit
scinla	1.4063721649951	up	2.94559380285823	up	Cytoskeleton	cytoplasmic actin-based contraction

						involved in cell motility
sdhc	1.17136954983114	up	3.01901841005159	up	-	-
sec13	2.34187184225564	up	-2.66644461265323	down	Function unknown	DDE superfamily endonuclease
swi5	-1.51985703999473	down	1.79039183310803	up	-	-
uchl3	-1.02556465966485	down	-2.01819250580399	down	Posttranslational modification, protein turnover, chaperones	Ubiquitin carboxyl-terminal esterase L3 (ubiquitin thiolesterase)

Chapter 7

Conclusions and Future Directions

7.1. Summary of findings

Taken together, the work presented in this thesis advances our current understanding of eye development through its investigation of a novel developmental structure, the superior ocular sulcus (SOS). Previous to the study by Hocking et al. in 2018, presented here in Chapter 3, any knowledge of the SOS was very limited, and we lacked any understanding of the molecular mechanisms regulating the formation and closure of the SOS or its function during eye development. Similarly, while ocular coloboma has been widely studied, descriptions of atypical, superior coloboma were extremely rare in the literature, and the study by Hocking et al. in 2018 and the subsequent work presented throughout this thesis represent the first steps in investigating the etiology in any form, genetic or otherwise, of superior coloboma.

In our initial investigation of atypical, superior coloboma, we used exome sequencing data of our superior coloboma patients to identify candidate genetic variants. Through our subsequent structural analyses in model and non-model organisms, we identified the superior ocular sulcus, a highly-transient structure in the dorsal eye that is present during early eye development. We demonstrated that disrupting dorsal-ventral (DV) eye axis patterning via loss of BMP signaling results in improper closure of the SOS. In addition, we found that the SOS acts as a conduit for blood vessels, and that aberrant SOS closure results in altered vasculogenesis in the early eye. This study was the first in the literature to describe the SOS in detail, outlining its conservation throughout evolution, elucidating the role of dorsal eye patterning genes in its formation and closure, and its functional role in early eye development.

I continued our investigation of the SOS through our study of *VAX2*, presented in Chapter 4. A variant of *VAX2* discovered in Patient #4 was of interest as *VAX2* is also involved in DV eye axis patterning, similar to those investigated previously. However, unlike the genes investigated in Chapter 3, *VAX2* is expressed exclusively in the ventral eye, and it was of great interest to us to elucidate the possible causal role of a ventrally-expressed gene on a dorsal eye structure. Indeed, I discovered that manipulation of *vax2* in zebrafish leads to improper SOS closure delay, similar to our observations in Chapter 3. I also began to investigate the role of apoptosis in SOS closure delay. This study supports a model in which proper maintenance of DV eye axis patterning is a crucial aspect of SOS closure in early eye development.

While the studies presented in Chapters 3 and 4 establish the role of DV eye axis patterning in proper SOS closure, I determined that it cannot be the only developmental process involved, as our analysis of patient-derived exome sequencing data revealed that only some, not all, of the patients have rare variants in genes associated with DV eye axis patterning. In Chapter 5, we identified a rare variant of *TSC2* in Patient #1, and I discovered that knockdown of *tsc2* in early zebrafish development also leads to SOS closure delay. Furthermore, there are rare reports of TSC patients that also present with atypical coloboma (Eagle et al., 2000; Bacci et al., 2021). Taken together with my findings that *tsc2* loss leads to SOS closure delay, this study expands our knowledge of the molecular mechanisms that regulate SOS closure, and it suggests a possible causal role of mTOR signaling in atypical, superior coloboma.

Lastly, I began to expand on our current data set for identifying candidate genes involved in SOS closure via RNA-Seq of our known SOS closure delay models. The study presented in Chapter 6 attempts to address our current reliance on our patient-derived exome sequencing data set, which lack any information regarding inheritance, and forced our previous studies to rely heavily on *in silico* projections and iterative pilot studies that are labour-intensive and expensive. Through this study, I created an RNA-Seq data set, which should not be solely relied upon for identification of candidate genes, but rather should be used together with the exome sequencing data and acts as an additional data set with which to cross-reference when identifying additional candidate genes to pursue.

7.2. Challenges in identification of additional genetic factors regulating the SOS

Ocular coloboma, the ocular disorder that most closely resembles superior coloboma, is widely studied, and its etiology has been associated with a great number of developmental processes as discussed in Chapter 1. However, while over 40 genes have been linked to its causality, the majority of ocular coloboma patients possess mutations in novel loci that have yet to be discovered and studied (Yoon et al., 2020). This is emblematic of the complexity surrounding its disease etiology and eye development as a whole. Many of the mutations in disease-associated loci have incomplete penetrance and are phenotypically undetectable. Conversely, even when

mutations result in a disease phenotype, their expressivity is varied and the severity of phenotypes are diverse; for example, while some patients with *PAX6* variants may present with iris coloboma, others may present with retinochoroidal coloboma (OMIM 607108). In addition, there is a stochastic nature of ocular coloboma as demonstrated by most coloboma patients presenting with unilateral coloboma, rather than bilateral coloboma. This suggests that regardless of the presence of genetic variants that result in ocular coloboma, there is also a randomness in its presentation that may be dictated by additional genetic and/or environmental factors.

Correspondingly, the processes that regulate SOS formation and closure are likely to be similarly complex. Through the studies presented in this thesis, we have identified DV eye axis patterning and mTOR signaling as developmental mechanisms that control SOS formation and closure. Furthermore, additional work from our research group has identified the role of non-canonical Wnt/planar cell polarity (PCP) signaling in regulating SOS closure (Wilson, 2020). However, as outlined in Chapter 1, eye development is an intricate process, and as discussed above, the presentation of ocular coloboma is multifaceted. As such, it is likely that more genetic factors independent of DV eye axis patterning, mTOR signaling, and Wnt/PCP signaling remain to be identified and studied.

These investigations are complicated by the nascent nature of investigations regarding the SOS. Simply put, there is very little that is currently known about the SOS, which leaves too many open avenues to be pursued. While the candidate genes investigated in this thesis were identified in superior coloboma patients, none of the discovered variants were shared amongst the patients. Additionally, while the variants studied here represent some of our best candidate genes identified through consideration of multiple factors, including *in silico* modeling, gene expression area, population frequency, and known functions, many others that meet the same criteria remain uninvestigated.

Paradoxically, the overabundance of candidate genes acts to narrow the scope of investigations into the SOS; our lack of understanding into the SOS also means that there is no certainty that investigation of these genes will yield any actionable information. Previous studies of other variants that meet or exceed the same criteria have failed to show any effect on SOS closure. In Hocking et al., 2018 (section not included in Chapter 3), we described a patient-

identified variant in *CYP1B1*, a gene that encodes a key retinoic acid (RA) synthesis enzyme, which strongly met all of our criteria as a possible candidate gene for regulation of SOS formation and closure; Patient #2 carried compound heterozygous mutations for *CYP1B1*, and both mutations were strongly predicted to be detrimental for protein structure and function. In addition, mutations in *CYP1B1* are known to cause ocular malformation, being identified as a major cause of congenital and adult glaucoma (Faiq et a., 2015). However, examination of zebrafish *cyp1b1*-null mutants failed to reveal any defects in SOS closure (Hocking et al., 2018). Similarly, investigations of patient-identified variants of *FZD4* (Patient #1) and *SHROOM3* (Patient #3), both of which are involved in non-canonical Wnt/PCP signaling and met the highest criteria in our identification of candidate genes, revealed no significant abnormal SOS closure phenotypes in zebrafish knockdown studies (Wilson, 2020). As these investigations are both laborious and expensive, but are not guaranteed to yield useful information, the barrier of entry to identifying additional genetic factors involved in SOS formation and closure remains high.

To address these challenges, future studies of the SOS could be supported by the creation of additional data sets with which to compare our current list of candidate genes. For example, single-cell RNA-Seq of the embryonic eye during the time of SOS formation and closure could elucidate the gene expression level changes that correspond with the structural changes. Furthermore, a single-cell RNA-Seq approach would allow the experimenter to investigate changes in gene expression within the cells that are specifically adjacent to the SOS. This may provide useful insight in identifying genes that play roles in highly-localized processes, such as breakdown of basement membrane or vasculature guidance, that may not affect the development of the entire eye, but are nevertheless crucial for proper SOS closure. In addition, a drug screen experiment using pharmacological activators/inhibitors of various signaling pathways may yield actionable information regarding the signaling pathways that are crucial for proper SOS formation and closure. Identification of signaling pathways involved in SOS formation and closure will provide the experimenter with yet another criterion through which the candidate genes can be filtered through, allowing a more efficient process in identifying variants that affect the SOS and are involved in the genetic etiology of superior coloboma. Furthermore, identification of pharmacological agents that affect SOS closure will allow for a more systematic, methodical

approach in studying the combinatorial effects of various genetic and/or environmental factors as discussed later.

While our studies of the SOS in animal models have been promising in identifying genes that affect SOS closure, the study of superior coloboma and its genetic etiology is further complicated by our lack of knowledge regarding its heritability; as the whole-exome sequencing data set is based on unrelated patients and no information regarding their family members exists, it is impossible to determine if disease etiology follows Mendelian inheritance patterns or is due to *de novo* mutations. Similar complexities in the study of rare diseases have been ameliorated in recent years through the increasingly widespread use of next-generation sequencing (NGS) technologies in conjunction with rapid development of databases and information-sharing capabilities. These advancements have allowed researchers to sequence the whole exomes or genomes of patients to screen for disease-causing genes and to share information regarding disease-causing genes, thereby uncovering disease etiology with greater efficiency and improving diagnostic accuracy (Shen et al., 2015; Fernandez-Marmiesse et al., 2018; Jia & Shi, 2017). As more cases become reported in the literature, it will be important to establish a better understanding of heritability in studying the genetic etiology of atypical, superior coloboma.

7.3. Complexities of identifying variability and comorbidities in superior coloboma patients

As discussed in Chapter 1, typical, inferior ocular coloboma manifests due to the failure of the choroid fissure to close, and the location of the coloboma along the long axis of the eye (front to back) depends on the severity of the choroid fissure closure failure. Correspondingly, questions regarding the variability in the presentation of superior coloboma remain. In our cohort of patients discussed in Chapter 3, many present with superior iris coloboma, but some patients present with additional retinochoroidal coloboma or optic nerve coloboma. In addition, more patients with superior iris and retinochoroidal colobomata have been identified in the literature (Jain et al., 2018; Kumar et al., 2020). The identification of atypical, superior colobomata that lie posterior to the iris suggests that it is possible that patients may present with superior retinochoroidal/optic nerve coloboma without the presence of iris coloboma, similar to that observed in ocular coloboma of

the inferior eye. Indeed, the identification of a patient with superior retinochoroidal coloboma without iris (Patient #7) within the cohort presented in Chapter 3 supports this idea. Since retinochoroidal/optic nerve coloboma cannot be identified without fundus imagery, it is possible that some patients with superior coloboma may go undetected.

Likewise, two of the superior coloboma patients presented in Chapter 3 present with microphthalmia. Microphthalmia is commonly associated with inferior ocular coloboma due to the two disorders sharing many overlaps in their respective genetic etiologies (Yoon et al., 2020). However, the association between microphthalmia and superior coloboma remains unclear; our current understanding of genetic etiology surrounding superior coloboma lacks depth. While I note the presence of microphthalmia in high-dosage *VAX2* mRNA-injected embryos in Chapter 4, microphthalmia can be caused by general mRNA toxicity at high dosages. Furthermore, other patients with microphthalmia in addition to superior coloboma have not been identified in the literature thus far. Despite this, due to the strong association between microphthalmia and inferior ocular coloboma, the possibility of an association between microphthalmia and atypical, superior coloboma remains an intriguing question for future investigations.

7.4. Future investigations of combinatory effects in etiology of superior coloboma

A rare disease is defined as any disease that affects fewer than 200,000 people in the United States (US) or less than 1 in 2,000 people in the European Union (Bavisetty et al., 2013). Collectively, an estimated 6,000-8,000 rare diseases have been identified, 75% of which affect children (Shen et al., 2015). Historically, the low prevalence and the heterogeneity of these diseases have led to major difficulties in understanding their etiology and developing treatments. It is believed that 80% or more of rare disease are genetic in nature, and while many involve just a single gene, others may involve multiple genes (Pober, 2010). In some diseases, a single mutation amongst multiple genes may result in a disease phenotype, while others are multigenic, requiring multiple genes to be affected simultaneously (D'Andrea, 2010; Dale & Link, 2009). In addition, disease severity is varies depending on the mutations present in a single gene or different combinations of mutations in multiple genes (Institute of Medicine, 2010).

These complexities are commonly found in diseases that affect the eye, and specifically, in MAC disorders. MAC disorders can be caused by mutations in various genes, and conversely, the genes associated with MAC are often pleiotropic and associated with other disorders. The effect of pleiotropy and the multigenic nature of MAC disorders are best exemplified in a study by Ye et al. (2010). In an investigation of patients carrying known variants of *GDF3* associated with MAC, it was discovered that the autosomal dominant p.Arg266Cys variant of *GDF3* led to bilateral coloboma and microphthalmia in a multigenerational pedigree from Europe, while the presence of the same allele in an unrelated pedigree found in North America led to skeletal phenotypes but was not strongly associated with ocular phenotypes (Ye et al., 2010). Yet, subsequent analysis in the zebrafish ortholog, *dvr1*, established the importance of *GDF3* in ocular and skeletal development, with *dvr1* loss leading to both ocular and skeletal abnormalities in zebrafish embryos (Ye et al., 2010). This suggests that the discrepancy between the two unrelated pedigrees may be due to the role of additional background mutations (inherited or *de novo*) that sensitize certain individuals to specific phenotypes.

As discussed throughout this thesis, similarities between ocular coloboma and superior coloboma are strong. First, we have identified multiple signaling pathways that affect SOS closure, similar to that seen in ocular coloboma and choroid fissure closure. Second, the genes involved in the etiology of superior coloboma are likely to be pleiotropic, as the superior coloboma patients discussed in Chapter 3 often present with other disorders (Table 3.1). Third, being an extremely rare disease with very few reported cases in the literature, superior coloboma is likely to be multifactorial in its disease etiology.

Furthermore, similar to other zebrafish studies of choroid fissure closure, we have found that a persistent abnormal SOS phenotype is extremely rare in our models of SOS closure delay (James et al., 2016; Hocking et al., 2018). Throughout the studies of the SOS described in this thesis, we have only noted two *gdf6a*$^{-/-}$ zebrafish with superior colobomata that persisted into adulthood (Fig. 3.9); superior coloboma was not found in any other adult zebrafish observed throughout these studies. The failure to identify superior colobomata even amongst other *gdf6a*$^{-/-}$ adult zebrafish suggests that the loss of *gdf6a* is not solely responsible for the superior coloboma phenotype, but rather that the two fish with persistent superior colobomata were made susceptible

to the phenotype due to additional sensitizing background mutations or unknown environmental factors.

The effect of background mutations on the presentation of superior coloboma is further complicated by the genotypic/phenotypic discrepancies observed between the zebrafish models of abnormal SOS closure and the human patients. Although we eventually observe normal eye formation following transient SOS closure delay in zebrafish homozygous mutant models, the superior coloboma patients are often heterozygous for the same genes. This suggests that the patients were made sensitized to the superior coloboma phenotype due to the presence of additional background mutations that have yet to be characterized. Thus, our findings support the idea that superior coloboma is a multifactorial disorder, with a single variant in a single signaling pathway being unlikely to result in disease phenotype.

Our deepening knowledge of the signaling pathways involved in SOS formation and closure should facilitate future investigations into the multifactorial nature of superior coloboma. In addition to identifying additional signaling pathways and genetic factors involved in superior coloboma, future studies should examine the consequences of manipulating a combination of signaling pathways that we have identified to be associated with SOS formation and closure. For example, future investigation could examine the combinatorial role of *vax2* loss and *vangl2* loss (identified in Wilson, 2019) on the persistence of abnormal SOS closure. In addition, the identification of pharmacological agents that can affect proper SOS closure as discussed above will allow for more efficient analysis of combinatorial effects, as it will alleviate the need to develop genetic models for each variant identified prior to studying the additive role of the signaling pathway affected.

As we continue to elucidate the underlying genetic causes of superior coloboma and the mechanisms that regulate SOS formation and closure, there will be growing pains associated with being in the nascent stages of investigating a novel embryonic structure. Nevertheless, continued studies of the SOS will expand our current understanding of eye development, especially as we begin to fully understand its role in embryogenesis. Uncovering these mechanisms will provide valuable insight into the etiology of superior coloboma and be crucial in subsequent applications in diagnostics and therapeutics.

References

Abouzeid, H., Favez, T., Schmid, A., Agosti, C., Youssef, M., Marzouk, I., . . . Schorderet, D. F. (2014). Mutations in ALDH1A3 represent a frequent cause of microphthalmia/anophthalmia in consanguineous families. *Hum Mutat, 35*(8), 949-953. doi:10.1002/humu.22580

Abouzeid, H., Meire, F. M., Osman, I., ElShakankiri, N., Bolay, S., Munier, F. L., & Schorderet, D. F. (2009). A new locus for congenital cataract, microcornea, microphthalmia, and atypical iris coloboma maps to chromosome 2. *Ophthalmology, 116*(1), 154-162 e151. doi:10.1016/j.ophtha.2008.08.044

Adler, R., & Belecky-Adams, T.L. (2002). The role of bone morphogenetic proteins in the differentiation of the ventral optic cup. *Dev Camb Engl*., 129: 3161–3171.

Abouzeid, H., Youssef, M. A., Bayoumi, N., ElShakankiri, N., Marzouk, I., Hauser, P., & Schorderet, D. F. (2012). RAX and anophthalmia in humans: evidence of brain anomalies. *Mol Vis, 18*, 1449-1456.

ALSomiry, A. S., Gregory-Evans, C. Y., & Gregory-Evans, K. (2019). An update on the genetics of ocular coloboma. *Hum Genet, 138*(8-9), 865-880. doi:10.1007/s00439-019-02019-3

Amarnath, S., & Agarwala, S. (2017). Cell-cycle-dependent TGFβ-BMP antagonism regulates neural tube closure by modulating tight junctions. *J Cell Sci*., 130: 119–131. doi: 10.1242/jcs.179192

Apfeld, J., & Alper, S. (2018). What can we learn about human disease from the nematode C. Elegans? In *Methods in Molecular Biology* (Vol. 1706, pp. 53–75). https://doi.org/10.1007/978-1-4939-7471-9_4

Asai-Coakwell, M., French, C. R., Berry, K. M., Ye, M., Koss, R., Somerville, M., . . . Lehmann, O. J. (2007). GDF6, a novel locus for a spectrum of ocular developmental anomalies. *Am J Hum Genet, 80*(2), 306-315. doi:S0002-9297(07)62688-3 [pii] 10.1086/511280

Asai-Coakwell, M., French, C. R., Ye, M., Garcha, K., Bigot, K., Perera, A. G., . . . Lehmann, O. J. (2009). Incomplete penetrance and phenotypic variability characterize Gdf6-attributable oculo-skeletal phenotypes. *Hum Mol Genet, 18*(6), 1110-1121. doi:ddp008 [pii] 10.1093/hmg/ddp008

Asai-Coakwell, M., March, L., Dai, X. H., Duval, M., Lopez, I., French, C. R., . . . Lehmann, O. J. (2013). Contribution of growth differentiation factor 6-dependent cell survival to early-onset retinal dystrophies. *Hum Mol Genet, 22*(7), 1432-1442. doi:10.1093/hmg/dds560

Ashkenazi-Hoffnung, L., Lebenthal, Y., Wyatt, A. W., Ragge, N. K., Dateki, S., Fukami, M., . . . Gat-Yablonski, G. (2010). A novel loss-of-function mutation in OTX2 in a patient with anophthalmia and isolated growth hormone deficiency. *Hum Genet, 127*(6), 721-729. doi:10.1007/s00439-010-0820-9

Averous, J., & Proud, C.G. (2006). When translation meets transformation: the mTOR story. *Oncogene*, 25(48):6423-35. doi: 10.1038/sj.onc.1209887. PMID: 17041627.

Azuma, N., Yamaguchi, Y., Handa, H., Hayakawa, M., Kanai, A., & Yamada, M. (1999). Missense mutation in the alternative splice region of the PAX6 gene in eye anomalies. *Am J Hum Genet, 65*(3), 656-663. doi:10.1086/302529

Azuma, N., Yamaguchi, Y., Handa, H., Tadokoro, K., Asaka, A., Kawase, E., & Yamada, M. (2003). Mutations of the PAX6 gene detected in patients with a variety of optic-nerve malformations. *Am J Hum Genet, 72*(6), 1565-1570. doi:10.1086/375555

Bacci, G.M., Polizzi, S., Mari, F., Conti, V., Caputo, R., & Guerrini, R. (2021). Atypical Ocular Coloboma in Tuberous Sclerosis-2: Report of Two Novel Cases. *J Neuroophthalmol*, 41(3):e363-e365. doi: 10.1097/WNO.0000000000001099. PMID: 33110010.

Bajpai, R., Chen, D. A., Rada-Iglesias, A., Zhang, J., Xiong, Y., Helms, J., . . . Wysocka, J. (2010). CHD7 cooperates with PBAF to control multipotent neural crest formation. *Nature, 463*(7283), 958-962. doi:10.1038/nature08733

Bakrania, P., Ugur Iseri, S. A., Wyatt, A. W., Bunyan, D. J., Lam, W. W., Salt, A., . . . Ragge, N. K. (2010). Sonic hedgehog mutations are an uncommon cause of developmental eye anomalies. *Am J Med Genet A, 152A*(5), 1310-1313. doi:10.1002/ajmg.a.33239

Bakrania, P., Efthymiou, M., Klein, J.C., Salt, A., Bunyan, D.J., Wyatt, A., et al. (2008). Mutations in BMP4 cause eye, brain, and digit developmental anomalies: overlap between the BMP4 and hedgehog signaling pathways. *Am J Hum Genet*, 82: 304–319. doi: 10.1016/j.ajhg.2007.09.023

Ballou, L.M.,& Lin, R.Z. (2008). Rapamycin and mTOR kinase inhibitors. *J Chem Biol*, 1(1-4):27-36. doi: 10.1007/s12154-008-0003-5. Epub 2008 May 15. PMID: 19568796; PMCID: PMC2698317.

Bar-Peled, L., Chantranupong, L., Cherniack, A.D., Chen, W.W., Ottina, K.A., Grabiner, B.C., Spear, E.D., Carter, S.L., Meyerson, M., & Sabatini, D.M. (2013). A Tumor suppressor complex with GAP activity for the Rag GTPases that signal amino acid sufficiency to mTORC1. *Science*, 340(6136):1100-6. doi: 10.1126/science.1232044. PMID: 23723238; PMCID: PMC3728654.

Barbieri, A. M., Broccoli, V., Bovolenta, P., Alfano, G., Marchitiello, A., Mocchetti, C., . . . Banfi, S. (2002). Vax2 inactivation in mouse determines alteration of the eye dorsal-ventral axis, misrouting of the optic fibres and eye coloboma. *Development, 129*(3), 805-813.

Barbieri, A. M., Lupo, G., Bulfone, A., Andreazzoli, M., Mariani, M., Fougerousse, F., . . . Banfi, S. (1999). A homeobox gene, vax2, controls the patterning of the eye dorsoventral axis. *Proc Natl Acad Sci U S A, 96*(19), 10729-10734. doi:10.1073/pnas.96.19.10729

Barrett, B.T., Bradley, A., & Candy, T.R. (2013). The relationship between anisometropia and amblyopia. *Prog Retin Eye Res*, 36: 120–158. doi: 10.1016/j.preteyeres.2013.05.001

Bavisetty, S., Grody, W.W., & Yazdani, S. (2013). Emergence of pediatric rare diseases: Review of present policies and opportunities for improvement. *Rare Dis*, 1:e23579. doi: 10.4161/rdis.23579. PMID: 25002987; PMCID: PMC3932940.

Bazin-Lopez, N., Valdivia, L.E., Wilson, S.W., & Gestri, G. (2015). Watching eyes take shape. *Curr Opin Genet Dev*, 32: 73–79. doi: 10.1016/j.gde.2015.02.004

Beaulieu, C.L., Majewski, J., Schwartzentruber, J., Samuels, M.E., Fernandez, B.A., Bernier, F.P., et al. (2014). FORGE Canada Consortium: outcomes of a 2-year national rare-disease gene-discovery project. *Am J Hum Genet*, 94: 809–817. doi: 10.1016/j.ajhg.2014.05.003

Behesti, H., Holt, J.K.L., & Sowden, J.C. (2006). The level of BMP4 signaling is critical for the regulation of distinct T-box gene expression domains and growth along the dorso-ventral axis of the optic cup. *BMC Dev Biol*, 6: 62 doi: 10.1186/1471-213X-6-62

Ben-Sahra, I., Howell, J.J., Asara, J.M., & Manning, B.D. (2013). Stimulation of de novo pyrimidine synthesis by growth signaling through mTOR and S6K1. *Science*, 339(6125):1323-8. doi: 10.1126/science.1228792. Epub 2013 Feb 21. PMID: 23429703; PMCID: PMC3753690

Bermejo, E., & Martínez-Frías, M. L. (1998). Congenital eye malformations: clinical-epidemiological analysis of 1,124,654 consecutive births in Spain. *American Journal of Medical Genetics*, *75*(5), 497–504.

Bernstein, C. S., Anderson, M. T., Gohel, C., Slater, K., Gross, J. M., & Agarwala, S. (2018). The cellular bases of choroid fissure formation and closure. *Dev Biol, 440*(2), 137-151. doi:10.1016/j.ydbio.2018.05.010

Betz, C., & Hall, M.N. (2013). Where is mTOR and what is it doing there? *J Cell Biol*, 203(4):563-74. doi: 10.1083/jcb.201306041. PMID: 24385483; PMCID: PMC3840941.

Bielen, H., & Houart, C. (2012). BMP signaling protects telencephalic fate by repressing eye identity and its Cxcr4-dependent morphogenesis. *Dev Cell*, 23: 812–822. doi: 10.1016/j.devcel.2012.09.006

Bilotta, J., & Saszik, S. (2001). The zebrafish as a model visual system. *International Journal of Developmental Neuroscience*. **19**, 621-629.

Blaner, W. S. (1989). Retinol-binding protein: the serum transport protein for vitamin A. *Endocr Rev, 10*(3), 308-316. doi:10.1210/edrv-10-3-308

Bogdanovic, O., Delfino-Machin, M., Nicolas-Perez, M., Gavilan, M. P., Gago-Rodrigues, I., Fernandez-Minan, A., . . . Martinez-Morales, J. R. (2012). Numb/Numbl-Opo antagonism

controls retinal epithelium morphogenesis by regulating integrin endocytosis. *Dev Cell, 23*(4), 782-795. doi:10.1016/j.devcel.2012.09.004

Bogdanova-Mihaylova, P., Alexander, M.D., Murphy, R.P., Chen, H., Healy, D.G., Walsh, R.A., & Murphy, S.M. (2019). Clinical spectrum of AIFM1-associated disease in an Irish family, from mild neuropathy to severe cerebellar ataxia with colour blindness. *J Peripher Nerv Syst*, 24(4):348-353. doi: 10.1111/jns.12348. Epub 2019 Oct 10. PMID: 31523922.

Bohnsack, B. L., & Kahana, A. (2013). Thyroid hormone and retinoic acid interact to regulate zebrafish craniofacial neural crest development. *Dev Biol, 373*(2), 300-309. doi:10.1016/j.ydbio.2012.11.005

Bondurand, N., Pingault, V., Goerich, D. E., Lemort, N., Sock, E., Le Caignec, C., . . . Goossens, M. (2000). Interaction among SOX10, PAX3 and MITF, three genes altered in Waardenburg syndrome. *Hum Mol Genet, 9*(13), 1907-1917. doi:10.1093/hmg/9.13.1907

Bouillet, P., Sapin, V., Chazaud, C., Messaddeq, N., Decimo, D., Dolle, P., & Chambon, P. (1997). Developmental expression pattern of Stra6, a retinoic acid-responsive gene encoding a new type of membrane protein. *Mech Dev, 63*(2), 173-186. doi:10.1016/s0925-4773(97)00039-7

Brandt, A. U., Meinert-Bohn, E., Rinnenthal, J. L., Zimmermann, H., Mikolajczak, J., Oberwahrenbrock, T., Papazoglou, S., Pfüller, C. F., Schinzel, J., Tackenberg, B., Paul, F., Hahn, K., & Bellmann-Strobl, J. (2016). Afferent Visual Pathway Affection in Patients with PMP22 Deletion-Related Hereditary Neuropathy with Liability to Pressure Palsies. *PloS One*, 11(10), e0164617. https://doi.org/10.1371/journal.pone.0164617

Braun, M. M., Etheridge, A., Bernard, A., Robertson, C. P., & Roelink, H. (2003). Wnt signaling is required at distinct stages of development for the induction of the posterior forebrain. *Development, 130*(23), 5579-5587. doi:10.1242/dev.00685

Brown, A., McKie, M., van Heyningen, V., & Prosser, J. (1998). The Human PAX6 Mutation Database. *Nucleic Acids Res, 26*(1), 259-264. doi:10.1093/nar/26.1.259

Brown, K. E., Keller, P. J., Ramialison, M., Rembold, M., Stelzer, E. H., Loosli, F., & Wittbrodt, J. (2010). Nlcam modulates midline convergence during anterior neural plate morphogenesis. *Dev Biol, 339*(1), 14-25. doi:10.1016/j.ydbio.2009.12.003

Brown, L. Y., Odent, S., David, V., Blayau, M., Dubourg, C., Apacik, C., . . . Muenke, M. (2001). Holoprosencephaly due to mutations in ZIC2: alanine tract expansion mutations may be caused by parental somatic recombination. *Hum Mol Genet, 10*(8), 791-796.

Brown, S. A., Warburton, D., Brown, L. Y., Yu, C. Y., Roeder, E. R., Stengel-Rutkowski, S., . . . Muenke, M. (1998). Holoprosencephaly due to mutations in ZIC2, a homologue of Drosophila odd-paired. *Nat Genet, 20*(2), 180-183.

Bryan, C. D., Casey, M. A., Pfeiffer, R. L., Jones, B. W., & Kwan, K. M. (2020). Optic cup morphogenesis requires neural crest-mediated basement membrane assembly. *Development, 147*(4). doi:10.1242/dev.181420

Bryan, C. D., Chien, C. B., & Kwan, K. M. (2016). Loss of laminin alpha 1 results in multiple structural defects and divergent effects on adhesion during vertebrate optic cup morphogenesis. *Dev Biol, 416*(2), 324-337. doi:10.1016/j.ydbio.2016.06.025

Burkitt Wright, E. M., Perveen, R., Bowers, N., Ramsden, S., McCann, E., O'Driscoll, M., . . . Black, G. C. (2010). VSX2 in microphthalmia: a novel splice site mutation producing a severe microphthalmia phenotype. *Br J Ophthalmol, 94*(3), 386-388. doi:10.1136/bjo.2009.159996

Burns, C. J., Zhang, J., Brown, E. C., Van Bibber, A. M., Van Es, J., Clevers, H., . . . Fuhrmann, S. (2008). Investigation of Frizzled-5 during embryonic neural development in mouse. *Dev Dyn, 237*(6), 1614-1626. doi:10.1002/dvdy.21565

Busch, C., Voitl, R., Goergen, B., Zemojtel, T., Gehle, P., & Salchow, D. J. (2018). Ocular findings in Loeys-Dietz syndrome. *Br J Ophthalmol, 102*(8), 1036-1040. doi:10.1136/bjophthalmol-2017-311254

Cao, M., Ouyang, J., Guo, J., Lin, S., & Chen, S. (2018). Metalloproteinase Adamts16 Is Required for Proper Closure of the Optic Fissure. *Invest Ophthalmol Vis Sci, 59*(3), 1167-1177. doi:10.1167/iovs.17-22827

Capowski, E. E., Wright, L. S., Liang, K., Phillips, M. J., Wallace, K., Petelinsek, A., . . . Gamm, D. M. (2016). Regulation of WNT Signaling by VSX2 During Optic Vesicle Patterning in Human Induced Pluripotent Stem Cells. *Stem Cells, 34*(11), 2625-2634. doi:10.1002/stem.2414

Carrara, N., Weaver, M., Piedade, W. P., Vöcking, O., & Famulski, J. K. (2019). Temporal characterization of optic fissure basement membrane composition suggests nidogen may be an initial target of remodeling. *Developmental Biology*, *452*(1), 43–54. https://doi.org/10.1016/j.ydbio.2019.04.012

Casey, J., Kawaguchi, R., Morrissey, M., Sun, H., McGettigan, P., Nielsen, J. E., . . . Ennis, S. (2011). First implication of STRA6 mutations in isolated anophthalmia, microphthalmia, and coloboma: a new dimension to the STRA6 phenotype. *Hum Mutat, 32*(12), 1417-1426. doi:10.1002/humu.21590

Cavodeassi, F., Carreira-Barbosa, F., Young, R. M., Concha, M. L., Allende, M. L., Houart, C., . . . Wilson, S. W. (2005). Early stages of zebrafish eye formation require the coordinated activity of Wnt11, Fz5, and the Wnt/beta-catenin pathway. *Neuron, 47*(1), 43-56. doi:10.1016/j.neuron.2005.05.026

Cavodeassi, F., Ivanovitch, K., & Wilson, S. W. (2013). Eph/Ephrin signalling maintains eye field segregation from adjacent neural plate territories during forebrain morphogenesis. *Development, 140*(20), 4193-4202. doi:10.1242/dev.097048

Chambers, D., Wilson, L., Maden, & M., Lumsden, A. (2007). RALDH-independent generation of retinoic acid during vertebrate embryogenesis by CYP1B1. *Dev Camb Engl*, 134: 1369–1383. doi: 10.1242/dev.02815

Chang, B., Smith, R. S., Peters, M., Savinova, O. V., Hawes, N. L., Zabaleta, A., . . . John, S. W. (2001). Haploinsufficient Bmp4 ocular phenotypes include anterior segment dysgenesis with elevated intraocular pressure. *BMC Genet, 2*, 18. doi:10.1186/1471-2156-2-18

Chang, L., Blain, D., Bertuzzi, S., & Brooks, B. P. (2006). Uveal coloboma: clinical and basic science update. *Current Opinion in Ophthalmology*, *17*(5), 447–470. https://doi.org/10.1097/01.icu.0000243020.82380.f6

Chassaing, N., Causse, A., Vigouroux, A., Delahaye, A., Alessandri, J. L., Boespflug-Tanguy, O., . . . Calvas, P. (2014). Molecular findings and clinical data in a cohort of 150 patients with anophthalmia/microphthalmia. *Clin Genet, 86*(4), 326-334. doi:10.1111/cge.12275

Chawla, B., Schley, E., Williams, A. L., & Bohnsack, B. L. (2016). Retinoic Acid and Pitx2 Regulate Early Neural Crest Survival and Migration in Craniofacial and Ocular Development. *Birth Defects Res B Dev Reprod Toxicol, 107*(3), 126-135. doi:10.1002/bdrb.21177

Chekuri, A., Guru, A.A., Biswas, P., Branham, K., Borooah, S., Soto-Hermida, A., … Ayyagari, R. (2018). IFT88 mutations identified in individuals with non-syndromic recessive retinal degeneration result in abnormal ciliogenesis. *Hum Genet*, 137(6-7):447-458. doi: 10.1007/s00439-018-1897-9. Epub 2018 Jul 5. PMID: 29978320; PMCID: PMC6150774.

Chen, H., Lun, Y., Ovchinnikov, D., Kokubo, H., Oberg, K. C., Pepicelli, C. V., . . . Johnson, R. L. (1998). Limb and kidney defects in Lmx1b mutant mice suggest an involvement of LMX1B in human nail patella syndrome. *Nat Genet, 19*(1), 51-55. doi:10.1038/ng0598-51

Chen, S., & Lechleider, R. J. (2004). Transforming growth factor-beta-induced differentiation of smooth muscle from a neural crest stem cell line. *Circ Res, 94*(9), 1195-1202. doi:10.1161/01.RES.0000126897.41658.81

Chen, X., Liu, Y., Sheng, X., Tam, P.O., Zhao, K., Chen, X., Rong, W., Liu, Y., Liu, X., Pan, X., Chen, L.J., Zhao, Q., Vollrath, D., Pang, C.P., & Zhao, C. (2014). PRPF4 mutations cause autosomal dominant retinitis pigmentosa. *Hum Mol Genet*, 23(11):2926-39. doi: 10.1093/hmg/ddu005. Epub 2014 Jan 12. PMID: 24419317.

Cho, J.H., Kim, K., Kim, S.A., Park, S., Park, B.O., Kim, J.H., Kim, S.Y., Kwon, M.J., Han, M.H., Lee, S.B., Park, B.C., Park, S.G., Kim, J.H., & Kim, S. (2021). Deubiquitinase OTUD5 is a positive regulator of mTORC1 and mTORC2 signaling pathways. *Cell Death Differ.*

28(3):900-914. doi: 10.1038/s41418-020-00649-z. Epub 2020 Oct 27. PMID: 33110214; PMCID: PMC7937674.

Chuang, J. C., & Raymond, P. A. (2001). Zebrafish genes rx1 and rx2 help define the region of forebrain that gives rise to retina. *Dev Biol, 231*(1), 13-30. doi:10.1006/dbio.2000.0125

Creuzet, S., Vincent, C., & Couly, G. (2005). Neural crest derivatives in ocular and periocular structures. *Int J Dev Biol, 49*(2-3), 161-171. doi:10.1387/ijdb.041937sc

Cukras, C., Gaasterland, T., Lee, P., Gudiseva, H. V., Chavali, V. R., Pullakhandam, R., . . . Ayyagari, R. (2012). Exome analysis identified a novel mutation in the RBP4 gene in a consanguineous pedigree with retinal dystrophy and developmental abnormalities. *PLoS One, 7*(11), e50205. doi:10.1371/journal.pone.0050205

Curatolo, P. (2015). Mechanistic target of rapamycin (mTOR) in tuberous sclerosis complex-associated epilepsy. *Pediatr Neurol*, 52(3):281-9. doi: 10.1016/j.pediatrneurol.2014.10.028. Epub 2014 Nov 20. PMID: 25591831.

Cvekl, A., & Tamm, E. R. (2004). Anterior eye development and ocular mesenchyme: new insights from mouse models and human diseases. *Bioessays, 26*(4), 374-386. doi:10.1002/bies.20009

Cybulski, N., & Hall, M.N. (2009). TOR complex 2: a signaling pathway of its own. *Trends Biochem Sci*, 34(12):620-7. doi: 10.1016/j.tibs.2009.09.004. Epub 2009 Oct 28. PMID: 19875293.

D'Andrea, A.D. (2010). Susceptibility pathways in Fanconi's anemia and breast cancer. *N Engl J Med*, 362(20):1909-19. doi: 10.1056/NEJMra0809889. PMID: 20484397; PMCID: PMC3069698.

Dale, D.C., & Link, D.C. (2009). The many causes of severe congenital neutropenia. *N Engl J Med*, 360(1):3-5. doi: 10.1056/NEJMp0806821. PMID: 19118300; PMCID: PMC4162527.

Dateki, S., Fukami, M., Sato, N., Muroya, K., Adachi, M., & Ogata, T. (2008). OTX2 mutation in a patient with anophthalmia, short stature, and partial growth hormone deficiency: functional studies using the IRBP, HESX1, and POU1F1 promoters. *J Clin Endocrinol Metab, 93*(10), 3697-3702. doi:10.1210/jc.2008-0720

Datta, S.R., Dudek, H., Tao, X., Masters, S., Fu, H., Gotoh, Y., & Greenberg, M.E. (1997). Akt phosphorylation of BAD couples survival signals to the cell-intrinsic death machinery. *Cell*, 91(2):231-41. doi: 10.1016/s0092-8674(00)80405-5. PMID: 9346240.

De Waele, L., Lagae, L., & Mekahli, D. (2015). Tuberous sclerosis complex: the past and the future. *Pediatr Nephrol*, 30(10):1771-80. doi: 10.1007/s00467-014-3027-9. Epub 2014 Dec 23. PMID: 25533384.

Dee, C. T., Szymoniuk, C. R., Mills, P. E., & Takahashi, T. (2013). Defective neural crest migration revealed by a Zebrafish model of Alx1-related frontonasal dysplasia. *Hum Mol Genet, 22*(2), 239-251. doi:10.1093/hmg/dds423

Del Rio-Tsonis, K., Washabaugh, C. H., & Tsonis, P. A. (1995). Expression of pax-6 during urodele eye development and lens regeneration. *Proc Natl Acad Sci U S A, 92*(11), 5092-5096. doi:10.1073/pnas.92.11.5092

den Hollander, A. I., Biyanwila, J., Kovach, P., Bardakjian, T., Traboulsi, E. I., Ragge, N. K., . . . Malicki, J. (2010). Genetic defects of GDF6 in the zebrafish out of sight mutant and in human eye developmental anomalies. *BMC Genet, 11*, 102. doi:10.1186/1471-2156-11-102

Doncheva, N. T., Kacprowski, T., & Albrecht, M. (2012). Recent approaches to the prioritization of candidate disease genes. *Wiley Interdisciplinary Reviews. Systems Biology and Medicine*, *4*(5), 429–442. https://doi.org/10.1002/wsbm.1177

Dreyer, S. D., Zhou, G., Baldini, A., Winterpacht, A., Zabel, B., Cole, W., . . . Lee, B. (1998). Mutations in LMX1B cause abnormal skeletal patterning and renal dysplasia in nail patella syndrome. *Nat Genet, 19*(1), 47-50. doi:10.1038/ng0598-47

Dudley, A. T., Lyons, K. M., & Robertson, E. J. (1995). A requirement for bone morphogenetic protein-7 during development of the mammalian kidney and eye. *Genes Dev, 9*(22), 2795-2807. doi:10.1101/gad.9.22.2795

Eagle, R.C. Jr, Shields, J.A., Shields, C.L., & Wood, M.G. (2000). Hamartomas of the iris and ciliary epithelium in tuberous sclerosis complex. *Arch Ophthalmol*, 118(5):711-5. doi: 10.1001/archopht.118.5.711. PMID: 10815166.

Eckert, P., Knickmeyer, M. D., & Heermann, S. (2020). In Vivo Analysis of Optic Fissure Fusion in Zebrafish: Pioneer Cells, Basal Lamina, Hyaloid Vessels, and How Fissure Fusion is Affected by BMP. *Int J Mol Sci, 21*(8). doi:10.3390/ijms21082760

Enikanolaiye, A., & Justice, M. J. (2019). Model systems inform rare disease diagnosis, therapeutic discovery and pre-clinical efficacy. *Emerging Topics in Life Sciences*, *3*(1), 1–10. https://doi.org/10.1042/etls20180057

Ekker, S. C., Ungar, A. R., Greenstein, P., von Kessler, D. P., Porter, J. A., Moon, R. T., & Beachy, P. A. (1995). Patterning activities of vertebrate hedgehog proteins in the developing eye and brain. *Curr Biol, 5*(8), 944-955.

Eom, D.S., Amarnath, S., Fogel, J.L., & Agarwala, S. (2011). Bone morphogenetic proteins regulate neural tube closure by interacting with the apicobasal polarity pathway. *Dev Camb Engl*, 138: 3179–3188. doi: 10.1242/dev.058602

Etchevers, H. C., Vincent, C., Le Douarin, N. M., & Couly, G. F. (2001). The cephalic neural crest provides pericytes and smooth muscle cells to all blood vessels of the face and forebrain. *Development, 128*(7), 1059-1068.

Evans, A. L., & Gage, P. J. (2005). Expression of the homeobox gene Pitx2 in neural crest is required for optic stalk and ocular anterior segment development. *Hum Mol Genet, 14*(22), 3347-3359. doi:10.1093/hmg/ddi365

Faiq, M.A., Dada, R., Qadri, R., & Dada, T. (2015). CYP1B1-mediated Pathobiology of Primary Congenital Glaucoma. *J Curr Glaucoma Pract*, 9(3):77-80. doi: 10.5005/jp-journals-10008-1189. Epub 2016 Feb 2. PMID: 26997841; PMCID: PMC4779945.

Ferda Percin, E., Ploder, L. A., Yu, J. J., Arici, K., Horsford, D. J., Rutherford, A., . . . McInnes, R. R. (2000). Human microphthalmia associated with mutations in the retinal homeobox gene CHX10. *Nat Genet, 25*(4), 397-401. doi:10.1038/78071

Fernandez-Marmiesse, A., Gouveia, S., & Couce, M.L. (2018). NGS Technologies as a Turning Point in Rare Disease Research , Diagnosis and Treatment. *Curr Med Chem*, 25(3):404-432. doi: 10.2174/0929867324666170718101946. PMID: 28721829; PMCID: PMC5815091.

Finkelstein, R., & Perrimon, N. (1990). The orthodenticle gene is regulated by bicoid and torso and specifies Drosophila head development. *Nature, 346*(6283), 485-488. doi:10.1038/346485a0

Fiordaliso, S.K., Iwata-Otsubo, A., Ritter, A.L., Quesnel-Vallières, M., Fujiki, K., Nishi, E., Hancarova, M., Miyake, N., Morton, J.E.V., Lee, S., Hackmann, K., Bando, M., Masuda, K., Nakato, R., Arakawa, M., Bhoj, E., Li, D., Hakonarson, H., Takeda, R., Harr, M., Keena, B., Zackai, E.H., Okamoto, N., Mizuno, S., Ko, J.M., Valachova, A., Prchalova, D., Vlckova, M., Pippucci, T., Seiler, C., Choi, M., Matsumoto, N., Di Donato, N., Barash, Y., Sedlacek, Z., Shirahige, K., & Izumi, K. (2019). Missense Mutations in NKAP Cause a Disorder of Transcriptional Regulation Characterized by Marfanoid Habitus and Cognitive Impairment. *Am J Hum Genet*, 105(5):987-995. doi: 10.1016/j.ajhg.2019.09.009. Epub 2019 Oct 3. PMID: 31587868; PMCID: PMC6848994.

Fitzgerald, D.E., Chung, I., & Krumholtz, I. (2005). An analysis of high myopia in a pediatric population less than 10 years of age. *Optom St Louis Mo*, 76: 102–114.

Forrester, M. B., & Merz, R. D. (2006). Descriptive epidemiology of anophthalmia and microphthalmia, Hawaii, 1986-2001. *Birth Defects Research. Part A, Clinical and Molecular Teratology*, *76*(3), 187–192. https://doi.org/10.1002/bdra.20237

French, C. R., Erickson, T., French, D. V., Pilgrim, D. B., & Waskiewicz, A. J. (2009). Gdf6a is required for the initiation of dorsal-ventral retinal patterning and lens development. *Dev Biol, 333*(1), 37-47. doi:S0012-1606(09)00985-3 [pii] 10.1016/j.ydbio.2009.06.018

French, C.R., Stach, T.R., March, L.D., Lehmann, O.J., & Waskiewicz, A.J. (2013). Apoptotic and proliferative defects characterize ocular development in a microphthalmic BMP model. *Invest Ophthalmol Vis Sci*., 54: 4636–4647. doi: 10.1167/iovs.13-11674

Fu, C. T., & Sretavan, D. (2012). Involvement of EphB/Ephrin-B signaling in axonal survival in mouse experimental glaucoma. *Investigative ophthalmology & visual science*, 53(1), 76–84. https://doi.org/10.1167/iovs.11-8546

Fuhrmann, S. (2010). Eye morphogenesis and patterning of the optic vesicle. *Curr Top Dev Biol*, 93: 61–84. doi: 10.1016/B978-0-12-385044-7.00003-5

Fuhrmann, S., Levine, E. M., & Reh, T. A. (2000). Extraocular mesenchyme patterns the optic vesicle during early eye development in the embryonic chick. *Development, 127*(21), 4599-4609.

Fujiki, K., Nakajima, A., Yasuda, N., Tanabe, U., & Kabasawa, K. (1982). Genetic analysis of microphthalmos. *Ophthalmic Genetics*, *1*(2), 139–149. https://doi.org/10.3109/13816818209031458

Fujita, K., Ogawa, R., Kawawaki, S., & Ito, K. (2014). Roles of chromatin remodelers in maintenance mechanisms of multipotency of mouse trunk neural crest cells in the formation of neural crest-derived stem cells. *Mech Dev, 133*, 126-145. doi:10.1016/j.mod.2014.05.001

Furuta, Y., Piston, D. W., & Hogan, B. L. (1997). Bone morphogenetic proteins (BMPs) as regulators of dorsal forebrain development. *Development, 124*(11), 2203-2212.

Gage, P. J., Rhoades, W., Prucka, S. K., & Hjalt, T. (2005). Fate maps of neural crest and mesoderm in the mammalian eye. *Invest Ophthalmol Vis Sci, 46*(11), 4200-4208. doi:10.1167/iovs.05-0691

Gage, P. J., Suh, H., & Camper, S. A. (1999). Dosage requirement of Pitx2 for development of multiple organs. *Development, 126*(20), 4643-4651.

Gago-Rodrigues, I., Fernandez-Minan, A., Letelier, J., Naranjo, S., Tena, J. J., Gomez-Skarmeta, J. L., & Martinez-Morales, J. R. (2015). Analysis of opo cis-regulatory landscape uncovers Vsx2 requirement in early eye morphogenesis. *Nat Commun, 6*, 7054. doi:10.1038/ncomms8054

García-Martínez, J.M., & Alessi, D.R. (2008). mTOR complex 2 (mTORC2) controls hydrophobic motif phosphorylation and activation of serum- and glucocorticoid-induced protein kinase 1 (SGK1). *Biochem J*, 416(3):375-85. doi: 10.1042/BJ20081668. PMID: 18925875.

George, A., Cogliati, T., & Brooks, B. P. (2020). Genetics of syndromic ocular coloboma: CHARGE and COACH syndromes. Experimental Eye Research, Vol. 193, p. 107940. https://doi.org/10.1016/j.exer.2020.107940

George, A., Zand, D. J., Hufnagel, R. B., Sharma, R., Sergeev, Y. V., Legare, J. M., . . . Brooks, B. P. (2016). Biallelic Mutations in MITF Cause Coloboma, Osteopetrosis, Microphthalmia, Macrocephaly, Albinism, and Deafness. *Am J Hum Genet, 99*(6), 1388-1394. doi:10.1016/j.ajhg.2016.11.004

Gestri, G., Bazin-Lopez, N., Scholes, C., & Wilson, S. W. (2018). Cell Behaviors during Closure of the Choroid Fissure in the Developing Eye. *Front Cell Neurosci, 12*, 42. doi:10.3389/fncel.2018.00042

Gestri, G., Osborne, R. J., Wyatt, A. W., Gerrelli, D., Gribble, S., Stewart, H., . . . Ragge, N. K. (2009). Reduced TFAP2A function causes variable optic fissure closure and retinal defects and sensitizes eye development to mutations in other morphogenetic regulators. *Hum Genet, 126*(6), 791-803. doi:10.1007/s00439-009-0730-x

Glardon, S., Callaerts, P., Halder, G., & Gehring, W. J. (1997). Conservation of Pax-6 in a lower chordate, the ascidian Phallusia mammillata. *Development, 124*(4), 817-825.

Gongal, P. A., French, C. R., & Waskiewicz, A. J. (2011). Aberrant forebrain signaling during early development underlies the generation of holoprosencephaly and coloboma. *Biochim Biophys Acta, 1812*(3), 390-401. doi:S0925-4439(10)00205-X [pii] 10.1016/j.bbadis.2010.09.005

Gonzalez-Rodriguez, J., Pelcastre, E. L., Tovilla-Canales, J. L., Garcia-Ortiz, J. E., Amato-Almanza, M., Villanueva-Mendoza, C., . . . Zenteno, J. C. (2010). Mutational screening of CHX10, GDF6, OTX2, RAX and SOX2 genes in 50 unrelated microphthalmia-anophthalmia-coloboma (MAC) spectrum cases. *Br J Ophthalmol, 94*(8), 1100-1104. doi:10.1136/bjo.2009.173500

Gosse, N. J., & Baier, H. (2009). An essential role for Radar (Gdf6a) in inducing dorsal fate in the zebrafish retina. *Proc Natl Acad Sci U S A, 106*(7), 2236-2241. doi:10.1073/pnas.0803202106

Graziano, C., Gusson, E., Severi, G., Isidori, F., Wischmeijer, A., Brugnara, M., . . . Rossi, C. (2017). A de novo PUF60 mutation in a child with a syndromic form of coloboma and persistent fetal vasculature. *Ophthalmic Genet, 38*(6), 590-592. doi:10.1080/13816810.2017.1318927

Green, E. S., Stubbs, J. L., & Levine, E. M. (2003). Genetic rescue of cell number in a mouse model of microphthalmia: interactions between Chx10 and G1-phase cell cycle regulators. *Development, 130*(3), 539-552. doi:10.1242/dev.00275

Gregory-Evans, C.Y., Williams, M.J., Halford, S., & Gregory-Evans, K. (2004). Ocular coloboma: a reassessment in the age of molecular neuroscience. *J Med Genet*, 41: 881–891. doi: 10.1136/jmg.2004.025494

Grindley, J. C., Davidson, D. R., & Hill, R. E. (1995). The role of Pax-6 in eye and nasal development. *Development, 121*(5), 1433-1442.

Gritsman, K., Zhang, J., Cheng, S., Heckscher, E., Talbot, W.S., & Schier, A.F. (1997). The EGF-CFC protein one-eyed pinhead is essential for nodal signaling. *Cell*, 97(1):121-32. doi: 10.1016/s0092-8674(00)80720-5. PMID: 10199408.

Gross, J. M., & Dowling, J. E. (2005). Tbx2b is essential for neuronal differentiation along the dorsal/ventral axis of the zebrafish retina. *Proc Natl Acad Sci U S A, 102*(12), 4371-4376. doi:10.1073/pnas.0501061102

Halder, G., Callaerts, P., & Gehring, W. J. (1995). Induction of ectopic eyes by targeted expression of the eyeless gene in Drosophila. *Science, 267*(5205), 1788-1792. doi:10.1126/science.7892602

Halfter, W., & Von Boxberg, Y. (199). Axonal Growth on Solubilized and Reconstituted Matrix from the Embryonic Chicken Retina Inner Limiting Membrane. *Eur J Neurosci*, 4: 840–852.

Hallonet, M., Hollemann, T., Pieler, T., & Gruss, P. (1999). Vax1, a novel homeobox-containing gene, directs development of the basal forebrain and visual system. *Genes Dev, 13*(23), 3106-3114. doi:10.1101/gad.13.23.3106

Hamano, Y., Grunkemeyer, J. A., Sudhakar, A., Zeisberg, M., Cosgrove, D., Morello, R., . . . Kalluri, R. (2002). Determinants of vascular permeability in the kidney glomerulus. *J Biol Chem, 277*(34), 31154-31162. doi:10.1074/jbc.M204806200

Hamburger, V., & Hamilton, H.L. (1951). A series of normal stages in the development of the chick embryo. *J Morphol*, 88: 49–92. doi: 10.1002/jmor.1050880104

Hanson, I. M., Seawright, A., Hardman, K., Hodgson, S., Zaletayev, D., Fekete, G., & van Heyningen, V. (1993). PAX6 mutations in aniridia. *Hum Mol Genet, 2*(7), 915-920. doi:10.1093/hmg/2.7.915

Hao, J., Ho, J.N., Lewis, J.A., Karim, K.A., Daniels, R.N., Gentry, P.R., et al. (2010). In vivo structure-activity relationship study of dorsomorphin analogues identifies selective VEGF and BMP inhibitors. *ACS Chem Biol*, 5: 245–253. doi: 10.1021/cb9002865

Harding, P., Toms, M., Schiff, E., Owen, N., Bell, S., Lloyd, I. C., & Moosajee, M. (2021). EPHA2 Segregates with Microphthalmia and Congenital Cataracts in Two Unrelated Families. *International journal of molecular sciences*, 22(4), 2190. https://doi.org/10.3390/ijms22042190

Harris, W. A., & Hartenstein, V. (1991). Neuronal determination without cell division in Xenopus embryos. *Neuron, 6*(4), 499-515. doi:10.1016/0896-6273(91)90053-3

Hasegawa, A., Iwasaka, H., Hagiwara, S., Asai, N., Nishida, T., & Noguchi, T. (2012). Alternate day calorie restriction improves systemic inflammation in a mouse model of sepsis induced by cecal ligation and puncture. *J Surg Res*, 174(1):136-41. doi: 10.1016/j.jss.2010.11.883. Epub 2010 Dec 9. PMID: 21195419.

Heavner, W., & Pevny, L. (2012). Eye development and retinogenesis. *Cold Spring Harb Perspect Biol, 4*(12). doi:10.1101/cshperspect.a008391

Heermann, S., Schutz, L., Lemke, S., Krieglstein, K., & Wittbrodt, J. (2015). Eye morphogenesis driven by epithelial flow into the optic cup facilitated by modulation of bone morphogenetic protein. *Elife, 4*. doi:10.7554/eLife.05216

Hehr, U., Pineda-Alvarez, D. E., Uyanik, G., Hu, P., Zhou, N., Hehr, A., . . . Muenke, M. (2010). Heterozygous mutations in SIX3 and SHH are associated with schizencephaly and further expand the clinical spectrum of holoprosencephaly. *Hum Genet, 127*(5), 555-561. doi:10.1007/s00439-010-0797-4

Hendee, K. E., Sorokina, E. A., Muheisen, S. S., Reis, L. M., Tyler, R. C., Markovic, V., . . . Semina, E. V. (2018). PITX2 deficiency and associated human disease: insights from the zebrafish model. *Hum Mol Genet, 27*(10), 1675-1695. doi:10.1093/hmg/ddy074

Henske, E.P., Jóźwiak, S., Kingswood, J.C., Sampson, J.R., & Thiele, E.A. (2016). Tuberous sclerosis complex. *Nat Rev Dis Primer*, 2: 16035 doi: 10.1038/nrdp.2016.35

Hesketh, G.G., Papazotos, F., Pawling, J., Rajendran, D., Knight, J.D.R., Martinez, S., Taipale, M., Schramek, D., Dennis, J.W., & Gingras, A.C. (2020). The GATOR-Rag GTPase pathway inhibits mTORC1 activation by lysosome-derived amino acids. *Science*, 370(6514):351-356. doi: 10.1126/science.aaz0863. PMID: 33060361.

Hirsch, N., & Harris, W. A. (1997). Xenopus Pax-6 and retinal development. *J Neurobiol, 32*(1), 45-61.

Hmeljak, J., & Justice, M. J. (2019). From gene to treatment: supporting rare disease translational research through model systems. *Disease Models & Mechanisms*, Vol. 12. https://doi.org/10.1242/dmm.039271

Hocking, J. C., Famulski, J. K., Yoon, K. H., Widen, S. A., Bernstein, C. S., Koch, S., . . . Waskiewicz, A. J. (2018). Morphogenetic defects underlie Superior Coloboma, a newly identified closure disorder of the dorsal eye. *PLoS Genet, 14*(3), e1007246. doi:10.1371/journal.pgen.1007246

Holt, R.J., Young, R.M., Crespo, B., Ceroni, F., Curry, C.J., Bellacchio, E., Bax, D.A., Ciolfi, A., Simon, M., Fagerberg, C.R., van Binsbergen, E., De Luca, A., Memo, L., Dobyns, W.B., Mohammed, A.A., Clokie, S.J.H., Zazo Seco, C., Jiang, Y.H., Sørensen, K.P., Andersen, H., Sullivan, J., Powis, Z., Chassevent, A., Smith-Hicks, C., Petrovski, S., Antoniadi, T., Shashi, V., Gelb, B.D., Wilson, S.W., Gerrelli, D., Tartaglia, M., Chassaing, N., Calvas, P.,

& Ragge, N.K. (2019). De Novo Missense Variants in FBXW11 Cause Diverse Developmental Phenotypes Including Brain, Eye, and Digit Anomalies. *Am J Hum Genet*, 105(3):640-657. doi: 10.1016/j.ajhg.2019.07.005. Epub 2019 Aug 8. PMID: 31402090; PMCID: PMC6731360.

Hosokawa, N., Hara, T., Kaizuka, T., Kishi, C., Takamura, A., Miura, Y., Iemura, S., Natsume, T., Takehana, K., Yamada, N., Guan, J.L., Oshiro, N., & Mizushima, N. (2009). Nutrient-dependent mTORC1 association with the ULK1-Atg13-FIP200 complex required for autophagy. *Mol Biol Cell*, 20(7):1981-91. doi: 10.1091/mbc.e08-12-1248. Epub 2009 Feb 11. PMID: 19211835; PMCID: PMC2663915.

Howe, K., Clark, M. D., Torroja, C. F., Torrance, J., Berthelot, C., Muffato, M., … Stemple, D. L. (2013). The zebrafish reference genome sequence and its relationship to the human genome. *Nature*, *496*(7446), 498–503. https://doi.org/10.1038/nature12111

Huang, J., & Manning, B.D. (2008). The TSC1-TSC2 complex: a molecular switchboard controlling cell growth. *Biochem J*, 412(2):179-90. doi: 10.1042/BJ20080281. PMID: 18466115; PMCID: PMC2735030.

Huang, X. F., Huang, Z. Q., Lin, D., Dai, M. L., Wang, Q. F., Chen, Z. J., . . . Wang, Y. (2017). Unraveling the genetic cause of a consanguineous family with unilateral coloboma and retinoschisis: expanding the phenotypic variability of RAX mutations. *Sci Rep, 7*(1), 9064. doi:10.1038/s41598-017-09276-0

Institute of Medicine (US) Committee on Accelerating Rare Diseases Research and Orphan Product Development; Field MJ, Boat TF, editors. Rare Diseases and Orphan Products: Accelerating Research and Development. Washington (DC): National Academies Press (US); 2010. 2, Profile of Rare Diseases. Available from: https://www.ncbi.nlm.nih.gov/books/NBK56184/

Iseri, S. U., Wyatt, A. W., Nurnberg, G., Kluck, C., Nurnberg, P., Holder, G. E., . . . Ragge, N. K. (2010). Use of genome-wide SNP homozygosity mapping in small pedigrees to identify new mutations in VSX2 causing recessive microphthalmia and a semidominant inner retinal dystrophy. *Hum Genet, 128*(1), 51-60. doi:10.1007/s00439-010-0823-6

Ittner, L. M., Wurdak, H., Schwerdtfeger, K., Kunz, T., Ille, F., Leveen, P., . . . Sommer, L. (2005). Compound developmental eye disorders following inactivation of TGFbeta signaling in neural-crest stem cells. *J Biol, 4*(3), 11. doi:10.1186/jbiol29

Jain, A. M., Ranjan, R., & Manayath, G. J. (2018). Atypical superior iris and retinochoroidal coloboma. *Indian J Ophthalmol, 66*(10), 1474-1475. doi:10.4103/ijo.IJO_531_18

James, A., Lee, C., Williams, A. M., Angileri, K., Lathrop, K. L., & Gross, J. M. (2016). The hyaloid vasculature facilitates basement membrane breakdown during choroid fissure closure in the zebrafish eye. *Dev Biol, 419*(2), 262-272. doi:10.1016/j.ydbio.2016.09.008

Jethani, J., Sharma, V.R., & Marwah, K. (2009). Superior Lens Coloboma with Superior Rectus Palsy and Congenital Ptosis. *J Optom*, 2: 67–69. doi: 10.3921/joptom.2009.67

Jia, J., & Shi, T. (2017). Towards efficiency in rare disease research: what is distinctive and important? *Sci China Life Sci*, 60(7):686-691. doi: 10.1007/s11427-017-9099-3. Epub 2017 Jun 16. PMID: 28639105.

Jia, S., Omelchenko, M., Garland, D., Vasiliou, V., Kanungo, J., Spencer, M., Wolf, Y., Koonin, E., & Piatigorsky, J. (2007). Duplicated gelsolin family genes in zebrafish: a novel scinderin-like gene (scinla) encodes the major corneal crystallin. *FASEB journal : official publication of the Federation of American Societies for Experimental Biology*, 21(12), 3318–3328. https://doi.org/10.1096/fj.07-8172com

Jordan, T., Hanson, I., Zaletayev, D., Hodgson, S., Prosser, J., Seawright, A., . . . van Heyningen, V. (1992). The human PAX6 gene is mutated in two patients with aniridia. *Nat Genet, 1*(5), 328-332. doi:10.1038/ng0892-328

Källén, B., Robert, E., & Harris, J. (1996). The descriptive epidemiology of anophthalmia and microphthalmia. *International Journal of Epidemiology*, *25*(5), 1009–1016. https://doi.org/10.1093/ije/25.5.1009

Kaufman, R., Weiss, O., Sebbagh, M., Ravid, R., Gibbs-Bar, L., Yaniv, K., et al. (2015). Development and origins of Zebrafish ocular vasculature. *BMC Dev Biol*, 15: 18 doi: 10.1186/s12861-015-0066-9

Kawaguchi, R., Yu, J., Honda, J., Hu, J., Whitelegge, J., Ping, P., . . . Sun, H. (2007). A membrane receptor for retinol binding protein mediates cellular uptake of vitamin A. *Science, 315*(5813), 820-825. doi:10.1126/science.1136244

Khan, T. N., Khan, K., Sadeghpour, A., Reynolds, H., Perilla, Y., McDonald, M. T., Gallentine, W. B., Baig, S. M., Task Force for Neonatal Genomics, Davis, E. E., & Katsanis, N. (2019). Mutations in NCAPG2 Cause a Severe Neurodevelopmental Syndrome that Expands the Phenotypic Spectrum of Condensinopathies. *American Journal of Human Genetics*, 104(1), 94–111. https://doi.org/10.1016/j.ajhg.2018.11.017

Khor, E.S., Noor, S.M., & Wong, P.F. (2016). Expression of zTOR-associated microRNAs in zebrafish embryo treated with rapamycin. *Life Sci*, 150:67-75. doi: 10.1016/j.lfs.2016.02.076. Epub 2016 Feb 23. PMID: 26916825.

Kim, J. W., & Lemke, G. (2006). Hedgehog-regulated localization of Vax2 controls eye development. *Genes Dev*, 20(20), 2833-2847. doi:10.1101/gad.1462706

Kim, S.H., Speirs, C.K., Solnica-Krezel, L., & Ess, K.C. (2011). Zebrafish model of tuberous sclerosis complex reveals cell-autonomous and non-cell-autonomous functions of mutant tuberin. *Dis Model Mech*, 4(2):255-67. doi: 10.1242/dmm.005587. Epub 2010 Oct 19. PMID: 20959633; PMCID: PMC3046101.

Kitambi, S.S., McCulloch, K.J., Peterson, R.T., & Malicki, J.J. (2009). Small molecule screen for compounds that affect vascular development in the zebrafish retina. *Mech Dev*, 126: 464–477. doi: 10.1016/j.mod.2009.01.002

Knickmeyer, M. D., Mateo, J. L., Eckert, P., Roussa, E., Rahhal, B., Zuniga, A., . . . Heermann, S. (2018). TGFbeta-facilitated optic fissure fusion and the role of bone morphogenetic protein antagonism. *Open Biol, 8*(3). doi:10.1098/rsob.170134

Koshiba-Takeuchi, K., Takeuchi, J. K., Matsumoto, K., Momose, T., Uno, K., Hoepker, V., . . . Ogura, T. (2000). Tbx5 and the retinotectum projection. *Science, 287*(5450), 134-137. doi:10.1126/science.287.5450.134

Kruse-Bend, R., Rosenthal, J., Quist, T.S., Veien, E.S., Fuhrmann, S., Dorsky, R.I., et al. (2012). Extraocular ectoderm triggers dorsal retinal fate during optic vesicle evagination in zebrafish. *Dev Biol*, 371: 57–65. doi: 10.1016/j.ydbio.2012.08.004

Kumar, N., Valliappan, A., & Bansal, R. (2020). Unusual superior iris and retinochoroidal coloboma. *Indian J Ophthalmol, 68*(5), 921. doi:10.4103/ijo.IJO_1876_19

Kwan, K. M., Otsuna, H., Kidokoro, H., Carney, K. R., Saijoh, Y., & Chien, C. B. (2012). A complex choreography of cell movements shapes the vertebrate eye. *Development, 139*(2), 359-372. doi:10.1242/dev.071407

Lagutin, O. V., Zhu, C. C., Kobayashi, D., Topczewski, J., Shimamura, K., Puelles, L., . . . Oliver, G. (2003). Six3 repression of Wnt signaling in the anterior neuroectoderm is essential for vertebrate forebrain development. *Genes Dev, 17*(3), 368-379. doi:10.1101/gad.1059403

Lalani, S. R., Safiullah, A. M., Fernbach, S. D., Harutyunyan, K. G., Thaller, C., Peterson, L. E., . . . Belmont, J. W. (2006). Spectrum of CHD7 mutations in 110 individuals with CHARGE syndrome and genotype-phenotype correlation. *Am J Hum Genet, 78*(2), 303-314. doi:10.1086/500273

Langenberg, T., Kahana, A., Wszalek, J. A., & Halloran, M. C. (2008). The eye organizes neural crest cell migration. *Dev Dyn, 237*(6), 1645-1652. doi:10.1002/dvdy.21577

Laplante, M., & Sabatini, D.M. (2009). mTOR signaling at a glance. *J Cell Sci*, 122(Pt 20):3589-94. doi: 10.1242/jcs.051011. PMID: 19812304; PMCID: PMC2758797.

Lawson, N.D., Wolfe, S.A. Forward and reverse genetic approaches for the analysis of vertebrate development in the zebrafish. *Developmental Cell.* **21** (1), doi:10.1016/j.devcel.2011.06.007 (2011).

Lee, H. S., Mood, K., Battu, G., Ji, Y. J., Singh, A., & Daar, I. O. (2009). Fibroblast growth factor receptor-induced phosphorylation of ephrinB1 modulates its interaction with Dishevelled. *Mol Biol Cell, 20*(1), 124-133. doi:10.1091/mbc.E08-06-0662

Lequeux, L., Rio, M., Vigouroux, A., Titeux, M., Etchevers, H., Malecaze, F., . . . Calvas, P. (2008). Confirmation of RAX gene involvement in human anophthalmia. *Clin Genet, 74*(4), 392-395. doi:10.1111/j.1399-0004.2008.01078.x

Li, H. S., Yang, J. M., Jacobson, R. D., Pasko, D., & Sundin, O. (1994). Pax-6 is first expressed in a region of ectoderm anterior to the early neural plate: implications for stepwise determination of the lens. *Dev Biol, 162*(1), 181-194. doi:10.1006/dbio.1994.1077

Lin, S., Harlalka, G. V., Hameed, A., Reham, H. M., Yasin, M., Muhammad, N., . . . Saleha, S. (2018). Novel mutations in ALDH1A3 associated with autosomal recessive anophthalmia/microphthalmia, and review of the literature. *BMC Med Genet, 19*(1), 160. doi:10.1186/s12881-018-0678-6

Liu, C., & Nathans, J. (2008). An essential role for frizzled 5 in mammalian ocular development. *Development, 135*(21), 3567-3576. doi:10.1242/dev.028076

Liu, C., Widen, S. A., Williamson, K. A., Ratnapriya, R., Gerth-Kahlert, C., Rainger, J., . . . Swaroop, A. (2016). A secreted WNT-ligand-binding domain of FZD5 generated by a frameshift mutation causes autosomal dominant coloboma. *Hum Mol Genet, 25*(7), 1382-1391. doi:10.1093/hmg/ddw020

Liu, Z. Z., Guo, J., Lu, Y., Liu, W., Fu, X., Yao, T., . . . Xu, H. A. (2019). Sema3E is required for migration of cranial neural crest cells in zebrafish: Implications for the pathogenesis of CHARGE syndrome. *Int J Exp Pathol, 100*(4), 234-243. doi:10.1111/iep.12331

Loeys, B. L., Chen, J., Neptune, E. R., Judge, D. P., Podowski, M., Holm, T., . . . Dietz, H. C. (2005). A syndrome of altered cardiovascular, craniofacial, neurocognitive and skeletal development caused by mutations in TGFBR1 or TGFBR2. *Nat Genet, 37*(3), 275-281. doi:10.1038/ng1511

Loeys, B. L., Schwarze, U., Holm, T., Callewaert, B. L., Thomas, G. H., Pannu, H., . . . Dietz, H. C. (2006). Aneurysm syndromes caused by mutations in the TGF-beta receptor. *N Engl J Med, 355*(8), 788-798. doi:10.1056/NEJMoa055695

London, N. J., Kessler, P., Williams, B., Pauer, G. J., Hagstrom, S. A., & Traboulsi, E. I. (2009). Sequence alterations in RX in patients with microphthalmia, anophthalmia, and coloboma. *Mol Vis, 15*, 162-167.

Loosli, F., Winkler, S., & Wittbrodt, J. (1999). Six3 overexpression initiates the formation of ectopic retina. *Genes Dev, 13*(6), 649-654. doi:10.1101/gad.13.6.649

Lu, B. X. (1989). [An analysis of 193 cases of congenital intraocular colobomas]. *[Zhonghua yan ke za zhi] Chinese journal of ophthalmology*, *25*(6), 357–359.

Lupo, G., Gestri, G., O'Brien, M., Denton, R. M., Chandraratna, R. A., Ley, S. V., . . . Wilson, S. W. (2011). Retinoic acid receptor signaling regulates choroid fissure closure through

independent mechanisms in the ventral optic cup and periocular mesenchyme. *Proc Natl Acad Sci U S A, 108*(21), 8698-8703. doi:10.1073/pnas.1103802108

Ma, X.M., & Blenis, J. (2009). Molecular mechanisms of mTOR-mediated translational control. *Nat Rev Mol Cell Biol*, 10(5):307-18. doi: 10.1038/nrm2672. Epub 2009 Apr 2. PMID: 19339977.

Macdonald, R., Barth, K. A., Xu, Q., Holder, N., Mikkola, I., & Wilson, S. W. (1995). Midline signalling is required for Pax gene regulation and patterning of the eyes. *Development, 121*(10), 3267-3278.

Macdonald, R., Scholes, J., Strahle, U., Brennan, C., Holder, N., Brand, M., & Wilson, S. W. (1997). The Pax protein Noi is required for commissural axon pathway formation in the rostral forebrain. *Development, 124*(12), 2397-2408.

Macken, W.L., Godwin, A., Wheway, G., Stals, K., Nazlamova, L., Ellard, S., Alfares, A., Aloraini, T., AlSubaie, L., Alfadhel, M., Alajaji, S., Wai, H.A., Self, J., Douglas, A.G.L., Kao, A.P., Guille, M., & Baralle, D. (2021). Biallelic variants in COPB1 cause a novel, severe intellectual disability syndrome with cataracts and variable microcephaly. *Genome Med*, 13(1):34. doi: 10.1186/s13073-021-00850-w. PMID: 33632302; PMCID: PMC7908744.

Mann, I., & Ross, J.A. (1929). A CASE OF ATYPICAL COLOBOMA ASSOCIATED WITH ABNORMAL RETINAL VESSELS. *Br J Ophthalmol*, 13: 608–612.

Martha, A., Strong, L. C., Ferrell, R. E., & Saunders, G. F. (1995). Three novel aniridia mutations in the human PAX6 gene. *Hum Mutat, 6*(1), 44-49. doi:10.1002/humu.1380060109

Martinez-Morales, J. R., & Wittbrodt, J. (2009). Shaping the vertebrate eye. *Curr Opin Genet Dev, 19*(5), 511-517. doi:10.1016/j.gde.2009.08.003

Mathers, P. H., Grinberg, A., Mahon, K. A., & Jamrich, M. (1997). The Rx homeobox gene is essential for vertebrate eye development. *Nature, 387*(6633), 603-607. doi:10.1038/42475

Matt, N., Dupe, V., Garnier, J. M., Dennefeld, C., Chambon, P., Mark, M., & Ghyselinck, N. B. (2005). Retinoic acid-dependent eye morphogenesis is orchestrated by neural crest cells. *Development, 132*(21), 4789-4800. doi:10.1242/dev.02031

Matt, N., Ghyselinck, N. B., Pellerin, I., & Dupe, V. (2008). Impairing retinoic acid signalling in the neural crest cells is sufficient to alter entire eye morphogenesis. *Dev Biol, 320*(1), 140-148. doi:10.1016/j.ydbio.2008.04.039

Maurus, D., Heligon, C., Burger-Schwarzler, A., Brandli, A. W., & Kuhl, M. (2005). Noncanonical Wnt-4 signaling and EAF2 are required for eye development in Xenopus laevis. *EMBO J, 24*(6), 1181-1191. doi:10.1038/sj.emboj.7600603

Mayer, U., Kohfeldt, E., & Timpl, R. (1998). Structural and genetic analysis of laminin-nidogen interaction. *Ann N Y Acad Sci, 857*, 130-142. doi:10.1111/j.1749-6632.1998.tb10113.x

McMahon, C., Gestri, G., Wilson, S. W., & Link, B. A. (2009). Lmx1b is essential for survival of periocular mesenchymal cells and influences Fgf-mediated retinal patterning in zebrafish. *Dev Biol, 332*(2), 287-298. doi:10.1016/j.ydbio.2009.05.577

Mic, F. A., Molotkov, A., Molotkova, N., & Duester, G. (2004). Raldh2 expression in optic vesicle generates a retinoic acid signal needed for invagination of retina during optic cup formation. *Dev Dyn, 231*(2), 270-277. doi:10.1002/dvdy.20128

Milunsky, J. M., Maher, T. A., Zhao, G., Roberts, A. E., Stalker, H. J., Zori, R. T., . . . Lin, A. E. (2008). TFAP2A mutations result in branchio-oculo-facial syndrome. *Am J Hum Genet, 82*(5), 1171-1177. doi:10.1016/j.ajhg.2008.03.005

Mintzer, K.A., Lee, M.A., Runke, G., Trout, J., Whitman, M., & Mullins, M.C. (2001). Lost-a-fin encodes a type I BMP receptor, Alk8, acting maternally and zygotically in dorsoventral pattern formation. *Development*, 128(6):859-69. PMID: 11222141.

Mirzoyan, Z., Sollazzo, M., Allocca, M., Valenza, A. M., Grifoni, D., & Bellosta, P. (2019). Drosophila melanogaster: A model organism to study cancer. *Frontiers in Genetics*, Vol. 10, p. 51. https://doi.org/10.3389/fgene.2019.00051

Mohammadi, S., Saberidokht, B., Subramaniam, S., & Grama, A. (2015). Scope and limitations of yeast as a model organism for studying human tissue-specific pathways. *BMC Systems Biology*, *9*(1), 96. https://doi.org/10.1186/s12918-015-0253-0

Molotkov, A., Molotkova, N., & Duester, G. (2006). Retinoic acid guides eye morphogenetic movements via paracrine signaling but is unnecessary for retinal dorsoventral patterning. *Development, 133*(10), 1901-1910. doi:10.1242/dev.02328

Moore, K. B., Mood, K., Daar, I. O., & Moody, S. A. (2004). Morphogenetic movements underlying eye field formation require interactions between the FGF and ephrinB1 signaling pathways. *Dev Cell, 6*(1), 55-67. doi:10.1016/s1534-5807(03)00395-2

Morcillo, J., Martinez-Morales, J. R., Trousse, F., Fermin, Y., Sowden, J. C., & Bovolenta, P. (2006). Proper patterning of the optic fissure requires the sequential activity of BMP7 and SHH. *Development, 133*(16), 3179-3190. doi:10.1242/dev.02493

Moreau, Y., & Tranchevent, L. C. (2012). Computational tools for prioritizing candidate genes: Boosting disease gene discovery. *Nature Reviews Genetics*, Vol. 13, pp. 523–536. https://doi.org/10.1038/nrg3253

Morrison, D., FitzPatrick, D., Hanson, I., Williamson, K., van Heyningen, V., Fleck, B., … Campbell, H. (2002). National study of microphthalmia, anophthalmia, and coloboma

(MAC) in Scotland: Investigation of genetic aetiology. *Journal of Medical Genetics*, *39*(1), 16–22. https://doi.org/10.1136/jmg.39.1.16

Mui, S. H., Kim, J. W., Lemke, G., & Bertuzzi, S. (2005). Vax genes ventralize the embryonic eye. *Genes Dev*, 19(10), 1249-1259. doi:10.1101/gad.1276605

Murali, D., Yoshikawa, S., Corrigan, R. R., Plas, D. J., Crair, M. C., Oliver, G., . . . Furuta, Y. (2005). Distinct developmental programs require different levels of Bmp signaling during mouse retinal development. *Development, 132*(5), 913-923. doi:10.1242/dev.01673

Muranishi, Y., Terada, K., Inoue, T., Katoh, K., Tsujii, T., Sanuki, R., . . . Furukawa, T. (2011). An essential role for RAX homeoprotein and NOTCH-HES signaling in Otx2 expression in embryonic retinal photoreceptor cell fate determination. *J Neurosci, 31*(46), 16792-16807. doi:10.1523/JNEUROSCI.3109-11.2011

Nakamura, K.M., Diehl, N.N., & Mohney, B.G. (2011). Incidence, ocular findings, and systemic associations of ocular coloboma: a population-based study. *Arch Ophthalmol Chic Ill 1960*, 129: 69–74. doi: 10.1001/archophthalmol.2010.320

Nedelec, B., Rozet, J. M., & Fares Taie, L. (2019). Genetic architecture of retinoic-acid signaling-associated ocular developmental defects. *Hum Genet, 138*(8-9), 937-955. doi:10.1007/s00439-019-02052-2

Neu, M. B., Bowling, K. M., & Cooper, G. M. (2019). Clinical utility of genomic sequencing. *Current Opinion in Pediatrics*, *31*(6), 732–738. https://doi.org/10.1097/MOP.0000000000000815

Noden, D. M. (1983). The role of the neural crest in patterning of avian cranial skeletal, connective, and muscle tissues. *Dev Biol, 96*(1), 144-165. doi:10.1016/0012-1606(83)90318-4

Nordquist, D., & McLoon, S.C. (1991). Morphological patterns in the developing vertebrate retina. *Anat Embryol (Berl)*, 184: 433–440.

Okuno, H., Renault Mihara, F., Ohta, S., Fukuda, K., Kurosawa, K., Akamatsu, W., . . . Okano, H. (2017). CHARGE syndrome modeling using patient-iPSCs reveals defective migration of neural crest cells harboring CHD7 mutations. *Elife, 6*. doi:10.7554/eLife.21114

Oliver, G., Mailhos, A., Wehr, R., Copeland, N. G., Jenkins, N. A., & Gruss, P. (1995). Six3, a murine homologue of the sine oculis gene, demarcates the most anterior border of the developing neural plate and is expressed during eye development. *Development, 121*(12), 4045-4055.

Onwochei, B. C., Simon, J. W., Bateman, J. B., Couture, K. C., & Mir, E. (2000). Ocular colobomata. *Surv Ophthalmol, 45*(3), 175-194. doi:10.1016/s0039-6257(00)00151-x

Orioli, I. M., Castilla, E. E., Ming, J. E., Nazer, J., Burle de Aguiar, M. J., Llerena, J. C., & Muenke, M. (2001). Identification of novel mutations in SHH and ZIC2 in a South American (ECLAMC) population with holoprosencephaly. *Hum Genet, 109*(1), 1-6. doi:10.1007/s004390100537

Ou, J., Bharti, K., Nodari, A., Bertuzzi, S., & Arnheiter, H. (2013). Vax1/2 genes counteract Mitf-induced respecification of the retinal pigment epithelium. *PLoS* One, 8(3):e59247. doi: 10.1371/journal.pone.0059247. Epub 2013 Mar 15. PMID: 23555005; PMCID: PMC3598659.

Ozeki, H., Shirai, S., Ikeda, K., & Ogura, Y. (1999). Anomalies associated with Axenfeld-Rieger syndrome. *Graefes Arch Clin Exp Ophthalmol, 237*(9), 730-734. doi:10.1007/s004170050304

Pagon, R. A., Graham, J. M., Jr., Zonana, J., & Yong, S. L. (1981). Coloboma, congenital heart disease, and choanal atresia with multiple anomalies: CHARGE association. *J Pediatr, 99*(2), 223-227. doi:10.1016/s0022-3476(81)80454-4

Pant, S.D., March, L.D., Famulski, J.K., French, C.R., Lehmann, O.J., & Waskiewicz, A.J. (2013). Molecular mechanisms regulating ocular apoptosis in zebrafish gdf6a mutants. *Invest Ophthalmol Vis Sci*, 54: 5871–5879. doi: 10.1167/iovs.12-11315

Patton, E. E., & Zon, L. I. (2001). The art and design of genetic screens: Zebrafish. *Nature Reviews Genetics*, Vol. 2, pp. 956–966. https://doi.org/10.1038/35103567

Payne, S., Burney, M. J., McCue, K., Popal, N., Davidson, S. M., Anderson, R. H., & Scambler, P. J. (2015). A critical role for the chromatin remodeller CHD7 in anterior mesoderm during cardiovascular development. *Dev Biol, 405*(1), 82-95. doi:10.1016/j.ydbio.2015.06.017

Pineda-Alvarez, D. E., Solomon, B. D., Roessler, E., Balog, J. Z., Hadley, D. W., Zein, W. M., . . . Muenke, M. (2011). A broad range of ophthalmologic anomalies is part of the holoprosencephaly spectrum. *Am J Med Genet A, 155A*(11), 2713-2720. doi:10.1002/ajmg.a.34261

Piro, R. M., & di Cunto, F. (2012). Computational approaches to disease-gene prediction: Rationale, classification and successes. *FEBS Journal*, Vol. 279, pp. 678–696. https://doi.org/10.1111/j.1742-4658.2012.08471.x

Pober, B.R. (2010). Williams-Beuren syndrome. N Engl J Med, 362(3):239-52. doi: 10.1056/NEJMra0903074. Erratum in: N Engl J Med. 2010 Jun 3;362(22):2142. PMID: 20089974.

Porges, Y., Gershoni-Baruch, R., Leibu, R., Goldscher, D., Zonis, S., Shapira, I., & Miller, B. (1992). Hereditary microphthalmia with colobomatous cyst. *American Journal of Ophthalmology*, *114*(1), 30–34. https://doi.org/10.1016/s0002-9394(14)77409-4

Potterf, S. B., Furumura, M., Dunn, K. J., Arnheiter, H., & Pavan, W. J. (2000). Transcription factor hierarchy in Waardenburg syndrome: regulation of MITF expression by SOX10 and PAX3. *Hum Genet, 107*(1), 1-6. doi:10.1007/s004390000328

Pressman, C. L., Chen, H., & Johnson, R. L. (2000). LMX1B, a LIM homeodomain class transcription factor, is necessary for normal development of multiple tissues in the anterior segment of the murine eye. *Genesis, 26*(1), 15-25.

Priest, J. R. (2017). A primer to clinical genome sequencing. *Current Opinion in Pediatrics*, Vol. 29, pp. 513–519. https://doi.org/10.1097/MOP.0000000000000532

Puschel, A. W., Gruss, P., & Westerfield, M. (1992). Sequence and expression pattern of pax-6 are highly conserved between zebrafish and mice. *Development, 114*(3), 643-651.

Ramirez-Miranda, A., & Zenteno, J.C. (2006). PAX6 gene intragenic deletions in Mexican patients with congenital aniridia. *Mol Vis*, 12: 318–323.

Ranchod, T. M., Quiram, P. A., Hathaway, N., Ho, L. Y., Glasgow, B. J., & Trese, M. T. (2010). Microcornea, posterior megalolenticonus, persistent fetal vasculature, and coloboma: a new syndrome. *Ophthalmology, 117*(9), 1843-1847. doi:10.1016/j.ophtha.2009.12.045

Rasmussen, J. T., Deardorff, M. A., Tan, C., Rao, M. S., Klein, P. S., & Vetter, M. L. (2001). Regulation of eye development by frizzled signaling in Xenopus. *Proc Natl Acad Sci U S A, 98*(7), 3861-3866. doi:10.1073/pnas.071586298

Raveh, E., Papsin, B. C., & Forte, V. (2000). Branchio-oculo-facial syndrome. *Int J Pediatr Otorhinolaryngol, 53*(2), 149-156. doi:10.1016/s0165-5876(00)00310-4

Reis, L. M., Khan, A., Kariminejad, A., Ebadi, F., Tyler, R. C., & Semina, E. V. (2011). VSX2 mutations in autosomal recessive microphthalmia. *Mol Vis, 17*, 2527-2532.

Rembold, M., Loosli, F., Adams, R. J., & Wittbrodt, J. (2006). Individual cell migration serves as the driving force for optic vesicle evagination. *Science, 313*(5790), 1130-1134. doi:10.1126/science.1127144

Ren, X., Ustiyan, V., Pradhan, A., Cai, Y., Havrilak, J.A., Bolte, C.S., Shannon, J.M., Kalin, T.V., & Kalinichenko, V.V. (2014). FOXF1 transcription factor is required for formation of embryonic vasculature by regulating VEGF signaling in endothelial cells. *Circ Res*, 115(8):709-20. doi: 10.1161/CIRCRESAHA.115.304382. Epub 2014 Aug 4. PMID: 25091710; PMCID: PMC4810682.

Richards, S., Aziz, N., Bale, S., Bick, D., Das, S., Gastier-Foster, J., … Rehm, H. L. (2015). Standards and guidelines for the interpretation of sequence variants: A joint consensus recommendation of the American College of Medical Genetics and Genomics and the

Association for Molecular Pathology. *Genetics in Medicine*, *17*(5), 405–424. https://doi.org/10.1038/gim.2015.30

Roberts, A. B., Sporn, M. B., Assoian, R. K., Smith, J. M., Roche, N. S., Wakefield, L. M., . . . et al. (1986). Transforming growth factor type beta: rapid induction of fibrosis and angiogenesis in vivo and stimulation of collagen formation in vitro. *Proc Natl Acad Sci U S A, 83*(12), 4167-4171. doi:10.1073/pnas.83.12.4167

Robitaille, A.M., Christen, S., Shimobayashi, M., Cornu, M., Fava, L.L., Moes, S., Prescianotto-Baschong, C., Sauer, U., Jenoe, P., & Hall, M.N. (2013). Quantitative phosphoproteomics reveal mTORC1 activates de novo pyrimidine synthesis. *Science*, 339(6125):1320-3. doi: 10.1126/science.1228771. Epub 2013 Feb 21. PMID: 23429704.

Rodgers, H. M., Huffman, V. J., Voronina, V. A., Lewandoski, M., & Mathers, P. H. (2018). The role of the Rx homeobox gene in retinal progenitor proliferation and cell fate specification. *Mech Dev, 151*, 18-29. doi:10.1016/j.mod.2018.04.003

Roos, L., Fang, M., Dali, C., Jensen, H., Christoffersen, N., Wu, B., . . . Tumer, Z. (2014). A homozygous mutation in a consanguineous family consolidates the role of ALDH1A3 in autosomal recessive microphthalmia. *Clin Genet, 86*(3), 276-281. doi:10.1111/cge.12277

Rothe, M., Kanwal, N., Dietmann, P., Seigfried, F.A., Hempel, A., Schütz, D., Reim, D., Engels, R., Linnemann, A., Schmeisser, M.J., Bockmann, J., Kühl, M., Boeckers, T.M., & Kühl, S.J. (2017). An Epha4/Sipa1l3/Wnt pathway regulates eye development and lens maturation. *Development*, 144(2):321-333. doi: 10.1242/dev.147462. Epub 2016 Dec 19. PMID: 27993984.

Rothfield, L. D., Cernichiaro-Espinosa, L. A., Alabiad, C. R., McKeown, C. A., Tran, K., Chang, T. C., & Berrocal, A. M. (2019). Microcornea, posterior megalolenticonus, persistent fetal vasculature, chorioretinal coloboma (MPPC) syndrome: Case series post vitrectomy. *Am J Ophthalmol Case Rep, 14*, 5-9. doi:10.1016/j.ajoc.2019.01.005

Rowley, S.A., O'Callaghan, F.J., & Osborne, J.P. (2001). Ophthalmic manifestations of tuberous sclerosis: a population based study. *Br J Ophthalmol*, 85(4):420-3. doi: 10.1136/bjo.85.4.420. PMID: 11264130; PMCID: PMC1723924.

Saint-Geniez, M., & D'Amore, P. A. (2004). Development and pathology of the hyaloid, choroidal and retinal vasculature. *Int J Dev Biol, 48*(8-9), 1045-1058. doi:10.1387/ijdb.041895ms

Sakuta, H., Takahashi, H., Shintani, T., Etani, K., Aoshima, A., & Noda, M. (2006). Role of bone morphogenic protein 2 in retinal patterning and retinotectal projection. *J Neurosci, 26*(42), 10868-10878. doi:10.1523/JNEUROSCI.3027-06.2006

Samuel, A., Rubinstein, A. M., Azar, T. T., Ben-Moshe Livne, Z., Kim, S. H., & Inbal, A. (2016). Six3 regulates optic nerve development via multiple mechanisms. *Sci Rep, 6*, 20267. doi:10.1038/srep20267

Sasagawa, S., Takabatake, T., Takabatake, Y., Muramatsu, T., & Takeshima, K. (2002). Axes establishment during eye morphogenesis in Xenopus by coordinate and antagonistic actions of BMP4, Shh, and RA. *Genes N Y N 2000*, 33: 86–96. doi: 10.1002/gene.10095

Schmitt, E.A., & Dowling, J.E. (1999). Early retinal development in the zebrafish, Danio rerio: light and electron microscopic analyses. *J Comp Neurol*, 404: 515–536.

Schmidt, K., Cavodeassi, F., Feng, Y., & Stephens, D. J. (2013). Early stages of retinal development depend on Sec13 function. *Biology Open*, 2(3), 256–266. https://doi.org/10.1242/bio.20133251

Schneider, A., Bardakjian, T., Reis, L. M., Tyler, R. C., & Semina, E. v. (2009). Novel SOX2 mutations and genotype-phenotype correlation in anophthalmia and microphthalmia. *American Journal of Medical Genetics, Part A*, *149*(12), 2706–2715. https://doi.org/10.1002/ajmg.a.33098

Schnetz, M. P., Handoko, L., Akhtar-Zaidi, B., Bartels, C. F., Pereira, C. F., Fisher, A. G., . . . Scacheri, P. C. (2010). CHD7 targets active gene enhancer elements to modulate ES cell-specific gene expression. *PLoS Genet, 6*(7), e1001023. doi:10.1371/journal.pgen.1001023

Schultz, L. E., Solin, S. L., Wierson, W. A., Lovan, J. M., Syrkin-Nikolau, J., Lincow, D. E., Severin, A. J., Sakaguchi, D. S., & McGrail, M. (2017). Vascular Endothelial Growth Factor A and Leptin Expression Associated with Ectopic Proliferation and Retinal Dysplasia in Zebrafish Optic Pathway Tumors. *Zebrafish*, 14(4), 343–356. https://doi.org/10.1089/zeb.2016.1366

Schulz, Y., Wehner, P., Opitz, L., Salinas-Riester, G., Bongers, E. M., van Ravenswaaij-Arts, C. M., . . . Pauli, S. (2014). CHD7, the gene mutated in CHARGE syndrome, regulates genes involved in neural crest cell guidance. *Hum Genet, 133*(8), 997-1009. doi:10.1007/s00439-014-1444-2

Sedletcaia, A. & Evans, T. (2011). Heart Chamber Size in Zebrafish is Regulated Redundantly by Duplicated Tbx2. *Genes Dev Dyn*, 240, 1548-1557.

Sedykh, I., Yoon, B., Roberson, L., Moskvin, O., Dewey, C. N., & Grinblat, Y. (2017). Zebrafish zic2 controls formation of periocular neural crest and choroid fissure morphogenesis. *Dev Biol, 429*(1), 92-104. doi:10.1016/j.ydbio.2017.07.003

Seigfried, F. A., Cizelsky, W., Pfister, A. S., Dietmann, P., Walther, P., Kuhl, M., & Kuhl, S. J. (2017). Frizzled 3 acts upstream of Alcam during embryonic eye development. *Dev Biol, 426*(1), 69-83. doi:10.1016/j.ydbio.2017.04.004

Seimiya, M., & Gehring, W. J. (2000). The Drosophila homeobox gene optix is capable of inducing ectopic eyes by an eyeless-independent mechanism. *Development, 127*(9), 1879-1886.

Semina, E. V., Reiter, R., Leysens, N. J., Alward, W. L., Small, K. W., Datson, N. A., . . . Murray, J. C. (1996). Cloning and characterization of a novel bicoid-related homeobox transcription factor gene, RIEG, involved in Rieger syndrome. *Nat Genet, 14*(4), 392-399. doi:10.1038/ng1296-392

Shah, S. P., Taylor, A. E., Sowden, J. C., Ragge, N. K., Russell-Eggitt, I., Rahi, J. S., & Gilbert, C. E. (2011). Anophthalmos, microphthalmos, and typical Coloboma in the United Kingdom: A prospective study of incidence and risk. *Investigative Ophthalmology and Visual Science*, *52*(1), 558–564. https://doi.org/10.1167/iovs.10-5263

Shah, S. P., Taylor, A. E., Sowden, J. C., Ragge, N., Russell-Eggitt, I., Rahi, J. S., & Gilbert, C. E. (2012). Anophthalmos, microphthalmos, and coloboma in the United Kingdom: Clinical features, results of investigations, and early management. *Ophthalmology*, *119*(2), 362–368. https://doi.org/10.1016/j.ophtha.2011.07.039

Shen, T., Lee, A., Shen, C., & Lin, C. J. (2015). The long tail and rare disease research: the impact of next-generation sequencing for rare Mendelian disorders. Genetics research, 97, e15. https://doi.org/10.1017/S0016672315000166

Sidhaye, J., & Norden, C. (2017). Concerted action of neuroepithelial basal shrinkage and active epithelial migration ensures efficient optic cup morphogenesis. *Elife, 6*. doi:10.7554/eLife.22689

Simeone, A., Acampora, D., Mallamaci, A., Stornaiuolo, A., D'Apice, M. R., Nigro, V., & Boncinelli, E. (1993). A vertebrate gene related to orthodenticle contains a homeodomain of the bicoid class and demarcates anterior neuroectoderm in the gastrulating mouse embryo. *EMBO J, 12*(7), 2735-2747.

Slavotinek, A. M. (2011). Eye development genes and known syndromes. Molecular Genetics and Metabolism, Vol. 104, pp. 448–456. https://doi.org/10.1016/j.ymgme.2011.09.029

Slavotinek, A.M., Chao, R., Vacik, T., Yahyavi, M., Abouzeid, H., Bardakjian, T., Schneider, A., Shaw, G., Sherr, E.H., Lemke, G., Youssef, M., & Schorderet, D.F. (2012). VAX1 mutation associated with microphthalmia, corpus callosum agenesis, and orofacial clefting: the first description of a VAX1 phenotype in humans. *Hum Mutat*, 33(2):364-8. doi: 10.1002/humu.21658. Epub 2011 Dec 27. PMID: 22095910; PMCID: PMC3401628.

Snelson, C.D., Santhakumar, K., Halpern, M.E., & Gamse, J.T. (2008). Tbx2b is required for the development of the parapineal organ. *Dev Camb Engl*, 135: 1693–1702. doi: 10.1242/dev.016576

Solomon, B. D., Lacbawan, F., Mercier, S., Clegg, N. J., Delgado, M. R., Rosenbaum, K., . . . Muenke, M. (2010). Mutations in ZIC2 in human holoprosencephaly: description of a novel ZIC2 specific phenotype and comprehensive analysis of 157 individuals. *J Med Genet, 47*(8), 513-524. doi:10.1136/jmg.2009.073049

Stoll, C., Alembik, Y., Dott, B., & Roth, M. P. (1997). Congenital eye malformations in 212,479 consecutive births. *Annales de Genetique*, *40*(2), 122–128.

Sun, P., Quan, Z., Zhang, B., Wu, T., & Xi, R. (2010). TSC1/2 tumour suppressor complex maintains Drosophila germline stem cells by preventing differentiation. *Development*, 137(15):2461-9. doi: 10.1242/dev.051466. Epub 2010 Jun 23. PMID: 20573703.

Takata, N., Abbey, D., Fiore, L., Acosta, S., Feng, R., Gil, H. J., . . . Oliver, G. (2017). An Eye Organoid Approach Identifies Six3 Suppression of R-spondin 2 as a Critical Step in Mouse Neuroretina Differentiation. *Cell Rep, 21*(6), 1534-1549. doi:10.1016/j.celrep.2017.10.041

Take-uchi, M., Clarke, J. D., & Wilson, S. W. (2003). Hedgehog signalling maintains the optic stalk-retinal interface through the regulation of Vax gene activity. *Development, 130*(5), 955-968. doi:10.1242/dev.00305

Takkar, B., Chandra, P., Kumar, V., & Agrawal, R. (2016). A case of iridofundal coloboma with persistent fetal vasculature and lens subluxation. *J AAPOS, 20*(2), 180-182. doi:10.1016/j.jaapos.2015.12.004

Tassabehji, M., Zhi, M. F., Hilton, E. N., McGaughran, J., Zhao, Z., de Bock, C. E., … Clarke, R. A. (2008). Mutations in GDF6 are associated with vertebral segmentation defects in Klippel-Feil syndrome. *Human Mutation*, *29*(8), 1017–1027. https://doi.org/10.1002/humu.20741

Tekin, M., Sirmaci, A., Yuksel-Konuk, B., Fitoz, S., & Sennaroglu, L. (2009). A complex TFAP2A allele is associated with branchio-oculo-facial syndrome and inner ear malformation in a deaf child. *Am J Med Genet A, 149A*(3), 427-430. doi:10.1002/ajmg.a.32619

Tetreault, M., Bareke, E., Nadaf, J., Alirezaie, N., & Majewski, J. (2015). Whole-exome sequencing as a diagnostic tool: Current challenges and future opportunities. *Expert Review of Molecular Diagnostics*, Vol. 15, pp. 749–760. https://doi.org/10.1586/14737159.2015.1039516

Thien, A., Prentzell, M.T., Holzwarth, B., Kläsener, K., Kuper, I., Boehlke, C., Sonntag, A.G., Ruf, S., Maerz, L., Nitschke, R., Grellscheid, S.N., Reth, M., Walz, G., Baumeister, R., Neumann-Haefelin, E., & Thedieck, K. (2015). TSC1 activates TGF-β-Smad2/3 signaling in growth arrest and epithelial-to-mesenchymal transition. *Dev Cell*, 32(5):617-30. doi: 10.1016/j.devcel.2015.01.026. Epub 2015 Feb 26. Erratum in: Dev Cell. 2015 May 4;33(3):366. PMID: 25727005.

Tomar, S., Sethi, R., & Lai, P. S. (2019). Specific phenotype semantics facilitate gene prioritization in clinical exome sequencing. *European Journal of Human Genetics*, *27*(9), 1389–1397. https://doi.org/10.1038/s41431-019-0412-7

Tomarev, S. I., Callaerts, P., Kos, L., Zinovieva, R., Halder, G., Gehring, W., & Piatigorsky, J. (1997). Squid Pax-6 and eye development. *Proc Natl Acad Sci U S A, 94*(6), 2421-2426. doi:10.1073/pnas.94.6.2421

Torres, M., Gomez-Pardo, E., & Gruss, P. (1996). Pax2 contributes to inner ear patterning and optic nerve trajectory. *Development, 122*(11), 3381-3391.

Tranchevent, L. ´ E.-C., Ardeshirdavani, A., Elshal, S., Alcaide, D., Aerts, J., Auboeuf, D., & Moreau, Y. (2016). Candidate gene prioritization with Endeavour. *Nucleic Acids Research*, *44*, 117–121. https://doi.org/10.1093/nar/gkw365

Trost, A., Schroedl, F., Lange, S., Rivera, F. J., Tempfer, H., Korntner, S., . . . Reitsamer, H. A. (2013). Neural crest origin of retinal and choroidal pericytes. *Invest Ophthalmol Vis Sci, 54*(13), 7910-7921. doi:10.1167/iovs.13-12946

Tsuji, N., Kita, K., Ozaki, K., Narama, I., & Matsuura, T. (2012). Organogenesis of mild ocular coloboma in FLS mice: failure of basement membrane disintegration at optic fissure margins. *Exp Eye Res, 94*(1), 174-178. doi:10.1016/j.exer.2011.12.004

Tumer, Z., & Bach-Holm, D. (2009). Axenfeld-Rieger syndrome and spectrum of PITX2 and FOXC1 mutations. *Eur J Hum Genet, 17*(12), 1527-1539. doi:10.1038/ejhg.2009.93

Ufartes, R., Schwenty-Lara, J., Freese, L., Neuhofer, C., Moller, J., Wehner, P., . . . Pauli, S. (2018). Sema3a plays a role in the pathogenesis of CHARGE syndrome. *Hum Mol Genet, 27*(8), 1343-1352. doi:10.1093/hmg/ddy045

Valdivia, L. E., Lamb, D. B., Horner, W., Wierzbicki, C., Tafessu, A., Williams, A. M., . . . Cerveny, K. L. (2016). Antagonism between Gdf6a and retinoic acid pathways controls timing of retinal neurogenesis and growth of the eye in zebrafish. *Development, 143*(7), 1087-1098. doi:10.1242/dev.130922

Veien, E.S., Rosenthal, J.S., Kruse-Bend, R.C., Chien, C-B., & Dorsky, R.I. (2008). Canonical Wnt signaling is required for the maintenance of dorsal retinal identity. *Dev Camb Engl*, 135: 4101–4111. doi: 10.1242/dev.027367

Verma, A. S., & Fitzpatrick, D. R. (2007). Anophthalmia and microphthalmia. *Orphanet Journal of Rare Diseases*, *2*, 47. https://doi.org/10.1186/1750-1172-2-47

Villarroel, C.E., Villanueva-Mendoza, C., Orozco, L., Alcántara-Ortigoza, M.A., Jiménez, D.F., Ordaz, J.C., et al. (2008). Molecular analysis of the PAX6 gene in Mexican patients with congenital aniridia: report of four novel mutations. *Mol Vis*, 14: 1650–1658.

Vissers, L. E., van Ravenswaaij, C. M., Admiraal, R., Hurst, J. A., de Vries, B. B., Janssen, I. M., . . . van Kessel, A. G. (2004). Mutations in a new member of the chromodomain gene family cause CHARGE syndrome. *Nat Genet, 36*(9), 955-957. doi:10.1038/ng1407

Vogel, A., Rodriguez, C., Warnken, W., & Izpisua Belmonte, J. C. (1995). Dorsal cell fate specified by chick Lmx1 during vertebrate limb development. *Nature, 378*(6558), 716-720. doi:10.1038/378716a0

Volkmann, B. A., Zinkevich, N. S., Mustonen, A., Schilter, K. F., Bosenko, D. V., Reis, L. M., . . . Semina, E. V. (2011). Potential novel mechanism for Axenfeld-Rieger syndrome: deletion of a distant region containing regulatory elements of PITX2. *Invest Ophthalmol Vis Sci, 52*(3), 1450-1459. doi:10.1167/iovs.10-6060

Vollrath, D., Jaramillo-Babb, V. L., Clough, M. V., McIntosh, I., Scott, K. M., Lichter, P. R., & Richards, J. E. (1998). Loss-of-function mutations in the LIM-homeodomain gene, LMX1B, in nail-patella syndrome. *Hum Mol Genet, 7*(7), 1091-1098. doi:10.1093/hmg/7.7.1091

Voronina, V. A., Kozhemyakina, E. A., O'Kernick, C. M., Kahn, N. D., Wenger, S. L., Linberg, J. V., . . . Mathers, P. H. (2004). Mutations in the human RAX homeobox gene in a patient with anophthalmia and sclerocornea. *Hum Mol Genet, 13*(3), 315-322. doi:10.1093/hmg/ddh025

Wallis, D. E., Roessler, E., Hehr, U., Nanni, L., Wiltshire, T., Richieri-Costa, A., . . . Muenke, M. (1999). Mutations in the homeodomain of the human SIX3 gene cause holoprosencephaly. *Nat Genet, 22*(2), 196-198.

Walther, C., & Gruss, P. (1991). Pax-6, a murine paired box gene, is expressed in the developing CNS. *Development, 113*(4), 1435-1449.

Wang, S-S., Huang, H-Y., Chen, S-Z., Li, X., Zhang, W-T., & Tang, Q-Q. (2013). Gdf6 induces commitment of pluripotent mesenchymal C3H10T1/2 cells to the adipocyte lineage. *FEBS J*, 280: 2644–2651. doi: 10.1111/febs.12256

Wang, X., & Proud, C.G. (2011). mTORC1 signaling: what we still don't know. *J Mol Cell Biol*, 3(4):206-20. doi: 10.1093/jmcb/mjq038. Epub 2010 Dec 7. PMID: 21138990.

Wangler, M. F., Yamamoto, S., Chao, H. T., Posey, J. E., Westerfield, M., Postlethwait, J., … Palmer, C. G. (2017). Model organisms facilitate rare disease diagnosis and therapeutic research. *Genetics*, Vol. 207, pp. 9–27. https://doi.org/10.1534/genetics.117.203067

Warr, N., Powles-Glover, N., Chappell, A., Robson, J., Norris, D., & Arkell, R. M. (2008). Zic2-associated holoprosencephaly is caused by a transient defect in the organizer region during gastrulation. *Hum Mol Genet, 17*(19), 2986-2996. doi:10.1093/hmg/ddn197

Waterston, R. H., Lindblad-Toh, K., Birney, E., Rogers, J., Abril, J. F., Agarwal, P., … Lander, E. S. (2002). Initial sequencing and comparative analysis of the mouse genome. *Nature*, *420*(6915), 520–562. https://doi.org/10.1038/nature01262

Watt, K. E. N., & Trainor, P. A. (2014). Chapter 17 - Neurocristopathies: The Etiology and Pathogenesis of Disorders Arising from Defects in Neural Crest Cell Development. In P. A. Trainor (Ed.), *Chapter 17 - Neurocristopathies: The Etiology and Pathogenesis of Disorders Arising from Defects in Neural Crest Cell Development* (pp. 361-394): Academic Press.

Weaver, M. L., Piedade, W. P., Meshram, N. N., & Famulski, J. K. (2020). Hyaloid vasculature and mmp2 activity play a role during optic fissure fusion in zebrafish. *Scientific Reports*, *10*(1). https://doi.org/10.1038/s41598-020-66451-6

Webb, T. R., Matarin, M., Gardner, J. C., Kelberman, D., Hassan, H., Ang, W., . . . Hardcastle, A. J. (2012). X-linked megalocornea caused by mutations in CHRDL1 identifies an essential role for ventroptin in anterior segment development. *Am J Hum Genet, 90*(2), 247-259. doi:10.1016/j.ajhg.2011.12.019

Wei, C. Y., Wang, H. P., Zhu, Z. Y., & Sun, Y. H. (2014). Transcriptional factors smad1 and smad9 act redundantly to mediate zebrafish ventral specification downstream of smad5. *The Journal of Biological Chemistry*, 289(10), 6604–6618. https://doi.org/10.1074/jbc.M114.549758

Weiner, G. A., & Nudleman, E. (2019). Microcornea, Posterior Megalolenticonus, Persistent Fetal Vasculature, and Coloboma Syndrome Associated With a New Mutation in ZNF408. *Ophthalmic Surg Lasers Imaging Retina, 50*(4), 253-256. doi:10.3928/23258160-20190401-10

Weiss, O., Kaufman, R., Michaeli, N., & Inbal, A. (2012). Abnormal vasculature interferes with optic fissure closure in lmo2 mutant zebrafish embryos. *Dev Biol, 369*(2), 191-198. doi:10.1016/j.ydbio.2012.06.029

Weiss, O., Kaufman, R., Mishani, E., & Inbal, A. (2017). Ocular vessel patterning in zebrafish is indirectly regulated by Hedgehog signaling. *Int J Dev Biol*, 61: 277–284. doi: 10.1387/ijdb.160273ai

Weston, C.R., Wong, A., Hall, J.P., Goad, M.E.P., Flavell, R.A., & Davis, R.J. (2003). JNK initiates a cytokine cascade that causes Pax2 expression and closure of the optic fissure. *Genes Dev*, 17: 1271–1280. doi: 10.1101/gad.1087303

White, T., Lu, T., Metlapally, R., Katowitz, J., Kherani, F., Wang, T. Y., . . . Young, T. L. (2008). Identification of STRA6 and SKI sequence variants in patients with anophthalmia/microphthalmia. *Mol Vis, 14*, 2458-2465.

Williams, R., & Taylor, D. (1985). Tuberous sclerosis. *Surv Ophthalmol*, 30(3):143-54. doi: 10.1016/0039-6257(85)90058-x. PMID: 4081976.

Williamson, K.A., & FitzPatrick, D.R. (2014). The genetic architecture of microphthalmia, anophthalmia and coloboma. *Eur J Med Genet*, 57: 369–380. doi: 10.1016/j.ejmg.2014.05.002

Wilson, M. (2020). *Investigating the Role of Cellular Polarity in the Causation of Superior Coloboma*. (Master's thesis). University of Alberta, Edmonton, Alberta, Canada.

Wise, A. L., Manolio, T. A., Mensah, G. A., Peterson, J. F., Roden, D. M., Tamburro, C., … Green, E. D. (2019). Genomic medicine for undiagnosed diseases. *The Lancet*, Vol. 394, pp. 533–540. https://doi.org/10.1016/S0140-6736(19)31274-7

Wyatt, A., Bakrania, P., Bunyan, D. J., Osborne, R. J., Crolla, J. A., Salt, A., . . . Ragge, N. (2008). Novel heterozygous OTX2 mutations and whole gene deletions in anophthalmia, microphthalmia and coloboma. *Hum Mutat, 29*(11), E278-283. doi:10.1002/humu.20869

Wyatt, A. W., Osborne, R. J., Stewart, H., & Ragge, N. K. (2010). Bone morphogenetic protein 7 (BMP7) mutations are associated with variable ocular, brain, ear, palate, and skeletal anomalies. *Hum Mutat, 31*(7), 781-787. doi:10.1002/humu.21280

Ye, M., Berry-Wynne, K. M., Asai-Coakwell, M., Sundaresan, P., Footz, T., French, C. R., . . . Lehmann, O. J. (2010). Mutation of the bone morphogenetic protein GDF3 causes ocular and skeletal anomalies. *Hum Mol Genet, 19*(2), 287-298. doi:ddp496 [pii] 10.1093/hmg/ddp496

Yoon, K.H., Fox, S.C., Dicipulo, R., Lehmann, O.J., & Waskiewicz, A.J. (2020). Ocular coloboma: Genetic variants reveal a dynamic model of eye development. *Am J Med Genet C Semin Med* Genet, 184(3):590-610. doi: 10.1002/ajmg.c.31831. Epub 2020 Aug 27. PMID: 32852110.

Yu, P.B., Hong, C.C., Sachidanandan, C., Babitt, J.L., Deng, D.Y., Hoyng, S.A., et al. (2008). Dorsomorphin inhibits BMP signals required for embryogenesis and iron metabolism. *Nat Chem Biol*, 4: 33–41. doi: 10.1038/nchembio.2007.54

Zhang, L., Mathers, P. H., & Jamrich, M. (2000). Function of Rx, but not Pax6, is essential for the formation of retinal progenitor cells in mice. *Genesis, 28*(3-4), 135-142.

Zhang, X.M., & Yang, X.J. (2001). Temporal and spatial effects of Sonic hedgehog signaling in chick eye morphogenesis. *Dev Biol*, 233: 271–290. doi: 10.1006/dbio.2000.0195

Zhao, L., Yuan, S., Cao, Y., Kallakuri, S., Li, Y., Kishimoto, N., DiBella, L., & Sun, Z. (2013). Reptin/Ruvbl2 is a Lrrc6/Seahorse interactor essential for cilia motility. *Proc Natl Acad Sci U S A*, 110(31):12697-702. doi: 10.1073/pnas.1300968110. Epub 2013 Jul 15. PMID: 23858445; PMCID: PMC3732945.

Zhu, C. C., Dyer, M. A., Uchikawa, M., Kondoh, H., Lagutin, O. V., & Oliver, G. (2002). Six3-mediated auto repression and eye development requires its interaction with members of the Groucho-related family of co-repressors. *Development, 129*(12), 2835-2849.

Zou, H., Wieser, R., Massagué, J., & Niswander, L. (1997). Distinct roles of type I bone morphogenetic protein receptors in the formation and differentiation of cartilage. *Genes Dev*,11: 2191–2203.

Appendix A

Visualization of the superior ocular sulcus during *Danio rerio* embryogenesis

A version of this chapter is published. Yoon, K.H., Widen, S.A., Wilson, M.M., Hocking, J.C., & Waskiewicz, A.J. (2019). Visualization of the Superior Ocular Sulcus during Danio rerio Embryogenesis. *J Vis Exp*, (145). doi: 10.3791/59259. PMID: 30985739.

A.1. Summary

Here, we present a standardized series of protocols to observe the superior ocular sulcus, a recently-identified, evolutionarily-conserved structure in the vertebrate eye. Using zebrafish larvae, we demonstrate techniques necessary to identify factors that contribute to the formation and closure of the superior ocular sulcus.

A.2. Abstract

Congenital ocular coloboma is a genetic disorder that is typically observed as a cleft in the inferior aspect of the eye resulting from incomplete choroid fissure closure. Recently, identification of individuals with coloboma in the superior aspect of the iris, retina, and lens led to the discovery of a novel structure, referred to as the superior fissure or superior ocular sulcus (SOS), that is transiently present on the dorsal aspect of the optic cup during vertebrate eye development. Although this structure is conserved across mice, chick, fish, and newt, our current understanding of the SOS is limited. In order to elucidate factors that contribute to its formation and closure, it is imperative to be able to observe it and identify abnormalities, such as delay in the closure of the SOS. Here, we set out to create a standardized series of protocols that can be used to efficiently visualize the SOS by combining widely available microscopy techniques with common molecular biology techniques such as immunofluorescent staining and mRNA overexpression. While this set of protocols focuses on the ability to observe SOS closure delay, it is adaptable to the experimenter's needs and can be easily modified. Overall, we hope to create an approachable method through which our understanding of the SOS can be advanced to expand the current knowledge of vertebrate eye development.

A.3. Introduction

The formation of the vertebrate eye is a highly-conserved process in which carefully orchestrated intercellular signaling pathways establish tissue types and specify regional identity

(Chow & Lang, 2001). Perturbations to early eye morphogenesis result in profound defects to the architecture of the eye and are frequently blinding (Slavotinek, 2011). One such disease results from failure to close the choroid ocular fissure in the ventral side of the optic cup (Gregory-Evans et al, 2004). This disorder, known as ocular coloboma, is estimated to occur in 1 out of 4-5000 live births and cause 3-11% of pediatric blindness, commonly manifesting as a keyhole-like structure that protrudes inferiorly from the pupil in the centre of the eye (Onwochei et al., 2000; Williamson & FitzPatrick, 2014; Chang et al., 2006). The function of the choroid fissure is to provide an entry point for early vasculature growing into the optic cup, after which the sides of the fissure will fuse to enclose the vessels (Kaufman et al., 2015).

While ocular coloboma has been known since ancient times, we have recently identified a novel subset of coloboma patients with tissue loss affecting the superior/dorsal aspect of the eye. Recent work in our lab has led to the discovery of an ocular structure in the zebrafish dorsal eye, which we refer to as the superior ocular sulcus (SOS) or superior fissure (Hocking et al, 2018). It is important to note that the structure has characteristics of both a sulcus and a fissure. Similar to a sulcus, it is a continual tissue layer that spans from the nasal to the temporal retina. In addition, the closure of the structure is not mediated by a fusion of the two opposing basement membrane, and it appears to require a morphogenetic process by which the structure is populated by cells. However, similar to a fissure, it forms a structure that separates the nasal and temporal sides of the dorsal eye with the basement membrane. For consistency, we will refer to it as SOS in this text.

The SOS is evolutionarily conserved across vertebrates, being visible during eye morphogenesis in fish, chick, newt, and mouse (Hocking et al, 2018). In contrast to the choroid fissure, which is present from 20-60 hours post-fertilization (hpf) in zebrafish, the SOS is highly transient, being easily visible from 20-23 hpf and absent by 26 hpf (Hocking et al, 2018). Recent research in our lab has found that, similar to the choroid fissure, the SOS plays a role in vascular guidance during eye morphogenesis (Hocking et al, 2018). Although the factors that control formation and closure of the SOS are not yet fully understood, our data did highlight roles for dorsal-ventral eye patterning genes (Hocking et al, 2018).

Zebrafish is an excellent model organism with which to study the SOS. As a model system, it provides a number of advantages in studying eye development: it is a vertebrate model; each

generation exhibits high fecundity (~200 embryos); its genome has been fully sequenced, which facilitates genetic manipulation; and approximately 70% of human genes have at least one zebrafish orthologue, making it an ideal genetics-based model of human disease (Lawson & Wolfe, 2011; Howe et al., 2013). Most importantly, its development takes place externally to the mother, and its larvae are transparent, which allows for the visualization of the developing eye with relative ease (Bilotta & Saszik, 2001).

In this set of protocols, we describe the techniques through which the SOS can be visualized in zebrafish larvae. The variety of visualization techniques used in this report will allow clear observation of the SOS during normal eye development, as well as the ability to detect SOS closure defects. Our example protocols will feature investigations of Gdf6, a BMP localized to the dorsal eye and known regulator of SOS closure. Further, these techniques can be combined with experimental manipulations to identify genetic factors or pharmacological agents that affect proper SOS formation and closure. In addition, we have included a protocol through which fluorescent imaging of all cell membranes is possible, allowing the experimenter to observe morphological changes to the cells surrounding the SOS. Our goal is to establish a set of standardized protocols that can be used throughout the scientific community to offer new insights into this novel structure of the developing eye.

A.4. Protocol

All methods described here have been approved by the University of Alberta Animal Care and Use Committee.

A.4.1. Protocol 1: Visualization of SOS using stereomicroscopy and DIC imaging

1.1) Embryo collection

1.1.1) In a tank of dechlorinated water, prepare crosses of *gdf6a*$^{+/-}$ zebrafish in the evening by pairing a male zebrafish with a female zebrafish. Be sure to separate the male from the female by using a divider to ensure that the embryos are born within a small range of time.

1.1.2) The following morning, pull the divider and allow the zebrafish to breed for no longer than 30 min. Collect the embryos in Petri dishes with E3 media, described in The Zebrafish Book (Westerfield, 2007), and place them in a 28.5°C incubator.

1.1.3) Remove any unfertilized eggs or dead embryos, which will appear white and opaque.

1.2) Preparation and live-imaging of zebrafish embryos

1.2.1) At 20 hpf, replace the E3 media with E3 media containing 0.004% 1-phenyl 2-thiourea (PTU) to prevent pigment production.

NOTE: Addition of PTU at a slightly later timepoint, such as 22-24 hpf, is unlikely to interfere with the experiment due to the early age of the embryos at the time of imaging. However, it is recommended to treat the embryos early to completely prevent pigmentation as there is a band of pigmentation that appears in the dorsal eye, which can interfere with the imaging of the SOS.

1.2.2) Ensure that all embryos are at the correct developmental stages at various points leading up to the time of observation. It is recommended that this is done at the stages at which somite number is clearly visible as outlined by Kimmel et al. (1995). Remove those that are developmentally immature.

1.2.3) Place the embryos under a dissecting microscope, and dechorionate the embryos by gently pulling apart the chorion using fine forceps. Visualize the SOS in the dorsal eye. The SOS may appear as an indentation at the dorsal margin of the eye, and a line should be visible across the dorsal eye. For normal SOS closure, observe the embryos at around 20-23 hpf. For examination of delayed SOS closure phenotypes, observe the embryos at 28 hpf or later.

1.2.4) Sort the embryos that show SOS closure delay from those that do not.

1.2.5) To photograph these embryos using a dissecting microscope, prepare a Petri dish containing 1% agarose in E3. Lightly prick the centre of the agarose to create a shallow hole in which the yolk of the embryo can sit when the embryo is placed on the agarose. This will ensure that the embryo is not at an oblique angle when being photographed.

1.2.6) Anesthetize embryos with 0.003% tricaine in E3 and place laterally on the agarose.

1.2.7) To image the embryos using a compound or confocal microscope, transfer the embryo into 35 mm Petri dish containing a small bolus of non-gelled 1% low-melting point agarose in E3 (w/v). Quickly position the embryo laterally using a fine fishing line or an eyelash and wait for the agarose to cool. Once the agarose is firm, pour enough E3 into the dish to cover the agarose. For more details, see Distel and Köster (2007).

NOTE: If using an inverted microscope, the embryo can be placed against the glass of a glass-coverslip-bottom dish and imaged with a standard 20X objective lens.

1.2.8) Use a water immersion 20X objective lens to visualize the SOS with a compound microscope. Following visualization, gently pull the agarose off of the embryos and fix in 4% paraformaldehyde (PFA) or allow to continue their development.

A.4.2. Protocol 2: Whole-mount immunofluorescent staining of laminin

<u>2.1) Whole-mount immunofluorescent staining of laminin: Day 1</u>

2.1.1) Dechorionate embryos as described in Step 1.2.3, if not already done. Fix embryos in a microcentrifuge tube at the desired timepoint in freshly made 4% PFA for 2 h on a room temperature (22-25°C) shaker. Wash in 1X PBST for 5 min, four times.

NOTE: Following gastrulation, embryos may fix better after dechorionation.

2.1.2) Permeabilize embryos in 10 μg/mL proteinase K at room temperature for 5 min. Incubation time will depend on the developmental stage at which the embryos are fixed (see Thisse and Thisse, 2008).

2.1.3) Wash in 1X PBST for 5 min, four times.

2.1.4) Block embryos in a solution of 5% goat serum and 2 mg/mL bovine serum albumin (BSA) in 1X PBST for 1-2 h on a room temperature shaker.

2.1.5) Prepare primary antibody solution by diluting rabbit anti-laminin antibody in block solution at a 1:200 dilution.

2.1.6) Incubate the embryos in anti-laminin primary antibody (Millipore Sigma) overnight on a 4°C shaker.

2.2) Whole-mount immunofluorescent staining of laminin: Day 2

2.2.1) Wash in 1X PBST for 15 min, five times.

2.2.2) Prepare secondary antibody solution by diluting goat anti-rabbit Alexa Fluor 488 antibody (Abcam) in 1X PBST to a dilution of 1:1000.

NOTE: It is possible to adapt this step to suit the resources available to the experimenter by using a different secondary antibody.

2.2.3) Incubate the embryos in secondary antibody overnight on a 4°C shaker. Shield from light as much as possible from this step onwards.

2.2.4) Wash in 1X PBST for 15 min, four times. The embryos can be stored at 4°C for up to a week, if necessary.

2.3) Dissection and mounting of embryonic eyes

2.3.1) If desired, place the embryos in a small Petri dish and deyolk the embryos in 1X PBST. Do this by gently disrupting the yolk with fine forceps and removing the yolk cells through mild scraping of the yolk sac.

2.3.2) Prepare the following concentrations of PBS-glycerol series solutions in microcentrifuge tubes: 30%, 50%, and 70% glycerol in PBS. Transfer embryos into 30% glycerol/PBS, making sure to place the embryos on top of the solution and transferring as little of the previous solution as possible. Wait for the embryos to sink to the bottom of the tube.

2.3.3) When embryos have sunk to the bottom, transfer them to 50% glycerol/PBS. Repeat and transfer to 70% glycerol/PBS.

2.3.4) Once the embryos have sunk in 70% glycerol/PBS, move them to a small plastic dish for dissections.

2.3.5) Sever the embryo posterior to the hindbrain, and use the posterior tissue for genotyping, if necessary.

2.3.6) Move the head to a glass slide, transferring as little glycerol as possible. Use forceps or other fine dissection tools to hold onto the posterior end to keep the head stationary. Use a fine minutien pin (Fine Science Tools) or other fine dissection tools to gently insert into the forebrain ventricle from the anterior and push downward to separate the right and left halves of the head from each other. Repeat this while moving posteriorly through the midbrain and into the hindbrain ventricle, essentially “fileting” the head down the midline. This minimizes manual manipulation of the eye and surrounding tissue, thereby leaving the SOS undamaged.

2.3.7) Mount each side of the head midline down, eye up. Position four posts of vacuum grease at the corners (an appropriate distance apart for the coverslip being used) and cover with a glass coverslip, pushing down sequentially on each post until the coverslip makes contact with the samples. Pipette 70% glycerol at the edge of the coverslip so that the glycerol is pulled underneath, filling the space between the coverslip and the slide.

2.3.8) Image samples within a day, or seal around the coverslip with nail polish and image samples only after the nail polish has dried. Store in the dark at 4°C.

A.4.3. Protocol 3: Visualization of SOS using eGFP-CAAX mRNA

3.1) Synthesis of eGFP-CAAX mRNA

3.1.1) Linearize 1 μg of pCS2-eGFP-CAAX plasmid (Kwan et al., 2012) with NotI in a reaction volume of 40 μL for 4 hours at 37°C.

3.1.2) To stop the restriction digest reaction, add 10 μL RNase-free water, 2.5 μL 10% SDS and 2.0 μL 10 mg/mL Proteinase K.

3.1.3) Incubate 1 hour at 50°C.

3.1.4) Add the following to the reaction (total volume 200 μL) and proceed to next step: 50 μL RNase-free water, 20 μL 3 M sodium acetate pH 5.2 and 75.5 μL RNase-free water

NOTE: RNase-free water is added in two separate occasions to prevent excessive dilution of the sodium acetate.

3.2) Purification of DNA through phenol/chloroform extraction and ethanol precipitation

3.2.1) Add 200 μL phenol:chloroform:isoamyl alcohol and vortex for 20 s. Separate the aqueous and organic phases through centrifugation at 18,000 x g for 5 min.

3.2.2) Transfer the upper aqueous layer to a new microcentrifuge tube, making sure to avoid the transfer of the bottom organic layer. Add equal volume of chloroform to the new tube.

NOTE: Addition of chloroform is optional, but it is recommended to ensure complete removal of phenol from the sample.

3.2.3) Vortex for 20 s. Separate the aqueous and organic phases through centrifugation at 18,000 x g for 5 min.

3.2.4) As before, transfer the upper aqueous layer to a new microcentrifuge tube, making sure to avoid the transfer of the bottom organic layer.

3.2.5) Add 1/10 volume of 3 M sodium acetate pH 5.2.

3.2.6) Precipitate DNA by adding 3 volumes of 100% RNase-free ethanol and chill at -20°C for 15 min. Centrifuge at 18,000 x g for 20 min at 4°C. A pellet should be visible. Decant the supernatant.

3.2.7) Wash the pellet with 100 μL of cold 70% ethanol/RNase-free water. After gently mixing to break the pellet loose, centrifuge at 18,000 x g for 15 min at 4°C. A pellet should be visible. Decant the supernatant.

3.2.8) Air-dry the pellet for 5 min and resuspend the DNA in 7 μL water.

NOTE: The pellet may need to be dried for longer than 5 min depending on the airflow available.

3.3) Transcription and purification of eGFP-CAAX mRNA

3.3.1) In an RNase-free manner, prepare an *in vitro* transcription reaction with a commercially available Sp6 RNA polymerase kit, using about 1 μg of purified linearized plasmid DNA obtained in Step 3.2. Incubate for 2 hours at 37°C.

NOTE: Sp6 RNA polymerase must be used for production of capped mRNA.

3.3.2) Add 1 μL of DNase (2 U/μL; RNase free) and incubate for 30 minutes at 37°C.

3.3.3) Purify the mRNA with any commercially available RNA purification kit. Aliquot the mRNA to avoid repeated freeze-thaw, and store at -80°C.

3.4) Injection and visualization

3.4.1) Obtain embryos as outlined in Protocol 1.1.

3.4.2) Using a microinjection apparatus, inject 300 pg of eGFP-CAAX mRNA at the 1-cell stage.

3.4.3) Screen for embryos with bright expression of eGFP in the eyes using a fluorescence stereoscope.

3.4.4) Image the embryos as described in Protocol 1.2.

3.4.5) Alternatively, dechorionate and fix the embryos at the desired timepoint in 4% PFA for 4 hours at room temperature or overnight at 4°C. Wash the embryos in 1X PBST for 5 minutes, four times, and dechorionate, if not previously done. Dissect the eyes and mount them on slides as described in Protocol 2.3.

A.5. Representative Results

The zebrafish SOS appears at 20 hpf in the presumptive dorsal retina (Hocking et al., 2018). By 23 hpf the SOS transitions from its initial narrow architecture to a wide indentation and by 26 hpf it is no longer visible (Hocking et al., 2018). Therefore, to examine the SOS during normal zebrafish eye development, the embryos must be observed between 20-23 hpf. During this period, the SOS is observable through the dissecting microscope and via DIC imaging as a thin line in the dorsal eye that separates the nasal and temporal halves of the developing retina (Figure A.1). In addition, a subtle indentation may be visible in the dorsal boundary of the eye (Figure A.1). Following immunofluorescent staining of laminin, the thin line can be confirmed to be the basement membrane (Figure A.1).

To examine molecular pathways resulting in delayed SOS closure, we chose to observe the embryos at 28 hpf as this is a timepoint that is sufficiently removed from the time of normal SOS

closure, and is, therefore, a reliable marker of SOS closure delay due to experimental manipulations. Through direct visualization of 28 hpf zebrafish under the dissecting microscope, it is possible to evaluate SOS closure delay due to experimental manipulation. When SOS closure is delayed, its prolonged presence can be seen as a pronounced cleft in the dorsal side of the eye under the dissecting microscope (Figure A.2). When observed under the compound microscope using DIC or Nomarski optics, this feature is even more prominent, and the nasal and temporal sides of the eye are separated by the SOS, which is clearly visible as a line in the dorsal eye (Figure A.3).

The SOS is lined with basal lamina components, including laminin. Therefore, immunofluorescent staining provides a complementary method of evaluating SOS closure in fixed embryos. When imaging the embryonic eye from a lateral view, the basal lamina demarcates the outside margin of the eye, both ocular fissures, and the border between the lens and the retina (Figure A.4). The SOS is oriented directly opposite to the choroid fissure in the dorsal aspect of the eye. Whole embryos can be mounted laterally, with somewhat better optical clarity achieved if eyes are previously microdissected. By 28 hpf, in wildtype zebrafish, laminin staining demonstrates clearly that the SOS is completely closed, which makes this the ideal stage for monitoring delays in fissure closure.

Injection of eGFP-CAAX mRNA allows visualization of the cell membranes of a live or fixed embryo (Figure A.5). Successful one-cell stage injection is sufficient to produce embryos with complete cell membrane fluorescence. In the lateral view, all cellular boundaries should be marked by GFP fluorescence, and as such, cell morphology is also clearly observed. This allows the visualization of the morphological changes to the cells that lead to SOS closure.

A.6. Discussion

Here, we present a standardized series of protocols to observe the SOS in the developing zebrafish embryo. To determine closure delay phenotypes, our protocols have focused on the ability to distinguish the separation of two discrete lobes of the dorsal-nasal and dorsal-temporal

sides of the eye, similar to techniques used to visualize choroid fissure closure delay phenotypes in the ventral eye.

These visualization techniques can be used in conjunction with a variety of genetic manipulation techniques to study the effects of inhibiting or inducing expression of certain genes to study their roles in the closure of the SOS. We have chosen to demonstrate these protocols using *gdf6a*$^{-/-}$ embryos as we have previously shown that its loss can affect proper closure of the SOS, but the protocols can be used to study the effects of manipulating the expression of any genes as required. It is recommended that any morphological changes to the dorsal eye are studied preliminarily with observations using the dissecting microscope. The other techniques should be used once an initial link is established definitively, as they are more time-consuming and lower throughput.

While the protocols can be easily modified to suit the needs of the experimenter, there are several aspects that must be followed carefully. Because of the transient nature of this structure, it is imperative to ensure that all observed embryos are of the same developmental stage. For our work, we find it important to allow only a small window of breeding time and to periodically sort the embryos throughout early development. The most important step of equalizing stages is at 20 hpf, when you can still accurately count somites (24) (Kimmel et al., 1995), and we find this much more reliable than the staging hallmarks that delineate time at 28 hpf. In addition, pigmentation must be inhibited or removed to ensure successful visualization of the structure. We have observed the pigmentation in the eye begins to start around 22 hpf, and there is a pattern of pigmentation in the dorsal eye that can interfere with proper visualization of the SOS. Therefore, it is highly recommended to treat the embryos with PTU prior to pigmentation to ensure successful visualization. Additionally, dissection of the embryonic eye prior to slide mounting without causing damage requires some practice. It is also imperative to laterally mount the eyes as parallel as possible to the slide. It is recommended that the experimenter practices these techniques with extra embryos prior to the experiment.

With the exception of the immunofluorescent staining of the basal lamina, all of the protocols described here can be completed using live embryos. This allows continual visualization of the SOS throughout early embryogenesis, allowing the experimenter to conduct time-lapse

studies of the morphological changes involved in the closure of the SOS. In the past, we have used retina-specific transgenes, such as *Tg(rx3:eGFP)*, which marks the neural retina during early development. Although it lacks the ability to visualize cell membranes, the use of *Tg(rx3:eGFP)* has the advantage of not requiring microinjections and has been our primary method of visualizing gross morphological changes to SOS architecture in real-time. That protocol has not been included here, as similar methods have been discussed previously in this journal (Gfrerer et al., 2013; Percival & Parant, 2016). However, investigation of cell biological basis of SOS formation and closure will require membrane fluorescent proteins. Specifically, the injection of eGFP-CAAX mRNA allows visualization of the cell membranes around the SOS as seen in Figure 5, which allows us to study the dynamics of cell shape changes in the dorsal eye that are required for proper SOS closure. While eGFP-CAAX can be useful for performing live-imaging of SOS closure, it is made difficult by the presence of the enveloping layer in zebrafish. In addition, care must be taken when analyzing results from mRNA injections because it can result in mosaicism, making it difficult to directly compare embryos based on quantification of eGFP expression strength. This could be ameliorated through the use of transgenic zebrafish lines that fluorescently label cell membranes specifically in the developing retina, such as *Tg(vsx2.2:GFP-caax)*.

One of the challenges of our protocols lies with any treatment that is not fully penetrant. We have previously noted that SOS delays can be seen in about 10% of control embryos at 28 hpf (Hocking et al., 2018), and this underlying presence of embryos with an SOS within any given experimental group could make it difficult to observe subtle effects of experimental manipulation. This could be addressed by blinding the experimenter to reduce experimenter bias and by increasing the number of embryos used within each experimental group to increase the power of the experiment. In addition, the stage of analysis could be shifted to 29-30 hpf.

With this set of protocols, we seek to standardize the way through which SOS closure delays are visualized. The techniques described above have been shown to be reliable in detecting and visualizing SOS closure delays in a variety of experimental settings and are adaptable to the experimenter's needs. While we have used techniques such as scanning electron microscopy or time-lapse imaging of transgenic embryos to visualize the SOS in greater detail, our aim here is to create a standardized set of protocols that are amenable to high-throughput experimental designs to visualize a large number of embryos in a single day with emphasis on the ability to score closure

delay phenotypes. In addition to its use with *gdf6a*$^{-/-}$ embryos, we have been able to observe SOS closure delay phenotypes using these visualization techniques alongside pharmacological treatments, morpholino injections, and RNA overexpression studies. As the role of the SOS in eye development is elucidated further through various means, we hope that this standardized set of protocols provide the scientific community a common language through which this novel structure is studied.

A.7. Figures

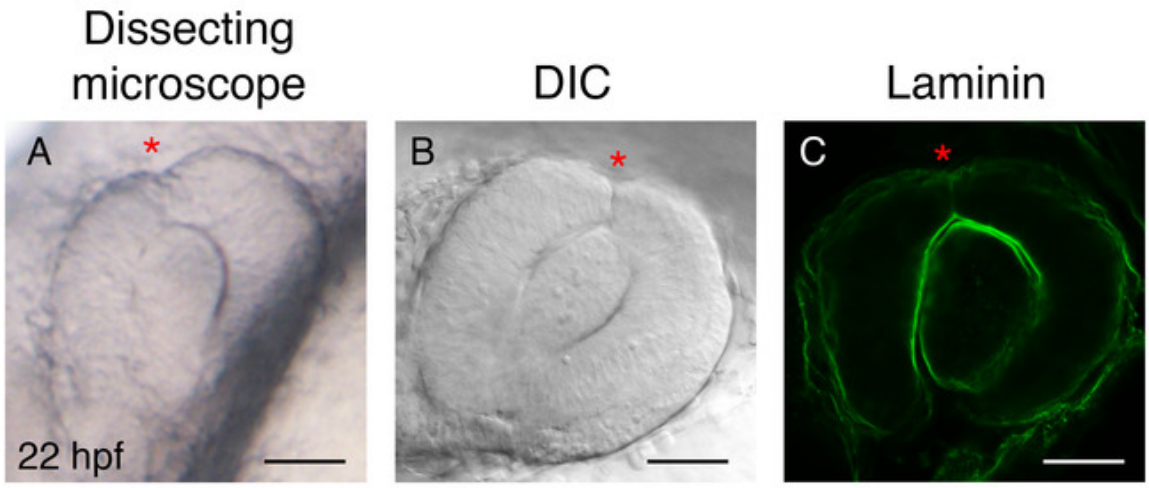

Figure A.1: Observation of SOS during normal zebrafish eye development. Zebrafish embryos were collected and imaged at 22 hpf. A-B. Lateral view of 22 hpf embryos live-imaged with the dissecting microscope (A) and via DIC imaging (B), respectively. The SOS is marked by a red asterisk. C. Laminin immunofluorescent staining of a 22 hpf embryo. Embryos were fixed in 4% PFA and obtained for whole-mount immunofluorescent staining of laminin. The embryos were fileted and mounted in 70% glycerol/PBS. Single slice images were obtained through confocal imaging with ZEN (Carl Zeiss) software. The SOS is marked by a white asterisk. All figures were annotated and assembled using Adobe Illustrator software. Scale bars represent 50 μm.

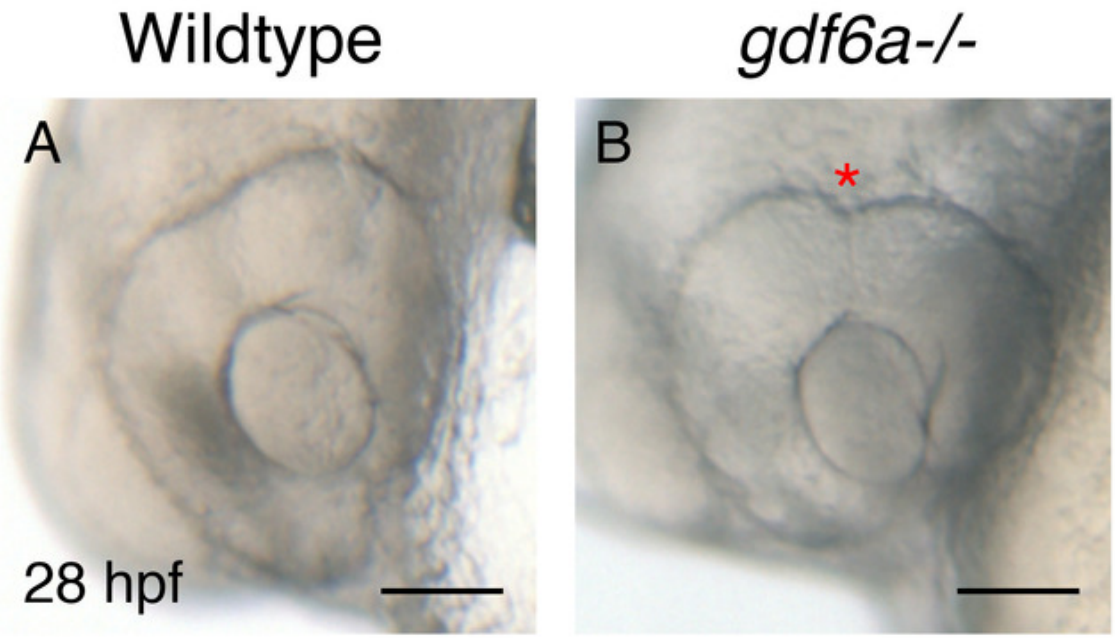

Figure A.2: Dissecting microscope images of SOS closure delay in zebrafish larvae. Wildtype and *gdf6a*$^{-/-}$ embryos were collected and live-imaged at 28 hpf. A. Lateral view of a wildtype embryo with a closed SOS. B. Lateral view of a *gdf6a*$^{-/-}$ embryo with a SOS closure delay (asterisk). A sharp depression is observable in the dorsal aspect of the eye due to the failure of the SOS to close appropriately. Scale bars represent 50 μm.

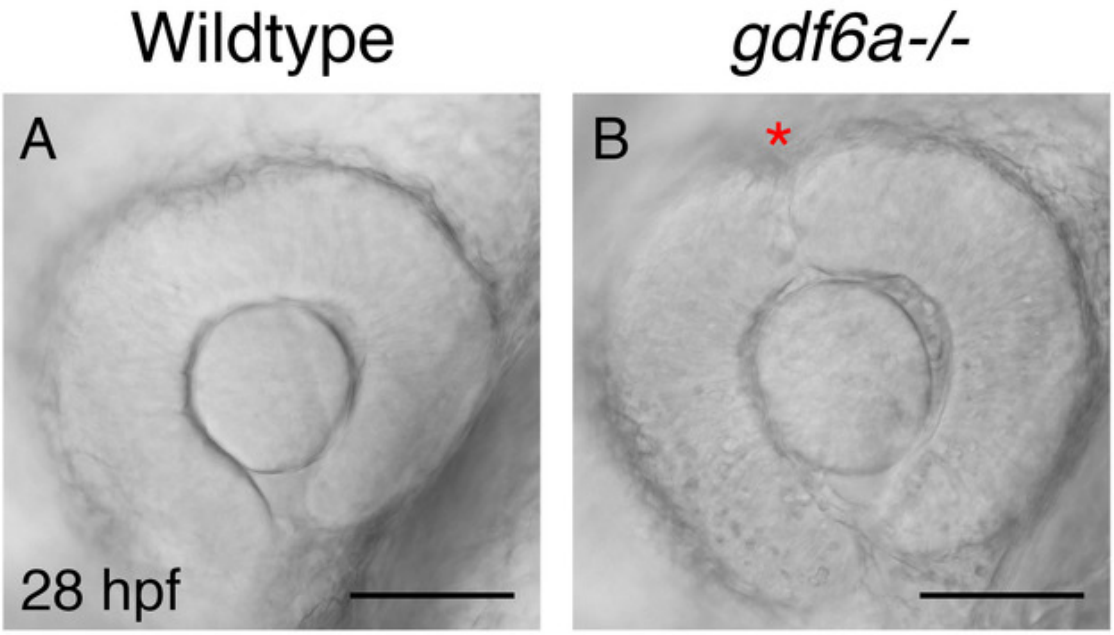

Figure A.3: Representative DIC images of the SOS in the zebrafish embryonic eye. Wildtype and *gdf6a*$^{-/-}$ embryos were collected, anesthetized, and placed laterally in 1% Ultrapure low-melting point agarose in E3 on a 35 mm Petri dish. The dish was filled with E3, and a compound microscope with a 20X water-dipping objective was used for DIC imaging. A. Lateral view of a wildtype embryo with a closed SOS. B. Lateral view of a *gdf6a*$^{-/-}$ embryo with a SOS closure delay (asterisk). The SOS is observable as a thin line in the dorsal aspect of the eye. Scale bars represent 50 μm.

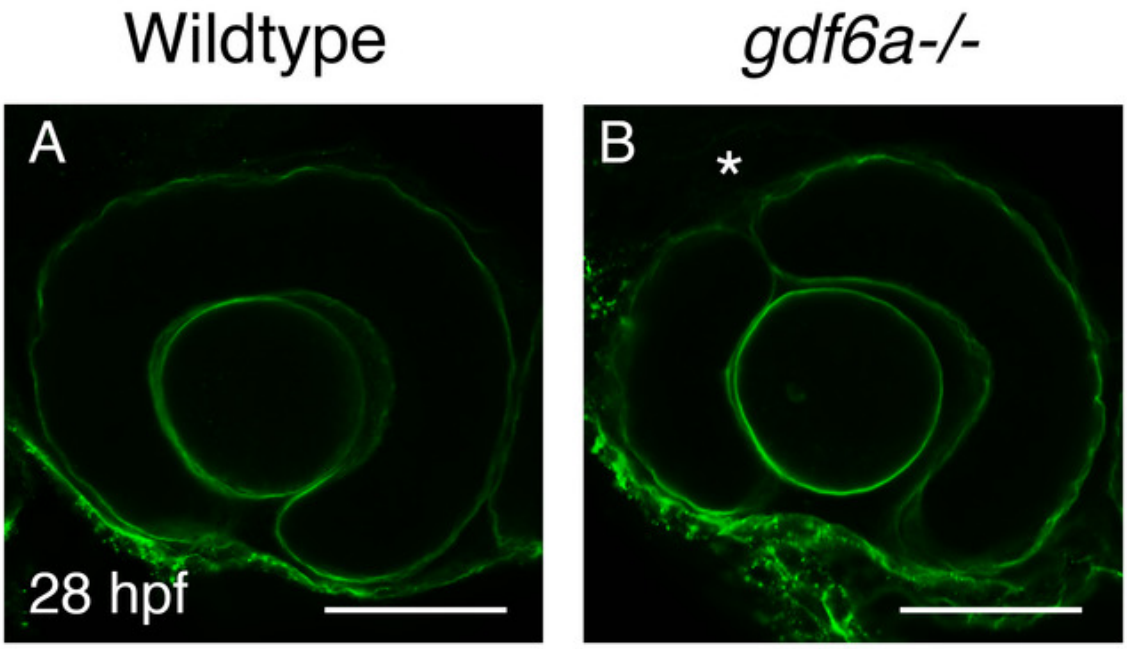

Figure A.4: Representative images of laminin immunofluorescent staining in embryonic zebrafish eye. Wildtype and *gdf6a*$^{-/-}$ embryos were collected and fixed in 4% PFA at 28 hpf. The basal lamina was immunostained, and the embryos were fileted and mounted in 70% glycerol/PBS for confocal imaging. Single slice images were obtained using ZEN software. A. Lateral view of a wildtype embryo with a closed SOS. B. Lateral view of a *gdf6a*$^{-/-}$ embryo with a SOS closure delay (asterisk). The basal lamina is shown outlining the eye in green, with the SOS visible in the dorsal part of the eye in *gdf6a*$^{-/-}$ embryos. Scale bars represent 50 μm.

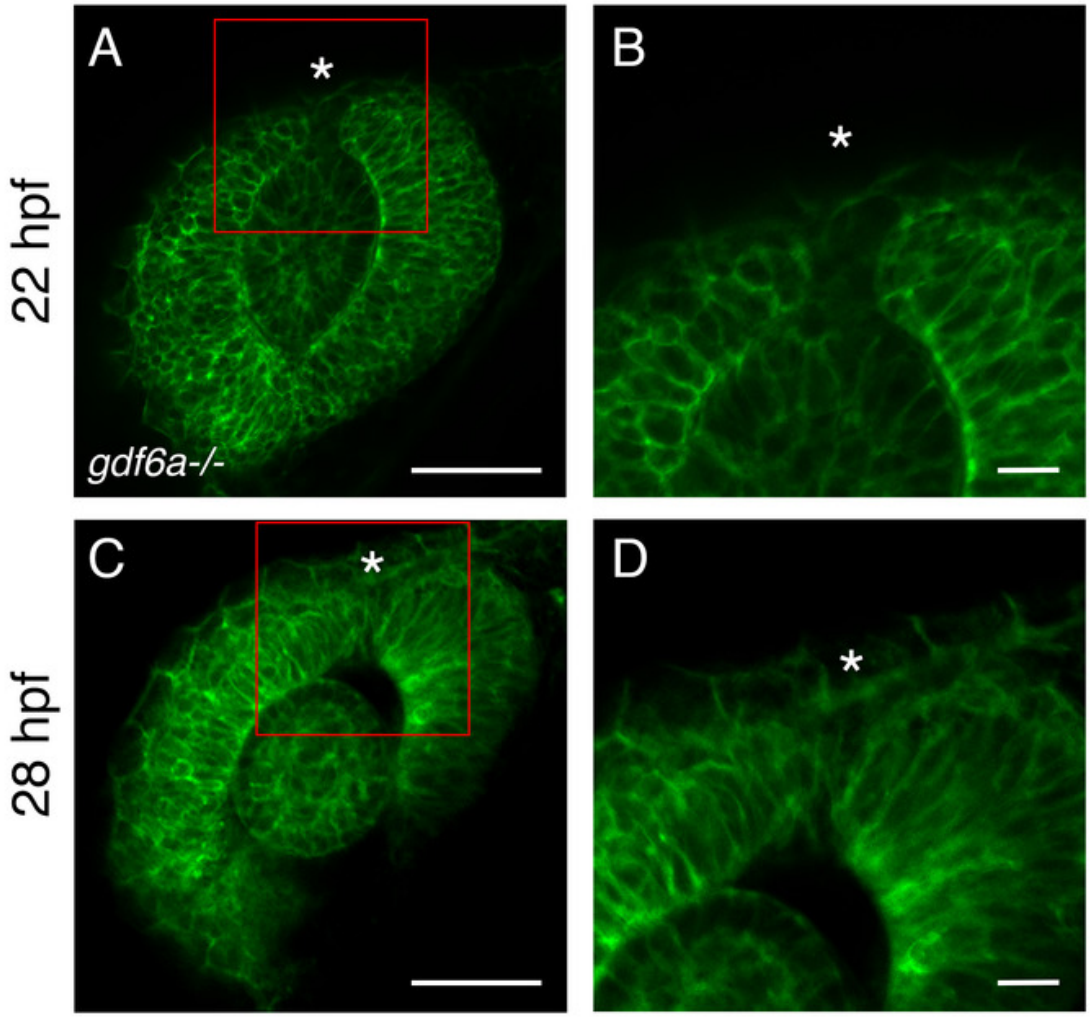

Figure A.5: Imaging of the zebrafish embryonic eye following eGFP-caax mRNA injection. Wildtype embryos were injected with 300 pg of eGFP-caax mRNA at 1-cell stage. At 22 hpf and 28 hpf, respectively, the embryos were anesthetized and mounted laterally in 1% Ultrapure low-melting point agarose in E3 on a 35 mm Petri dish. A confocal microscope with a 20X water-dipping objective was used for imaging, and single slice images were obtained using ZEN software. A. Lateral view of a *gdf6a*$^{-/-}$ embryo at 22 hpf with a visible open SOS (asterisk). B. Enlarged panels of a *gdf6a*$^{-/-}$ embryo at 22 hpf. C. Lateral view of a *gdf6a*$^{-/-}$ embryo at 28 hpf with a SOS closure delay. D. Enlarged panels of a *gdf6a*$^{-/-}$ embryo at 28 hpf. Scale bars represent 50 μm and 10 μm in Panels A and C, and B and D, respectively.

A.8. References

Bilotta, J., Saszik, S. The zebrafish as a model visual system. *International Journal of Developmental Neuroscience*. **19**, 621-629 (2001).

Chang, L., Blain, D., Bertuzzi, S., Brooks, B.P. Uveal coloboma: clinical and basic science update. *Current Opinion in Ophthalmology*. **17**, 447–470 (2006).

Chow, R.L., Lang, R.A. Early eye development in vertebrates. *Annual Review of Cell and Developmental Biology.* **17**, doi:10.1146/annurev.cellbio.17.1.255 (2001).

Distel, M., Köster, R.W. In vivo time-lapse imaging of zebrafish embryonic development. Cold Spring Harbor Protocols. doi: 10.1101/pdb.prot4816 (2007).

Gfrerer, L., Dougherty, M., Liao, E. C. Visualization of Craniofacial Development in the sox10: kaede Transgenic Zebrafish Line Using Time-lapse Confocal Microscopy. *J. Vis. Exp.* (79), e50525, doi:10.3791/50525 (2013).

Gregory-Evans, C.Y., Williams, M.J., Halford, S., Gregory-Evans, K. Ocular coloboma: a reassessment in the age of molecular neuroscience. *Journal of Medical Genetics.* **41** (12), doi: 10.1136/jmg.2004.025494 (2004).

Hocking, J.C., et al. Morphogenetic defects underlie Superior Coloboma, a newly identified closure disorder of the dorsal eye. *PLOS Genetics.* **14** (3), doi:10.1371/journal.pgen.1007246 (2018).

Howe, K., et al. The zebrafish reference genome sequence and its relationship to the human genome. *Nature*. **496** (7446), doi: 10.1038/nature12111 (2013).

Kaufman, R., et al. Development and origins of Zebrafish ocular vasculature. *BMC Developmental Biology*. **15** (18), doi:10.1186/s12861-015-0066-9 (2015).

Kimmel, C.B., Ballard, W.W., Kimmel, S.R., Ullmann, B., Schilling, T.F. Stages of embryonic development of the zebrafish. *Developmental Dynamics.* **203**, 253–310 (1995).

Kwan, K.M., Otsuna, H., Kidokoro, H., Carney, K.R., Saijoh, Y., Chien C. A complex choreography of cell movements shapes the vertebrate eye. *Development*. **139**: 359-372, doi: 10.1242/dev.071407 (2012).

Lawson, N.D., Wolfe, S.A. Forward and reverse genetic approaches for the analysis of vertebrate development in the zebrafish. *Developmental Cell.* **21** (1), doi:10.1016/j.devcel.2011.06.007 (2011).

Onwochei, B.C., Simon, J.W., Bateman, J.B., Couture, K.C., Mir, E. Ocular colobomata. *Survey of Ophthalmolgy*. **45**, 175–194 (2000).

Percival, S. M., Parant, J. M. Observing Mitotic Division and Dynamics in a Live Zebrafish Embryo. *J. Vis. Exp.* (113), e54218, doi:10.3791/54218 (2016).

Thisse, C., Thisse, B. High-resolution in situ hybridization to whole-mount zebrafish embryos. *Nature Protocols*. **3**, 59-69 (2008).

Slavotinek, A.M. Eye development genes and known syndromes. *Molecular Genetics and Metabolism*. **104** (448-456), (2011).

Westerfield, M. The Zebrafish Book; A guide for the laboratory use of zebrafish (Danio rerio). 5th edition, University of Oregon Press. Eugene, Oregon. (2007).

Williamson, K.A., FitzPatrick, D.R. The genetic architecture of microphthalmia, anophthalmia and coloboma. *European Journal of Medical Genetics*. **57**, 369–380 (2014).

Appendix B

A conserved acetylation switch enables pharmacological control of tubby-like protein stability

A version of this chapter is published. Kerek, E.M., Yoon, K.H., Luo, S.Y., Chen, J., Valencia, R., Julien, O., Waskiewicz, A.J., Hubbard, B.P. (2020), A conserved acetylation switch enables pharmacological control of tubby-like protein stability. *Journal of Biological Chemistry*, 296:100073. doi: 10.1074/jbc.RA120.015839)

*Supplemental data referenced in this chapter may be found in online supporting information (doi: 10.1074/jbc.RA120.015839)

B.1. Summary

Tubby-like proteins (TULPs) are characterized by a conserved C-terminal domain that binds phosphoinositides. Collectively, mammalian TULP1-4 proteins play essential roles in intracellular transport, cell differentiation, signaling, and motility. Yet, little is known about how the function of these proteins is regulated in cells. Here, we present the protein–protein interaction network of TULP3, a protein that is responsible for the trafficking of G-protein-coupled receptors to cilia and whose aberrant expression is associated with severe developmental disorders and polycystic kidney disease. We identify several protein interaction nodes linked to TULP3 that include enzymes involved in acetylation and ubiquitination. We show that acetylation of two key lysine residues on TULP3 by p300 increases TULP3 protein abundance and that deacetylation of these sites by HDAC1 decreases protein levels. Furthermore, we show that one of these sites is ubiquitinated in the absence of acetylation and that acetylation inversely correlates with ubiquitination of TULP3. This mechanism is evidently conserved across species and is active in zebrafish during development. Finally, we identify this same regulatory module in TULP1, TULP2, and TULP4 and demonstrate that the stability of these proteins is similarly modulated by an acetylation switch. This study unveils a signaling pathway that links nuclear enzymes to ciliary membrane receptors via TULP3, describes a dynamic mechanism for the regulation of all tubby-like proteins, and explores how to exploit it pharmacologically using drugs.

B.2. Introduction

The *tubby* phenotype, characterized by mature-onset obesity, insulin resistance, sterility, and hearing and vision impairment, was first observed in an inbred strain of C57BL/6J mice (Coleman & Eicher, 1990; Ohlemiller et al., 1995; Kleyn et al., 1996; Mukhopadhyay & Jackson, 2011). Using positional cloning, the cause of these pathologies was later determined to be a splicing defect in the eponymous tubby (TUB) gene (Noben-Trauth et al., 1996). TUB and its related tubby-like proteins (TULPs) comprise a family of proteins present in both plant and animal kingdoms that are distinguished by a highly conserved C-terminal domain (Ikeda et al., 2002). This domain consists of a central alpha helix enclosed by a beta barrel structure and includes two

amino acids (Lys330 and Arg332) that coordinate binding to membrane phosphoinositides such as phosphatidylinositol 4,5,-bisphosphate (PIP2) through an electrostatic interaction (Santagata et al., 2001). The N-terminal regions of TUB and TULP homologs are variable and may be divided into three distinct classes: (1) those containing WD40 domains and/or suppressor of cytokine signaling (SOCS) motifs, (2) those without any apparent domains/motifs, and (3) those containing F-box domains (Wang et al., 2018). TUB/TULPs carry out a diverse range of important physiological functions ranging from biotic and abiotic stress defense in plants to regulation of cell metabolism, intracellular transport, and neural differentiation in animals (Wang et al., 2018). Mutations in these genes have been associated with numerous conditions including impaired development (Ikeda et al., 2018), altered life span (Mukhopadhyay et al., 2005), kidney disease (Legue & Liem, 2019; Hwang et al., 2019), and several cancers (Sartor et al., 2019; Sartor et al., 2014).

Four TULPs (TULP1-4) displaying unique tissue distribution, intracellular localization, and function have been described in mammals (Mukhopadhyay & Jackson, 2011). TULP1 and TULP2 display selective expression in the retina and testis, respectively (North et al., 1997). In contrast, both TULP3 and TULP4 show widespread expression throughout development and in adulthood (Li et al., 2001; Nishina et al., 1998). TULP3 is distributed equally in nuclear and cytoplasmic compartments, while TULP1 is localized to the inner segment of photoreceptors, and TULP2–TULP4 are predominately cytoplasmic (Mukhopadhyay & Jackson, 2011; Grossman et al., 2009). Mutations in TULP1 result in progressive photoreceptor degeneration in mice and retinitis pigmentosa in humans (Mukhopadhyay & Jackson, 2011; Banerjee et al., 1998). The severity of this phenotype is further worsened in a *tubby* background (Hagstrom et al., 2001). To date, TULP2 and TULP4 knockout mice have not been generated (Mukhopadhyay & Jackson, 2011).

Whole-body knockout of TULP3 in mice causes polydactyly (Cameron et al., 2009) and failed neural tube closure resulting in embryonic lethality (Ikeda et al., 2018). Furthermore, nephron-specific TULP3 knockout mice develop cystic kidneys (Legue & Liem, 2019; Hwang et al., 2019). These striking phenotypes have been attributed to improper trafficking of membrane proteins to cilia caused by TULP3 deletion (Mukhopadhyay & Jackson, 2011). The N-terminus of TULP3 contains a conserved helix that interacts with the IFT-A complex, a component of intraflagellar transport (IFT) particles, which are required to assemble cilia and for trafficking

inside cilia (Mukhopadhyay & Jackson, 2011; Han et al., 2019; Mukhopadhyay et al., 2010). With the IFT-A complex, TULP3 acts as an adaptor for the transport of at least 16 class A cilia-targeted G-protein-coupled receptors (GPCRs) including melanin-concentrating hormone receptor, neuropeptide Y receptors, and GPR161, a repressor of sonic hedgehog signaling (Badgandi et al., 2017). TULP3-IFT-A is also responsible for the ciliary transport of other integral membrane proteins such as the Polycistin 1/2 complex, which is implicated in polycystic kidney disease (PKD) (Badgandi et al., 2017). Three steps have been proposed for how this transport occurs: (1) capture of membrane cargo by TULP3 in a PIP2-dependent manner, (2) association with IFT-A and transport to cilia, and (3) release into a PIP2-deficient ciliary membrane (Badgandi et al., 2017). Overexpression of Inpp5e, an enzyme that hydrolyzes the 5′ phosphate from PIP2, has been shown to reduce TULP3 and GPR161 localization to cilia, indicating that low levels of PIP2 are required to anchor these proteins in place (Garcia-Gonzalo et al., 2015).

TULP3 contains a nuclear localization sequence that overlaps with its IFT-A binding region (Mukhopadhyay & Jackson, 2011). Furthermore, it has been demonstrated that hydrolysis of PIP2 induces relocalization of TULP3 to the nucleus (Wang et al., 2018). While some evidence suggests that TULP3 and other TULPs might have the ability to directly bind DNA and act as transcription factors, their function in the nucleus is unclear (Boggon et al., 1999). Moreover, little is known about how the localization, stability, and activity of tubby-like proteins might be regulated.

Here, we use Immunoprecipitation–Mass Spectrometry (IP-MS) to catalog the entire protein interaction network of TULP3. In addition to confirming previously validated interactions, we identify many new putative interactors, including enzymes such as SIRT1 and HDAC1 and Cullin-3, which regulate lysine acetylation (Hubbard et al., 2013a; Leus et al., 2017) and ubiquitination (Dubiel et al., 2018), respectively. We find that acetylation of TULP3 by p300 on several key residues including Lys316 and Lys389 increases its protein stability, while deacetylation by HDAC1 decreases TULP3 protein levels through a pathway involving proteasomal degradation. We use LC-MS/MS to map the ubiquitination sites on TULP3 and identify one site (Lys316) that can support either acetylation or ubiquitination and show that TULP3 ubiquitination correlates inversely with acetylation. We establish that this regulatory mechanism is active in zebrafish during embryonic development.

Highlighting the fundamental importance of this regulatory pathway, we find that some of these lysine residues are partially conserved and that Lys389 is fully conserved throughout all members of the tubby-like protein family in mammals. We show that TULP1, TULP2, and TULP4 protein levels are regulated by a parallel lysine acetylation switch. These data help define a new posttranslational regulatory pathway that facilitates rapid cross talk between chromatin modulating enzymes in the nucleus and membrane-bound receptors in cilia via TULP3. Additionally, through the application of small-molecule p300 and histone deacetylase (HDAC) inhibitors, this study presents a framework for future therapeutic applications by illustrating how the stability of all tubby-like proteins can be altered using drugs.

B.3. Experimental Procedures

B.3.1. Experimental models

This project used two female human cell lines, HEK293T cells and HeLa cells that were originally obtained from the American Type Culture Collection (ATCC) and were tested and found to be *mycoplasma*-free. Cells were cultured in a humidified atmosphere with 5% CO_2 at 37°C. In addition, this project used unisex zebrafish (sex undifferentiated). All animal procedures used protocols that were approved by the University of Alberta Animal Care and Use Committee, Biosciences (#0082).

B.3.2. Reagents

Rabbit anti-TULP1 (ab97281) and rabbit anti-TULP3 antibody (ab155317) were obtained from Abcam. HDAC Inhibitor XXIV (OSU-HDAC-44) was obtained from Calbiochem. Cycloheximide (2112S), MG-132 (2194S), rabbit antiacetylated lysine (#9441S), rabbit anti-beta actin (13E5, #4970S), rabbit anti-CUL3 (#2759S), rabbit anti-HA tag (C29F4, #3724T), mouse anti-HDAC1 (10E2, #5356S), antimouse IgG, HRP linked antibody (7076S), rabbit anti-Myc tag (71D10, #2278S), rabbit anti-P300 (D1M7C, #70088S), rabbit anti-Rad18 (D2B8, #9040S), rabbit

anti-SIRT1 (C14H4, #2496S), anti-rabbit IgG, HRP linked antibody (7074S), rabbit antiubiquitin (#3933S), Trichostatin A (9950S) were obtained from Cell Signaling Technology, Inc. Rabbit anti-PP6R3 (16944-1-AP) was obtained from Proteintech. Anacardic Acid (A7236), Anti-FLAG (M2, #F1804), C646 (SML0002), EX-527 (E7034), MC1568 (M1824), mouse antiacetyl lysine (4G12, 05-515), mouse anti-TULP2 (2B5, WH0007288M3), MS-275 (EPS002), and nicotinamide (N3376) were obtained from Sigma Aldrich.

B.3.3. Plasmids, cloning, and site-directed mutagenesis

HDAC1-FLAG was a gift from Eric Verdin (Addgene plasmid # 13820; http://n2t.net/addgene:13820; RRID: Addgene_13820). pCMVβ-p300-myc was a gift from Tso-Pang Yao (Addgene plasmid # 30489; http://n2t.net/addgene:30489; RRID: Addgene_30489). pMD2.G was a gift from Didier Trono (Addgene plasmid # 12259; http://n2t.net/addgene:12259; RRID: Addgene_12259). psPAX2 was a gift from Didier Trono (Addgene plasmid # 12260; http://n2t.net/addgene:12260; RRID: Addgene_12260). N-terminally tagged FLAG- TULP3 was cloned into the retrovirus compatible MSCV vector using the Xho1 restriction site. Successful clones were screened by Sanger sequencing. Site-directed mutagenesis was performed using the Q5 site-directed mutagenesis kit according to the manufacturer′s instructions.

B.3.4. Cell culture and transfection

HEK293T and HeLa cells were maintained in DMEM (11995-065, Gibco) supplemented with 10% fetal bovine serum (FBS) (F1051, Sigma Aldrich), 1% Penicillin Streptomycin (15140-122, Gibco), and 1% Glutamine (25030-081, Gibco). Cells were cultured in a 37°C/5% CO2 incubator with 97% humidity. For transfection, cells were seeded the day before transfection at 25% confluency using a Z2 Coulter Particle Count and Size Analyzer (Beckman Coulter). HEK293T cells were transfected with Effectene Transfection Reagent (Qiagen) according to the manufacturer′s instructions. HeLa cells were transfected with Lipofectamine 3000 (Invitrogen)

according to the manufacturer′s instructions. siRNAs were transfected using Lipofectamine RNAiMAX according to the manufacturer's instructions. Cells were harvested 48-h posttransfection (72 h for siRNA experiments).

B.3.5. Identification of TULP3 protein interactors by IP-LC-MS/MS

Lysates from HEK293T cells stably expressing either empty MSCV or MSCV FLAG-TULP3 were harvested, normalized for protein concentration, and subject to immunoprecipitation using anti-FLAG beads as described above. Subsequently, SDS-PAGE was performed using equal volumes of mock-FLAG and FLAG-TULP3 samples followed by either silver staining using the Pierce Silver Stain Kit (24612, ThermoFisher) (for gel analysis) or Coomassie staining using BioSafe Coomassie G-250 (for mass spectrometry identification). Protein bands of interest were excised from the Coomassie-stained gel and in-gel trypsin digestion on the samples was performed. The tryptic peptides were resolved and ionized by using nanoflow-HPLC (Thermo Scientific Easy-nLC 1000 system) coupled to a Q Exactive Orbitrap mass spectrometer (Thermo Scientific) with C18 columns described above. Data was processed using Proteome Discoverer 1.4 (Thermo Scientific), and the uniport human database (2016–11–26) was searched using SEQUEST (Thermo Scientific). Search parameters included a strict FDR of 0.01 using a decoy database, a relaxed FDR of 0.05, a maximum of three missed trypsin cleavages, a precursor mass tolerance of 10 ppm and a fragment mass tolerance of 0.01 Da, constant modification carbamidomethylation (C), and variable modifications of deamidation (N/Q) and oxidation (M). The maximum number of variable modifications was set to 4.

B.3.6. Coimmunoprecipitation experiments

Following transfection with the appropriate plasmids, cells were harvested and washed with ice cold PBS and lysed on a rotator for 30 min at 4°C with protein lysis buffer: 1% Triton X-100, 50 mM Tris-HCl pH 8.0, 150 mM NaCl supplemented with complete ultra protease inhibitor cocktail (05892791001, Roche). Cell lysates were centrifuged at 13,000 rpm for 15 min, and the

supernatants were added to EZview Red ANTI-FLAG M2 Affinity Gel or EZview Red ANTI-HA Affinity Gel and immunoprecipitated on a rotator for 2 h at 4°C. The beads were then washed five times with protein lysis buffer and eluted with 100 μg/ml 3x FLAG peptide on a rotator for 1 h. Laemmli buffer was added to samples prior to gel electrophoresis and western blotting.

B.3.7. Acetylation and ubiquitination experiments in cells

HEK293T cells stably expressing FLAG-TULP3 were transfected with the indicated plasmids for 24 or 48 h. For ubiquitin experiments, 10 μM MG-132 was added to cells 9 h before harvesting to allow ubiquitinated TULP3 to accumulate. Subsequently, cells were washed with PBS and lysed in buffer containing 8 M urea, 150 mM NaCl, and 50 mM Tris-HCl pH 8.0 and 1% NP40. Genomic DNA was sheared by passing the lysate through a 22-gauge needle 20 times. Cell lysates were then diluted tenfold in protein lysis buffer and immunoprecipitated as described. For acetylation experiments, cells were washed in PBS and lysed in protein lysis buffer supplemented with 20 mM Nicotinamide (NAM) and 1 μM Trichostatin A (TSA), used during subsequent washes as well. Samples were then analyzed by gel electrophoresis and western blotting. Five percent BSA in TBST was used for all stages of ubiquitin and acetylation immunoblotting. For immunoprecipitation experiments, protein equalization was performed prior to loading on a gel to ensure that an equal amount of TULP3 protein was present across all experimental groups, facilitating comparison.

B.3.8. Analysis of acetyl-lysine modifications by LC-MS/MS

HEK293T cells stably expressing FLAG-TULP3 were transfected with plasmids encoding tagged p300, PCAF, or GCN5 acetyltransferases and harvested as described above but with protein lysis buffer supplemented with 20 mM NAM and 1 μM TSA to inhibit deacetylases. FLAG-TULP3 was then immunoprecipitated as described above and subject to SDS-PAGE followed by staining with Coomassie G-250 according to the manufacturer′s instructions. In short, peptides were separated using a nanoflow-HPLC coupled to a LTQ Orbitrap Mass Spectrometer (Thermo

Fisher Scientific). Data were analyzed using Sequest (Sequest ver 28 rev 13) against the TULP3 sequence (uniprot/O75386). Search parameters included a precursor mass tolerance of 50 ppm, a fragment mass tolerance of 1 Da, with the constant modification carbamidomethylation (C), and variable modifications of oxidation (M), phosphorylation (STY), and/or acetyl (uncleaved K). The maximum number of variable modifications was set to 6. The results can be found in Supplemental Files 2 and 3.

B.3.9. Real-time qRT-PCR

RNA from HEK293T cells or zebrafish embryos was extracted using TRIzol Reagent (Invitrogen) according to the manufacturer's instructions and quantified using a Nanophotometer NP80 (Implen). For mammalian cell work, qRT-PCR reactions were performed using the iTaq Universal SYBR Green One-Step Kit (BioRad) while zebrafish reactions were carried out using the iScript cDNA Synthesis Kit (BioRad) and iQ SYBR Green Supermix (BioRad). Reactions were run on a CFX96 C1000 Touch real-time instrument (BioRad). Calculations were performed using a comparative method ($2^{-\Delta\Delta CT}$) using Beta Actin mRNA and 18S rRNA loading controls for HEK293T cells and zebrafish lysates, respectively.

B.3.10. Viral production, transduction, and siRNA experiments

For experiments employing shRNAs (Dharmacon Horizon Discovery), human pLKO.1 lentiviral vectors were cotransfected with pMD2.G and psPAX2 plasmids into HEK293T cells. The following shRNA sequences were used: HDAC1 shRNA 1 (TRCN0000004814) 5′-TATGGTTCAAAGTTAAGAACG-3′, HDAC1 shRNA 2 (TRCN0000004815) 5′-TTACGAATGGTGTAACCACCG-3′, HDAC1 shRNA 3 (TRCN0000004816) 5′-ATTACTTTGGACATGACCGGC-3′, HDAC1 shRNA 4 (TRCN0000004817) 5′-AAGTTGGAAGAGTTCTTGCGG-3′, EP300 shRNA 1 (TRCN0000009882) 5′-TACCATGCCAAGACTTGTCTG-3′, EP300 shRNA 2 (TRCN0000009883) 5′-TCTCAAGATGTCTCGGAATTG-3′, EP300 shRNA 3 (TRCN0000039885) 5′-

ATGTCTCGGAATTGTGAAGGC-3′, TRC Non-targeting control shRNA (RHS6848) 5′-CCGGTTGGTTTACATGTTGTGTGACTCGAGTCACACAACATGTAAACCATTTTTG-3′

To generate FLAG-TULP3 retroviral particles, the Murine Stem Cell Virus (MSCV) vector was cotransfected alongside VSV-G and GAG-Pol plasmids into HEK293T cells. For both sets of experiments, viral supernatants were collected 48 h posttransfection and supplemented with 10 μg/ml polybrene prior to being added to HEK293T or HeLa cells for 24 h. Transduced cells were selected by incubating cells in the presence of 2 μg/ml puromycin for three days. Stable transduction was verified by western blot. siRNA for Cul-3 knockdown was ordered as a SMARTPool (Dharmacon Horizon Discovery M-010224-02-0005) and transfected using Lipofectamine RNAiMAX into 293T cells. Protein levels were analyzed 72 h posttransfection by western blot.

B.3.11. Cycloheximide pulse-chase experiments

HEK293T cells stably transduced with FLAG-TULP3 or the respective mutant proteins were seeded at 66% confluency the day before the cycloheximide (CHX) chase. In total, 150 μg/ml CHX dissolved in DMSO was added to cells, which were then harvested and lysed at different timepoints, as described.

B.3.12. Nuclear/cytoplasmic cell fractionation

The day before fractionation, HEK293T cells were seeded at 75% confluency using a Z2 Coulter Particle Count and Size Analyzer (Beckman Coulter) on a 60 mm plate. Cells were then harvested and washed twice in ice-cold PBS with Ca and Mg. The crude cytoplasmic fraction was prepared by adding 400 uL of PBS with Ca/Mg, 0.27 M sucrose, 6.25% Ficoll PM 400 (F4375, Sigma Aldrich), and 0.1% NP40 and gently resuspending the cell pellet followed by 5 min of centrifugation at 1300*g* at 4°C. The supernatant containing cytoplasmic proteins was collected into a fresh microcentrifuge tube while the nuclear pellet was washed in an additional 500 uL of lysis

buffer and centrifuged at 1300*g* for 5 min. The crude cytoplasmic fraction was then centrifuged at 13,000 rpm for 10 min to remove residual nuclei, and the supernatant was collected as the final cytoplasmic fraction. The washed nuclear pellet was then lysed in 100 µl RIPA buffer by vortexing at maximum speed every 10 min for 1 h on ice. Nuclear debris was pelleted by centrifuging at 13,000 rpm for 10 min after which the supernatant was collected and moved to a fresh microcentrifuge tube as the final nuclear fraction. Cytoplasmic and nuclear samples were quantified using the Pierce BCA Protein Assay kit and equalized prior to being subject to gel electrophoresis and western blotting. Lamin A/C and alpha tubulin were used as standards to assess nuclear and cytoplasmic fraction purity, respectively.

B.3.13. Analysis of ubiquitin modifications by LC-MS/MS

HEK293T cells stably expressing FLAG-TULP3 were treated with 10 µM MG-132 for 9 h to allow ubiquitylated TULP3 to accumulate prior to lysis and immunoprecipitation. FLAG-TULP3 protein was eluted from FLAG-beads by boiling in Laemmli buffer, run on an SDS-PAGE gel, and subjected to a Blue-Silver stain, according to the manufacturer's instructions. Each gel lane was cut into four pieces and destained in a solution of 50 mM ammonium bicarbonate/50% acetonitrile at 37°C. Subsequently, gel pieces were dried by incubating with acetonitrile at 37°C, rehydrated and reduced with 175 µl of reducing solution (5 mM β-mercaptoethanol, 100 mM ammonium bicarbonate) at 37°C for 30 min, and alkylated with 175 µl of alkylating solution (50 mM iodoacetamide, 100 mM ammonium bicarbonate) at 37°C for 30 min. The gel pieces were washed twice with 175 µl of 100 mM ammonium bicarbonate at 37°C for 10 min and completely dried by incubating with acetonitrile at 37°C. Proteins in each well were digested using 1 µg of sequencing-grade trypsin (Promega Inc.) in 75 µl of 50 mM ammonium bicarbonate and incubated overnight. Tryptic peptides in the gel pieces were extracted by incubating with 2% acetonitrile, 1% formic acid, then with 50% acetonitrile, 0.5% formic acid, each at 37°C for 1 h. The extracted peptides were transferred to another round-bottom 96-well plate, dried using a Genevac (EZ-2 plus). For *in vitro* assays, fractionated peptides in the same sample were combined to be injected onto MS together. Peptides were separated using a nanoflow-HPLC (Thermo Scientific EASY-nLC 1200 System) coupled to Orbitrap Fusion Lumos Tribrid Mass Spectrometer (Thermo

Scientific). A trap column (5 μm, 100 Å, 100 μm × 2 cm, Acclaim PepMap 100 nanoViper C18; Thermo Scientific) and an analytical column (2 μm, 100 Å, 50 μm × 15 cm, PepMap RSLC C18; Thermo Scientific) were used for the reverse-phase separation of the peptide mixture. Peptides were eluted over a linear gradient over the course of 90 min from 3.85% to 36.8% acetonitrile in 0.1% formic acid. The peaklists were generated with ProteoWizard (msconvert, v3.0.20044-d751fcb4e) (Chambers et al., 2012) and analyzed using ProteinProspector (v5.22.1) against the TULP3 sequence (uniprot/O75386). Search parameters included a maximum of three missed trypsin cleavages, a precursor mass tolerance of 15 ppm, a fragment mass tolerance of 0.8 Da, with the constant modification carbamidomethylation (C), and variable modifications of acetylation (protein N-term), deamidation (N/Q), oxidation (M), GlyGly (uncleaved K), or acetylation (uncleaved K). The maximum number of variable modifications was set to 4. The results can be found in Supplemental Files 2 and 3.

B.3.14. In vitro acetylation assay

In total, 0.5 μg of recombinant human TULP3 protein (H00007289-P01, Novus Biologicals) was incubated in the absence or presence of 0.5 μg of recombinant human p300 (catalytic domain) (BML-SE451-0100, Enzo Life Sciences), 20 μM acetyl-coA, or 30 μM C646, as indicated, for 1 h at 37°C. Samples were then prepared for in-gel trypsin digestion and mass spectrometry as described above.

B.3.15. Zebrafish husbandry and animal care

All experiments conducted were approved by the University of Alberta Animal Care and Use Committee, Biosciences (#0082). Anesthesia and euthanasia were performed with tricaine methanesulfonate (Syndel). Adult and embryonic zebrafish were cared for according to standard protocols. Embryos were grown at 28.5°C in E3 embryo media. Developing embryos were staged according to standard morphological milestones (Kimmel et al., 1995). The AB strain was used as the wild-type strain.

B.3.16. Pharmacological treatment and imaging of zebrafish embryos

Zebrafish embryos were raised to 70% epiboly, dechorionated with pronase E (Sigma-Aldrich), and treated until 24 hpf with the indicated concentration of C646 (Sigma-Aldrich) dissolved in E3 media. Phenotypic analysis was performed on anesthetized embryos at 24 hpf using an Olympus stereomicroscope (SZX-12).

B.3.17. Morpholino design

A sequenced transcript (zmp:0000000711; ENSDART00000093236.6) previously identified to be orthologous to human TULP3 was used to design a morpholino to target zebrafish *tulp3*. A splice-blocking morpholino (5′-GCCCTCTGTCAATGCACAAACACTG-3′; Gene Tools LLC) was designed to the boundary of the 3′ splice acceptor of intron 3 and exon 4. Eight nanograms of *tulp3* morpholino was coinjected with 2 ng of zebrafish p53 morpholino (5′-GCGCCATTGCTTTGCAAGAATTG-3′) at the one-cell stage. A standard control morpholino (5′-CCTCTTACCTCAGTTACAATTTATA-3′; Gene Tools LLC) was used as a negative control.

B.3.18. Generation of zebrafish overexpressing TULP3 mRNA and microinjection

Wild-type and K316Q/K389Q variant human TULP3 sequences were cloned and ligated into pCS2+ vectors. Following linearization with NotI (NEB), mRNA was transcribed using the mMachine SP6 Transcription Kit (Invitrogen) and purified using Amicon Ultra-0.5 Centrifugal Filter columns (Ultracel-50; Fisher/Millipore). Wild-type zebrafish embryos were injected with either 100 pg of wild-type TULP3 or the K316Q/K389Q mutant TULP3 mRNA at the one-cell stage. *gfp* mRNA was prepared as above and used as a negative control.

B.3.19. Quantification and statistical analysis

Numbers of trial replicates and appropriate statistical measures and tests are denoted in Figure captions.

B.4. Results

B.4.1. TULP3 interacts with a diverse set of cytoplasmic and nuclear proteins

To better understand the biological role of TULP3 in the nucleus and to identify potential regulatory mechanisms for this protein, we performed an IP-MS experiment to profile its protein interactome. We transfected HEK293T cells with either mock-FLAG or FLAG-TULP3 and immunoprecipitated the resulting complexes using anti-FLAG coated beads (Fig. B.1*A*). After identifying proteins in the IPs by mass spectrometry (Supplemental File 1; tabs 1,2), we generated a high-confidence list of TULP3 interactors by removing proteins present in the mock-FLAG IP as well as proteins having high average spectral counts of >2.1 in the CRAPome database (Mellacheruvu et al., 2013) (Supplemental File 1; tabs 3,4). We used the top 35 of these 221 hits, ordered by Protein Score, to generate a STRING (Szklarczyk et al., 2019) network diagram (Fig. B.1, *B–C*). This analysis revealed several nodes containing proteins involved in the IFT-A complex, nucleic acid repair, transcription, and splicing, mediators of cell signaling, and components of the Cullin-3 RING ubiquitin ligase complex (CRL-3) (Fouad et al., 2019) (Fig. B.1*C*). Of particular interest, we also identified interactions with several nuclear lysine deacetylase enzymes including SIRT1 and HDAC1 (Hubbard et al., 2013a; Leus et al., 2017; Han et al., 2013) (Fig. B.1, *B–C*, Supplemental File 1). Subsequently, we validated the results from our mass spectrometry screen by performing coimmunoprecipitation (co-IP) followed by western blot. We confirmed that FLAG-TULP3 pulled down SIRT1 in reciprocal co-IP experiments (Fig. B.1*D*, Fig. S1*A*). As well, we validated TULP3 interactions with two other potential regulatory enzymes, RAD18 (Fig. B.1*E*), a ubiquitin ligase involved in DNA double-strand break repair (Inagaki et al., 2011), and PP6R3/SAPS3 (Fig. B.1*F*), a regulatory subunit of protein phosphatase 6 (Heo et al., 2020).

B.4.2. Acetylation of TULP3 by p300 increases its protein levels in cells

Based on our observations that TULP3 physically interacts with enzymes involved in lysine acetylation and ubiquitination, we hypothesized that TULP3 might be posttranslationally regulated by one or both of these modifications. To explore potential acetylation of TULP3, we performed an immunoprecipitation of HA-tagged TULP3 from 293T cells in the absence or presence of tagged histone acetyltransferase (HAT) enzymes including p300, PCAF, and GCN5 and probed the resulting western blot with a pan-acetyl antibody. We observed a strong acetylation signal resulting from p300 stimulation (Fig. B.2*A*), but not the other HATs, which overlapped with the predicted molecular weight of TULP3. This effect was associated with an apparent increase in the total protein levels of TULP3 in the input of the experiment (Fig. B.2*A*). Next, we used LC-MS/MS to validate that the observed acetylation signal was due to acetylation on TULP3. We identified a total of five acetylated lysine residues (Lys37, Lys268, Lys316, Lys320, Lys389) in the presence of p300, several of which were also present under basal conditions, or in the presence of exogenous PCAF or GCN5 (Fig. B.2*B*). To further investigate the p300-dependent increase in TULP3 levels observed in Figure B.2*A*, we expressed exogenous p300 in HeLa cells and performed a western blot to evaluate TULP3 protein expression. Consistent with our previous result, TULP3 protein levels were increased by nearly twofold following p300 stimulation (Fig. B.2*C*, Fig. S1*B*). Importantly, TULP3 mRNA expression was unchanged by p300, suggesting that the increase in protein levels was not due to increased transcription of the gene (Fig. B.2*D*). We next examined the effect of knocking down p300 in HeLa cells on TULP3 protein levels. Stable knockdown of endogenous p300 protein resulted in a reduction in TULP3 protein levels (Fig. B.2*E*, Fig. S1*C*). To distinguish if inhibition of p300 enzymatic activity *versus* complete loss of protein was sufficient to replicate these results, we treated cells with 30 μM of C646 or 50 μM anacardic acid, two potent small-molecule p300 inhibitors (Babu et al., 2018). Consistent with our knockdown results, we found that pharmacological inhibition of p300 HAT activity resulted in a reduction in TULP3 protein levels in excess of fivefold (Fig. B.2*F*). This effect was not due to reduced TULP3 mRNA expression (Fig. B.2*G*). To investigate if this effect was associated with a decrease in TULP3 acetylation, we performed an immunoprecipitation of FLAG-TULP3 from cells treated with either DMSO or C646, normalized protein levels between

the two IPs, and probed with a pan-acetyl antibody. Indeed, drug treatment resulted in a decrease in total TULP3 acetylation, concomitant with reduced protein levels in the input (Fig. B.2*H*). Finally, we confirmed a protein–protein interaction between TULP3 and p300 in cells by performing reciprocal co-IP experiments (Fig. S1, *D–E*) and demonstrated the ability of p300 to directly acetylate TULP3 using an *in vitro* assay (Fig. S1*F*). Overall, these results demonstrate that TULP3 is acetylated in a p300-dependent manner and that its hyperacetylation is associated with an increase in its protein abundance.

B.4.3. Mutation of Lys316, Lys320, and Lys389 each increases TULP3 stability

Previous studies have demonstrated a strong link between lysine acetylation and protein stability, often in the context of lysine acetylation/ubiquitination switches (Caron et al., 2005). Of the five acetylation sites we identified, four are located within the conserved tubby domain, and one is located within the N-terminal IFT-A interaction domain (Fig. B.3*A*). We hypothesized that acetylation at one or more of these residues might directly affect TULP3 protein stability. To examine this possibility, we generated stable cells lines expressing Lys->Gln (acetyl mimetic) and Lys->Arg (deacetyl mimetic) mutant proteins (Hubbard et al., 2013a) corresponding to each residue using site-directed mutagenesis. All of these proteins displayed nuclear-cytoplasmic localization patterns similar to the wild-type protein (Fig. S2). Next, we compared their stabilities to the wild-type protein by performing cycloheximide pulse-chase experiments. While the half-life of the wild-type protein was <3 h (Fig. B.3*B*), we found that mutation of Lys316 or Lys389 to Gln or Arg greatly increased this (Fig. B.3, *C–F*). Substitutions at other sites appeared to have little effect with the exception of K320Q, which also increased protein half-life (Fig. S3). Dual substitution of Lys316/Lys389 with Q or R increased TULP3 half-life by >20- and >7-fold, respectively, blocking virtually all degradation throughout the 12-h time window tested (Fig. B.3, *G–I*). Moreover, these proteins were completely resistant to C646-induced TULP3 degradation (Fig. B.3*J*). These data suggest that the mechanism by which p300 regulates TULP3 stability involves modification of key residues including Lys316 and Lys389.

B.4.4. HDAC1 deacetylates TULP3 and reduces its protein levels

Based on the results of the protein interaction screen (Fig. B.1, Supplemental File 1), we reasoned that SIRT1 and HDAC1 were likely deacetylase candidates for TULP3. To test this assertion, we treated cells with various class I and class II HDAC as well as sirtuin inhibitors (Hubbard et al., 2013b) and evaluated changes in FLAG-TULP3 acetylation (following normalization of protein levels) and total protein levels by immunoblot. We found that inhibition of SIRT1 using nicotinamide or EX-527 had no effect on TULP3 acetylation or protein levels (Fig. S4). However, treatment with several class I and class II HDAC inhibitors, namely trichostatin A (TSA), HDAC inhibitor XXIV, and MS-275, all boosted TULP3 protein levels by more than threefold and similarly affected protein acetylation levels (Fig. B.4*A*). TSA is a pan-HDAC inhibitor while MS-275 selectively inhibits HDACs 1 and 3 and HDAC inhibitor XXIV inhibits numerous HDACs including HDAC1, but not HDAC3 (Leus et al., 2017). These results served to strengthen the hypothesis that HDAC1 might deacetylate TULP3 in cells. To confirm this, we expressed HA-HDAC1 in 293T cells and examined the effect on TULP3 protein levels and acetylation. We found that HDAC1 decreased TULP3 protein levels by >50% in addition to reducing its acetylation by an equal degree (Fig. B.4*B*). We repeated this experiment in HeLa cells and found that HDAC1 expression lowered TULP3 protein without affecting its mRNA levels (Fig. B.4, *C–D*). Next, we stably knocked down endogenous levels of HDAC1 in HeLa cells using lentivirus and examined the effect on TULP3 protein levels. We found that reduced levels of HDAC1 correlated with increased abundance of TULP3 (Fig. B.4*E*), consistent with our hypothesis. We also validated the prospective TULP3–HDAC1 interaction that was initially identified by mass spectrometry (Supplemental File 1) by performing reciprocal co-IP experiments using FLAG-TULP3 and HA-HDAC1 (Fig. B.4, *F–G*). These results identify HDAC1 as a primary TULP3 deacetylase.

B.4.5. Acetylation of TULP3 blocks its ubiquitination

To build upon the observation that TULP3 interacts with Cullin-3 (Fig. B.1) and to examine if polyubiquitination and subsequent proteasomal degradation might underlie the changes

in protein stability caused by differential acetylation, we treated cells with the proteasome inhibitor MG-132, and observed its effect on expression of endogenous and exogenous TULP3. We found that MG-132 increased protein abundance of TULP3 over the course of a 9-h interval by approximately threefold without changing its mRNA levels (Fig. B.5*A*, Fig. S5, *A–C*). Next, we set out to test whether the effects of p300 on TULP3 stability occur via this same mechanism or an independent mechanism. To do this, we expressed p300 in HeLa cells in the presence or absence of MG-132. While p300 and MG-132 each increased TULP3 protein individually, the effect was not additive, suggesting that both operate through a common pathway (Fig. B.5*B*, Fig. S5*D*). Based on these results, we surmised that acetylation could be stabilizing TULP3 by blocking its ubiquitination. We immunoprecipitated FLAG-TULP3 cotransfected with HA-ubiquitin (and treated with MG-132) in the absence or presence of exogenous p300 and probed with an HA-antibody to detect ubiquitination. We found that p300 decreased TULP3 ubiquitination (Fig. B.5*C*). To evaluate the corollary that TULP3 deacetylation increases its ubiquitination, we repeated with experiment with HDAC1 in place of p300. Consistent with our hypothesis, TULP3 ubiquitination levels were increased by expression of Myc-HDAC1 (Fig. B.5*D*). These results were also reproduced using an antibody to endogenous ubiquitin (Fig. S5, *E–F*). To examine the interplay between acetylation at Lys316 and Lys389 and ubiquitination, we transfected cells with FLAG-tagged K316Q/K389Q and K316R/K389R TULP3 mutants alongside HA-ubiquitin in the presence of MG-132 and subsequently immunoprecipitated the mutant proteins and analyzed their ubiquitination levels by western blot. Compared with wild-type FLAG-TULP3, we found that both of the double acetylation mutant proteins displayed decreased levels of polyubiquitination, implicating these lysine residues in playing a role in TULP3 degradation (Fig. S5*G*). Next, we used LC-MS/MS to map ubiquitination sites on TULP3. We identified five ubiquitination sites (Fig. B.5*E*), including Lys316, a target of p300-mediated acetylation and a mediator of TULP3 protein stability (Fig. B.2 and Fig. B.3). Finally, to test if the CRL-3 complex might be a cognate E3 ligase responsible for polyubiquitination of TULP3, we validated the putative interaction between TULP3 and Cullin-3 (Fig. B.5*F*), and performed pooled siRNA knockdown of endogenous Cullin-3 to examine its effect on FLAG-TULP3 protein levels in cells. We found that knockdown of Cullin-3 increased TULP3 protein abundance by more than twofold and partially reversed the drop in TULP3 protein levels associated with C646 treatment (Fig. B.5*G*).

Collectively, these results demonstrate that an acetylation switch controls TULP3 protein stability and that p300, HDAC1, and the Cullin-3 RING ligase complex are involved in this mechanism.

B.4.6. Deletion of the tubby domain in TULP3 renders the protein refractory toward C646 and MG-132 treatment

To fully map the determinants of the acetylation switch, we constructed a series of TULP3 truncation and deletion variants, spanning the N-terminal region (1–183) as well as the tubby domain (residues 184–442) (Fig. S6*A*). Initially, we performed nuclear-cytoplasmic cell fractionation with cells expressing the mutant proteins to establish their intracellular localization. Despite the removal of an NLS, we found that all TULP3 N-terminal deletion mutants remained distributed in both cytoplasmic and nuclear compartments (Fig. S6*B*). However, deletion of the tubby domain, which contains a second NLS sequence, resulted in complete redistribution of the protein to the cytoplasm (Fig. S6*B*). Unlike the wild-type protein or N-terminal deletion variants, we observed that the protein levels of these cytoplasmic, tubby-domain devoid TULP3 variants were unaltered by treatment with either C646 or MG-132 (Fig. S6, *C–D*). These data suggest that the residues responsible for controlling the stability of TULP3 via acetylation are contained within the tubby domain and/or that the enzymes mediating the effects of these drugs are sequestered in the nucleus.

B.4.7. Acetylation regulates TULP3 protein stability in zebrafish

A sequence alignment of TULP3 orthologs in a variety of species revealed complete conservation of Lys316 and Lys389 (Fig. S7*A*). Since TULP3 plays a critical role in development (Ikeda et al., 2001), we chose to examine the physiological activity of the acetylation switch in zebrafish, an established model for studying embryonic development (Babu et al., 2018). While no studies on TULPs in zebrafish have been conducted, several studies have explored the role of p300 in the development of this organism (Babu et al., 2018, Fauquier et al., 2018). Both genetic knockdown and pharmacological inhibition of p300 in zebrafish embryos result in a severe

phenotype characterized by growth retardation, neural malformation, and developmental delay leading to eye, jaw, and heart defects in adults (Babu et al., 2018). Given the phenotypic similarities between p300 and TULP3 knockdown in multiple organisms, we hypothesized that low levels of TULP3 may underlie some of the effects of p300 inhibition. First, we treated zebrafish embryos with 3 or 5 μM C646 until 24-h post fertilization (hpf). Mirroring our results in mammalian cells, C646 induced a drop in TULP3 protein levels in zebrafish embryos (Fig. B.6*A*). This was associated with a marked delay in embryonic development including failure to undergo proper tail extension and head and brain formation in nearly 100% of animals, consistent with previous reports (Babu et al., 2018) (Fig. B.6, *B–C*). Next, we designed an intron 3–4 splice-blocking morpholino to knockdown TULP3 and injected it into zebrafish at the single-cell stage. We verified the ability of this morpholino to knockdown TULP3 protein *versus* a control (Fig. B.6*D*). In parallel, we coinjected either 100 pg of wild-type TULP3 mRNA or K316Q/K389Q-TULP3 mRNA into knockdown embryos to attempt to rescue any potential phenotypes. We found that TULP3 knockdown mimicked C646 treatment, resulting in developmental delay in a large percentage of the population (Fig. B.6, *E–F*). In addition, we observed apoptosis in the hindbrain (mild) or hindbrain and forebrain (severe) in roughly 50% of TULP3 knockdown embryos (Fig. B.6, *E–F*). Importantly, while coinjection with wild-type TULP3 mRNA had relatively little effect on these phenotypes, coinjection with K316Q/K389Q-TULP3 mRNA almost completely reversed the developmental abnormalities (Fig. B.6*F*). Indicative of enhanced stability, K316Q/K389Q-TULP3 protein was present at levels approximately fourfold higher than its wild-type counterpart (Fig. B.6*G*).

Past work has shown that p300 expression decreases throughout zebrafish development (Babu et al., 2018). To see if this decrease might be coupled to a decrease in TULP3 protein levels, we performed an immunoblot for p300 and TULP3 protein extracted from untreated zebrafish embryos at several time points. We observed a drop in p300 levels at 24- and 32-h postfertilization in excess of sixfold that was accompanied by a decrease in TULP3 protein (Fig. B.6*H*) but not mRNA expression (Fig. S7*B*). Together, these experiments provide evidence that the acetylation switch present on mammalian TULP3 is functionally conserved in zebrafish.

B.4.8. Protein levels of TULP1, TULP2, and TULP4 are also regulated by acetylation and ubiquitination

While Lys316 is exclusive to TULP3, Lys320 is partially conserved and Lys389 is fully conserved throughout all tubby-like protein paralogs in mammals (Fig. B.7*A*). Given this, we wondered if the acetylation switch on TULP3 might be a conserved mechanism that regulates the stability of one or more additional members of the tubby-like protein family. To examine this assertion, we expressed HA-p300 in 293T cells and measured the levels of TULP1, TULP2, and TULP4 proteins. We found that the protein abundance of all three of these was increased (Fig. B.7*B*) to a similar degree as TULP3 (Fig. B.2*C*). To extend this analysis further, we treated 293T cells with C646 and performed an immunoblot to measure its effect on TULP1, TULP2, and TULP4 protein levels. Consistent with our previous experiment, we found that all of these proteins were reduced by approximately threefold by treatment with the drug (Fig. B.7*C*). A similar decrease in TULP1, TULP2, and TULP4 proteins levels was observed following shRNA knockdown of p300 (Fig. B.7*D*). Next, we investigated if HDAC1 might mediate the stability of these TULPs via deacetylation. Expression of Myc-HDAC1 caused a twofold drop in TULP1 and TULP4 protein levels, but had only a marginal effect on TULP2 levels (Fig. B.7*E*). Reduction of endogenous basal levels of HDAC1 using lentiviral shRNA caused an increase in TULP1 and TULP4 protein levels but had a modest effect on TULP2, further implying a role for HDAC1 in the regulation of TULP1 and TULP4 but not TULP2 (Fig. B.7*F*). Finally, to determine if TULP1, TULP2, and TULP4 were subject to ubiquitination and proteasomal degradation similar to TULP3, we treated cells with MG-132 and measured their protein levels. We observed an approximate twofold increase in the levels of all three proteins in response to the drug, an effect that was slightly more pronounced for TULP1 and TULP4 than TULP2 (Fig. B.7*G*). Overall, these results demonstrate that in addition to TULP3, p300 plays a role in modulating protein levels of TULP1, TULP2, and TULP4, while HDAC1 displays differential effects on different TULP paralogs.

B.5. Discussion

Despite their tremendous physiological importance, little work has been done to understand how tubby-like proteins are regulated. Here, we describe a p300/HDAC1-mediated reversible acetylation switch that mediates ubiquitination and subsequent degradation of TULP3 (Fig. S8). There is substantial phenotypic data to support the model that TULP3 acts downstream of p300/HDAC1 and the CRL-3 pathway. First, knockout of p300 in mice is associated with a delay in neural tube closure and ultimately leads to embryonic lethality (Goodman & Smolik, 2000). Moreover, in addition to head, hand, and feet anomalies, polydactyly has been reported in children with Rubinstein–Taybi syndrome (RSTS), a disease caused by mutations in CBP or p300 (Sachdeva et al., 2016). These phenotypes are astonishingly similar to those displayed by TULP3 knockout mice (Cameron et al., 2009). Second, numerous pieces of evidence point to a critical role for HDAC1 in neural development (Bahari-Javan et al., 2017; Bardai et al., 2012). Third, Culin-3 RING ubiquitin ligase complexes (CRL-3) have been shown to act as master regulators of mammalian cell differentiation and neurogenesis (Dubiel et al., 2018). While these effects have classically been attributed to regulation of RhoA protein stability (Dubiel et al., 2018), our data detailing an interaction between TULP3 and CUL-3 and its associated Kelch BTB-domain adaptor proteins (KBTB6, KBTB7) (Fouad et al., 2019) (Fig. B.1, *B–C*), and our data showing an increase in TULP3 protein levels following CUL-3 knockdown, suggest that CRL-3 also regulates TULP3. It is tempting to speculate that lack of TULP3 due to hypoacetylation could underlie many of the developmental defects ascribed to p300 deficiency or aberrant HDAC1 or CRL-3 activity.

While the role of p300 and HDAC1 in controlling gene transcription by regulating the acetylation status of histones, chromatin regulators, and transcription factors is well established (Chan & La Thangue, 2001), less is known regarding how these proteins might quickly transmit signals from the nucleus to the cytoplasm or cilia. Our model (Fig. S8) unveils a new posttranslational signalling pathway that enables rapid cross talk between the nucleus and cilia. In the first step, nuclear TULP3 acts as a sensor for p300/HDAC1 activity and becomes stabilized (acetylated) or marked for degradation (deacetylated). It is interesting to consider that since p300 relies on acetyl-CoA as a cofactor (Montgomery et al., 2015), TULP3 acetylation might indirectly be coupled to the metabolic state of the cell. Second, the protein is then shuttled to the cytoplasm where it is either polyubiquitinated by CRL-3 and degraded by the proteasome or binds PIP2 and forms a complex with IFT-A. Finally, the acetylated TULP3/IFT-A complex associates with

receptors and mobilizes them to the cilia where they receive extracellular signals. Interestingly, many of the receptors that are trafficked by TULP3 have the ability to transmit signals back to the nucleus (Mukhopadhyay et al., 2013), allowing for cross talk. For example, activation of GPR161 initiates formation of the Gli3 repressor complex, which shuttles to the nucleus and suppresses transcription of sonic hedgehog target genes (Mukhopadhyay et al., 2013). This model provides a functional explanation for the presence of TULP3 in the nucleus.

We show that the TULP3 acetylation switch we identify in mammalian cells is also active in zebrafish and that Lys316 and Lys389 are fully conserved among TULP3 orthologs in diverse species (Fig. B.6, Fig. S7). While we provide compelling evidence that the residues mediating the acetylation switch are likely confined to the tubby domain (Fig. S6), it is plausible that additional lysine residues, besides those identified in this study, could also play a role in this regulatory mechanism. For example, in addition to the ubiquitination sites mapped in this work, other studies have identified this modification on Lys268 (Akimov et al., 2018; Wagner et al., 2011), another site that we found to be acetylated (Fig. B.2*B*). Future studies could be aimed at examining the role of these additional acetylation and/or ubiquitination sites and determining if the effects of acetylation on ubiquitination are confined to overlapping or adjacent residues on TULP3 or potentially distal sites as well.

The posttranslational regulatory mechanism described in this work applies not only to TULP3, but also to TULP1, TULP2, and TULP4 (Fig. B.7). It has been proposed that TULPs, which only exist in eukaryotes, evolved from an ancestral member of the prokaryotic phospholipid scramblase family (PLSCRs) via TUB through divergent evolution and segmental duplication events (Mukhopadhyay & Jackson, 2011; Bateman et al., 2009). Owing to conservation of key lysine residues that mediate the acetylation switch (Fig. B.7), the effects of p300 acetylation on tubby-like proteins appear to be universal. Thus, this posttranslational pathway has the capacity to regulate the entire protein family in concert. All of the mammalian TULPs, which are expressed in different tissues and under different promoters, play important roles in development (Mukhopadhyay & Jackson, 2011). Given the complexities of coordinating the transcriptional regulation of these four proteins, we propose that the acetylation switch may have evolved as a mechanism to increase the abundance of all of these proteins together during early embryonic development, in response to rising p300 levels (Chen et al., 2009). This same mechanism could be

used to induce their rapid degradation as p300 levels wane during adulthood (Chen et al., 2009). This is supported by our data on zebrafish showing that as development proceeds, p300 mRNA and protein levels decrease (Babu et al., 2018), concomitant with a decrease in TULP3 protein but not mRNA (Fig. B.6*H* and Fig. S7*B*). Based on their tissue distributions and substrate specificities, HDACs may superimpose an additional layer of regulation to enable individual targeting of TULPs. While we show that HDAC1 acts as a deacetylase for TULP3, TULP1, and TULP4 (Fig. B.4 and Fig. B.7), we found that this enzyme did not seem to regulate the stability of TULP2 to an equal extent, suggesting that other deacetylases might be important in different contexts.

Dysregulation of TULPs has been implicated in a number of human diseases including retinitis pigmentosa (TULP1 and TULP2) (Mukhopadhyay & Jackson, 2011; Grossman et al., 2014), PKD (TULP3) (Legue & Liem, 2019), and several cancers (TULP3) (Sartor et al., 2019; Sartor et al., 2014). In fact, we queried the COSMIC (the Catalog of Somatic Mutations In Cancer) (Tate et al., 2019) database for mutations in TULP3 associated with cancer and identified with cancer and identified K320R, a mutation associated with endometrial carcinoma, which corresponds to a site of acetylation that we identified (Fig. B.3*A*). Unfortunately, despite their important role in these clinical diseases, TULPs have traditionally been classified as nondruggable due to their lack of enzymatic activity. This study unveils a strategy for controlling TULP protein expression using p300 and HDAC inhibitors that could have therapeutic value (Fig. B.2–B.4, Fig. B.7). For example, HDAC1 inhibitors could be used to boost TULP3 levels in diseases caused by hypomorphic alleles such as K407I-TULP3, which is associated with PKD (Legue & Liem, 2019). The fact that the safety of HDAC inhibitors in humans has already been established in clinical trials for several cancers (Romero, 2019) could facilitate their repurposing for TULP-related disorders. Alternatively, small-molecule p300 activators, such as CTPB (N-(4-chloro-3-trifluoromethyl-phenyl)-2-ethoxy-6-pentadecyl-benzamide) (Hegarty et al., 2016), could be used to perform the same function while p300 inhibitors could be used to treat diseases caused by TULP gain of function. Future studies could be designed to test the viability of this approach.

This study sheds light on the posttranslational regulation of TULP3 and its related tubby-like proteins by identifying a conserved p300/HDAC1-mediated acetylation switch that modulates the protein levels of this family. In addition, it describes a pathway that enables cross talk between chromatin factors in the nucleus and a wide range of receptors localized to cilia. Finally, it details

a new pharmacological strategy for globally controlling TULP protein stability. We anticipate that these findings will be of ongoing significance as the list of physiological functions and disease-causing mutations attributed to tubby-like proteins continues to expand.

B.6. Figures

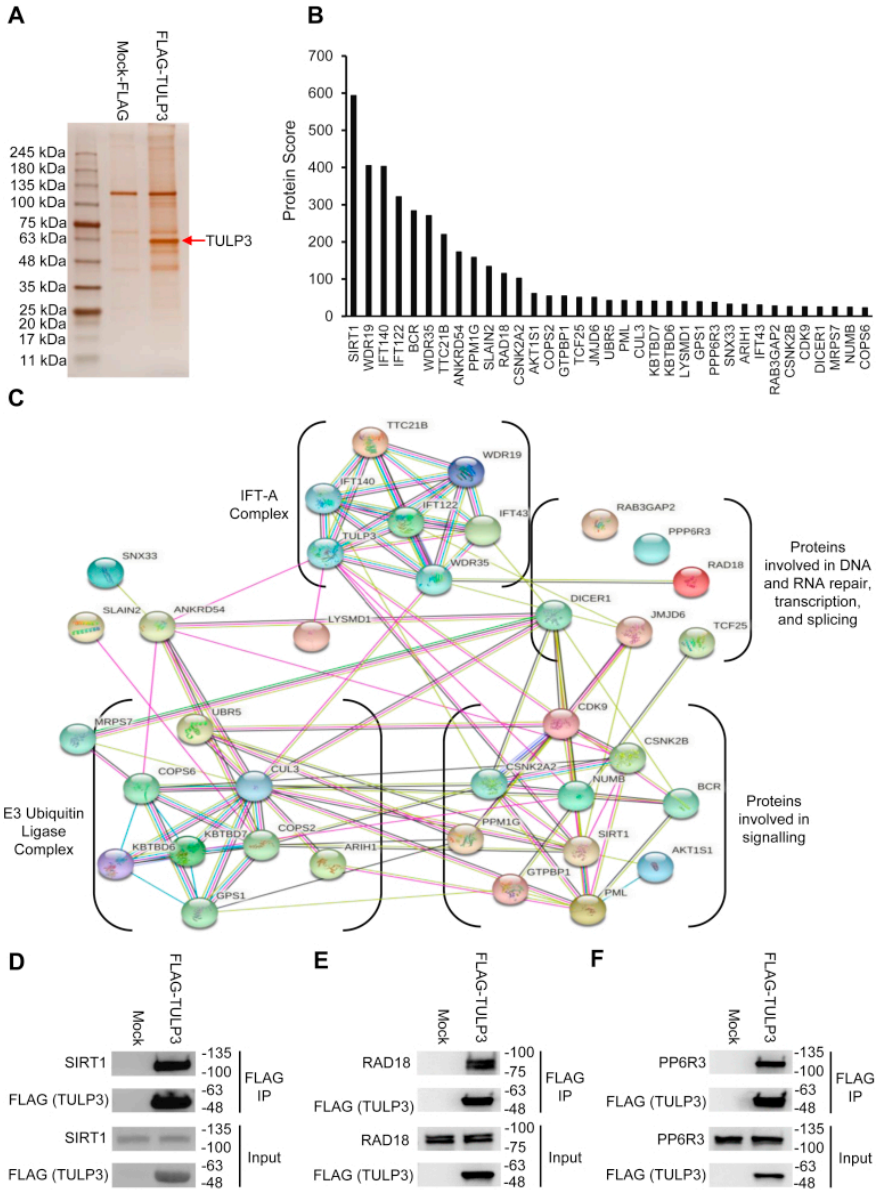

Figure B.1: Identification and validation of TULP3 protein–protein interactions. *A*, silver stained gel showing proteins coimmunoprecipitated alongside mock-FLAG or FLAG-TULP3 from 293T cells. The band corresponding to FLAG-TULP3 is indicated by a *red arrow*. *B*, bar graph ranking the top 35 high-confidence hits in (*A*) as identified by mass spectrometry. *C*, STRING diagram outlining the interconnectedness of TULP3 interactors identified in (*B*). Western blots showing coimmunoprecipitation of FLAG-TULP3 with (*D*) SIRT1, (*E*) RAD18, and (*F*) PP6R3 in 293T cells.

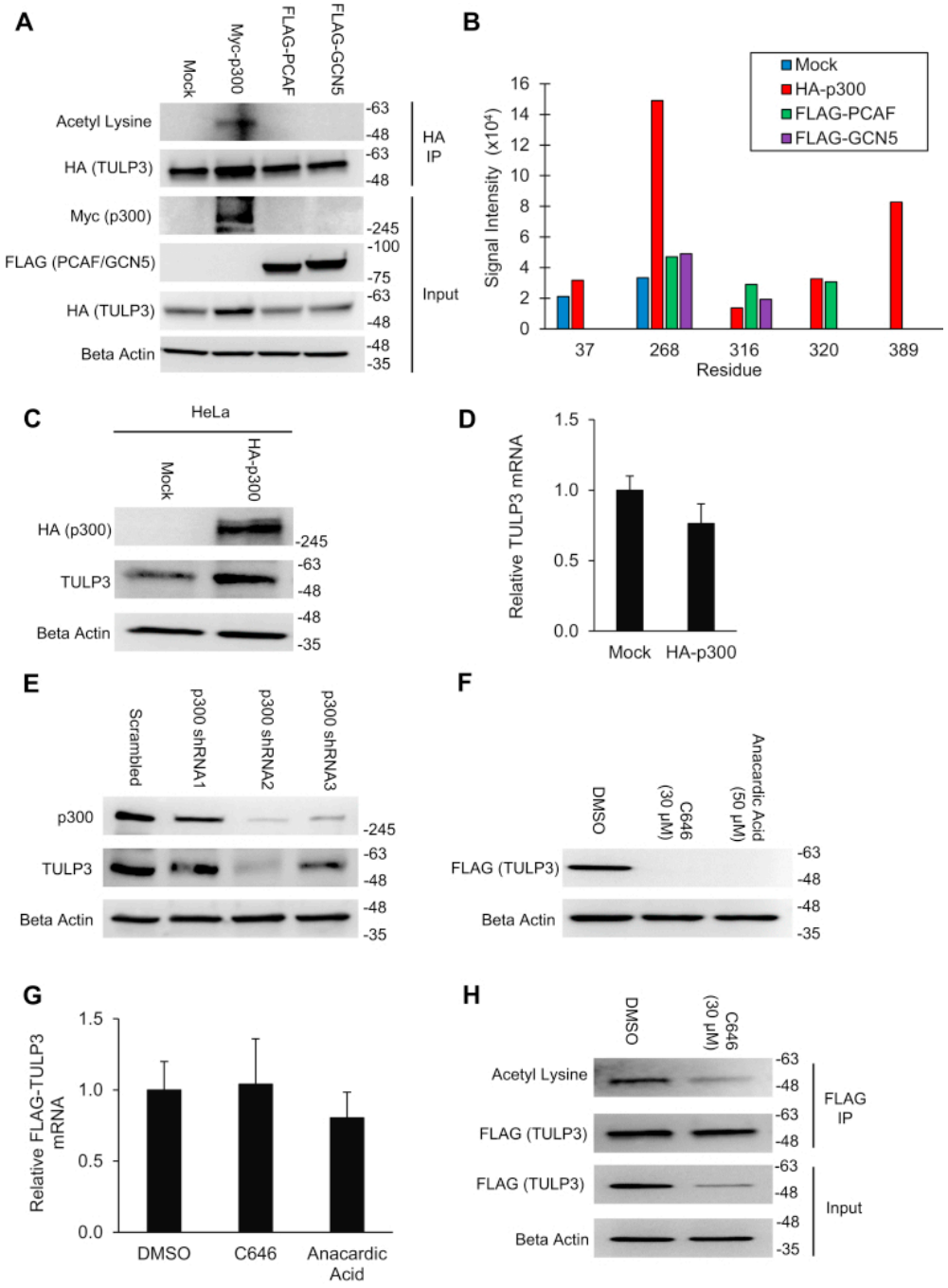

Figure B.2: Acetylation of TULP3 by p300 increases its protein abundance in cells. *A*, western blot showing TULP3 acetylation levels in 293T cells in the presence of either empty pcDNA 3.1(+), Myc-p300, FLAG-PCAF, or FLAG-GCN5 following immunoprecipitation. Cells were harvested 48 h posttransfection. *B*, semiquantitative LC-MS/MS-based comparison of TULP3 acetylation corresponding to the conditions in (*A*). *C*, western blot showing total levels of endogenous TULP3 in HeLa cells following transfection with empty pcDNA 3.1(+) or a plasmid encoding HA-p300.

Cells were harvested 48 h posttransfection. *D*, mRNA levels of endogenous TULP3 corresponding to samples in (*C*) examined using quantitative real-time PCR; n = 4 technical replicates, Mean ± S.D. shown. *E*, western blot of p300 and TULP3 protein levels following stable transduction of p300 shRNAs into HeLa cells. *F*, immunoblot of stably expressed FLAG-TULP3 protein in 293T cells following treatment with either DMSO, 30 μM C646, or 50 μM anacardic acid for 24 h. *G*, mRNA levels of FLAG-TULP3 corresponding to samples in (*F*) analyzed using quantitative real-time PCR; n = 4 technical replicates, Mean ± S.D. shown. *H*, acetylation levels of FLAG-TULP3 in stably expressing 293T cells following treatment with DMSO or 30 μM C646 for 9 h.

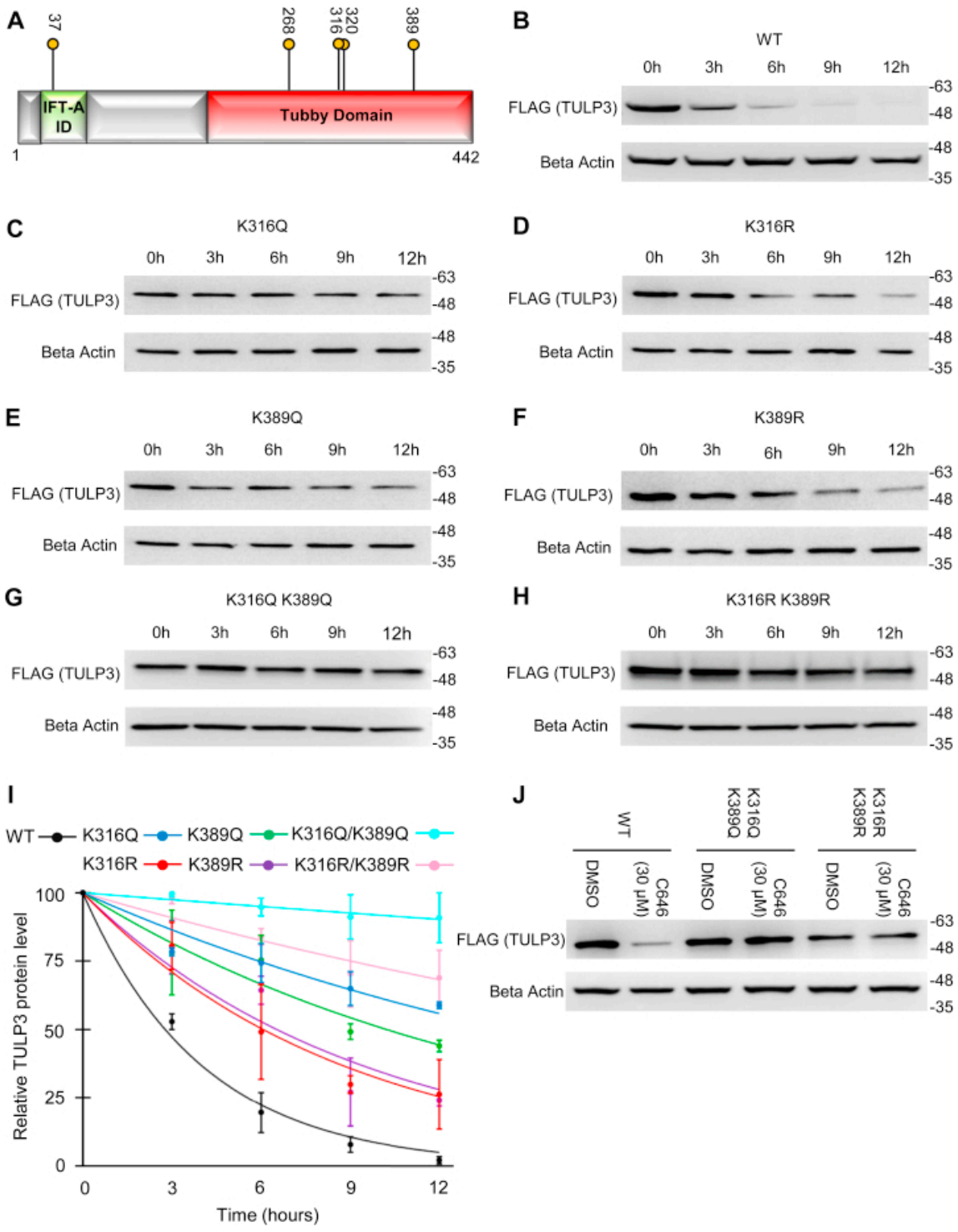

Figure B.3: Modification of K316, K320, and K389 each influences TULP3 stability. *A*, schematic outlining key functional domains in TULP3 and the location of acetylation sites. IFT-A ID denotes Intraflagellar Transport Complex A interacting domain. Western blots representing cycloheximide pulse-chase experiments for stably expressed (*B*) FLAG-TULP3 wild-type protein

or (*C*) K316Q, (*D*) K316R, (*E*) K389Q, (*F*) K389R, (*G*) K316Q/K389Q, (*H*) K316R/K389R mutants in 293T cells. *I*, plot corresponding to experiments in (*B–H*) quantifying relative TULP3 protein levels *versus* time; n = 3 biological replicates, Mean ± S.D. shown. *J*, protein levels of FLAG-TULP3, FLAG-TULP3 K316Q/K389Q, and K316R/K389R mutants stably expressed in 293T cells following treatment with DMSO or 30 μM C646 for 9 h.

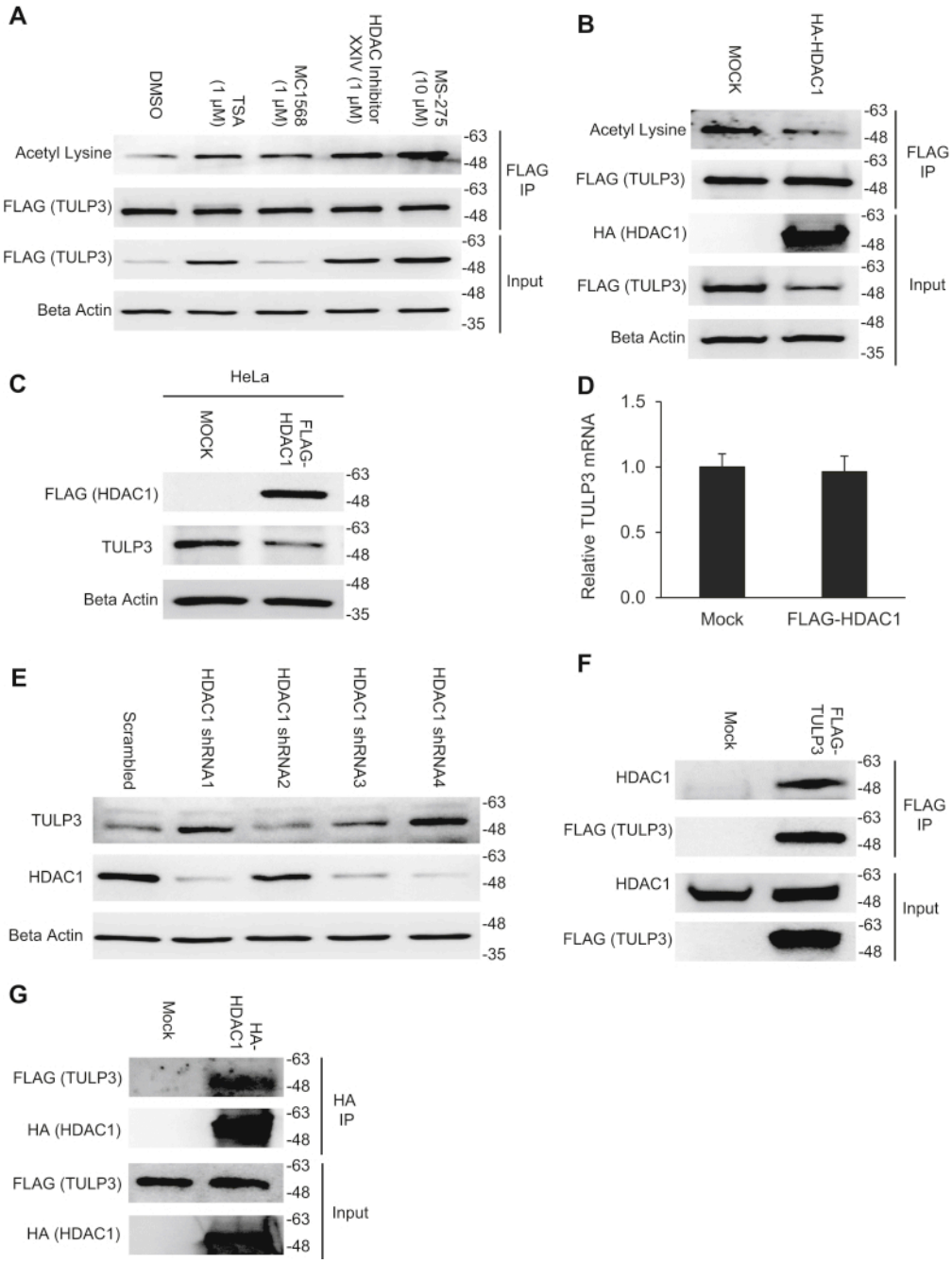

Figure B.4: HDAC1 deacetylates TULP3 and reduces its protein levels. *A*, western blot showing acetylation and total protein levels of stably expressed FLAG-TULP3 in 293T cells treated with DMSO, 1 μM TSA, 1 μM MC1568, 1 μM HDAC Inhibitor XXIV, or 10 μM MS-275 for 16 h. *B*, acetylation and total protein levels of stably expressed FLAG-TULP3 in 293T cells transfected with empty pcDNA 3.1(+) or a plasmid encoding HA-HDAC1. Cells were harvested 48 h posttransfection. *C*, western blot showing endogenous levels of TULP3 in Hela cells

transfected with either empty pcDNA 3.1(+) or a plasmid encoding FLAG-HDAC1. Cells were harvested 48 h posttransfection. *D*, mRNA levels of endogenous TULP3 corresponding to treatments in (*C*) analyzed by qRT-PCR; n = 4 technical replicates, Mean ± S.D. shown. *E*, western blot of HDAC1 and TULP3 protein levels following stable transduction of HDAC1 shRNAs into HeLa cells. Western blots showing coimmunoprecipitation of *F* FLAG-TULP3 with HDAC1 or *G* HA-HDAC1 with FLAG-TULP3 in 293T cells.

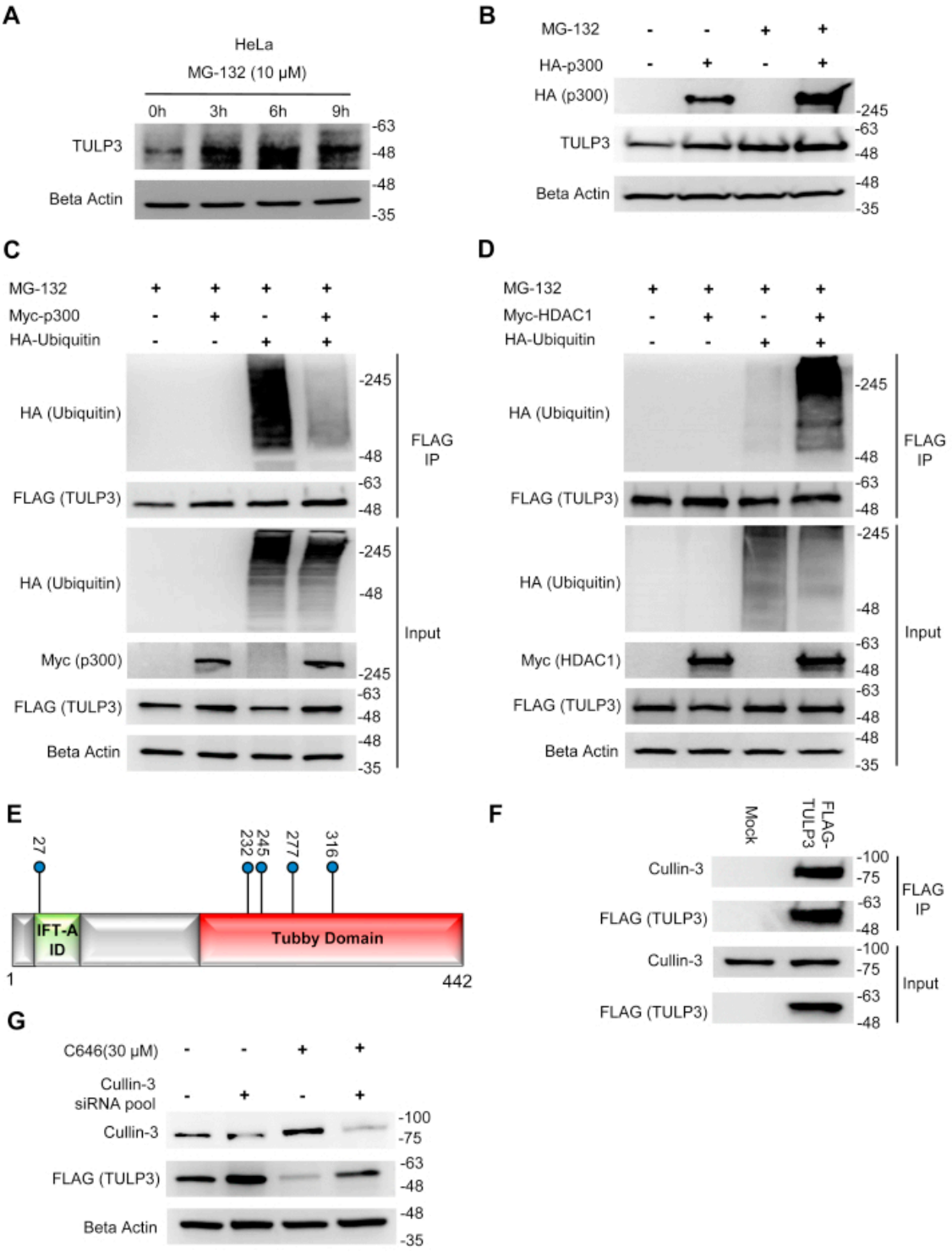

Figure B.5: TULP3 protein stability is regulated by polyubiquitination and by Cullin-3. *A*, western blot showing TULP3 levels in HeLa cells treated with 10 μM MG-132 for the time intervals indicated. *B*, TULP3 protein levels in the absence or presence of 10 μM MG-132 and transfected with a plasmid encoding HA-p300 as indicated. Cells were harvested 48 h

posttransfection following 9 h of MG-132 treatment. *C*, immunoblot analysis of ubiquitination levels on FLAG-TULP3 immunoprecipitated from 293T cells treated with MG-132 and transfected with plasmids encoding HA-Ubiquitin or Myc-p300 as indicated. Cells were harvested 48 h posttransfection following 9 h of MG-132 treatment. *D*, western blot showing ubiquitination levels on FLAG-TULP3 immunoprecipitated from 293T cells treated with MG-132 and transfected with plasmids encoding HA-Ubiquitin or Myc-HDAC1 as indicated. Cells were harvested 48 h posttransfection following 9 h of MG-132 treatment. *E*, schematic outlining key functional domains in TULP3 and the location of ubiquitination sites identified by mass spectrometry. IFT-A ID denotes Intraflagellar Transport Complex A interacting domain. *F*, western blot showing coimmunoprecipitation of FLAG-TULP3 with Cullin-3 in 293T cells. *G*, immunoblot showing levels of FLAG-TULP3 protein in 293T cells in the absence or presence of C646 following transfection with a pool of siRNAs targeting Cullin-3 or a scrambled control. Cells were collected 72 h posttransfection; 30 μM C646 was added to cells 48 h posttransfection as indicated.

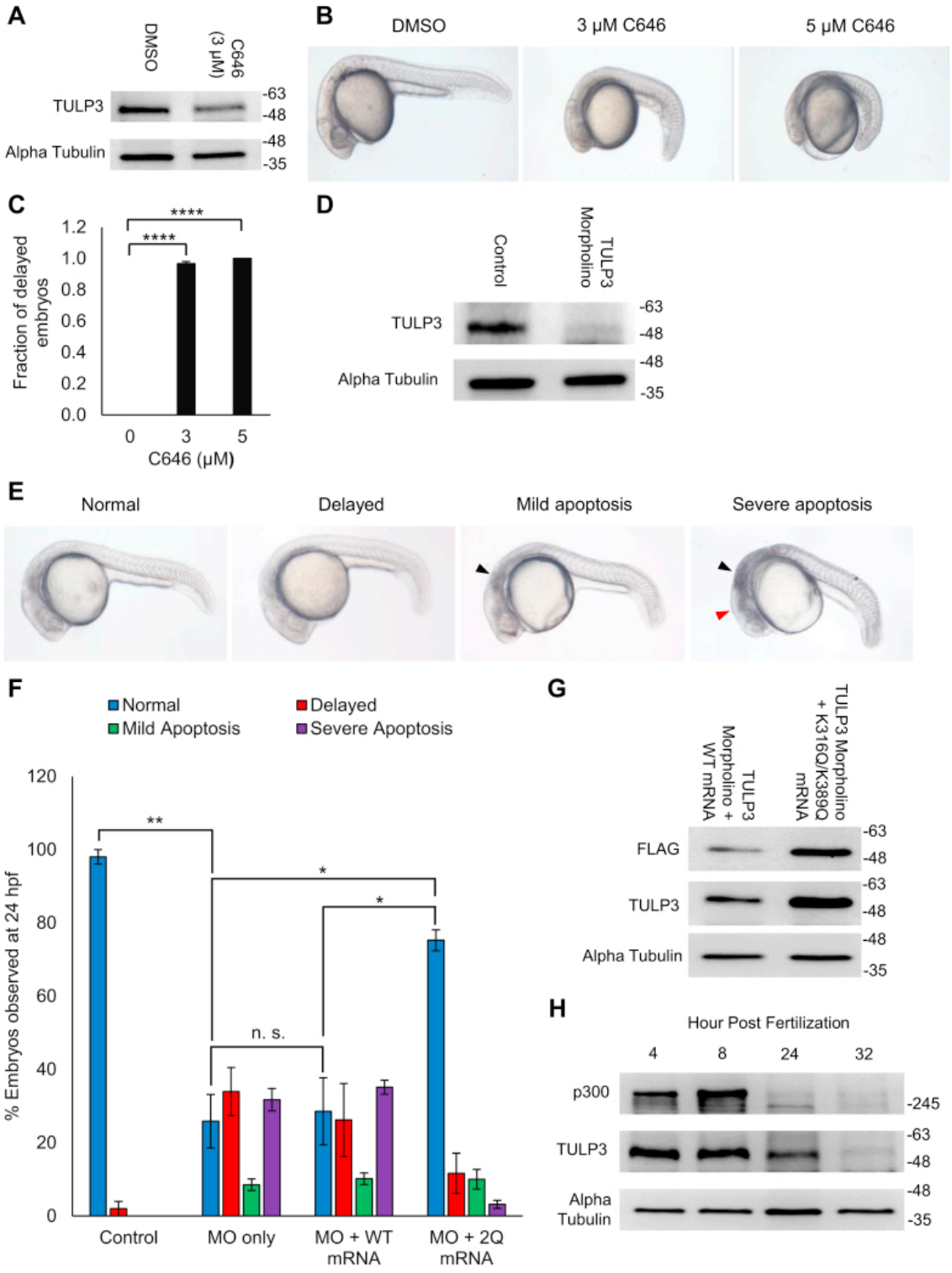

Figure B.6: An acetylation switch actively regulates TULP3 levels in zebrafish during development. *A*, immunoblot showing TULP3 protein levels in zebrafish embryo lysates harvested 10 h postfertilization following treatment with DMSO or 3 μM C646 for 10 h. *B*, representative photos of zebrafish embryos 24 h postfertilization treated with either DMSO or 3 or

5 μM C646 for 24 h. *C*, graph quantifying the frequency of the phenotypes observed in panel (*B*); n = 120, 123 or 123 for 0, 3, and 5 μM C646 groups respectively. Mean ± S.D. shown. **** denotes $p < 0.0001$ (*t* test). *D,* western blot showing levels of TULP in zebrafish embryos 24 h postfertilization in the absence or presence of 8 ng TULP3 morpholino. *E*, representative photos of zebrafish embryos 24 h postfertilization displaying normal, delayed, mild apoptosis, and severe apoptosis phenotypes. The *black* and *red arrows* indicate apoptosis in the hindbrain and forebrain, respectively. *F*, graph quantifying the frequency of the phenotypes observed in panel (*E*); n = 271, 248, 317, or 292 for control, morpholino only, morpholino + WT, or morpholino + 2Q mutant, respectively. Mean ± S.D. shown. * denotes $p < 0.05$, ** denotes $p < 0.01$, and n.s. indicates nonsignificance (*t* test). *G*, levels of TULP3 protein in morpholino-injected zebrafish rescued with either wild-type TULP3 mRNA or K316Q/K389Q TULP3 mRNA. Lysates were harvested 8 h postfertilization. *H*, immunoblot showing protein levels of TULP3 and p300 in zebrafish embryo lysates harvested at 4, 8, 24, and 32 h postfertilization.

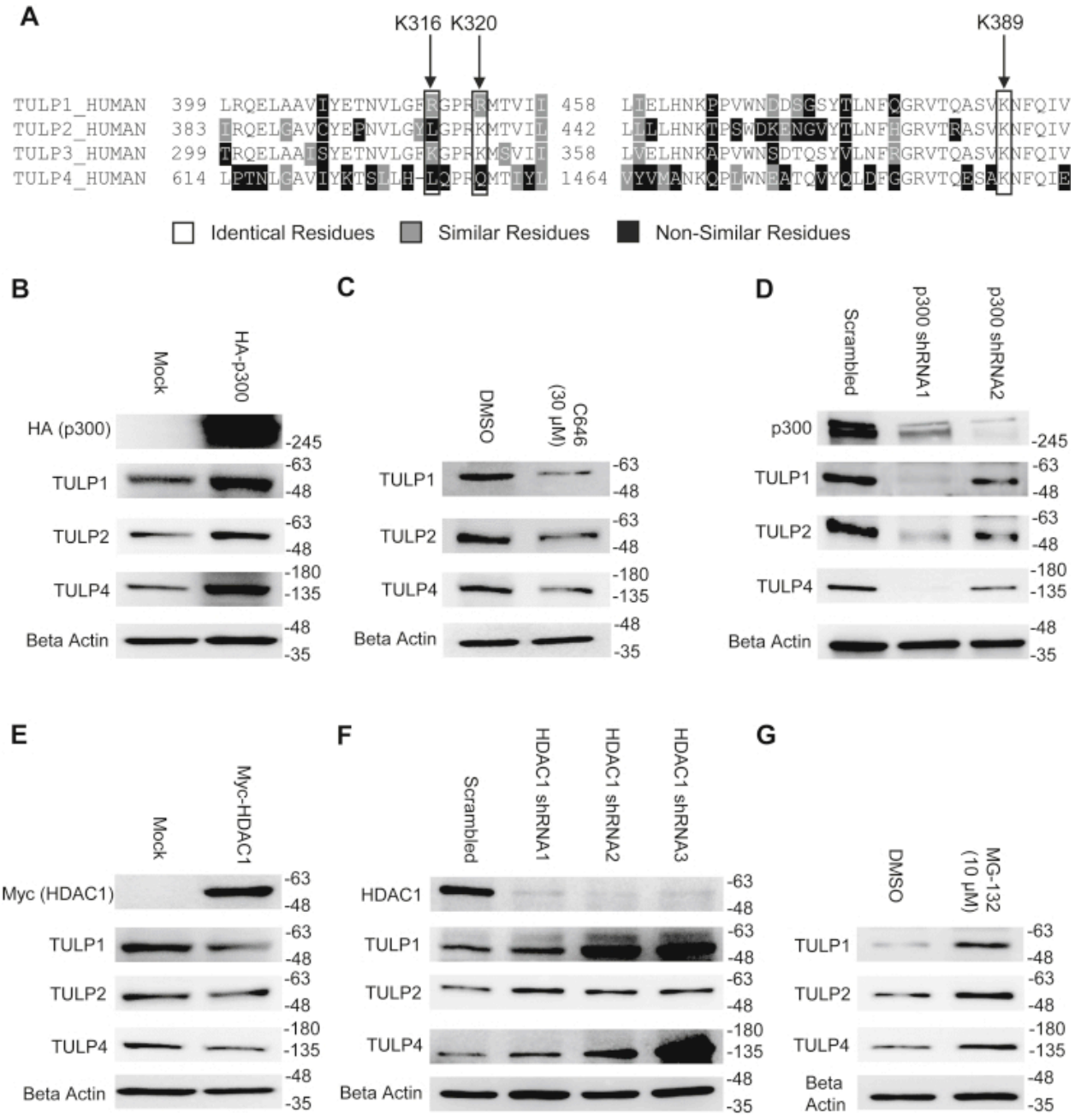

Figure B.7: p300 and HDAC1 influence the stability of multiple tubby-like proteins. *A*, sequence alignment of the four human TULP proteins (TULP1-4) performed using ClustalW software. Identical, similar, and nonsimilar residues are color coded as indicated. Key acetylation sites are indicated with *arrows*. *B*, western blot showing TULP1, TULP2, and TULP4 protein levels in 293T cells transfected with either a control plasmid or a plasmid encoding HA-p300. Cells were harvested 48 h posttransfection. *C*, western blot showing levels of TULP1, TULP2, and TULP4 in 293T following 24 h treatment with either DMSO or 30 μM C646. *D*, western blot of

p300, TULP1, TULP2, and TULP4 protein levels following stable transduction of p300 shRNAs into 293T cells. *E*, western blot showing TULP1, TULP2, and TULP4 protein levels in 293T cells transfected with either a control plasmid or a plasmid encoding Myc-HDAC1. Cells were harvested 48 h posttransfection. *F*, immunoblot showing p300, TULP1, TULP2, and TULP4 protein levels following stable transduction of HDAC1 shRNAs into 293T cells. *G*, western blot showing levels of TULP1, TULP2, and TULP4 in 293T cells following 9 h treatment with either DMSO or 10 μM MG-132.

B.7. References

Akimov V., Barrio-Hernandez I., Hansen S.V.F., Hallenborg P., Pedersen A.K., Bekker-Jensen D.B., Puglia M., Christensen S.D.K., Vanselow J.T., Nielsen M.M., Kratchmarova I., Kelstrup C.D., Olsen J.V., Blagoev B. UbiSite approach for comprehensive mapping of lysine and N-terminal ubiquitination sites. *Nat. Struct. Mol. Biol.* 2018;25:631–640.

Babu A., Kamaraj M., Basu M., Mukherjee D., Kapoor S., Ranjan S., Swamy M.M., Kaypee S., Scaria V., Kundu T.K., Sachidanandan C. Chemical and genetic rescue of an ep300 knockdown model for Rubinstein Taybi Syndrome in zebrafish. *Biochim. Biophys. Acta Mol. Basis Dis.* 2018;1864:1203–1215.

Badgandi H.B., Hwang S.H., Shimada I.S., Loriot E., Mukhopadhyay S. Tubby family proteins are adapters for ciliary trafficking of integral membrane proteins. *J. Cell Biol.* 2017;216:743–760.

Bahari-Javan S., Varbanov H., Halder R., Benito E., Kaurani L., Burkhardt S., Anderson-Schmidt H., Anghelescu I., Budde M., Stilling R.M., Costa J., Medina J., Dietrich D.E., Figge C., Folkerts H. HDAC1 links early life stress to schizophrenia-like phenotypes. *Proc. Natl. Acad. Sci. U. S. A.* 2017;114:E4686–E4694.

Banerjee P., Kleyn P.W., Knowles J.A., Lewis C.A., Ross B.M., Parano E., Kovats S.G., Lee J.J., Penchaszadeh G.K., Ott J., Jacobson S.G., Gilliam T.C. TULP1 mutation in two extended Dominican kindreds with autosomal recessive retinitis pigmentosa. *Nat. Genet.* 1998;18:177–179.

Bardai F.H., Price V., Zaayman M., Wang L., D'Mello S.R. Histone deacetylase-1 (HDAC1) is a molecular switch between neuronal survival and death. *J. Biol. Chem.* 2012;287:35444–35453.

Bateman A., Finn R.D., Sims P.J., Wiedmer T., Biegert A., Soding J. Phospholipid scramblases and Tubby-like proteins belong to a new superfamily of membrane tethered transcription factors. *Bioinformatics.* 2009;25:159–162.

Boggon T.J., Shan W.S., Santagata S., Myers S.C., Shapiro L. Implication of tubby proteins as transcription factors by structure-based functional analysis. *Science.* 1999;286:2119–2125.

Cameron D.A., Pennimpede T., Petkovich M. Tulp3 is a critical repressor of mouse hedgehog signaling. *Dev. Dyn.* 2009;238:1140–1149.

Caron C., Boyault C., Khochbin S. Regulatory cross-talk between lysine acetylation and ubiquitination: role in the control of protein stability. *Bioessays.* 2005;27:408–415.

Chambers M.C., Maclean B., Burke R., Amodei D., Ruderman D.L., Neumann S., Gatto L., Fischer B., Pratt B., Egertson J., Hoff K., Kessner D., Tasman N., Shulman N., Frewen B.

A cross-platform toolkit for mass spectrometry and proteomics. *Nat. Biotechnol.* 2012;30:918–920.

Chan H.M., La Thangue N.B. p300/CBP proteins: HATs for transcriptional bridges and scaffolds. *J. Cell Sci.* 2001;114:2363–2373.

Chen G., Zhu J., Lv T., Wu G., Sun H., Huang X., Tian J. Spatiotemporal expression of histone acetyltransferases, p300 and CBP, in developing embryonic hearts. *J. Biomed. Sci.* 2009;16:24.

Coleman D.L., Eicher E.M. Fat (fat) and tubby (tub): two autosomal recessive mutations causing obesity syndromes in the mouse. *J. Hered.* 1990;81:424–427.

Dubiel W., Dubiel D., Wolf D.A., Naumann M. Cullin 3-based ubiquitin ligases as master regulators of mammalian cell differentiation. *Trends Biochem. Sci.* 2018;43:95–107.

Fauquier L., Azzag K., Parra M.A.M., Quillien A., Boulet M., Diouf S., Carnac G., Waltzer L., Gronemeyer H., Vandel L. CBP and P300 regulate distinct gene networks required for human primary myoblast differentiation and muscle integrity. *Sci. Rep.* 2018;8:12629.

Fouad S., Wells O.S., Hill M.A., D'Angiolella V. Cullin ring ubiquitin ligases (CRLs) in cancer: responses to ionizing radiation (IR) treatment. *Front Physiol.* 2019;10:1144.

Garcia-Gonzalo F.R., Phua S.C., Roberson E.C., Garcia G., 3rd, Abedin M., Schurmans S., Inoue T., Reiter J.F. Phosphoinositides regulate ciliary protein trafficking to modulate hedgehog signaling. *Dev. Cell.* 2015;34:400–409.

Goodman R.H., Smolik S. CBP/p300 in cell growth, transformation, and development. *Genes Dev.* 2000;14:1553–1577.

Grossman G.H., Pauer G.J., Narendra U., Peachey N.S., Hagstrom S.A. Early synaptic defects in tulp1-/- mice. *Invest Ophthalmol. Vis. Sci.* 2009;50:3074–3083.

Grossman G.H., Beight C.D., Ebke L.A., Pauer G.J., Hagstrom S.A. Interaction of tubby-like protein-1 (Tulp1) and microtubule-associated protein (MAP) 1A and MAP1B in the mouse retina. *Adv. Exp. Med. Biol.* 2014;801:511–518.

Hagstrom S.A., Adamian M., Scimeca M., Pawlyk B.S., Yue G., Li T. A role for the Tubby-like protein 1 in rhodopsin transport. *Invest Ophthalmol. Vis. Sci.* 2001;42:1955–1962.

Han J., Hubbard B.P., Lee J., Montagna C., Lee H.W., Sinclair D.A., Suh Y. Analysis of 41 cancer cell lines reveals excessive allelic loss and novel mutations in the SIRT1 gene. *Cell Cycle.* 2013;12:263–270.

Han S., Miyoshi K., Shikada S., Amano G., Wang Y., Yoshimura T., Katayama T. TULP3 is required for localization of membrane-associated proteins ARL13B and INPP5E to primary cilia. *Biochem. Biophys. Res. Commun.* 2019;509:227–234.

Hegarty S.V., O'Leary E., Solger F., Stanicka J., Sullivan A.M., O'Keeffe G.W. A small molecule activator of p300/CBP histone acetyltransferase promotes survival and neurite growth in a Cellular model of Parkinson's disease. *Neurotox Res.* 2016;30:510–520.

Heo J., Larner J.M., Brautigan D.L. Protein kinase CK2 phosphorylation of SAPS3 subunit increases PP6 phosphatase activity with Aurora A kinase. *Biochem. J.* 2020;477:431–444.

Hubbard B.P., Loh C., Gomes A.P., Li J., Lu Q., Doyle T.L., Disch J.S., Armour S.M., Ellis J.L., Vlasuk G.P., Sinclair D.A. Carboxamide SIRT1 inhibitors block DBC1 binding via an acetylation-independent mechanism. *Cell Cycle.* 2013a;12:2233–2240.

Hubbard B.P., Gomes A.P., Dai H., Li J., Case A.W., Considine T., Riera T.V., Lee J.E., E S.Y., Lamming D.W., Pentelute B.L., Schuman E.R., Stevens L.A., Ling A.J., Armour S.M. Evidence for a common mechanism of SIRT1 regulation by allosteric activators. *Science.* 2013b;339:1216–1219.

Hwang S.H., Somatilaka B.N., Badgandi H., Palicharla V.R., Walker R., Shelton J.M., Qian F., Mukhopadhyay S. Tulp3 regulates renal Cystogenesis by trafficking of Cystoproteins to cilia. *Curr. Biol.* 2019;29:790–802. e795.

Ikeda A., Ikeda S., Gridley T., Nishina P.M., Naggert J.K. Neural tube defects and neuroepithelial cell death in Tulp3 knockout mice. *Hum. Mol. Genet.* 2001;10:1325–1334.

Ikeda A., Nishina P.M., Naggert J.K. The tubby-like proteins, a family with roles in neuronal development and function. *J. Cell Sci.* 2002;115:9–14.

Inagaki A., Sleddens-Linkels E., van Cappellen W.A., Hibbert R.G., Sixma T.K., Hoeijmakers J.H., Grootegoed J.A., Baarends W.M. Human RAD18 interacts with ubiquitylated chromatin components and facilitates RAD9 recruitment to DNA double strand breaks. *PLoS One.* 2011;6

Kimmel C.B., Ballard W.W., Kimmel S.R., Ullmann B., Schilling T.F. Stages of embryonic development of the zebrafish. *Dev. Dyn.* 1995;203:253–310.

Kleyn P.W., Fan W., Kovats S.G., Lee J.J., Pulido J.C., Wu Y., Berkemeier L.R., Misumi D.J., Holmgren L., Charlat O., Woolf E.A., Tayber O., Brody T., Shu P., Hawkins F. Identification and characterization of the mouse obesity gene tubby: a member of a novel gene family. *Cell.* 1996;85:281–290.

Legue E., Liem K.F., Jr. Tulp3 is a ciliary trafficking gene that regulates polycystic kidney disease. *Curr. Biol.* 2019;29:803–812. e805.

Leus N.G., van den Bosch T., van der Wouden P.E., Krist K., Ourailidou M.E., Eleftheriadis N., Kistemaker L.E., Bos S., Gjaltema R.A., Mekonnen S.A., Bischoff R., Gosens R., Haisma H.J., Dekker F.J. HDAC1-3 inhibitor MS-275 enhances IL10 expression in RAW264.7 macrophages and reduces cigarette smoke-induced airway inflammation in mice. *Sci. Rep.* 2017;7:45047.

Li Q.Z., Wang C.Y., Shi J.D., Ruan Q.G., Eckenrode S., Davoodi-Semiromi A., Kukar T., Gu Y., Lian W., Wu D., She J.X. Molecular cloning and characterization of the mouse and human TUSP gene, a novel member of the tubby superfamily. *Gene.* 2001;273:275–284.

Mellacheruvu D., Wright Z., Couzens A.L., Lambert J.P., St-Denis N.A., Li T., Miteva Y.V., Hauri S., Sardiu M.E., Low T.Y., Halim V.A., Bagshaw R.D., Hubner N.C., Al-Hakim A., Bouchard A. The CRAPome: a contaminant repository for affinity purification-mass spectrometry data. *Nat. Methods.* 2013;10:730–736.

Montgomery D.C., Sorum A.W., Guasch L., Nicklaus M.C., Meier J.L. Metabolic regulation of histone acetyltransferases by endogenous Acyl-CoA cofactors. *Chem. Biol.* 2015;22:1030–1039.

Mukhopadhyay A., Deplancke B., Walhout A.J., Tissenbaum H.A. C. elegans tubby regulates life span and fat storage by two independent mechanisms. *Cell Metab.* 2005;2:35–42.

Mukhopadhyay S., Wen X., Chih B., Nelson C.D., Lane W.S., Scales S.J., Jackson P.K. TULP3 bridges the IFT-A complex and membrane phosphoinositides to promote trafficking of G protein-coupled receptors into primary cilia. *Genes Dev.* 2010;24:2180–2193.

Mukhopadhyay S., Jackson P.K. The tubby family proteins. *Genome Biol.* 2011;12:225.

Mukhopadhyay S., Wen X., Ratti N., Loktev A., Rangell L., Scales S.J., Jackson P.K. The ciliary G-protein-coupled receptor Gpr161 negatively regulates the Sonic hedgehog pathway via cAMP signaling. *Cell.* 2013;152:210–223.

Nishina P.M., North M.A., Ikeda A., Yan Y., Naggert J.K. Molecular characterization of a novel tubby gene family member, TULP3, in mouse and humans. *Genomics.* 1998;54:215–220.

Noben-Trauth K., Naggert J.K., North M.A., Nishina P.M. A candidate gene for the mouse mutation tubby. *Nature.* 1996;380:534–538.

North M.A., Naggert J.K., Yan Y., Noben-Trauth K., Nishina P.M. Molecular characterization of TUB, TULP1, and TULP2, members of the novel tubby gene family and their possible relation to ocular diseases. *Proc. Natl. Acad. Sci. U. S. A.* 1997;94:3128–3133.

Ohlemiller K.K., Hughes R.M., Mosinger-Ogilvie J., Speck J.D., Grosof D.H., Silverman M.S. Cochlear and retinal degeneration in the tubby mouse. *Neuroreport.* 1995;6:845–849.

Romero D. HDAC inhibitors tested in phase III trial. *Nat. Rev. Clin. Oncol.* 2019;16:465.

Sachdeva P., Minocha P., Choudhary A., Sitaraman S., Goya M. An unusual presentation of Rubinstein-Taybi Syndrome with bilateral postaxial polydactyly. *J. Pediatr. Neonatal Individualized Med.* 2016;5

Santagata S., Boggon T.J., Baird C.L., Gomez C.A., Zhao J., Shan W.S., Myszka D.G., Shapiro L. G-protein signaling through tubby proteins. *Science.* 2001;292:2041–2050.

Sartor I.T., Zeidan-Chulia F., Albanus R.D., Dalmolin R.J., Moreira J.C. Computational analyses reveal a prognostic impact of TULP3 as a transcriptional master regulator in pancreatic ductal adenocarcinoma. *Mol. Biosyst.* 2014;10:1461–1468.

Sartor I.T.S., Recamonde-Mendoza M., Ashton-Prolla P. TULP3: a potential biomarker in colorectal cancer? *PLoS One.* 2019;14

Szklarczyk D., Gable A.L., Lyon D., Junge A., Wyder S., Huerta-Cepas J., Simonovic M., Doncheva N.T., Morris J.H., Bork P., Jensen L.J., Mering C.V. STRING v11: protein-protein association networks with increased coverage, supporting functional discovery in genome-wide experimental datasets. *Nucleic Acids Res.* 2019;47:D607–D613.

Tate J.G., Bamford S., Jubb H.C., Sondka Z., Beare D.M., Bindal N., Boutselakis H., Cole C.G., Creatore C., Dawson E., Fish P., Harsha B., Hathaway C., Jupe S.C., Kok C.Y. COSMIC: the catalogue of somatic mutations in cancer. *Nucleic Acids Res.* 2019;47:D941–D947.

Wagner S.A., Beli P., Weinert B.T., Nielsen M.L., Cox J., Mann M., Choudhary C. A proteome-wide, quantitative survey of *in vivo* ubiquitylation sites reveals widespread regulatory roles. *Mol. Cell Proteomics.* 2011;10 M111 013284.

Wang M., Xu Z., Kong Y. The tubby-like proteins kingdom in animals and plants. *Gene.* 2018;642:16–25.